Optimising of Design Parameters of the TESLA Vertex Detector and Search for Events with Isolated Leptons and Large Missing Transverse Momentum with the ZEUS-Experiment (HERA II)

Dissertation
zur Erlangung des Doktorgrades
des Departments Physik
der Fakultät für Mathematik,
Informatik und Naturwissenschaften
der Universität Hamburg

vorgelegt von:

Volker Adler

aus Lüneburg

Hamburg
2006

Gutachter der Dissertation:	Prof. Dr. R. Klanner Prof. Dr. P. Schleper
Gutachterin/Gutachter der Disputation:	Prof. Dr. C. Hagner Dr. A. Geiser
Datum der Disputation:	10. Mai 2006
Vorsitzender des Prüfungsausschusses:	Dr. H. D. Rüter
Vorsitzender des Promotionsausschusses:	Prof. Dr. G. Huber
Leiter des Departments Physik:	Prof. Dr. R. Klanner
Dekan der Fakultät für Mathematik, Informatik und Naturwissenschaften:	Prof. Dr. A. Frühwald

Diese Arbeit ist Luci gewidmet,
der während ihrer Enstehung Lesen, Schreiben und Rechnen lernte —
und Flöte spielen.

Abstract

In this thesis, a search for events with isolated leptons and large missing transverse momentum at HERA is presented. Data with an integrated luminosity of 40.76 pb^{-1} of e^+p-collisions collected with the ZEUS detector at a CMS energy of 318 GeV during the HERA II running period in the years 2003 and 2004 were used. Some extensions of the Standard Model contain FCNC processes at tree level, which could lead to a significantly enhanced rate of singly produced t-quarks at HERA ($e^{\pm}p \to e^{\pm}tX$). The signature of interest originates from the decay $t \to bW^+$ with a subsequent leptonic decay of the W-boson ($W^+ \to e^+\nu_e, \mu^+\nu_\mu, \tau^+\nu_\tau$). After the final selection, one event was found in data in the combined e- and μ-channels, where 1.27 ± 0.15 were expected from SM predictions. The selection efficiency in these channels was $13.4^{+1.8}_{-0.8}\%$ for a t-quark mass of 175 GeV. In combination with independent searches in HERA I data in both, the leptonic and hadronic channel, limits on the FCNC couplings through photon and Z-boson exchange were derived. The NLO limit $\kappa_{tu\gamma} < 0.160^{+0.014}_{-0.012}$ at 95% CL for a t-quark mass of 175 GeV is the most stringent so far. Together with the most stingent limit on v_{tuz} of 0.37, an upper cross section limit of $\sigma_{single\,t} < 0.186^{+0.029}_{-0.012}$ pb was obtained. Also a limit on the cross section of single W-boson production of $\sigma_{single\,W} < 1.54^{+0.67}_{-0.41}$ pb was obtained at 95% CL.

In this thesis, also a simulation study to optimise design parameters of a MAPS based vertex detector for a future ILC is presented. The study was based on the TESLA TDR. In order to evaluate the effect of different design options for the vertex detector on the physics performance of the whole detector, the reconstruction of the t-quark mass from the signal process $e^+e^- \to t\bar{t}$ in the all-hadronic decay channel was used. The fast simulation program SGV was equipped with a neural-network based heavy-flavour tagging, where the b-tagging achieved a purity of 86% at an efficiency of 70%. It was found that the reconstruction of the t-quark mass was not successful due to resolution limitations in SGV. Nevertheless, today the combination of SGV and heavy-flavour tagging is used internationally for vertex detector design studies using other analysis branches.

Zusammenfassung

In diese Arbeit wird die Suche nach Ereignissen mit isolierten Leptonen und großem fehlenden Transversalimpuls bei HERA beschrieben. Dazu wurden Daten aus e^+p-Kollisionen mit einer integrierten Luminosität von $40.76\,\mathrm{pb}^{-1}$ verwendet, die mit dem ZEUS-Detektor bei einer Schwerpunktsenergie von 318 GeV während der HERA II Datennahmeperiode in den Jahren 2003 und 2004 genommen wurden. Einige Erweiterungen des Standardmodells eröffnen die Möglichkeit von FCNC-Prozessen, die zu einer messbaren Rate einzeln erzeugter t-Quarks bei HERA ($e^{\pm}p \to e^{\pm}tX$) führen können. Die gesuchte Signatur wird durch den Zerfall $t \to bW^+$ mit nachfolgendem leptonischen Zerfall des W-Bosons ($W^+ \to e^+\nu_e, \mu^+\nu_\mu, \tau^+\nu_\tau$) hervorgerufen. In den kombinierten e- und μ-Kanälen wurde ein Ereignis in den Daten gefunden, während 1.27 ± 0.15 aus Vorhersagen des Standardmodells erwartet werden. Die Effizienz der Selektion in diesen Kanälen betrug $13.4^{+1.8}_{-0.8}\%$. Zusammen mit unabhängigen Suchen in HERA I-Daten sowohl im leptonischen als auch im hadronischen Kanal wurden Grenzen für die FCNC-Kopplungen durch Photon- und Z-Boson-Austausch abgeleitet. Die NLO-Grenze $\kappa_{tu\gamma} < 0.160^{+0.014}_{-0.012}$ mit 95% CL, errechnet für eine t-Quark-Masse von 175 GeV, ist die bisher strengste. Zusammen mit der strengsten Grenze für v_{tuz} von 0.37 wurde eine obere Grenze für den Wirkungsquerschnitt von $\sigma_{single\,t} < 0.186^{+0.029}_{-0.012}\,\mathrm{pb}$ erhalten. Außerdem wurde eine Grenze für den Wirkungsquerschnitt der Erzeugung einzelner W-Bosonen von $\sigma_{single\,W} < 1.54^{+0.67}_{-0.41}\,\mathrm{pb}$ mit 95% CL erhalten.

Ebenfalls in dieser Arbeit wird eine Simulationsstudie zur Optimierung von Designparametern eines MAPS-basierten Vertexdetektors für einen zukünftigen ILC auf der Basis der TESLA TDR präsentiert. Um die Auswirkungen von Änderungen im Vertexdetektordesign auf die physikalische Leistungsfähigkeit des gesamten Detektors zu untersuchen, wurde die Rekonstruktion der t-Quark-Masse im vollständig hadronischen Zerfallskanal des Signalprozesses $e^+e^- \to t\bar{t}$ verwendet. Das schnelle Simulationsprogramm SGV wurde dazu mit einer Identifikation von schweren Quarks basierend auf neuronalen Netzen versehen, wobei die b-Identifikation eine Reinheit von 86% bei einer Effizienz von 70% erreichte. Aufgrund der Auflösungsgrenzen von SGV konnte die t-Quark-Masse allerdings nicht rekonstruiert werden. Inzwischen ist die Kombination von SGV mit der Identifikation von schweren Quark heute in Vertexdetektor-Designstudien mit anderen Analyseansätzen international im Einsatz.

Contents

Chapter 1

Introduction

The Standard Model of particle physics (SM) describes the electro-weak and strong interactions of elementary particles with excellent accuracy over the whole energy range currently accessible to experiments. However, many fundamental facts remain unexplained like e.g. the quark-lepton symmetry and the structure of the gauge groups. Also the incorporation of gravity has not succeeded yet. It is generally assumed, that in fact the Standard Model is a low-energy approximation of a more complete theory. The experimental observation of deviations from the Standard Model could pave the way for a theory, which provides a deeper understanding of the structure of matter. Rare Standard Model processes with clean experimental signatures in extreme regions of the phase space are good candidates to look for such deviations.

At HERA, events with isolated leptons and large missing transverse momentum are an example for such processes. The event rate expected from the Standard Model is very small and any excess over these predictions would provide a hint of new physics beyond the Standard Model. One Standard Model process, the direct production of single W-bosons, has a measurable cross section at HERA of about 1 pb. The signature of interest originates from the subsequent leptonic decay of the W-boson. The production of single t-quarks via flavour-changing neutral currents (FCNC) also leads to isolated leptons and large missing transverse momentum by its dominant decay to a W-boson and a b-quark with the W-boson decaying leptonically. However, in the Standard Model no sizable cross section is predicted. These events would be characterised by the presence of additional large hadronic transverse momentum originating from the b-quark. Some extensions to the Standard Model contain processes, which enhance the rate of FCNC with singly produced t-quarks. In the past, the H1 and ZEUS experiments at HERA observed excesses in this regime. H1 reported an accumulating excess of such events in the electron/positron and muon decay channels. On the other hand, ZEUS observed an excess in the τ-lepton channel with a Poisson-probability of 1.8% for the data taken during 1994 –

2000.

In the analysis presented here, events with isolated leptons and large missing transverse momentum in data of an integrated luminosity of $40.76\,\mathrm{pb}^{-1}$ collected with the ZEUS detector in the years 2003 and 2004 at a center-of-mass energy of 318 GeV were searched for.

Besides looking for deviations from the Standard Model with existing experiments, the validity of certain models, like supersymmetry, can be tested by experiments of striking accuracy at energies, which were inaccessible in the past and where the effect of these extensions is expected to become more visible. An important mile-stone is the Large Hadron Collider (LHC) presently built in Geneva, Switzerland, a proton-proton collider with a center-of-mass energy of 14 TeV – seven times higher than the energies achieved so far. The next step is also under preparation: An international linear collider (ILC) with electron-positron collisions up to the TeV-regime will contribute significantly with discoveries and precision measurements to the completion of our knowledge about the structure of matter. A worldwide research and development effort is ongoing. The TESLA project proposed at the Deutsches Elektronen-Synchrotron (DESY), Hamburg, Germany, represents one branch of the ILC design.

The vertex detector for a future ILC detector will need to provide an unprecedented accuracy in order to reconstruct the decay of unstable particles with long lifetimes. Several sensor technologies are presently being developed and their performance is being studied. Also the most effective architecture for the future vertex detector is being investigated.

In this thesis, a simulation study to obtain optimised design parameters of a vertex detector based on the technology of monolithic active pixel sensors is presented. A full physics analysis was applied to simulated data. These data were generated using an existing fast simulation and reconstruction tool, which was upgraded to contain a sophisticated heavy-flavour tagging algorithm. The study was carried out using the TESLA parameters. In the meantime, TESLA has merged with the worldwide ILC community.

This thesis is organised as follows: Chapter two outlines the theoretical framework relevant for the following analysis. The Standard Model is described and SM processes in electron/positron-proton collisions at HERA considered in the analysis are explained for both, signal and background sources. Also models beyond the Standard Model are sketched and expected HERA reactions are described, which could produce the signature of interest with emphasis on supersymmetric models. Chapter three describes the HERA collider and the ZEUS experiment, which were used for the actual analysis. Chapter four gives the general strategy of the analysis and explains, how the signal processes and several background sources contribute to the signature of interest. Chapter five gives an overview of the data taken with the ZEUS detector and the Monte Carlo simulations used. The latter play a key role in

the final determination of limits. In chapter six, the variables used in the analysis are defined and their reconstruction is explained. The search for events with isolated leptons and large missing transverse momentum is described in chapter eight. It is split in five selection stages: A sample selection with very basic requirements on the selected events based on earlier analyses of HERA I data was used to study the backgrounds in HERA II not originating from electron/positron-proton collisions. The additional rejection of such backgrounds leads to the control selection, where kinematic variables were monitored for a rather large data sample. In the pre-selection, events with isolated lepton candidates were selected and isolated tracks were identified as electron/positron, muon or τ-lepton. The final selection of W-boson candidates rejected the most important SM background processes individually for each leptonic channel and the final selection of t-quark candidates was used to isolate events with the typical signature of singly produced t-quarks at HERA. In chapter eight, the results of this search are discussed. Based on these results for the electron/positron and muon channel, limits on the production of single t-quarks via FCNC were computed. Also a limit on the production cross section for single W-bosons was derived from the results of the fourth selection stage. The results in the τ-lepton channel were monitored with respect to the excess observed in the earlier search. In chapter nine, Monte Carlo studies for the design of the vertex detector of the future ILC are described. The TESLA project, which was the basis for this study, is introduced and various possible sensor technologies for the vertex detector are described including monolithic active pixel sensors, for which this study was carried out. The fast simulation program SGV used in this study is described and the implementation of a neural-network based heavy-flavour tagging algorithm into SGV is explained. This implementation was necessary to cope with the extremely high reconstruction accuracy of the proposed vertex detector. Monte Carlo studies for one particular physics process were made and compared with a similar analysis based on a full simulation of the TESLA detector. Chapter ten summarises the results of both, the ZEUS analysis and the TESLA simulation studies.

Chapter 2

Theoretical Overview

This chapter introduces the Standard Model of particle physics as the present basic framework of high-energy physics. Also some extensions to the Standard Model are discussed, if relevant for this analysis. Lepton-proton scattering at HERA is discussed emphasising the processes to be considered in a search for isolated leptons. Finally, possible production mechanisms of isolated leptons – within and beyond the Standard Model – are described.

2.1 The Standard Model

In the *Standard Model* (SM) of particle physics, the fundamental constituents of matter are spin-1/2 particles (*fermions*), which are described in quantum field theories as complex field quanta governed by Lagrangian densities. The requirement that the Lagrangian must not be changed by a local phase transformation (*gauge invariance*) leads directly to the existence of an external field, which is generated by a gauge transformation of the vacuum. This gauge transformation compensates for the local phase transformation. The corresponding field quantum is a massless spin-1 particle (*boson*): the *gauge boson*. It acts as mediator of the force between the fermions.

Three basic forces (*interactions*) are contained in the Standard Model: the *electromagnetic*, the *weak* and the *strong interaction*. The strong interaction, described by *quantum chromodynamics* (QCD), is represented by gauge transformations of the group $SU(3)$. The electromagnetic interaction, described by *quantum electrodynamics* (QED), and the weak interaction are unified into one *electroweak interaction* in the gauge group $SU(2)_L \times U(1)$ [1]. While gauge invariance requires massless gauge bosons, the weak interaction is experimentally known to be mediated by massive bosons, thus breaking the gauge invariance. The problem is solved by treating them

[1] The index L denotes a coupling to the left-handes chirality component only.

as massless and creating their masses afterwards from a scalar background field, which shields the weak interaction and does not change the gauge invariance. The electroweak unification can take place at an energy of the order of the weak gauge boson masses. The scalar background field is called the *Higgs field* [2]. This effect is called *hidden gauge invariance* [3] or *spontaneous symmetry breaking*. The Higgs boson has not been observed so far, with a current mass limit at $m_H > 114.4\,\mathrm{GeV}$[2]. From the theoretical point of view, the compensation of divergencies in the weak interaction through the introduction of the Z^0-boson in addition to the $W^{\pm}$-bosons works only for

$$m_H < \left(\frac{8\pi\sqrt{2}}{3G_F}\right)^{1/2} \approx 1\,\mathrm{TeV}, \tag{2.1}$$

with the Fermi constant $G_F = 1.166 \cdot 10^{-5}\,\mathrm{GeV}^{-2}$.

The weak and the strong interaction are described by renormalisable *non-Abelian* (non-commutative) gauge theories[3]. The non-Abelian nature brings about self-coupling of the gauge bosons. Renormalisability, which is needed to obtain finite results in *perturbation theory*, leeds to running coupling constants. For example, the electromagnetic coupling α depends on Q^2 like

$$\alpha(Q^2) = \frac{\alpha}{1 - \frac{\alpha}{3\pi}\ln\frac{Q^2}{Q_0^2}} \tag{2.2}$$

with $Q_0^2 = m_e^2$[4] and $\alpha = \alpha(Q_0^2) \approx 1/137$. The strong interaction α_s depends on Q^2 so, that the coupling increases for lower Q^2 and becomes zero for $Q^2 \to \infty$ [10] as seen at one-loop level from

$$\alpha_s(Q^2) = \frac{12\pi}{(33 - 2N_f)\ln\frac{Q^2}{\Lambda^2}} \tag{2.3}$$

with

$$\Lambda^2 = Q_0^2 \exp\left(-\frac{12\pi}{(33 - 2N_f)\alpha_s(Q^2)}\right) \tag{2.4}$$

and the number of degrees of freedom $N_f \leq 16$. $N_f = 6$ is assumed (two fermionic degrees of freedom for each generation) and Λ is not calculable in QCD. Its definition is arbitrary and depends on the considered process. The case of decreasing coupling is called *asymptotic freedom*, whereas a coupling of the order of 1 describes the case of *confinement*. In the latter case an analytical treatment by perturbation theory is not possible for calculations. The interactions of the Standard Model and the gauge bosons are listed in Tab. 2.1. *Gravity* as the fourth interaction is not incorporated

[2] All numbers and constants given in this section are from [4].

[3] It is proven, that non-Abelian gauge theories are renormalisable [9].

[4] electron mass $m_e = 0.511\,\mathrm{MeV}$

	Interaction			
	el.-magn.	weak		strong
Gauge boson	*photon* (γ)	$W^{\pm}$	Z^0	8 *gluons* (g)
Mass (GeV)	$< 6 \cdot 10^{-26}$	80.425 ± 0.038	91.188 ± 0.0021	0
Charge	0	± 1	0	0
Gauge group	$SU(2)_L \times U(1)$			$SU(3)$

Table 2.1: Fundamental forces of the Standard Model
For the gauge bosons, the mass eigenstates are listed. In fact, the neutral electroweak gauge bosons γ and Z^0 are mixtures of the field quanta W^0 and B^0 of the electroweak theorie. They are connected via the *weak mixing angle (Weinberg angle)* [5] with $\sin^2 \theta_W = 0.23149(15)$. Charges are given in units of the elementary charge.

in the Standard Model. Anyway it is 36 orders of magnitude weaker than the other interactions and irrelevant for the considered energy region.

The fermions are divided into two groups, the *leptons* (l) and the *quarks* (q) [11], and each group has three *doubletts* with two particles each. The doubletts of each group differ only by the particle masses, not by interactions (*universality*). The quark and lepton-doublett of one order in mass form a *generation*[5]. In addition for each particle X there exists an antiparticle $\bar{X}$, which has the same mass but opposite quantum numbers. Also the charged fermions obtain their masses from the Higgs field. This results in proportionality of the Higgs-fermion coupling to these masses. The fermions are listed in Tab. 2.2

Whether a particular particle participates in an interaction depends on its charge. The photon couples to *electric charges*, the weak gauge bosons couple to *weak hypercharges* and the gluons to *colour charges*. Due to confinement free quarks and gluons cannot exist, but are forced to form colour neutral objects (colour singletts): the *hadrons*. Through electroweak unification, electric charge and weak hypercharges are connected via the Weinberg angle as the neutral gauge bosons are. In addition, quarks of charge $-1/3$ do not couple directly to the weak gauge bosons but via superpositions with quarks from other families [6]. This allows weak transitions from one quark doublett to another. The corresponding mixing angles form the *Cabibbo-Kobayashi-Maskawa (CKM) matrix* V_{CKM}. The complex phase in the off-diagonal elements of V_{CKM}[6] allows CP*-violation* for weak decays. Indeed, CP-violation is one of three requirements[7] for the particle-antiparticle asymmetry in the universe and

[5] Our "world" is built from the charged particles of the first generation: the u- and d-quark from the first quark-doublett and the electron from the first lepton-doublett.

[6] The existance of this complex phase requires at least three generations.

[7] The other requirements are baryon number violation (see 2.2.1) and thermal non-equilibrium in a certain early phase of the universe.

		Doubletts			
		Quarks		Leptons	
Generation	1 Mass (MeV)	d 4–8	u 1.5–4	e^- 0.511	ν_e $< 3 \cdot 10^{-6}$
	2 Mass (MeV)	s 80–130	c 1150–1350	μ^- 105.7	ν_μ < 0.19
	3 Mass (GeV)	b 4.1–4.9	t 174.3 ± 5.1	τ^- 1.777	ν_τ < 0.0182
Charge		$-1/3$	$+2/3$	-1	0
Interaction	el.-magn.	yes	yes	yes	no
	weak	yes	yes	yes	yes
	strong	yes	yes	no	no

Table 2.2: Fundamental fermions of the Standard Model
Note, that masses are given on different scales. Charges are given in units of the elementary charge. Everything is also valid for the corresponding antiparticles (charges with opposite sign).

so for the existence of life in the end [7]. Additional transitions from one family to another occur within neutrinos (*neutrino-oscillation*), which implies that neutrinos have mass.

Thus, a complete description of the Standard Model is given in terms of gauge invariance, the threefold symmetry $SU(3) \times SU(2)_L \times U(1)$ and the three fermion generations with two doubletts each. In addition, 33 natural constants are needed, which are unpredicted within the Standard Model and have to be determined experimentally. They are [8]:

- the 12 fermion masses,
- the gravitational constant G_N and the cosmological constant Ω_Λ,
- the strong coupling constant α_s,
- three constants to describe the electroweak interaction, e.g. the electromagnetic coupling constant α, the Fermi constant G_F and the Weinberg angle θ_W,
- four constants of the CKM-matrix (three angles and one phase),
- four constants to describe CP-violation phenomenologically,
- four constants to describe neutrino-oscillation,

- the speed of light c, the reduced Planck constant $\hbar$ and the Higgs mass m_H.

The Standard Model has been tested extensively over many years and with highest precision. No significant deviations from its predictions have been found so far. However, there are still open questions and problems. Some of them are listed in the following:

Higgs boson: As mentioned above, the Higgs boson has not been observed so far. Its existence is essential for the validity of the Standard Model.

Fine-tuning problem: At higher scales, radiative corrections to the Higgs mass are many orders of magnitude higher than the Higgs mass itself.

Hierarchy problem: Why are scales so different? The electroweak unification takes place around the mass of the Z^0 (m_Z). The unification with the strong coupling is extrapolated to take place at about 10^{16} GeV, which is 14 orders of magnitude higher.

Particle masses: The particle masses are not explained by the Standard Model. Their spread over many orders of magnitude is puzzling.

Number of Generations: The existence of three particle families is not explained by the Standard Model.

Gravity: Gravity is not incorporated in the Standard Model. The weakness of its coupling is not understood.

It is widely believed that the Standard Model is only a low energy approximation to a more complete theory. Extensions to the Standard Model have been proposed, such as e.g. Grand Unified Theories (GUT), Supersymmetry (SUSY)[8] or string theories. Therefore, searches for deviations from the Standard Model are also searches for indications of a more general theory.

2.2 Beyond the Standard Model

Although the Standard Model has been rather successful in predicting experimental results in the past, one expects new physics at an energy scale around 1 TeV, that will be accessible in the near future. However, new phenomena are not only accessible at that energy scale. Even at lower energies it makes sense to search for indications of physics *beyond the Standard Model* (BSM), which might manifest itself via virtual contributions. This strategy was successful in the past by e.g. pinning down the t-quark mass via electroweak measurements at LEP [14].

[8] see 2.2.1 and 2.2.2, respectively

In the following, short descriptions of some theories beyond the Standard Model are given with emphasis on the best understood and promising ones, the Grand Unified Theories and Supersymmetry. How they possibly can contribute to the signature of interest in this analysis is described in more detail in 2.4.2.2 and 2.4.3. The given descriptions of the theories are partially based on the summaries in [15].

2.2.1 Grand Unified Theories

The philosophy of *Grand Unified Theories (*GUT*)* is based on the hypothesis, that electromagnetic, weak and strong interaction are different branches of one single interaction. The unification takes place at rather high energies of more then $10^{14}\,\mathrm{GeV}$, where the couplings are of similar strength and one single symmetry dominates. With today's experiments, we only can see the low energy part, where this symmetry is broken and the couplings split up.

The underlying assumption in GUT is, that there is only one single gauge symmetry with the symmetry group $G_{\mathrm{GUT}} = SU(N)$ and $SU(3) \times SU(2)_L \times U(1) \subset G_{\mathrm{GUT}}$. It is spontaneously broken by a Higgs field, which gives mass to the so-called *X-bosons* with an estimated mass of $m_X \simeq 5 \times 10^{14}\,\mathrm{GeV} < m_P = 10^{19}\,\mathrm{GeV}$, where m_P denotes the *Planck mass*. Only the second symmetry breaking at the weak scale gives then mass to quarks, leptons and the gauge bosons. The simplest GUT is $SU(5)$ with 24 gauge bosons: the twelve we already know and six coulored, charged bosons and their antiparticles. They are called *leptoquarks* and can convert quarks into leptons and vice versa. Lepton number (L) and baryon number (B) are not conserved then, but $B - L$.

Although GUT gives some correct predictions like e.g. for the Weinberg angle, there are some essential problems: GUT predicts magnetic monopoles without electric charge, that have not been observed so far. And it also predicts the proton decay on a time scale, which has been excluded experimentally already. But the most essential problem is, that – contrary to its name – GUT alone is *not* able to unify the couplings exactly in one point! This is shown in Fig. 2.1(a).

2.2.2 Supersymmetry

The concept of *Supersymmetry (*SUSY*)* has been developed to solve problems of the Standard Model like e.g. the hierarchy or the fine-tuning problem. *Fine-tuning* means a highly accurate renormalisation in all orders of perturbation theory to get rid of divergencies from radiative corrections to the Higgs mass, which is rather "unnatural"[9]. Since bosons and fermions contribute with different signs to these corrections, the idea is to connect them via a new symmetry so, that the corrections

[9]The fine-tuning problem is also called *naturalness problem*

cancel out each other. In the simplest case, this can be achieved, if every particle X has a *super-partner* $\tilde{X}$ with the same gauge quantum numbers and a spin difference of 1/2. SUSY does not distinguish between fermions (particles) and bosons (interactions). It doubles the number of particles. Pairs of a particle and its super-partner constitute a *super-multiplett* as the representation of the SUSY algebra. There is a SUSY transformation between the super-partners and they even have the same mass. However, no *Sparticle*[10] has been observed so far. Thus, SUSY must be broken to let the Sparticles gain higher masses. Finally, a correction of

$$\Delta(m_H^2) = \mathcal{O}\left(\left(\frac{\alpha}{4\pi}\right)\left|m_b^2 + m_f^2\right|\right) \tag{2.5}$$

remains to the Higgs mass m_H, where m_b and m_f are the masses of the bosonic (S)particle and its fermionic super-partner, respectively. And this correction stays small, as long as $\left|m_b^2 + m_f^2\right| < 1\,\text{TeV}$ (*weak* SUSY breaking).

The simplest SUSY extension to the Standard Model is called *Minimal Supersymmetric Model* (MSSM). It contains the minimal number of new particles and interactions and every super-multiplett contains one fermion and one boson as super-partners with the same number of degrees of freedom. The SM fermions have scalar super-partners with spin 0 (*scalar* or *chiral super-multiplett*)[11], the SM gauge bosons have fermionic super-partners with spin 1/2 (*gauge super-multiplett*) and the *graviton*[12] (G, spin 2) has a super-partner with spin 3/2. The SM Higgs particle is a scalar and so it belongs to a chiral super-multiplett. Contrary to the Standard Model, two Higgs dubletts ($H_d = (H_d^0, H_d^-)$, $H_u = (H_u^+, H_u^0)$) are needed, which differ in the weak hypercharge and have eight degrees of freedom. Three of them contribute to the masses of the weak gauge bosons, the other five form the mass eigenstates of five Higgs bosons:

- light neutral scalar h^0 (SM Higgs)
- heavy neutral scalar H^0
- neutral pseudo-scalar A^0
- charged scalars H^+, H^-

h^0 and H^0 are mixings of $Re\,(H_d^0)$ and $Re\,(H_u^0)$ with the mixing angle α. The A^0 is a mixing of $Im\,(H_d^0)$ and $Im\,(H_u^0)$ and H^+ and H^- are mixings of H_d^- and H_u^+ with the common mixing angle β. The chiral and the gauge super-multipletts are listed in Tabs. 2.3 and 2.4, respectively.

[10] SUSY particle

[11] Since the fermions have two degrees of freedom from their spin, even the scalars need two degrees of freedom from complexity.

[12] The graviton is the gauge boson of gavity.

super-field quantum		fermion	scalar
quarks, *Squarks*	Q_i	u_L, d_L	$\tilde{u}_L$, $\tilde{d}_L$
(3 generations)	$\bar{U}_i$	u_R^*	$\tilde{u}_L^C$
	$\bar{D}_i$	d_R^*	$\tilde{d}_L^C$
leptons, *Sleptons*	L_i	ν_L, e_L	$\tilde{\nu}_L$, $\tilde{e}_L$
(3 generations)	$\bar{E}_i$	e_R^*	$\tilde{e}_L^C$
Higgs, *Higgsino*	H_d	$\tilde{H}_d^0$, $\tilde{H}_d^-$	H_d^0, H_d^-
	H_u	$\tilde{H}_u^+$, $\tilde{H}_u^0$	H_u^+, H_u^0

Table 2.3: Chiral super-multiplett
The index i denotes the generations. The asterisk $*$ denotes conjugated, the superscript C charge-conjugated states. The subscripts L and R of the fermions denote their chirality, those of the scalars the chirality of the super-partner.

super-field quantum	gauge boson	fermion (*gaugino*)
gluon, *gluino*	g	$\tilde{g}$
W-boson, *Wino*	$W^\pm$, W^0	$\tilde{W}^\pm$, $\tilde{W}^0$
B-boson, *Bino*	B^0	$\tilde{B}^0$

Table 2.4: Gauge super-multiplett
With electroweak symmetry breaking, W^0 and B^0 mix to Z^0 and γ. Similarly, $\tilde{W}^0$ and $\tilde{B}^0$ mix to $\tilde{Z}^0$ (Zino) and $\tilde{\gamma}$ (photino).

While the SM fermions gain their masses from the Higgs mechanism, for the scalar super-partners an additional mass term exists, which causes the SUSY breaking. The SUSY breaking mechanism itself is still unknown and a parametrising ansatz leads to 105 (!) free parameters in the MSSM. But experimental constraints showed relations between these parameters and with some reasonable additional assumptions only 14 parameters stay independent. This model is able now to unify the coupling constants as shown in Fig. 2.1(b) [17]. The compared coupling constants are:

$$\alpha_1 = \frac{5\alpha}{3\cos^2\theta_W}, \tag{2.6}$$

$$\alpha_2 = \frac{\alpha}{\sin^2\theta_W}, \tag{2.7}$$

$$\alpha_3 = \frac{g_s^2}{4\pi}, \tag{2.8}$$

where g_s is proportional to $\sqrt{\alpha_s}$. From the unifying fit one can predict the scales

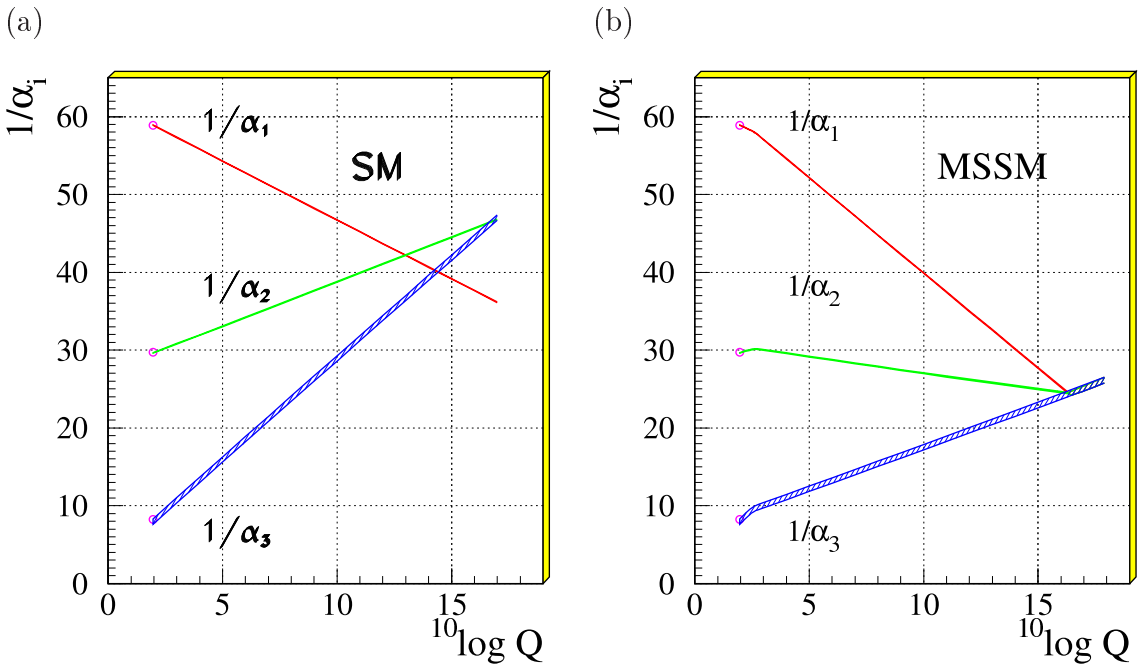

Figure 2.1: Extrapolations of coupling constants in GUT
The coupling constants $\alpha_i, i = 1, 2, 3$ are explained in the text. (a) GUT is the only extension to the SM. The coupling constants do not unify there. (b) The MSSM is added and the couplings unify at $Q \approx 2 \cdot 10^{16}$ GeV.

M_{SUSY} and M_{GUT} as well as the coupling constant α_{GUT}:

$$\begin{aligned} M_{\text{SUSY}} &= 10^{3.4\pm0.9\pm0.4}\,\text{GeV}, \\ M_{\text{GUT}} &= 10^{15.8\pm0.3\pm0.1}\,\text{GeV}, \\ \alpha_{\text{GUT}}^{-1} &= 126.3 \pm 1.9 \pm 1.0\,, \end{aligned} \tag{2.9}$$

where the first error comes from the errors on the coupling constants and the second error from the mass splitting in MSSM. If one assumes the two Higgs dubletts from SUSY to be realised, the theoretical relation of the gradients of the coupling constants gives 0.714, where a value of $0.719 \pm 0.008 \pm 0.03$ has been measured [16].

Furtheron, one can assume a universality of masses, which means that all masses of the supersymmetric scalars and gauginos are equal at the GUT scale. Then the number of parameters is reduced to five, where one usually uses:

- $m_{1/2}$ (gaugino mass),
- m_0^2 (scalar mass),
- m_A (mass of Higgsino A),
- $\tan\beta = \frac{<H_u>}{<H_d>}$ and
- phase of complex mass term μ with the Higgs mass $\sqrt{m_0^2 + \mu^2}$.

How the masses split, can be seen in the examples in Fig. 2.2. In particular, the evolution of $m_{H_u}^2$ is remarkable, because it becomes negative for low energies, which results automatically in the electroweak symmetry breaking.

Two proposals for the SUSY breaking mechanism are favoured at the moment:

***Minimal Supergravity* (mSUGRA):** This model assumes, that the SUSY breaking terms are caused by gravity or new physics at the Planck scale. The *gravitino* ($\tilde{G}$) is very heavy

***Gauge Mediated* SUSY *Breaking* (GMSB):** Here the SUSY breaking is caused by the gauge interactions with a light $\tilde{G}$, which usually is the *lightest* SUSY *particle* (LSP). The lightest *neutralino* ($\tilde{Z}$ or $\tilde{\gamma}$) can decay into a $\tilde{G}$ and a SM particle.

SUSY introduces a new multiplicative quantum number: the *R-parity*. It is defined as

$$P_R = (-1)^{3(B-L)+2S} \tag{2.10}$$

with the particle spin S. SM particles have $P_R = +1$ and Sparticles have $P_R = -1$. If P_R is conserved, Sparticles can be produced only in pairs, every vertex has an

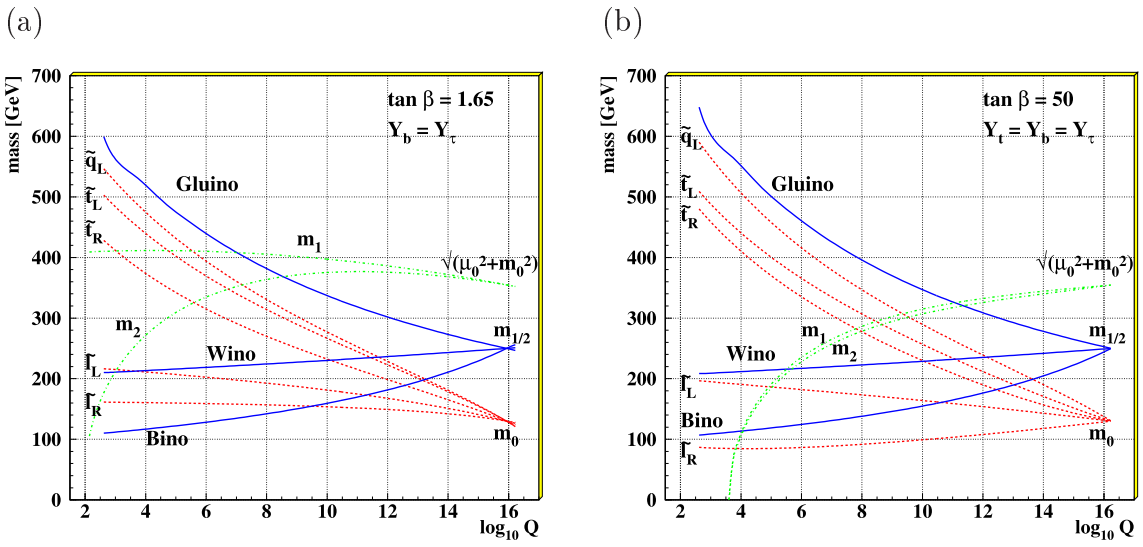

Figure 2.2: Evolution of Sparticle masses and soft SUSY breaking parameters [17]
Examples are given for (a) low and (b) high values of $\tan\beta$. m_1 and m_2 denote the soft SUSY breaking parameters $m^2_{H_d}$ and $m^2_{H_u}$, respectively.

even number of Sparticles and the LSP is stable. In case that the LSP is neutral, it would be a good candidate for *dark matter*. But also *R-parity violation* (RPV) is allowed by the most general Lagrangian. There the term

$$\mathcal{L}_{RPV} = \lambda_{ijk} L^i_L L^j_L \bar{E}^k_R + \lambda'_{ijk} L^i_L Q^j_L \bar{D}^k_R + \lambda''_{ijk} \bar{U}^i_L \bar{D}^j_L \bar{D}^k_R + \text{h.c.} \tag{2.11}$$

exists with the coupling parameters λ, λ', λ'' and the generation indices i, j, k. The capital letters denote the chiral superfields of leptons (L), charged leptons (E), quarks (Q), d-type quarks (D) and u-type quarks (U). The indices L and R denote left-handed doubletts and right-handed singletts, respectively. One can see, that the first two couplings do not conserve the lepton number L while the third coupling does not conserve the baryon number B. Further one can see, that different collider experiments are sensitive to different couplings: lepton-lepton colliders like LEP[13] or a future ILC[14] are sensitive to λ and hadron-hadron colliders like TEVATRON or LHC[15] to λ''. HERA as a lepton-hadron collider provides the opportunity to test λ'. This option can be explored by a search for deviations from the Standard Model in the production of isolated leptons as explained in 2.4.3.1.

[13] Large Electron-Positron collider
[14] International Linear Collider
[15] Large Hadron Collider

2.3 Lepton-Proton Scattering at HERA

Scattering experiments have been a rich source of insight for understanding the structure of matter. Scattering leptons on hadrons is a very appropriate method to study the structure of the hadron, since the pointlike lepton acts as a probe for the proton, whose kinematic properties are known very well. At HERA[16], electrons (e^-) or positrons (e^+)[17] are brought to collision with protons (p) at a center-of-mass (CMS) energy of 318 GeV. Besides the structure of the proton this also probes the nature of electroweak and strong interactions with high precision.

2.3.1 Kinematics

Fig. 2.3 illustrates electron-proton scattering at HERA. The incoming electron

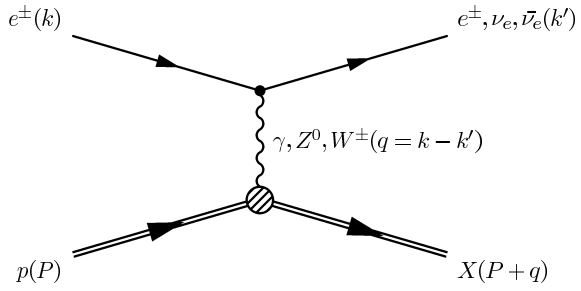

Figure 2.3: Illustration of lepton-proton scattering at HERA
X denotes the outgoing hadronic system (*hadronic final state*). The four-vectors of the particles are given in parenthesis.

interacts with the incoming proton via the exchange of a virtual vector boson in a *charged current* (CC) or *neutral current* (NC) process. The NC process is mediated by the sum of photon and Z^0-boson exchange. In the CC process, a W-boson is exchanged, which transforms the incoming electron into an outgoing neutrino.

Given the four-vectors of the initial and final state, $k = (E_e, \vec{k})$, $P = (E_p, \vec{P})$ and $k' = (E'_l, \vec{k'})$, $P' = (E'_X, \vec{P'})$, where E_e, $\vec{k}$ and E_p, $\vec{P}$ are the energies and momenta of the incoming electron and proton, respectively, and E'_l, $\vec{k'}$ and E'_X, $\vec{P'}$ the energies and momenta of the outgoing lepton and hadronic system, respectivly, the event kinematics for unpolarised electrons and protons can be described in terms of the

[16] HERA and its experiments are described in more detail in 3.
[17] Both are commonly referred to as "electrons" e in this thesis, if not indicated differently.

following Lorentz-invariant variables:

$$\begin{aligned} s &= (k+P)^2\,, && (2.12)\\ Q^2 &= -q^2 \\ &= -(k-k')^2, \quad 0 \le Q^2 \le s\,, && (2.13)\\ x &= \frac{Q^2}{2P\cdot q}, \qquad 0 \le x \le 1\,, && (2.14)\\ y &= \frac{P\cdot q}{P\cdot k}, \qquad 0 \le y \le 1\,. && (2.15) \end{aligned}$$

$\sqrt{s}$ is the CMS energy, and Q^2 is the negative square mass of the exchanged boson, which denotes its virtuality and determines the resolution of the interaction by way of the *Heisenberg uncertainty principle*:

$$\lambda = \frac{1}{\sqrt{Q^2}}\,. \tag{2.16}$$

At HERA virtualities up to $Q^2 = 40000\,\mathrm{GeV}^2$ are accessible. This is equivalent to a distance scale of $\lambda = 10^{-18}\,\mathrm{m}$. In the *quark parton model* (QPM) [12], the *Bjorken scaling variable* x [13] denotes the fraction of the proton momentum carried by the parton, that interacts with the electron. This parton is identified with a constituent of the proton, which can be a valence or a sea quark. The *inelasticity parameter* y can be interpreted as the fraction of the lepton energy transferred to the hadronic system in the rest frame of the proton. In this system HERA collisions are equivalent to fixed target collisions with an incident lepton energy of about 50 TeV. The variables are related by the equation

$$Q^2 = sxy\,. \tag{2.17}$$

Since $\sqrt{s}$ is fixed at HERA[18], only two of the four variables are independent.

2.3.2 Deep Inelastic Scattering

Deep inelastic scattering (DIS) of electrons and protons is defined as the interaction of a highly virtual gauge boson[19] emitted from the incoming electron with the proton. In the QPM, DIS is described as the incoherent sum of elastic scattering processes of the lepton off electrically charged point-like constituents (*partons*) of the proton. The partons, which do not interact amongst themselves in this model, are identified with the quarks in the proton. Neglecting radiative corrections, DIS can be described

[18] see 3.1
[19] $Q^2 > 1\,\mathrm{GeV}^2$

in terms of the *structure functions* $F_1(x,Q^2)$, $F_2(x,Q^2)$, $F_3(x,Q^2)$[20] and $F_L(x,Q^2)$[21], which describe the distribution of the charged constituents of the proton. At leading order, the double differential cross sections with respect to x and Q^2 for NC and CC DIS in ep-scattering is given in terms of these structure functions as:

$$\frac{d^2\sigma^{NC}(e^{\pm}p \to e^{\pm}X)}{dx\,dQ^2} = \frac{2\pi\alpha^2}{xQ^4}\left[Y_+F_2^{NC} \mp Y_-xF_3^{NC}\right], \tag{2.18}$$

$$\frac{d^2\sigma^{CC}(e^{\pm}p \to \nu X)}{dx\,dQ^2} = \frac{G_F^2}{4\pi}\left(\frac{M_W^2}{M_W^2+Q^2}\right)^2\left[Y_+F_2^{CC} \mp Y_-xF_3^{CC}\right], \tag{2.19}$$

with $Y_\pm = 1 \pm (1-y)^2$. In the QPM, F_1 and F_2 can be expressed as a sum of the quark- and antiquark densities in the proton and are related by the Callan-Gross relation [18]:

$$F_2 = 2xF_1\,. \tag{2.20}$$

At low $Q^2 \ll M_{Z,W^\pm}^2$, the ep cross section is dominated by photon exchange. The exchange of weak gauge bosons is suppressed by their large masses and contributes only for large values of Q^2:

$$\frac{\sigma(Z,W^\pm)}{\sigma(\gamma)} \propto \left(\frac{Q^2}{Q^2+M_{Z,W^\pm}^2}\right)^2. \tag{2.21}$$

Fig. 2.4 shows the differential NC and CC cross sections measured at HERA as a function of Q^2 for e^-p- and e^+p-scattering. The CC cross section is suppressed with respect to the NC cross section below values of Q^2 close to the weak gauge boson masses ($\mathcal{O}(10^4\,\mathrm{GeV}^2)$). At that scale, γ-Z-interference becomes important and leads to sizable deviations from the pure QED-prediction. The CC cross section is larger for e^-p-scattering than for e^+p-scattering due to the larger u-quark content of the proton, which is relevant for the W^--exchange in e^-p CC processes, as opposed to the smaller d-quark content, which is relevant for the W^+-exchange in e^+p CC processes.

At present the distribution of partons in hadrons cannot be calculated from first principles. A separation of the short-range high-energy part (hard process) of a DIS interaction from the long-range low-energy part (soft process) is introduced, called *factorisation*. In this approach, the proton structure function F_2 is expressed as a convolution of the perturbatively calculable hard scattering subprocess and the *parton distribution functions* (PDF) f_i:

$$F_2(x,Q^2) = \sum_i \int_x^1 \mathrm{d}x'\, f_i(x',\mu_F^2)\,\hat{\sigma}_i\left(\frac{x}{x'},Q^2,\mu_F^2\right), \tag{2.22}$$

[20] The parity violating structure function F_3 is negligible at $Q^2 \ll M_{Z,W^\pm}$.

[21] At first order in perturbative QCD, the longitudinal structure function F_L is zero.

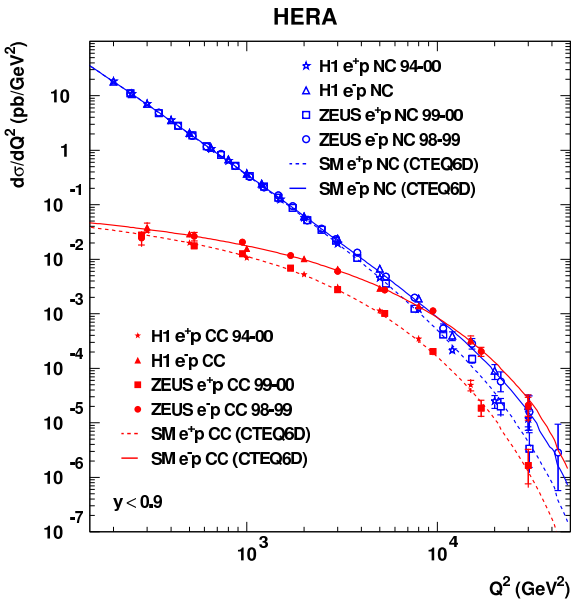

Figure 2.4: Differential DIS cross sections at HERA [19]
Differential NC and CC cross sections as a function of Q^2 measured at HERA. Lines correspond to fits to global DIS data.

where $f_i(x', \mu_F^2)$ is the probability to find parton i with momentum fraction x' in the proton and $\hat{\sigma}_i\left(\frac{x}{x'}, Q^2, \mu_F^2\right)$ is the cross section for that parton to scatter elastically off a photon with virtuality Q^2. The quark can radiate a gluon before interacting, thus lowering its effective momentum fraction of the total proton momentum from x' to x. The *factorisation scale* μ_F defines the scale at which this gluon radiation is absorbed into the PDF rather than into the hard scattering cross section. The structure function F_2 as a physical observable is independent of the arbitrary choice of μ_F. Fig. 2.5 shows measurements of F_2 from HERA and fixed-target experiments compared to SM predictions. For $x > 0.1$, F_2 stays almost constant over the whole Q^2-range as predicted for Björken scaling in the QPM. This is interpreted such that scattering at valence quarks is dominant in this x-range. At lower x, F_2 increases with Q^2, which indicates contributions from an increasing number of partons. In this x-range gluons and sea quarks become eminent and are resolved better with increasing Q^2.

It is possible to calculate the evolution of the PDFs as a function of Q^2, using the DGLAP evolution equations [20, 21]. These equations use the determined values of the PDFs at a given scale to predict their evolution to some new scale. The knowledge of the evolution of the PDFs can be exploited to determine them experimentally. If the perturbative part is calculated and the cross section of a certain process is

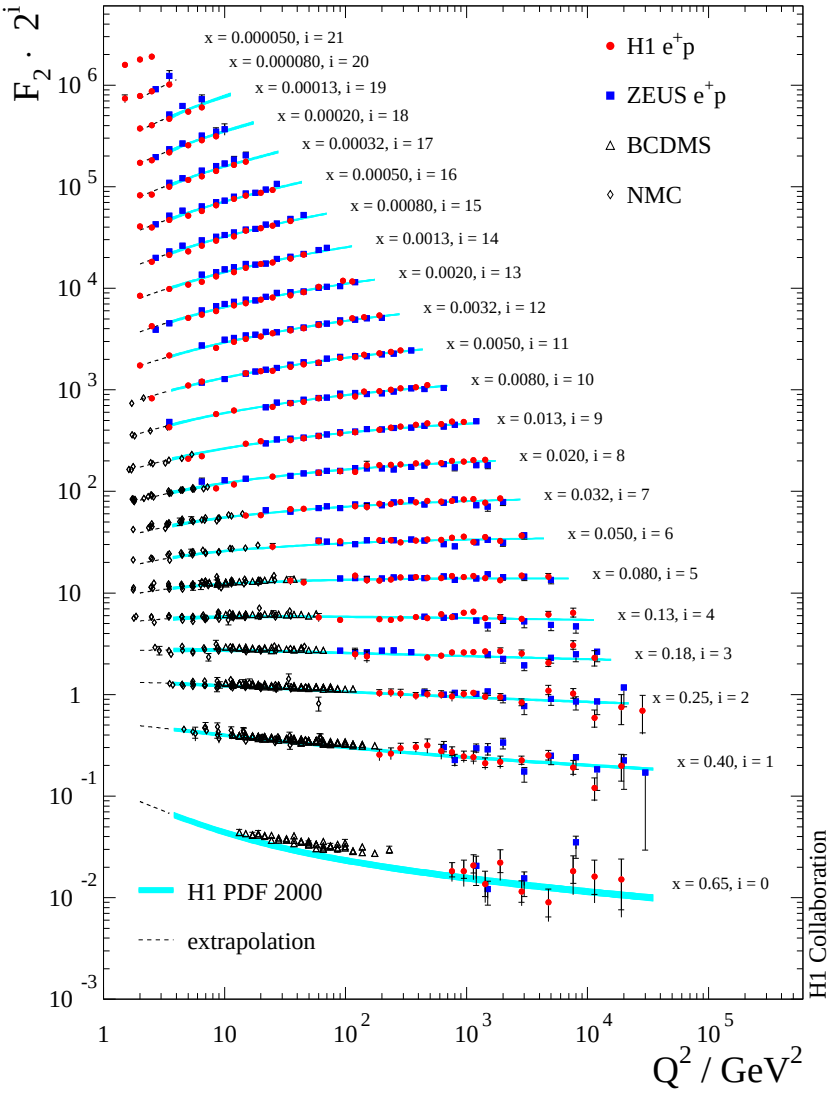

Figure 2.5: Structure function F_2 at HERA [19]
F_2 as function of Q^2 for various values of x. F_2 is scaled by powers of 2, which increase with decreasing x. The symbols indicate data from HERA and fixed-target experiments. The lines show SM predictions.

measured, the PDFs can be extracted from data. The factorisation theorem of QCD states that the PDFs are process independent. Once determined for a given process, they can be used to make predictions for another process. As an example, Fig. 2.6 shows proton PDFs extracted at HERA.

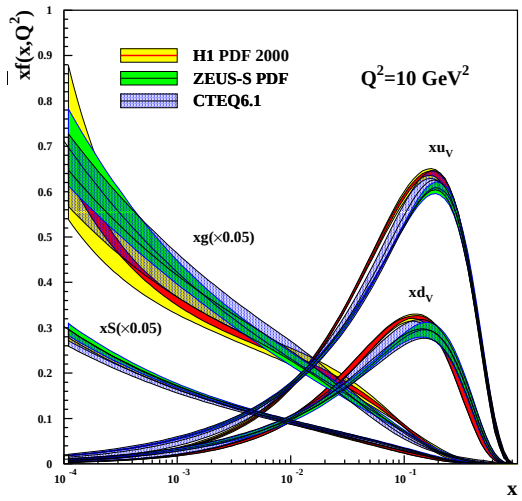

Figure 2.6: Proton PDFs at HERA [19]
Gluon (g), sea (S), u- and d-valence-quark (u_V and d_V, respectively) PDFs extracted at HERA compared to a commonly used parametrisation (CTEQ 6.1). The g- and S-PDFs are scaled.

2.3.3 Photoproduction

Photoproduction (PhP) is defined as the interaction of a (quasi-)real photon[22] with the proton ($\gamma p \to X$). It is the dominant process at HERA with a total cross section of approximately 150 µb. The majority of the γp interactions are soft, i.e. the transverse energy of the hadronic final state particles is small and hence they are not observed in the main detector. Hard γp interactions, resulting in jets at high transverse momenta, allow for perturbative QCD calculations to be made. The hard interactions can be subdivided into two types:

***Direct PhP*:** In the direct process the photon couples as a point-like particle to a parton from the proton. The two direct processes at leading order (LO) are

[22] $Q^2 \ll 1\,\mathrm{GeV}^2$

the QCD *Compton process* (Fig. 2.7(a)) and *boson-gluon fusion* (BGF, Fig. 2.7(b)).

***Resolved PhP*:** In this process the photon acts as a source of partons via vacuum fluctuations. One of these partons, carrying a fraction of the total photon momentum, interacts strongly with a parton from the proton. Fig. 2.7(c) shows an example diagram for a resolved photon interaction. Similarly to the proton, the resolved photon structure can be subdivided into a part, which can be treated by perturbation theory and a non-perturbative part, which needs to be determined from data.

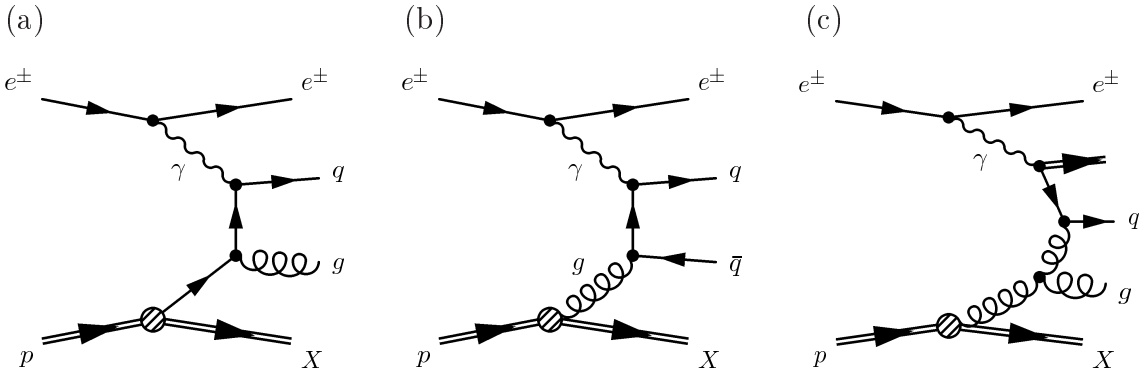

Figure 2.7: LO Feynman diagrams of hard PhP processes at HERA
(a) QCD Compton process (direct), (b) boson-gluon-fusion (direct), (c) resolved process.

2.3.4 Lepton Pair Production

At HERA, lepton pairs are produced mainly in the following two processes:

***Bethe-Heitler process*:** The dominant production mechanism for lepton pairs is the Bethe-Heitler process [22] $\gamma\gamma \to l^+l^-$. A quasi-real photon emitted from the beam electron interacts with a photon radiated from a quark inside the proton. The two photons produce a lepton-antilepton pair as shown in Fig. 2.8(a). The total cross section for the γ-γ interactions is large, but falls off steeply with the transverse momentum of the produced leptons $\propto p_T^{-3}$. The leptons are produced with opposite charge and have a back-to-back topology. There are elastic reactions with low momentum transfer on the proton side, where the proton stays intact in the scattering process. In quasi-elastic reactions the proton is transformed into an excited nucleon state. In inelastic

reactions the proton breaks apart and many hadrons are produced in a cascade. In case of high momentum transfer on the electron side, the scattered electron can be observed in the main detector.

Internal photon conversion and Z^0 production: An example for the production of a gauge boson with subsequent decay to a lepton pair is shown in Fig. 2.8(b). The lepton pairs are produced with a back-to-back topology and the cross section peaks at low values of the invariant mass of the two-lepton system and at the invariant mass of the Z^0-boson.

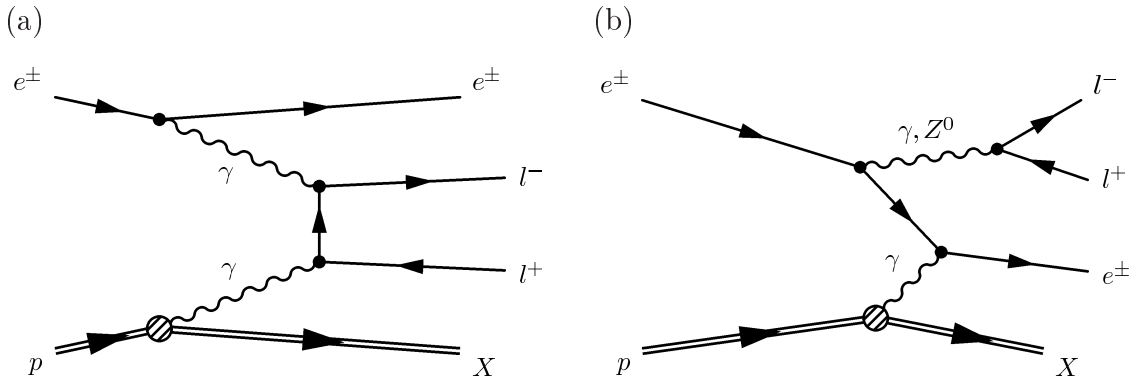

Figure 2.8: Feynman diagrams of lepton pair production at HERA
(a) Bethe-Heitler process and (b) QED Compton process as an example for internal photon conversion and Z^0 production, where a photon or a Z^0 is emitted by the initial state electron with a subsequent leptonic conversion or decay.

Requiring that at least one of the produced leptons is accepted by the main detector and has a transverse momentum of more than 5 GeV, a total cross section for lepton pair production of approximately 120 pb is expected at HERA.

2.4 Production Mechanisms of Isolated Leptons in Events with Large Missing Transverse Momentum at HERA

This section describes various sources of isolated leptons in events with large missing transverse momentum at HERA. Common to most of them is, that the direct source is the decay of a W-boson into a lepton and its corresponding anti-neutrino. In this sense, describing the origin of isolated leptons actually means to describe the production mechanisms of W-bosons. In addition, RPV SUSY would be a source of isolated leptons from Squark decays, which is described in 2.4.3.

2.4.1 Production of Single W-Bosons

At HERA single W-bosons can be produced via the SM-processes $ep \to eWX$ and $ep \to \nu WX$ [23]. The process $ep \to \nu WX$ is ignored in the following, because its cross section is very small ($\sim 5\%$ of the total cross section of W-boson production). In Fig. 2.9 the lowest order Feynman diagrams for the process $ep \to eWX$ are displayed. The diagrams (a) and (b) show W-radiation from the incoming and outgoing quark, respectively. These processes have the largest contribution to the W-boson production cross section. Diagram (c) shows the $WW\gamma$ triple-gauge-boson coupling. The diagram (d) contains a virtual W-boson, and the diagrams (e) and (f) show the coupling of the W-boson to the incoming positron and scattered neutrino from a CC process, respectively.

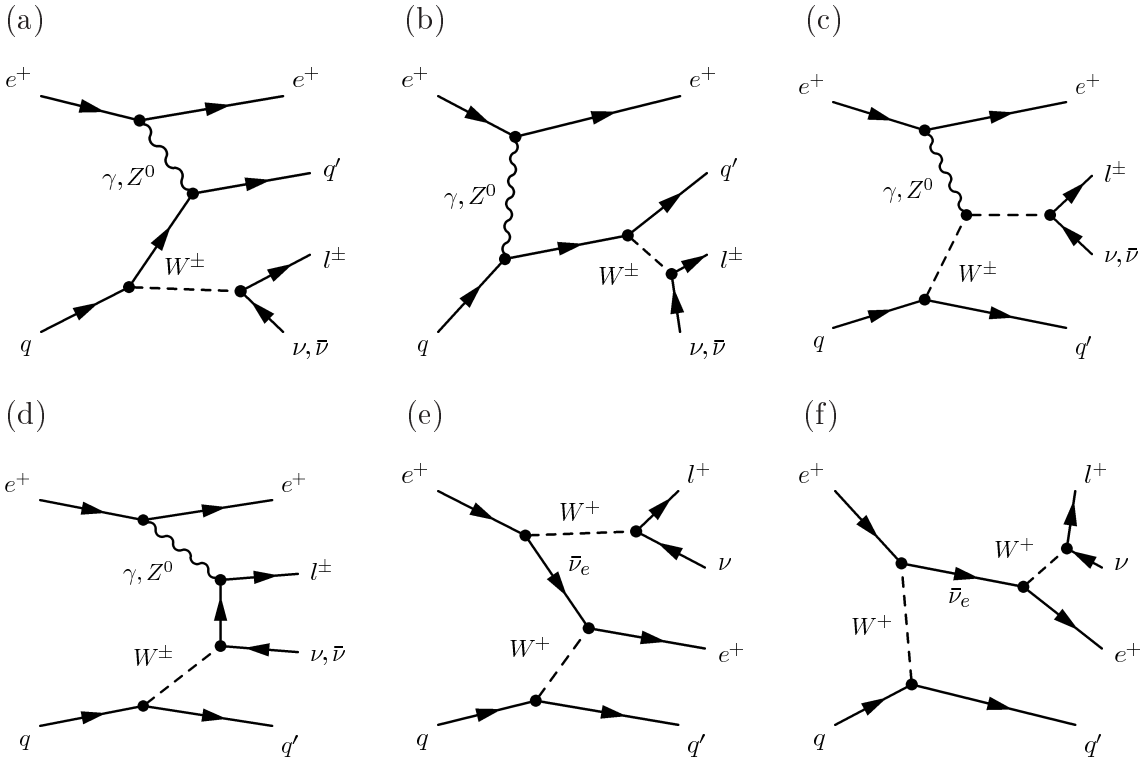

Figure 2.9: LO Feynman diagrams of single W-boson production at HERA The case of e^+-quark scattering is shown, including a leptonic decay of the W-boson. (a) W-radiation from incoming quark, (b) W-radiation from outgoing quark, (c) $WW\gamma$ triple-gauge-boson coupling, (d) virtual W-boson, (e) W-radiation from incoming lepton and (f) W-radiation from outgoing lepton.

In order to calculate the total cross section of single W-boson production at HERA at NLO, also QCD corrections have to be taken into account. Some examples

are shown in Fig. 2.10. This cross section amounts to 1.16 pb at HERA [24] with a

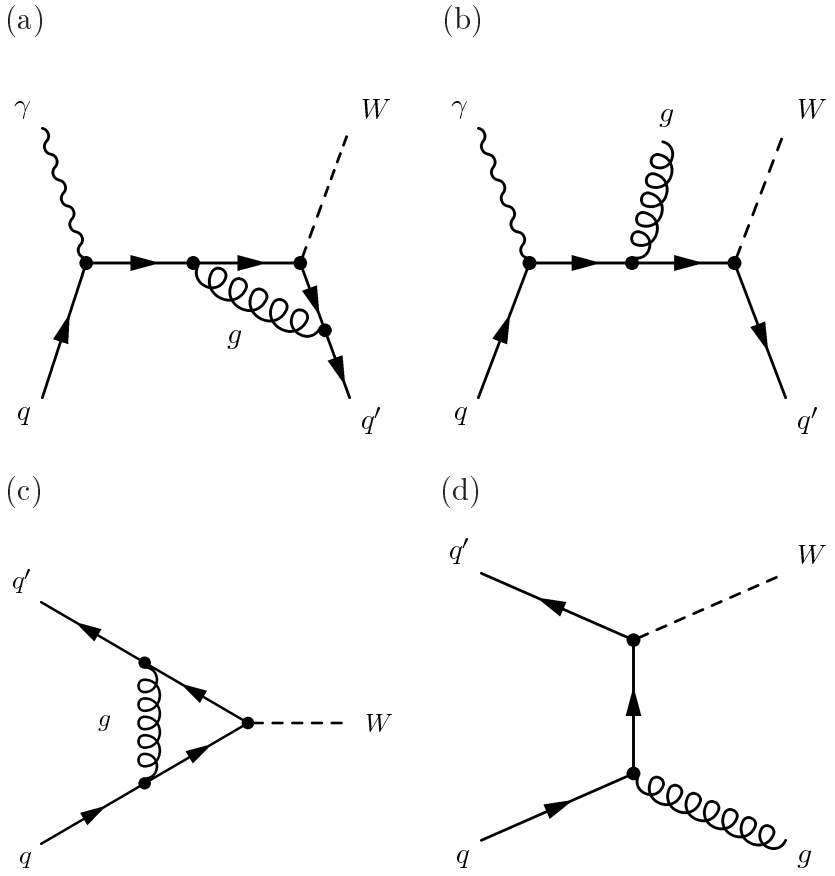

Figure 2.10: NLO QCD corrections to single W-boson production
The given examples are: (a) virtual and (b) real correction to the direct process, (c) virtual and (d) real correction to the resolved process.

theoretical uncertainty of approximately 15%. It is dominated by the PhP regime.

The experimental signature for W-boson production depends on the subsequent decay of the W-boson. For the leptonic decay one expects a lepton with high transverse momentum and missing transverse momentum in the event due to the undetected neutrino. For the leptonic decay $W \to \tau\nu_\tau$ the signature depends on the subsequent decay of the τ-lepton. For the leptonic τ-decays $\tau \to e\nu_e\nu_\tau$ and $\tau \to \mu\nu_\mu\nu_\tau$ the signature is similar to the corresponding W-decay, except for the large missing transverse momentum from the additional neutrino. For the hadronic τ-decay a hadronic jet with small spatial extent and additional missing transverse momentum from the neutrino in the τ-decay is expected. Hadronic W-decays $W \to qq'$ lead to two jets. An additional jet is expected in all W-decay modes in case of a

sizable momentum transfer to the scattered quark. However, these events are very rare due to the domination by the PhP regime.

2.4.2 Production of Single t-Quarks

Besides the direct production as described in 2.4.1, W-bosons can also emanate from the decay of singly produced t-quarks at HERA[23]. Due to its broad decay width, the t-quark decays rapidly ($\tau \approx 10^{-24}$ s) almost exclusively through the single mode $t \to bW$ before it can hadronise. In this case, in addition to the signature of directly produced W-bosons, one expects a jet with high transverse energy from the b-quark. Since the t-quark is not expected to be produced with significant transverse momentum at HERA energies, this jet and the decay products of the W-boson have a back-to-back topology in the azimuthal plane.

2.4.2.1 Production within the Standard Model

In the Standard Model single t-quarks can be produced via CC ep-interactions as shown in Fig. 2.11(a),(b). Due to the very small values of the corresponding off-

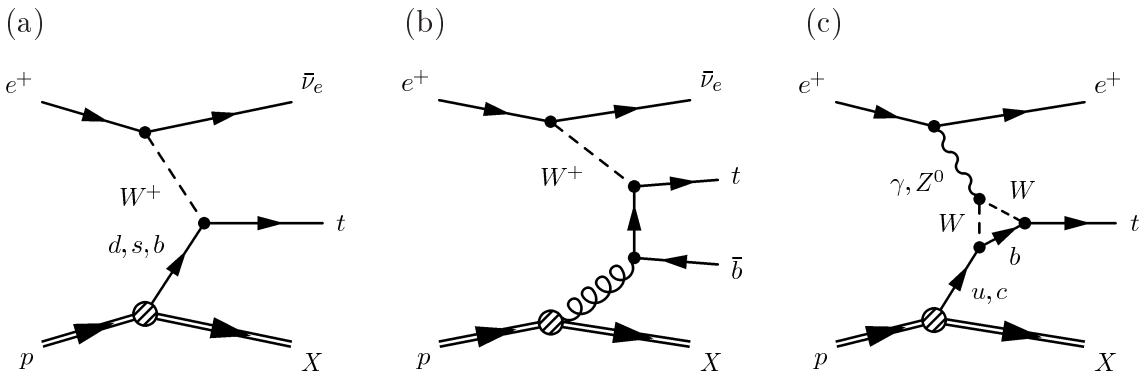

Figure 2.11: SM t-quark production at HERA
The given examples show (a) direct CC process, (b) resolved CC process and (c) FCNC process at lowest order within the Standard Model in e^+p collisions.

diagonal elements of the CKM-matrix [6], these flavour changing processes are highly suppressed. The expected total cross section for SM CC single t-quark production at HERA energies amounts to about 1 fb [25].

NC ep-interactions preserve the quark flavour at LO in the Standard Model. Thus flavour changing processes are present only via higher order radiative corrections. Fig. 2.11(c) shows an example of such a one-loop *flavour changing neutral current*

[23]The CMS energy of HERA does not allow for t-quark pair production.

(FCNC) process at HERA. Since the suppression due to the *Glashow-Iliopoulos-Maiani* (GIM) mechanism [26, 27] leads to the disappearence of such contributions for degenerate quark masses, sizable cross sections are expected only in cases with the t-quark involved. First observations of FCNC processes have been made by the CLEO collaboration in the decay $b \to s\gamma$ [28][24]. No sizable cross sections are predicted in the Standard Model for FCNC processes between a t-quark on the one side and a c- or u-quark on the other side. The predicted branching ratios for such FCNC decays are [29]:

$$\begin{aligned} BR(t \to c\gamma) &= 4.6 \cdot 10^{-14} \\ BR(t \to u\gamma) &= 3.7 \cdot 10^{-16}\,, \end{aligned}$$

and the corresponding branching ratios with a Z-boson involved instead of a photon are even lower by a factor of about five [27][25]. These small branching ratios make an experimental observation of such processes very difficult.

Anyway, with a t-quark mass of $m_t = 175\,\text{GeV}$ and taking into account the incident lepton energy of $E_e = 27.5\,\text{GeV}$ at HERA, the struck quark needs to have a minimum momentum[26] of about 278 GeV, which corresponds to $x \approx 0.3$ for the production of a single t-quark. As can be seen in Fig. 2.6, the parton density for $x \geq 0.3$ is much higher for u-quarks than for c-quarks, which appear only in the quark sea S. So in spite of the higher branching ratio, the cross section of FCNC processes involving the c-quark are expected to be much lower than with the u-quark involved.

In the presence of BSM anomalous FCNC couplings of the t-quark to c- and u-quarks, a large enhancement of the branching ratios is expected in high-energy collision experiments [27, 30–33] as discussed in the following.

2.4.2.2 Production beyond the Standard Model

Since some extensions to the Standard Model predict an enhanced rate of FCNC processes, a search for FCNC t-quark couplings at HERA is sensitive to physics beyond the Standard Model. The present experimental limits come from the non-observation of the decays $t \to qZ, q\gamma$ at the TEVATRON and the absence of single t-quark production $e^+e^- \to t\bar{q}, \bar{t}q$ at LEP and $ep \to etX$ at HERA. The best limits obtained so far are $BR(t \to cZ + uZ) \leq 0.159$ [37], $BR(t \to c\gamma + u\gamma) \leq 0.032$ [38] and $BR(t \to u\gamma) \leq 0.011$ [39, 40], all at 95% confidence level (CL).

Examples for theories with enhanced FCNC couplings are:

[24] FCNC decays of u-type quarks are strongly GIM-suppressed due to the bigger masses of the decay products compared to LO weak decays.

[25] The branching ratios with a gluon or a Higgs-boson involved are not discussed here, since they do not contribute at HERA.

[26] Quark mass set to 0.

Supersymmetry: New couplings of Sparticles to SM particles could result in effective FCNC couplings. In the MSSM the enhancement of FCNC couplings is expected to be about eight orders of magnitude [41]. However, HERA is expected to be not sensitive enough for an observation, since the existing limit of $BR(t \to u\gamma)$ is too small, even if extrapolated to the full expected HERA luminosity. In RPV models, the effective coupling could be enhanced even further by contributions as exemplified in Fig. 2.12(a). There the FCNC process arises through the product of RPV couplings $\lambda'_{i1k} \times \lambda'_{i3k}$ of a Slepton from the ith generation to SM d-type quarks from the kth generation and to a u- and a t-quark. The branching ratios can be of the order of $BR(t \to c\gamma) \sim 10^{-5}$ and $BR(t \to cZ) \sim 10^{-4}$ [42].

Two-Higgs-doublett models: In some models with more than one Higgs-doublett[27], FCNC is possible at tree level. If not so, the additional Higgs-doublett(s) could at least contribute effectively via a loop as shown in Fig. 2.12(b). Both possibilities could enhance the branching ratios of interest by several orders of magnitude [43].

Exotic quarks: In models with additional quarks the CKM matrix is not unitary anymore and the GIM mechanism is relaxed. The branching ratios could increase to e.g. $BR(t \to qZ) \approx 1.1 \cdot 10^{-4}$ [29, 44].

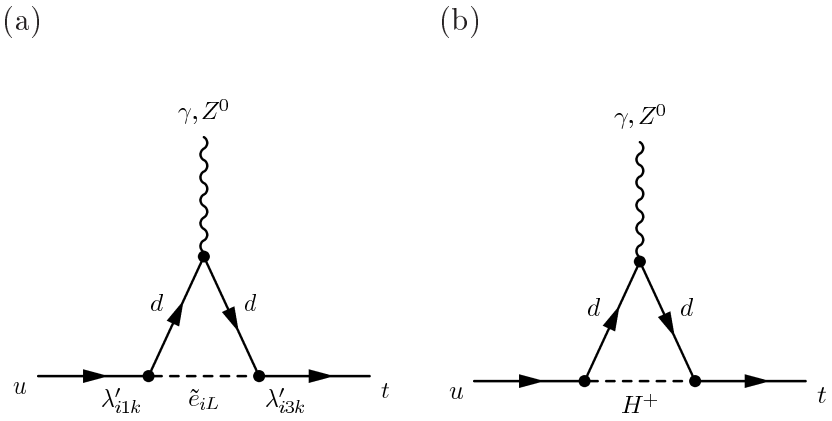

Figure 2.12: Effective FCNC couplings in BSM theories
The given examples show (a) Slepton exchange in RPV SUSY and (b) exchange of a charged Higgs-boson in 2HDM.

An effective anomalous FCNC coupling can be expressed through an anomalous magnetic coupling $\kappa_{tu\gamma}$ at the $tu\gamma$-vertex and an anomalous vector coupling v_{tuZ} at

[27] Two-Higgs-doublett models (2HDM)

the tuZ-vertex as shown in Fig. 2.13 for single t-quark production. The Z^0-exchange

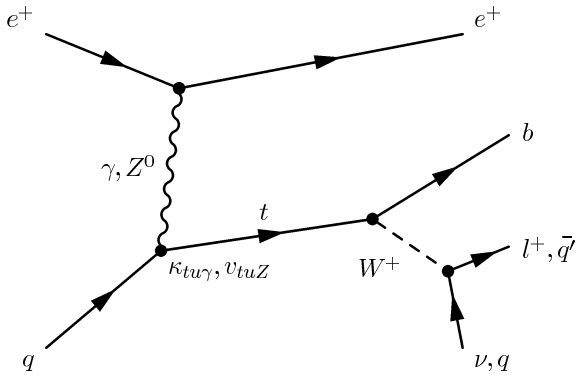

Figure 2.13: Anomalous single t-quark production via FCNC at HERA
The SM t-quark decay $t \to bW$ is included in the diagram.

is suppressed for $Q^2 \ll M_Z^2$. On the other hand, the cross section falls with $1/Q^4$, so that the γ-exchange at low Q^2 dominates at HERA. To describe the anomalous coupling one uses the effective Lagrangian [32,45]:

$$\Delta\mathcal{L}_{eff} = ee_t\,\bar{t}\,\frac{i\sigma_{\mu\nu}q^\nu}{\Lambda}\kappa_{tu\gamma}uA^\mu + \frac{g}{2\cos\theta_W}\,\bar{t}\gamma_\mu v_{tuZ}uZ^\mu + \text{h.c.}\,, \tag{2.23}$$

with the electron and t-quark electric charges e and e_t, the *weak coupling constant* g and $\sigma_{\mu\nu} = \frac{1}{2}(\gamma^\mu\gamma^\nu - \gamma^\nu\gamma^\mu)$[28]. Λ is a high mass scale, which is characteristic for the new interaction. By convention, it is set to the mass of the t-quark m_t. t and u are the interacting fermion fields of the t- and u-quark, q is the momentum of the exchanged boson and A^μ and Z^μ denote the fields of the photon and Z-boson, respectively. In the Standard Model $\kappa_{tu\gamma}$ and v_{tuZ} are 0 at tree level and very small at one-loop level. In the following it is assumed, that they are real and positive.

With a parametrisation of the LO anomalous t-quark production cross section

$$\sigma_{single\,t} = c_\gamma \cdot \kappa_{tu\gamma}^2 + c_Z \cdot v_{tuZ}^2 + c_{\gamma Z} \cdot \kappa_{tu\gamma} \cdot v_{tuZ}\,, \tag{2.24}$$

and a parametrisation of the LO decay widths

$$\begin{aligned} \Gamma_{t\to bW^+} &= w_{SM} \\ \Gamma_{t\to u\gamma} &= w_\gamma \cdot \kappa_{tu\gamma}^2 \\ \Gamma_{t\to uZ} &= w_Z \cdot v_{tu\gamma}^2 \end{aligned} \tag{2.25}$$

a LO cross section and decay width calculation has been performed [46] using the program COMPHEP [47]. It leads to the coefficients listed in Tab. 2.5 [46]. The

[28] $\gamma^{\mu,\nu}$ are the *Dirac γ-matrices*.

m_t (GeV)	c_γ (pb)	c_Z (pb)	$c_{\gamma Z}$ (pb)	w_{SM} (MeV)	w_γ (MeV)	w_Z (MeV)
170	7.520	0.2861	-0.01940	1404	293	1297
175	6.076	0.2340	-0.01842	1554	302	1449
180	4.886	0.1899	-0.01308	1713	310	1610

Table 2.5: Parametrisation coefficients from LO cross section and decay widths calculation for anomalous FCNC t-u couplings [46]
The calculation of the cross section has been performed for $\sqrt{s} = 318\,\text{GeV}$ for different t-quark masses m_t.

dominance of γ-exchange is clearly seen through the much higher coefficient. In addition, a small variation of m_t by $\pm 5\,\text{GeV}$ causes a variation of c_γ by approximatily $\mp 25\%$. The interference between γ- and Z^0-exchange, parametrised by $c_{\gamma Z}$, lowers the cross section slightly. But the effect is below 1% all over the considered parameter space and can be neglected. Fig. 2.14(a) shows the calculated LO cross section for anomalous single t-quark production via FCNC as a function of the anomalous couplings $\kappa_{tu\gamma}$ and v_{tuZ}. The steeper rise with $\kappa_{tu\gamma}$ compared to v_{tuZ} corresponds to the suppression of Z^0-exchange at low Q^2.

For single t-quark production by γ-exchange, also NLO QCD calculations are available [45]. From these, NLO cross section calculations have been performed as shown in Fig, 2.14(b) [46]. The Born-level cross sections are in very good agreement with the LO cross sections with $v_{tuZ} = 0$.

As for the branching ratios, experimental limits have been set on the anomalous couplings. They are summarised in Fig. 2.15 [39]. The most stringent limits for $m_t = 175\,\text{GeV}$ so far are $\kappa_{tu\gamma} < 0.174$ for $v_{tuZ} = 0$ [39] and $v_{tuZ} < 0.37$ for $\kappa_{tu\gamma} = 0$ [36]. Introducing these limits to Eq. 2.24 with the coefficients from Tab. 2.5 leads to an upper limit of the cross section for the anomalous production of single t-quarks at HERA of

$$\sigma_{single\,t} < 0.215\,\text{pb}. \tag{2.26}$$

At this limit, a total number of about nine singly produced t-quarks is expected in the analysed data (see 5.1). Corresponding to the W-boson BR, about three of them are expected to lead to isolated leptons.

2.4.3 Further Possible Production Mechanisms of Isolated Leptons Beyond the Standard Model

Besides the decay of a W-boson from direct production or a t-quark decay, there exist also other production mechanisms of isolated leptons in events with large missing transverse momentum at HERA in theories beyond the Standard Model [1].

(a) (b)

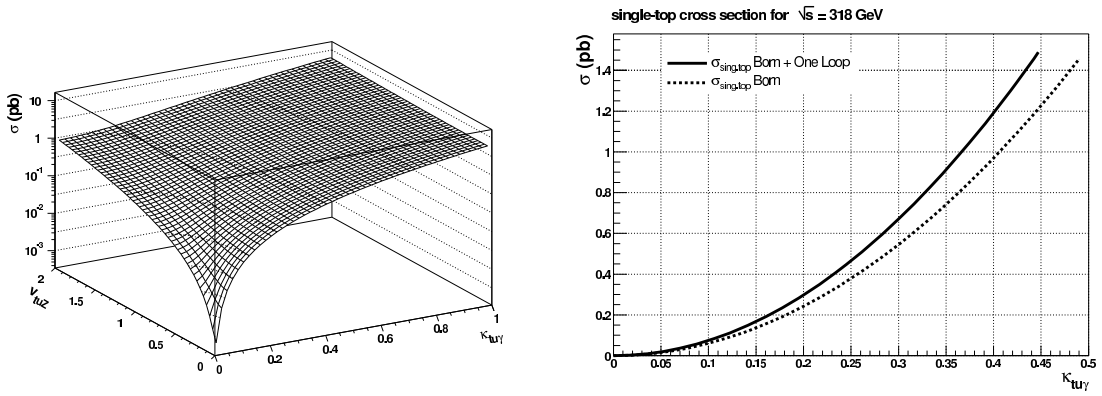

Figure 2.14: Cross sections for single t-quark production as function of the couplings [46]
The shown cross sections are (a) LO cross section as a function of $\kappa_{tu\gamma}$ and v_{tuZ} and (b) NLO cross section as a function of $\kappa_{tu\gamma}$, both for $m_t = 175\,\text{GeV}$.

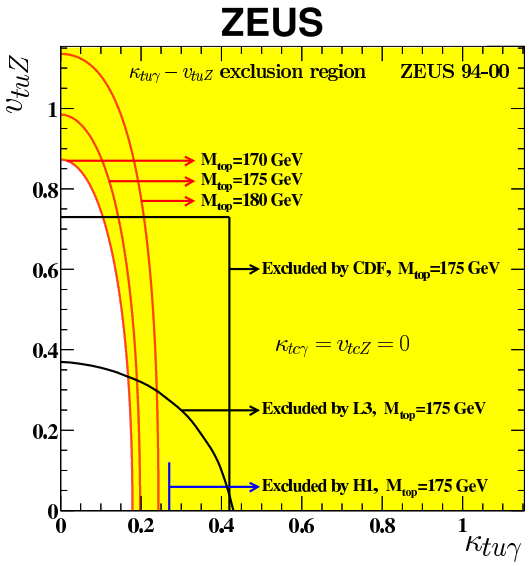

Figure 2.15: Exclusion limits on the anomalous couplings $\kappa_{tu\gamma}$ and v_{tuZ}.
The limits from ZEUS are given at 95% CL for three values of m_t assuming $\kappa_{tc\gamma} = v_{tuZ} = 0$. Also the limits obtained by CDF, L3 and H1 are shown.

2.4.3.1 R-Parity Violating Supersymmetry

One possible production mechanism of isolated leptons and large missing transverse momentum at HERA is the resonant RPV t-channel Squark production[29] and its subsequent decay. The light Stop $\tilde{t}_1$ is the best candidate to be the lightest Squark [48]. Hence, this section focusses on it.

Light Stops could be produced at HERA via the reaction $e^+d \rightarrow \tilde{t}_1$ with the Yukawa coupling λ'_{131} involved as described in Eq. 2.11. In scenarios where the decay $\tilde{t}_1 \rightarrow t\tilde{\chi}^0_i, t\tilde{g}$ is kinematically forbidden, isolated leptons and large missing transverse momentum could be produced in the decay $\tilde{t}_1 \rightarrow b\tilde{\chi}^+_j$ [49] as shown in Fig. 2.16(a). The isolated lepton and the neutrino carrying the missing transverse momentum originate from the subsequent $\tilde{\chi}^+$-decay into a $\tilde{\chi}^0$. Such events contain a jet from the b-quark and additionally possible decay products from the neutralino. Another possibility is the anomalous W-boson production [50] as shown in Fig. 2.16(b). However, this only occurs in models with the light Sbeauty $\tilde{b}_1$ being lighter than the light Stop. Furthermore a second RPV vertex with the Stop decaying to SM particles could arise as shown in Fig. 2.16(c). Especially the decay $\tilde{t}_1 \rightarrow b\tau$ is important in a region of the parameter space which is not excluded by experiments so far [51]. This process is particularly interisting, since an excess in the τ-channel would not be accompanied by an excess in the μ- or e-channel as it should be in the case of chargino or enhanced W-boson production.

2.4.3.2 Heavy Majorana Neutrinos

The existence of heavy neutrino states might be signalled by the observation of non-vanishing neutrino masses [52]. In most BSM scenarios these states are massive *Majorana particles* (N) of about $m_N \approx 10^2 - 10^{18}\,\text{GeV}$. At HERA these particles could occur in direct s-channel production [53] as well as in t-channel exchange [54]. The final states of these events could contain one or two isolated leptons, where the case with two leptons also contains a neutrino. If one of the leptons remained undetected, the event topology of interest could arise. Anyway, the expected cross sections in a reasonable parameter space are tiny in the e- and μ-channel for coupling strengths not excluded so far by low energy experiments [55]. And even though the limits for the τ-channel are weaker and the production is enhanced by a factor of 3 for final states with two distinct lepton flavours, an observation at HERA is not expected.

[29] The Squark mass has to be less than $\sqrt{s}$.

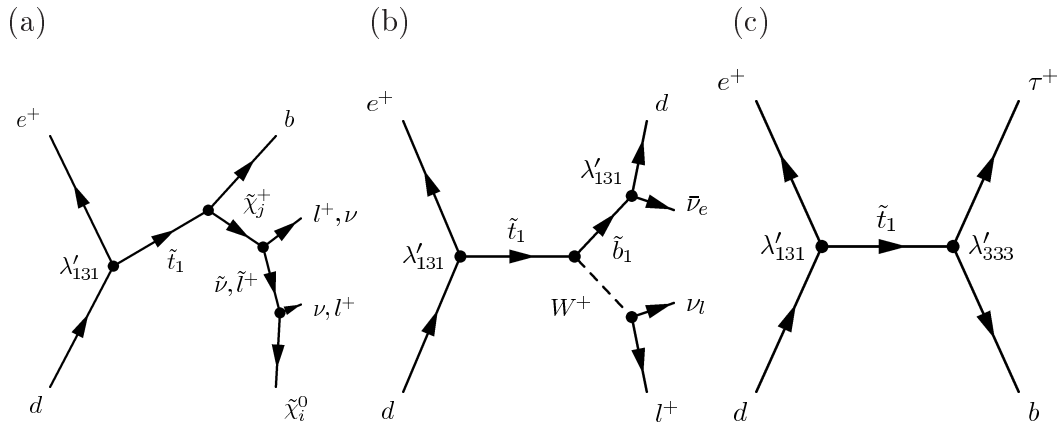

Figure 2.16: RPV Stop production at HERA and examples for decays with isolated leptons and missing transverse momentum
The Stop decays to (a) a b-quark and a chargino, which then decays to a neutralino radiating a lepton and the corresponding neutrino, (b) a Sbeauty and a W^+-boson, which decays leptonically or (c) a b-quark and a τ-lepton via another RPV coupling λ'_{333}.

Chapter 3

The Storage Ring HERA and the ZEUS Experiment

This chapter introduces the lepton-proton collider HERA and the high-energy physics detector ZEUS.

3.1 The Storage Ring HERA

HERA[1] [56] is a high-energy physics storage ring facility, where electrons or positrons (e) are brought to collision with protons (p). This worldwide unique machine is located at the research centre DESY[2] in Hamburg, Germany and operating since 1992. Consisting of two separate storage rings for e and p, HERA was built from 1984 to 1990 in an $10-25\,\mathrm{m}$ underground circular tunnel of 6336 m length and 5.2 m inner diameter. The machine operates with a combination of conventional and super-conducting techniques for acceleration, beam bending and focussing. The storage rings are run with energies of 27.5 GeV for e and 920 GeV for p (820 GeV before 1998), which results in a CMS energy of 318 GeV (300 GeV before 1998). The ep-collisions take place at a bunch crossing rate of 10.4 MHz at zero crossing angle.

HERA has four experimental areas, where two (south and north) are dedicated for ep-collisions. Contrary to pp-collisions, this kind of collisions takes advantage of the pointlike structure of the electron. There the experiments H1 and ZEUS probe mainly the structure of the proton and the properties of the strong force. The resolution reaches $10^{-18}\,\mathrm{m}$, which corresponds to 1‰ of the p-radius. In addition these experiments test aspects of the Standard Model of particle physics (SM) and search for new particles and phenomena. The ZEUS experiment is described in more detail in 3.2. The remaining two experimental areas (west and east) are used

[1] Hadron-Electron Ring-Accelerator
[2] Deutsches Elektronen-Synchrotron

by fixed-target experiments. Since 1995 the HERMES experiment explores the spin structure of nuclei. For this purpose the e-beam (longitudinally polarised in this area) is brought into collision with a polarised gas target. The target contains either hydrogen to measure the proton spin structure or deuterium or helium-3 to measure the neutron spin structure. The HERA-B experiment took data in the years 1999 to 2003. It was designed to identify B-meson decays in a dense hadronic environment. The B-mesons are produced by collisions of the p-beam halo with an aluminium wire target. A schematic overview of HERA and its experiments is shown in Fig. 3.1. An extensive overview of physics at HERA is found in [57, 58].

During the years 2000/2001, HERA was upgraded to deliver more luminosity [60]. The running period before this upgrade is referred as "HERA I". Accordingly after the upgrade, we talk about "HERA II". The design peak luminosity in HERA II is now $75\,\mathrm{mb}^{-1}\,\mathrm{s}^{-1}$ ($15\,\mathrm{mb}^{-1}\,\mathrm{s}^{-1}$ in HERA I). This increase in luminosity has been achieved mainly by a significantly stronger focussing of the beams at the interaction points (IP). The IP size is at $118\times32\,\mu\mathrm{m}^2$ [59] after $286\times60\,\mu\mathrm{m}^2$ in HERA I. A summary of the integrated luminosities delivered by HERA to the ZEUS experiment can be found in Fig. 3.2 and in Tab. B.1. Besides the increase in luminosity, HERA was enabled to deliver longitudinally polarised e-beams also for the collider experiments in HERA II (3.2.8).

3.2 The ZEUS Experiment

This section introduces the high-energy physics detector ZEUS. An overview is given and the components mainly used in this analysis are decribed in more detail. A complete desription of the detector is given in [61].

3.2.1 Overview

ZEUS is a *hermetic*[3] general purpose high-energy physics detector to study various aspects of ep-scattering at HERA[4]. The subdetectors are arranged coaxially around the beam axis. ZEUS has a longitudinally asymmetric design to account for the imbalance of the beam energies and the resulting boost of most final state particles from the ep-interaction into the direction of the p-beam (referred to as *forward* direction). The detector weighs 3600 t and its dimensions are $12\times10\times19\,\mathrm{m}^3$. Schematic cross sections of the ZEUS detector are shown in Fig. 3.3. The ZEUS coordinate system (Fig. 3.4) is orthogonal and right-handed with the origin at the IP, the z-axis pointing into forward direction, the x-axis pointing to the centre of HERA and the y-axis pointing upwards. The *polar angle* θ is measured with respect to the z-axis,

[3] covering the whole solid angle of 4π around the IP

[4] The physics case is described in more detail in 2.3

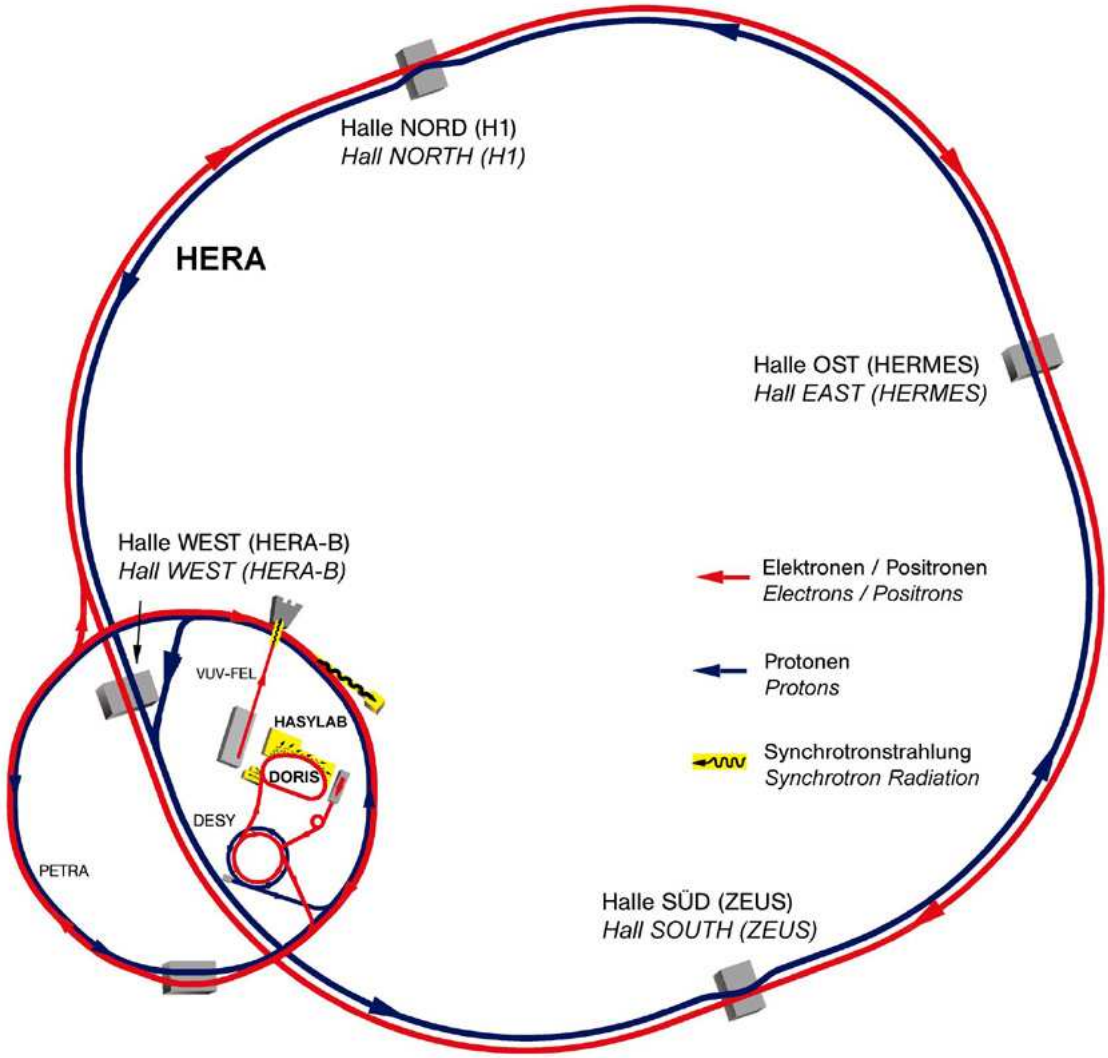

Figure 3.1: HERA map
Schematic overview showing HERA, its experimental areas, its pre-accelerator complex and further accelerators at DESY. One can identify, that HERA consists of four circular and four straight sections. The circular sections have a radius of 779 m, the straight sections are 360 m long.

(a) (b)

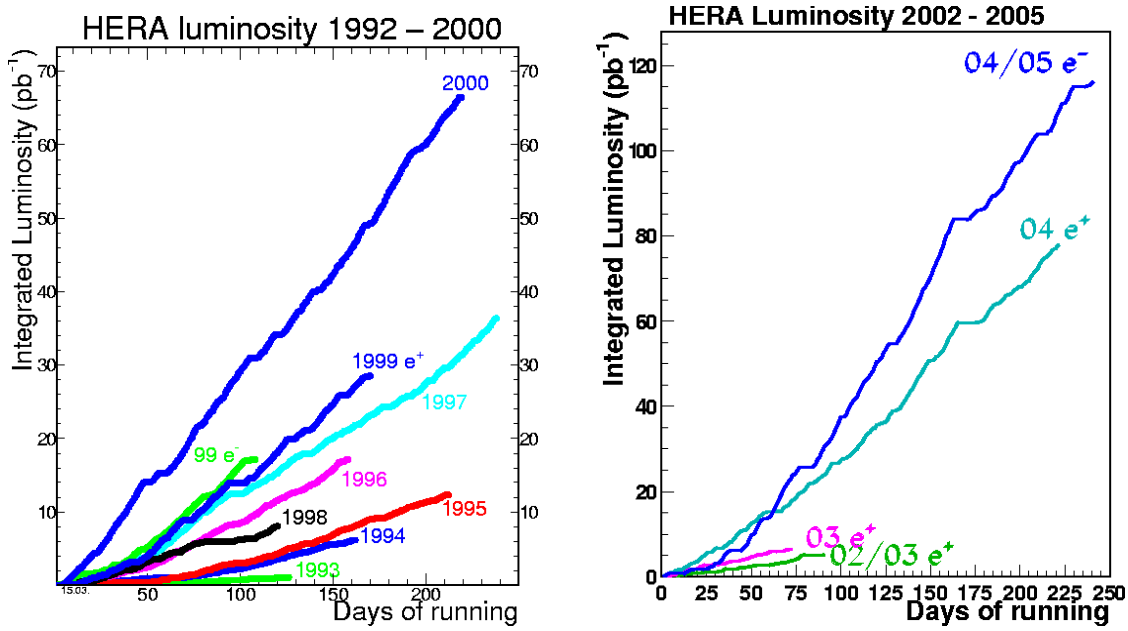

Figure 3.2: HERA delivered integrated luminosities
HERA I (a) and HERA II (b) integrated luminosities delivered for ZEUS per running period.

(a) (b)

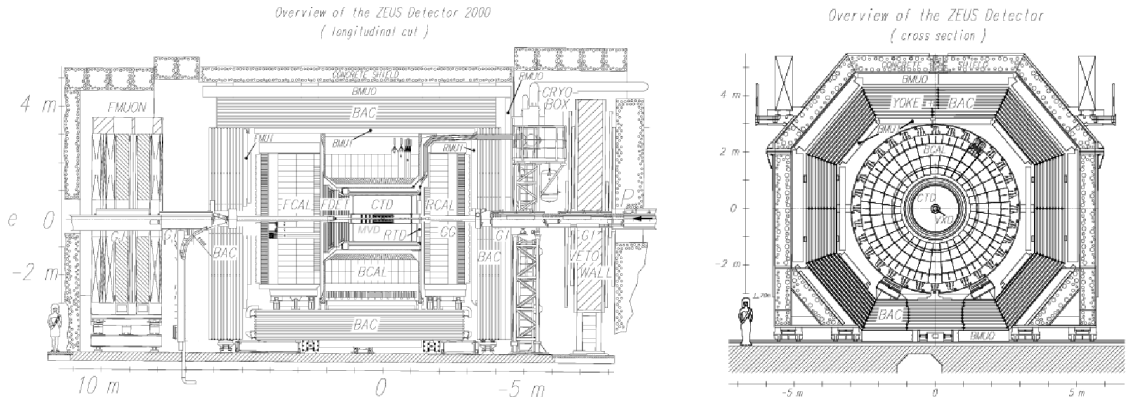

Figure 3.3: Cross sections of the ZEUS detector
(a) Along the beam axis, the asymmetry of the ZEUS detector is clearly seen. Protons cone from the right. (b) The coaxial shape is visible from the view perpendicular to the beam axis.

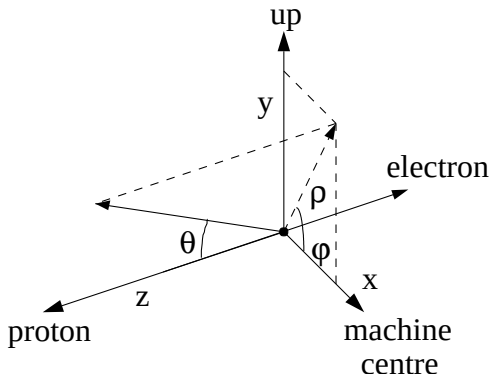

Figure 3.4: ZEUS coordinate system
This sketch introduces the orthogonal (x, y, z) and polar (ρ, θ, ϕ) coordinates at ZEUS and their relation to the accelerator geometry.

and the *azimuth angle* ϕ is measured with respect to the x-axis in the range from -π to π. Often the Lorentz-invariant *pseudorapidity* $\eta = -\ln \tan(\theta/2)$ is used instead of θ.

The ZEUS detector has been modified and upgraded continiously over the years to face new challenges and to allow for the growing physical and technical understanding and experience. The most recent major upgrade was performed for the HERA II running and the technical desciptions given in this section refer to this status. Detector components with a reference to a following subsection are described in more detail there.

Closest to the IP, the tracking detectors are situated to measure tracks of charged final state particles. The innermost is the Micro-Vertex Detector (MVD, s. 3.2.2) made of silicon strip detectors and situated directly around the beampipe for vertex identification. It is surrounded by the Central Tracking Detector (CTD, s. 3.2.3), a wire drift chamber to determine particle momenta and charges. These components are enclosed by a super-conducting solenoid magnet, which provides an almost uniform magnetic field of 1.43 T to enable the charge and momentum determination for charged particles. Then the asymmetric detector design is reflected in an extension of the tracking in forward direction[5]. Here the Forward Tracking Detector (FTD) [62] and the Straw-Tube Tracking Detector (STT) [63] take place to measure tracks down to a polar angle of 5°. The FTD consists of three separate chambers with three layers of drift cells each, where one drift cell contains six signal wires arranged perpendicular to the beam axis. The cells of each layer are rotated by 60°with respect to the other layers of the corresponding chamber to allow accurate position measurements of particle impacts. The space between the three FTD cham-

[5]labeled as FDET in Fig. s. 3.3(a)

bers is filled with the two pairs of STT superlayers. Each superlayer consists of six sectors of straw-tubes, tube-like drift chambers with one single sense wire each. In the rear direction the Rear Tracking Detector (RTD) provides tracking information up to a polar angle of 170°. It consists of one chamber similar to those of the FTD. At very large angles ($162° < \theta < 176°$) a finely segmented szintillator strip detector, the Small-Angle Rear Tracking Detector (SRTD) [64] increases the angular coverage of the ZEUS tracking system.

Enclosing the tracking system, energy measurements take place with a high-resolution compensating sampling calorimeter (CAL, s. 3.2.4). This is surrounded by an iron yoke (YOKE), which returns the magnetic field flux of the solenoid and is instrumented to measure particles escaping the CAL. This system of absorbing yoke and instrumentation is called backing calorimeter (BAC, . 3.2.5).

Special muon detectors (MUON, s. 3.2.6) are mounted on both the in- and outside of the yoke. Here the design of the outer forward muon detectors is special, since they should provide a completely independent measurement of muon momenta. For this reason they are supplemented by a toroidal magnet system to cope with the special physics case of forward muons at HERA (s. [61, Ch. 9]).

An iron-scintillator detector located at $z = -7.5\,\mathrm{m}$, called VETO wall, is used to reject beam related non-ep background. Furthermore, several sub-detectors are installed outside the main detector along the beampipe to allow measurements of particles at very high $|\eta|$. Also the HERA luminosity measurements are performed this way (s. 3.2.7). The e-beam polarisation is measured from the energy and angle asymmetries of back-scattered Compton photons (s. 3.2.8).

The data gained by the ZEUS experiment is filtered by a three-level trigger system, formatted by the data acquisition and written to tape (s. 3.2.9).

3.2.2 The Micro-Vertex Detector

The MVD [65] is a silicon-strip tracking detector for high-precision track measurements and vertex identification including the reconstruction of secondary vertices. It was installed during the HERA luminosity upgrade in 2000/01 to improve tracking capabilities and the tracking acceptance, especially in forward direction. In particular this is important for:

- identification and cross section measurements of mesons containing heavy quarks (long life-time, which leads to secondary vertices), in both photoproduction events at high energy and deep inelastic scattering at large Q^2,
- search for physics beyond the Standard Model, e.g. by:
  - an improved track reconstruction in the forward direction, which leads to a more accurate measurement of the polar angle of the scattered electron

(improving the measurement of neutral current events at very high Q^2),

– identification of τ-leptons or of mesons containing strange or heavy quarks, which are produced in many models beyond the Standard Model.

These physics goals, together with the available space inside the ZEUS detector, the costs and the time available for the construction, led to the following design specifications:

- polar angle coverage: $10^\circ < \theta < 170^\circ$ (equivalent to $2.43 > \eta > -2.43$),
- at least three spatial measurements per track, each in two projections,
- intrinsic hit resolution: 20 µm,
- impact parameter resolution: $\sim$100 µm at 90°, decreasing to 1 mm at 20°, for track momenta of more than 2 GeV,
- noise occupancy: $< 1‰$,
- efficiency of single hit reconstruction: more than 97%,
- alignment accuracy: 20 µm,
- resolution in separating two tracks: 200 µm.

The MVD has a cylindrical shape with a diameter of 319 mm and its length amounts to 2150 mm [66]. It is divided into three parts:

1. The forward part (FMVD) consists of four annular detector components (*wheels*) arranged along and perpendicular to the beam axis. The wheels are positioned at distances of 32, 45, 60 and 75 cm from the IP and detect particles in the region of $7.6^\circ < \theta < 22.3^\circ$ measured from the IP. Fig. 3.5(a) shows the schematic layout of a wheel.

2. The barrel part (BMVD) surrounding the IP consists of sensor arrays (*ladders*) located in three cylindrical layers (*cylinders*) parallel to the beam axis. Its length of 622 mm is adapted to the fairly broad z-distribution of the IP at HERA. Fig. 3.5(b) shows the arrangement of the ladders within the cylinders.

3. The rear part contains the wiring of the MVD for power, monitoring and readout.

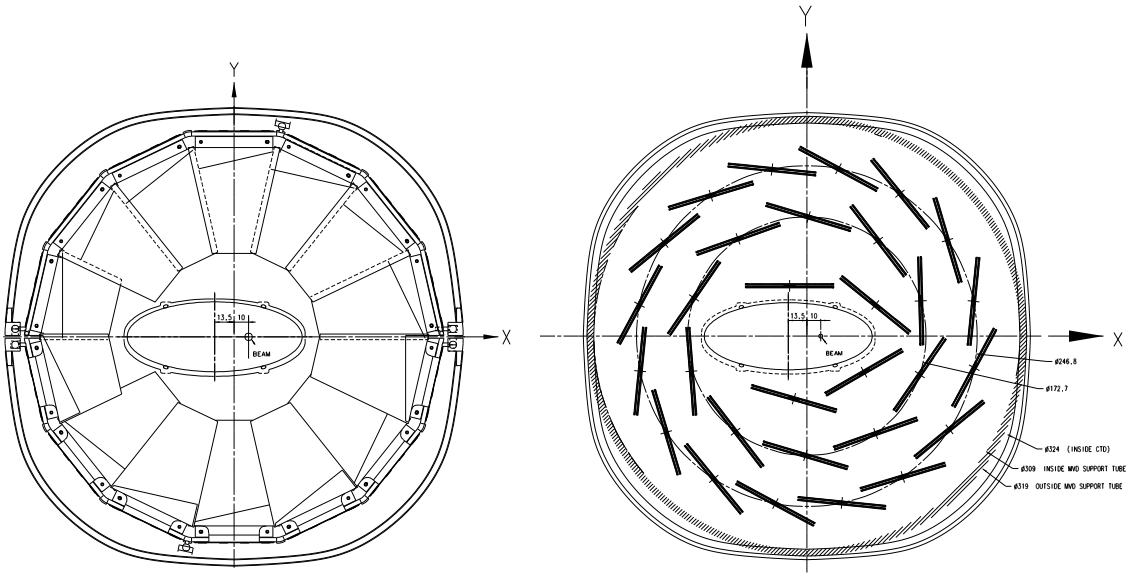

(a) (b)

Figure 3.5: Cross sections of the MVD
View in the backward directions of the MVD. (a) Cross section of the FMVD: One can see one of the wheels with segments from the single detector elements (modules) and the beam pipe (elliptical element in the centre) with the interaction point inside. (b) Cross section of the BMVD: One can see the arrangement of the ladders (thick double lines) and the beam pipe. The cylinders contain (from inner to outer) four, ten and sixteen ladders. The inner cylinder does not enclose the IP completely, because the elliptical beam pipe is not concentric to the beam axis to avoid synchrotron radiation to hit material.

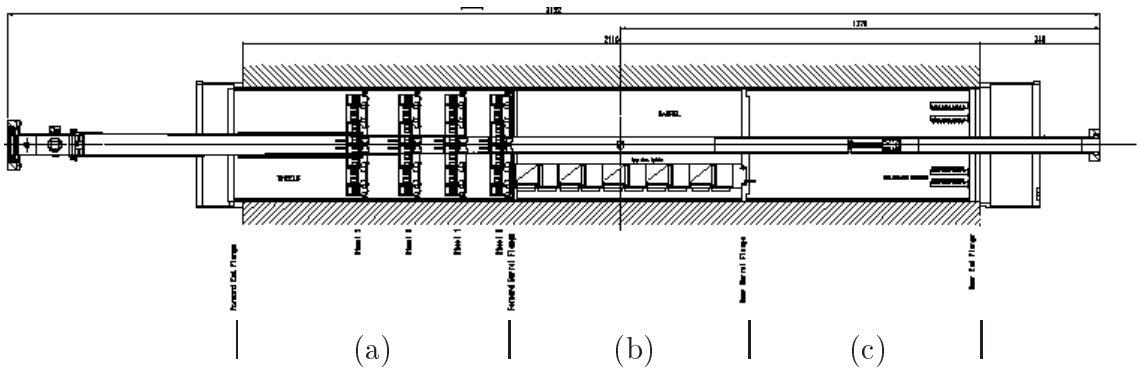

Figure 3.6: Schematic longitudinal section of the MVD [68]
Protons enter the detector from the right. One can see (a) the FMVD containing the wheels on the left, (b) the BMVD containing the ladders in the middle (one ladder shown as example) and (c) the rear part of the MVD housing the cables on the right. Also the part of the beam pipe housed on the axis of the MVD can be seen along the horizontal plane in the middle.

A sketch of the complete MVD is shown in Fig. 3.6.

Both, wheels and ladders are made of the basic detector element of the MVD: the *modules*. A wheel contains fourteen modules of trapezoidal shape[6]. The four modules with the same position and numbering within the wheels are called a *sector*. A ladder consists of five rectangular modules. A module consists of two half-modules, which are glued together. One half-module is composed of two sensors (wheels: only one) and the readout electronics mounted on a so-called *hybrid*. The MVD sensors [69] are single sided Si-strip detectors. On the surface p^+-Si implantations with a pitch of 20 µm are fabricated, where each sixth of them is read out. The five remaining strips operate as intermediate strips to improve the resolution by the effect of *charge sharing*. The intrinsic detector resolution of 7.2 ± 0.2 µm has been measured in testbeams [67].

3.2.3 The Central Tracking-Detector

The CTD [70] is a wire drift chamber to measure directions and momenta of charged particles and their energy loss dE/dx, which is used for particle identification. For particle tracks with a transverse momentum of more than 150 MeV, measured in at least three superlayers and fitted to the interaction vertex, the transverse momentum

[6] as visible in Fig. 3.5(a)

resolution of the CTD alone is given by [71]:

$$\frac{\sigma(p_T)}{p_T} = 0.0058 \cdot p_T \oplus 0.0065 \oplus \frac{0.0014}{p_T}\,, \tag{3.1}$$

where p_T is the transverse momentum of the track in GeV and the symbol $\oplus$ indicates the quadratic sum. The first term is due to the hit position resolution, whereas the second and third term are due to multiple scattering effects inside resp. before the CTD. Integrating the MVD into the track reconstruction improves the resolution to [72]

$$\frac{\sigma(p_T)}{p_T} = 0.0026 \cdot p_T \oplus 0.0104 \oplus \frac{0.0019}{p_T}\,. \tag{3.2}$$

The additional material of the MVD worsens the terms depending on multiple scattering, but the term due to the hit position resolution improves drastically.

The CTD has a cylindrical shape and its active volume, filled with argon (Ar, 82%), ethane (C_2H_6, 15%) and carbon dioxide (CO_2, 3%) [73], ranges from $z = -100\,\text{cm}$ to $z = 104\,\text{cm}$ with an inner and outer radius of 18.2 cm and 79.4 cm, respectively. It covers polar angles of $15° < \theta < 164°$ from the IP and has complete azimuthal coverage. The 4608 sense wires are arranged in 72 radial layers pooled together to nine *superlayers* (SL) consisting of eight layers each. One octant of the CTD is shown in Fig. 3.7. One group of eight sense wires within a superlayer is

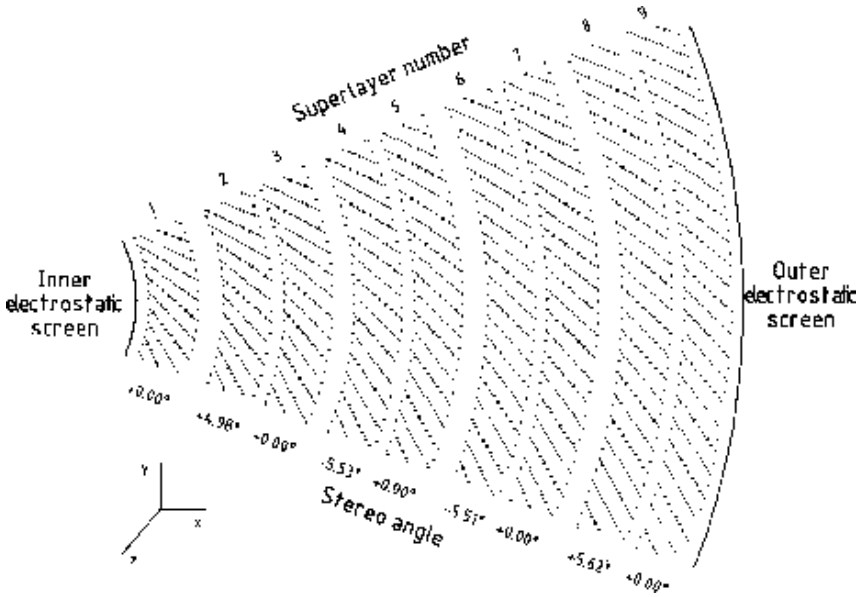

Figure 3.7: Cross section (xy-plane) of one CTD octant
The dots indicate sense wires.

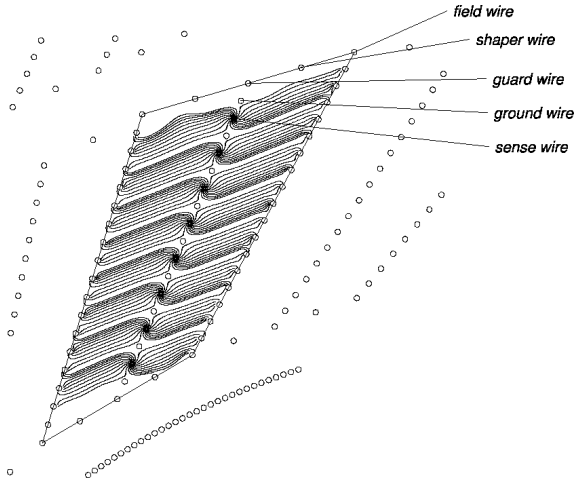

Figure 3.8: Layout of a CTD cell
The thin lines indicate the electric flux lines.

called a *cell* (shown in Fig. 3.8). To compensate for the Lorentz angle[7] of 45°, the planes of the sense wires inside a cell are tilted. The wires of the odd numbered SLs are parallel to the beam axis, whereas those of the even numbered SLs are inclined by an angle of about ±5°(*stereo angle*) to allow for a better determination of the z-coordinate.

3.2.4 The Uranium Calorimeter

In HERA physics, it is essential to measure hadronic jets and/or missing transverse momenta with the highest achievable accuracy, which is also true in this analysis. Therefore the detector response should be equal for both electrons and hadrons of the same energy ($e/h = 1$) in order to reduce the systematic error. This property is called *compensation*. The CAL [74] is a high-resolution compensating sampling calorimeter, which consists of alternating layers[8] of depleted uranium-alloy (98.1% U^{238}, 1.7% Nb, 0.2% U^{235}) absorbers and organic plastic scintillators. It surrounds the tracking detectors and the solenoid and covers 99.7% of the 4π solid angle.

Since most conventional calorimeters are undercompensating ($e/h > 1$), compensation can be achieved by both enhancement of the hadronic response and suppression of the electromagnetic response. The hadronic response can be enhanced by an efficient detection of neutrons (n) and photons (γ)[9], whereas the electromagnetic

[7] measured with respect to the radial axis
[8] *sandwich calorimeter*
[9] in order not to lose energy coming from nuclear deexcitations of the detector material

response can be suppressed by the choice of a material with a high atomic number (Z). To adjust for $e/h = 1$, within a few percent, the thicknesses of the absorber and the scintillator layers are optimised to 3.3 mm, what refers to about one radiation length (X_0), and to 2.6 mm respectively. The total depth of the calorimeter is designed so, that 90% of all jets of maximum energy (∼800 GeV) deposit at least 95% of the energy in the CAL.

Geometrically the CAL is divided into three parts: the forward (FCAL), barrel (BCAL) and rear (RCAL). These parts are subdivided into single *modules*, where the FCAL and RCAL modules are rectangular and BCAL modules have a wedge-shape due to the cylindrical overall-design. The modules consist of so called *towers* of $20\times20\,\mathrm{cm}^2$, which are longitudinally subdivided into one electromagnetic section (EMC) and two (one for RCAL) hadronic sections (HAC1, HAC2). The sections are separated by metal plates of $1\,X_0$ thickness. The EMC sections are further transversely subdivided into four (two for RCAL) cells. Since a *cell* constitutes the smallest readout-unit of the CAL, even the single sections of a HAC tower will be referred to as cells in this thesis. Tab. 3.1 summerises properties of the CAL parts.

CAL part		FCAL	BCAL	RCAL
θ coverage		2.2° – 39.9°	36.7° – 129.1°	128.1° – 176.5°
Number of modules		23	32	23
Number of layers	EMC	25	23	25
	HAC	160	98	80
Depth	EMC (X_0)	26	25	26
	HAC (λ)	6.2	3.9	3.1
Total weight (t)		238	320	154

Table 3.1: Properties of CAL parts
One layer means one pair of absorber and szintillator. In addition to the number of layers, each section contains a single scintillator layer. X_0 and λ are the radiation length and the interaction length ($1\lambda \approx 25X_0$).

The light produced in the scintillators of one cell is read out via wavelength shifters (WLS) and converted into electrical signals in two photomultiplier tubes (PMT) per cell. As an example, Fig. 3.9 shows the structure of an FCAL module. The summed signal is used for energy and timing measurements. The energy resolution for the CAL has been determined in testbeam measurements [75] as

$$\frac{\sigma_e}{E} = \frac{18\%}{\sqrt{E}} \text{ and } \frac{\sigma_h}{E} = \frac{35\%}{\sqrt{E}} \tag{3.3}$$

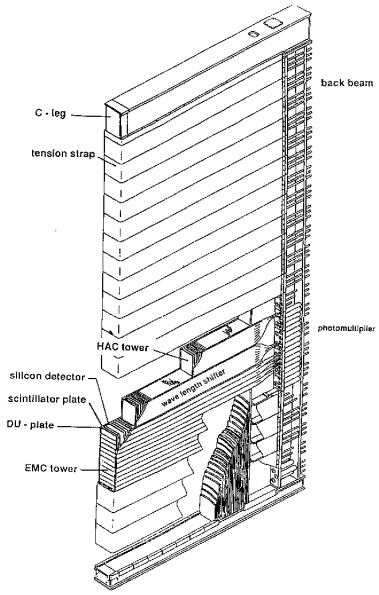

Figure 3.9: Layout of an FCAL module
Particles coming from the IP enter from the left. The module is 2 m deep and 4.6 m high.

for electromagnetic and hadronic showers, with E in GeV. The excellent timing resolution of the order of 1 ns for energy depositions larger than 4.5 GeV is used to reject non-ep events by their characteristic timing patterns already at trigger level. The proportion of the two PMT-signals (*energy sharing*) provides a measurement of the horizontal position (local y-coordinate) of the incidence of an electron with a resolution of

$$\sigma_y = \frac{1.52\,\mathrm{cm}}{\sqrt{E}} + 0.15\,\mathrm{cm}\,, \tag{3.4}$$

where part of the constant term is due to the resolution of the testbeam measurement. The same method using the proportion of the energy deposition in the neighbouring cells of the struck cell gives a resolution in the local x-coordinate of

$$\sigma_x = \frac{\alpha}{\sqrt{E}}\,, \tag{3.5}$$

where $\alpha = 5.2\,\mathrm{cm}$ in the centre of the cell and $\alpha = 4.0\,\mathrm{cm}$ at the edge.

The natural radioactivity of U^{238} produces a stably constant signal in the PMTs (*dark current*). To reduce these dark currents, the uranium plates are wrapped into stainless steel foils. The thickness of this foil is adjusted to 0.2 mm for the EMC and 0.4 mm for the HAC to allow for an unbiased physics measurement on the one

hand, but to have still a signal high enough for calibration purposes on the other hand [76]. Beside this main calibration tool, the PMTs and the readout electronics are calibrated using laser, LED and test pulses. The steel foils also contribute to the compensation by suppressing 3% of the electromagnic signals.

3.2.5 The Backing Calorimeter

The BAC [77] is designed to correct CAL measurements for leaking energy and to track muons traversing the YOKE, that is important especially in regions where no muon detectors are present like e.g. the bottom of the ZEUS detector. Since it is able to distinguish hadron from muon showers, the BAC contributes to muon identification and trigger. Additionally one can benefit from the intrinsic CAL resolution by vetoing events with hadron showers leaking out of the CAL.

The BAC is a tracking calorimeter using the YOKE as absorber. It is built from modules of tubular aluminium proportional chambers of $11\times15\,\mathrm{mm}^2$ cross section and several meters length. For the chambers a gas mixture of argon (Ar, 85 – 90%) and carbon dioxyd (CO_2, 10 – 15%) is used The BAC *modules* are formed by seven or eight of such tubes (*cells*) and are inserted layerwise into the YOKE. Tab. 3.2 lists the inventory of the BAC. Inside each tube a gold plated tungsten wire of 50 µm diameter is stretched with support every 50 cm. The wires have both, analog and

Region	Barrel	Bottom	Forward	Rear	Total
Area (m^2)	1902	296	460	322	2980
Gas volume (m^3)	38.04	5.92	9.20	6.44	59.60
Number of layers	9	9	10	7	–
Number of 8-tube-modules	2252	204	800	560	3816
Number of 7-tube-modules	672	106	320	224	1322
Module length (m)	4.5 or 5.5	7.3	1.8 – 3.6	1.8 – 3.6	
Number of wire towers	102	10	30	30	172
Number of pad towers	1122	150	208	208	1456
Shaped cathode channels	–	438	–	–	–

Table 3.2: BAC inventory
The bottom is listed separately from the barrel BAC, because it is equipped to compensate for the missing muon chambers in this region.

digital readout. For energy measurements, the analog signal is summed up in non-projective *wire towers*, which are formed by the wires of two to four neighbouring modules (width of about 25 cm to 50 cm) over the full depth of the BAC. The digital readout provides hit patterns to track particles in two dimensions. Additionally, the

modules are equipped with 50 cm long and 0.7 mm thick aluminium cathode pads mounted on the top of the aluminium extrusion. They are grouped in non-projective *pad towers* to distribute and localise energy and hits along the wires. In width and depth these pad towers are formed equivalent to the wire towers and have the length of one pad, thus resulting in a a size of about $50 \times 50\,\mathrm{cm}^2$ (four modules). These configuration results in an energy resolution of

$$\frac{\sigma_e}{E} = \frac{1.1}{\sqrt{E}} \tag{3.6}$$

with the particle energy E given in GeV, whereas the spatial resolution obtained is about 1 mm perpendicular to the wires and of the order of the pad length along the wires. To allow for the measurement of muon trajectories underneath the ZEUS detector, where no muon detectors are present, layers 1, 5 and 9 of the bottom BAC chambers are equipped with special shaped cathode pads with a spatial resolution of about 1 mm along the wires.

3.2.6 The Muon Detectors

Since muons are part of the final state of many physics processes of high relevance at HERA like e.g. heavy quark production or production of isolated leptons, emphasis is put on identification and reconstruction of muons down to lowest polar angles in ZEUS. Due to the limited momentum resolution of the tracking detectors at small polar angles and the higher average momentum of muons in the forward direction, these tasks are much more challenging in the latter region. For this reason the effort spent into the forward muon detector is bigger than for other forward sub-detectors compared to their barrel and rear counterparts. The forward muon detector (FMUON, 3.2.6.1) is also completley independent from the barrel and rear muon detectors (B/RMUON, 3.2.6.2).

Generally the muon detectors consist of two parts, one on the inside and the other on the outside of the YOKE with respect to the IP. They provide a momentum measurements independent from the tracking detectors and contribute to the trigger.

3.2.6.1 Forward Muon Detector

FMUON is designed to provide a completely independent momentum measurement at low polar angles for muons up to at least 100 GeV [61, Ch. 9]. In addition, non-ep background is rejected at trigger level on the bases of directionality and momentum cuts.

FMUON consists of:

Toroids: Two large toroidal magnets provide a magnetic field of 1.7 T to measure muon momenta in the region $5^\circ < \theta < 16^\circ$.

Limited streamer tubes: Four *limited streamer tubes* (LST) [78] trigger planes (LST1 – LST4) have the aim to trigger on muon candidates and to reconstruct the azimuthal and radial coordinates of their tracks. One plane is made of four chambers grouped in two half-planes. One chamber (*quadrant*) consists of two layers of horizontally positioned LSTs within a plastic sheet. The tubes of the two layers are displaced by 0.5 cm to allow for complete geometrical acceptance. Each quadrant is contained in an air tight aluminium box with copper strips glued on the outside in polar geometry. The LSTs induce a signal in the copper strip, if a particle crosses the plane. There are 132 radial (ρ) strips of 1.9 cm width per quadrant, which are divided along the bisector of the quadrant so that the simplest readout unit is an octant. The number of azimuthal (ϕ) strips per octant is 32. Each covers an angle of 1.4°. Both types of strips are read out digitally.
Two planes of limited streamer tubes (*wall planes*, LW1 and LW2) cover the angular gap between BMUON and the toroids ($16° < \theta < 32°$) to achieve the desired geometrical acceptance of FMUON. Each plane consists of eight air tight aluminium wrappings with one LST layer inside. The LST signal is induced in copper strips with radial arrangement. The 64 ϕ-strips per octant cover 0.7°, and the 192 ρ-strips per octant cover 1.8 cm each. The ϕ-strips are read out digitally, while the ρ-strips are read out digitally and analogly.

Drift chambers: The four planes of drift chambers (DC1 – DC4) are needed in order to obtain a good momentum resolution. Each plane consists of four individual chambers grouped two by two into half layers. The basic element of a chamber is the *cell* made of four sense wires and the set of wires needed to generate the appropiate electric field. The sense wires measure the radial coordinate (ρ). The signal from the wires is sent to a time-to-digital converter (TDC), which converts them into a time interval related to the drift distance by a known relation.

LST1 and DC1 are situated inside the YOKE and make up the inner region of FMUON (FMUI), the remaining components form the outer region of FMUON (FMUO) on the outside of the YOKE. Fig. 3.10 shows the schematic structure of FMUON.

3.2.6.2 Barrel and Rear Muon Detectors

The ZEUS barrel and rear muon detectors (B/RMUON) [79] cover a very large area of about 1800 m^2 and consist of LSTs as active elements. The chambers are situated inside (BMUI, RMUI) and outside (BMUO, RMUO) the YOKE. Each chamber consists of two double layers of LSTs with wires running parallel to the beam axis in the barrel and normal to it in the rear. The double layers are separated and

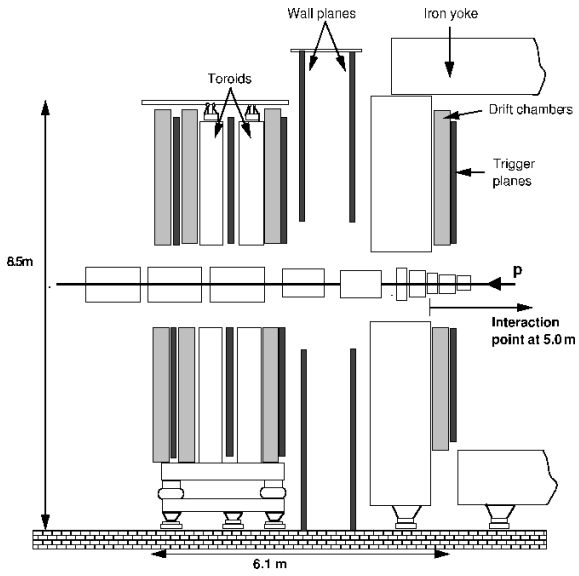

Figure 3.10: Schematic view of FMUON along the beam axis
The thick black lines indicate the limited streamer tubes, from the left to the right: LST4, LST3 (between the toroids), LST2, LW1 and LW2 (wall planes) and LST1 (within the YOKE). The grey areas show the drift cambers, DC4 to DC1 from the left to the right.

supported by aluminium honeycomb frames of a thickness of 127 mm (304 mm for BMUO). Within a double layer the individual layers are displaced by 8.3 mm in order to minimise dead areas for particles traversing at 90°with respect to the wire plane. Each LST is made of a plastic profile containing eight 1 cm wide cells with a 100 µm copper-beryllium wire, which is read out via a TDC. The LST planes are equipped on one side by 13 mm wide readout strips running normal to the wires with a 15 mm pitch. They have an analog readout [80]. The achieved resolutions are 200 µm orthogonal and 700 µm parallel to the wires. A three-dimensional view of the B/RMUON chambers including the wire and strips arrangement can be seen in Fig. 3.11.

3.2.7 Luminosity Measurements

For the luminosity measurement at ZEUS [82], the process of ep-bremsstrahlung ($ep \to e'p\gamma$) with the lepton and the photon scattered at very low angles θ_e and θ_γ with respect to the incoming electron is chosen. The cross section of this process is large enough ($\sigma \geq 20\,\text{mb}$) to yield sufficient statistics and is very well known by theory. The differential cross section as function of the photon energy is described

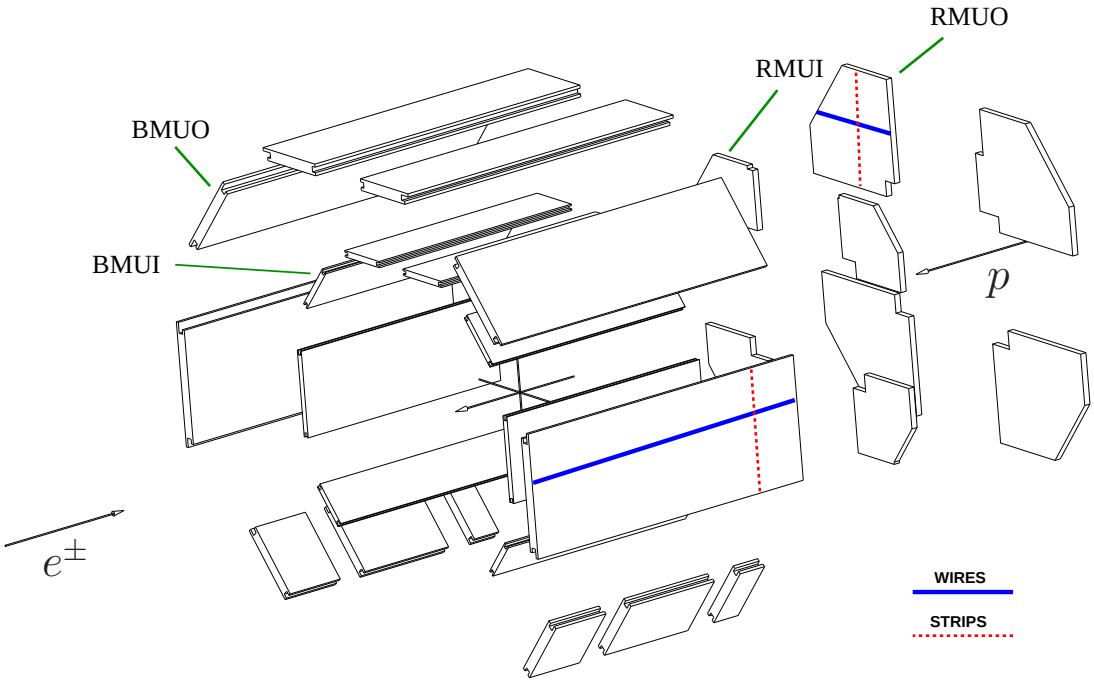

Figure 3.11: Schematic view of B/RMUON [81]
Gaps between the planes are inserted in this sketch to have a better perspective.

by the Bethe-Heitler formula [22] and is known with an accuracy of 0.5%:

$$\frac{d\sigma_{BH}}{dk} = 4\alpha r_e^2 \frac{E'}{kE}\left(\frac{E}{E'} + \frac{E'}{E} - \frac{2}{3}\right)\left(\ln\frac{4E_pEE'}{m_em_pk} - \frac{1}{2}\right), \tag{3.7}$$

where α is the fine structure constant, r_e the classical electron radius, k, E, E' and E_p the energies of the photon, the incoming electron, the outgoing electron and the proton and m_e and m_p the masses of the electron and the proton. The recoil of the proton can be neglected to a very good approximation, which gives

$$E = E' + E_\gamma\,. \tag{3.8}$$

At ZEUS, only the bremsstrahlung photon rate is measured to determine the luminosity. The photons are radiated with $\theta_\gamma \leq 1\,\text{mrad}$ and travel along the p-beampipe until this is bent upwards from about $z \approx -80\,\text{m}$ on. They leave the beampipe through an aluminium exit window of 1 cm thickness at $z = -92.5\,\text{m}$. Then the photon rate is measured by two independent systems.

10% of the photons convert into an e^+e^--pair in the exit window and are bent out of the photon direction by a spectrometer dipole magnet. The photon rate is measured now indirectly by counting e^+e^--coincidences in two small tungsten scinillator calorimeters away from the photon flight direction. This spectrometer has small acceptance in conincidence ($\approx$3%) and no acceptance for low energy photons, so that the probability of pile-up and synchrotron radiation (SR) photon coincidence is small. The main systematic error of this method is due to the error in the knowledge of the acceptance. The acceptance is measured by coincidence rates with bremsstrahlung electrons in a small tungsten scintillator fibre calorimeter at $z = 5.3\,\mathrm{m}$ (6-meter tagger, TAG6), which has 100% acceptance in an window of E' where the spectrometer acceptance is maximised. These electrons can be detected, because the e-beam bending magnets close to the IP act as spectrometer magnets bending off-beam energy electrons towards the centre of the HERA ring. A coincidence due to a Bethe-Heitler event should give an total energy $E' + E_\gamma$ equal to the e-beam energy. Monte Carlo simulations have shown, that a total systematic error of 1.4% in the luminosity measurement with the spectrometer should be attainable.

The second method of counting the photon rate measures the bremsstrahlung photons directly. Photons traversing the exit window without conversion travel along a 12.7 m long vacuum pipe. Then two absorbers (*filters*) and two aerogel Cherenkov counters block the SR and can be used to correct for the energy loss of bremsstrahlung photons in the filters. At $z = -107\,\mathrm{m}$, a lead sandwich calorimeter of a depth of $22\,X_0$ with additional vertical scintillator fingers measures energy and horizontal position of the photons for $\theta_\gamma \leq 0.5\,\mathrm{mrad}$. The energy resolution depends on the accuracy of the energy loss correction applied. The spatial resolution is of the order of 3 mm [84] corresponding to an uncertainty of the reconstructed θ_γ of about 30 µrad. Due to the problem of photon pile-up, a number of corrections have to be applied to the luminosity measurement. Simulations have shown, that the corresponding systematic error can be kept below 2%.

A sketch of the ZEUS luminosity monitor is shown in Fig. 3.12.

3.2.8 Polarisation Measurements

The availability of longitudinally polarised e-beams at HERA II opens up the possibility of detailed studies of electroweak physics along with other benefitting to the HERA collider experiments [58,85]. For example, in the SM the cross section of CC in DIS depends linearly on the longitudinal polarisation of the e-beam. The cross section for $e^-(e^+)$p CC DIS at a polarisation of +1(-1) is predicted to be zero.

Measuring the total cross section as a function of polarisation allows the SM to be tested through searches for right-handed CC. Fig. 3.13 shows the actual status of such measurements at ZEUS. They are also of importance for analyses of events with missing transverse momentum, where CC DIS events are background. Besides

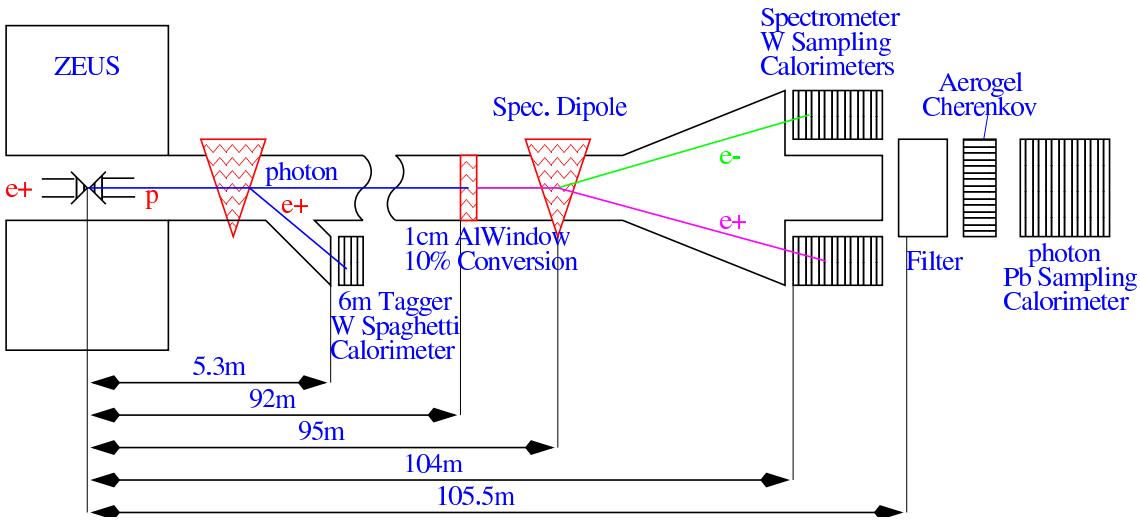

Figure 3.12: Schematic view of the ZEUS luminosity monitor system (side view)
A bremsstrahlung photon produced at the IP converts in the exit window and the e^+e^- pair coincidence is recorded by the two tungsten sampling calorimeters. The scattered bremsstrahlung electron is detected by TAG6. Non-converted photons are detected by the lead sampling calorimeter.

that, searches for BSM-physics with chiral couplings like e.g. in RPV SUSY can benefit from longitudinally polarised e-beams as well as measurements of DVCS.

By the emission of synchrotron radiation, e-beams become polarised tranversly (*Sokolov-Ternov effect* [87]). This transverse polarisation can be converted into longitudinal polarisation and vice versa by spin rotators [88]. In HERA II, three experiments benefit from this technique to make longitudinally polarised e-beams available as shown in Fig. 3.14. To fulfill the goals of the polarised physics programme, a precise measurement of the e-beam polarisation is necessary. Therefore two polarimeters are installed in HERA: one to measure the transverse (TPOL), one the longitudinal polarisation (LPOL), whose measurements should agree with each other. Both polarimeters make use of the polarisation dependence of *Compton scattering*. Circularly polarised intense pulsed laser beams[10] are used as photon sources. For the HERA II upgrade, both polarimeters have been equipped to provide also single bunch polarisation measurements to deal with the polarisation difference between colliding and non-colliding bunches.

The LPOL [89] measures the energy asymmetry between the backscattered photons from left- and right-handed polarised laser beams with an electromagnetic

[10] *Nd*-YAG laser operated at a wavelength of 532 nm

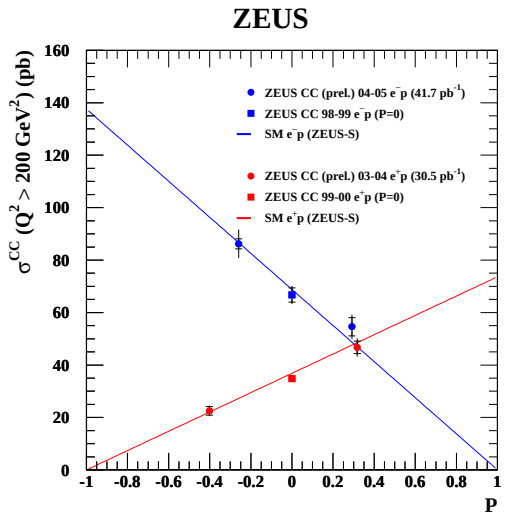

Figure 3.13: Charged current cross sections with longitudinally polarised lepton beams at ZEUS [86]
The unpolarised cross sections were measured with HERA I data.

calorimeter consisting of four optically isolated $NaBi(WO_4)_2$ crystals, which are shielded from SR by two 6 mm thick lead plates. The e-beam polarisation is determined with an absolute statistical precision of 1% per minute and a fractional systematic uncertainty of 1.6%.

The TPOL [90] measures the energy dependent angular asymmetry of the backscattered photons. Compared to the LPOL, the TPOL calorimeter is segmented into an upper and lower half to measure the up-down-asymmetry of the energy from left- and right-handed polarised laser beams. To calibrate the position measurement, a silicon strip-detector is installed in front of the calorimeter. The e-beam polarisation is determined with an absolute statistical precision of 5‰ per minute and a fractional systematic uncertainty of 3.4%.

The measurements of both detectors agree within 1% for the HERA II 2003/04 e^+p-running with an combined systematic error of 3.25% [91].

3.2.9 Trigger and Data Acquisition

As described in 3.1, the bunch crossing rate at HERA is 10.4 MHz, where the rate of physics ep-events varies from e.g. 0.1 Hz for NC DIS events with $Q^2 > 100\,\mathrm{GeV}^2$ to 250 Hz for soft PhP (for an instantaneous luminosity of $2{\cdot}10^{31}\,\mathrm{cm}^{-1}\mathrm{s}^{-1}$). On the

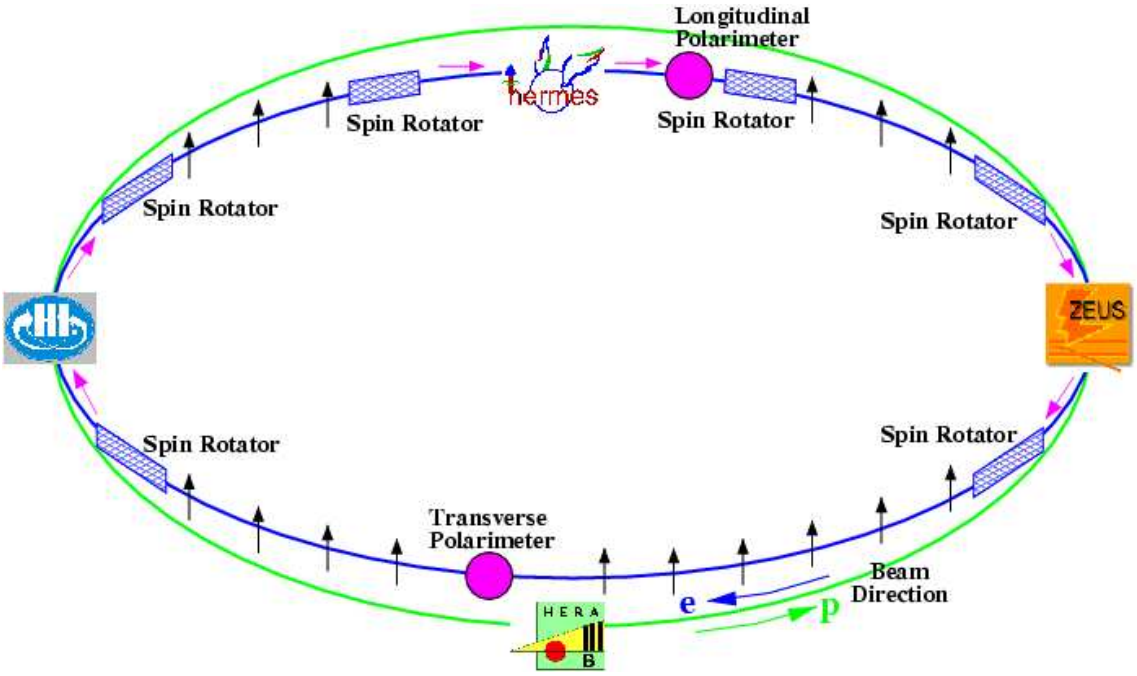

Figure 3.14: HERA II polarisation and polarimeters
A schematic sketch of HERA and its experiments is shown. The black vertical arrows indicate transverse polarisation of the e-beam, the pink arrows indicate longitudinal polarisation and the pink dots show the position of the polarimeters.

other hand, the rate of non-ep background events[11] can exceed the rate of physics events by several orders of magnitude. Since the total data size per event is 150 kB and the writing speed at ZEUS is limited to about 1.5 MB/s, a significant reduction of the data rate and size with a maximum efficiency for physics events is required.

A three level trigger system [92] with increasing complexity of the decision making algorithms and decreasing throughput is used to select events online. The trigger and data acquisition (DAQ) scheme is illustrated in Fig. 3.15. In the following the trigger levels are described.

First level trigger (FLT): The FLT is a hardware based trigger, which uses programmable logic to reject background events. Each ZEUS subcomponent has its own FLT, which make decisions based on properties like e.g. global and local energy sums, timing or tracking information as far as achievable in the short time on-hand (1.0 – 2.5 µs). The global FLT (GFLT) then combines these individual decisions to a final one whithin the fixed FLT latency of 4.4 µs. Since

[11] decribed in 4.2.2

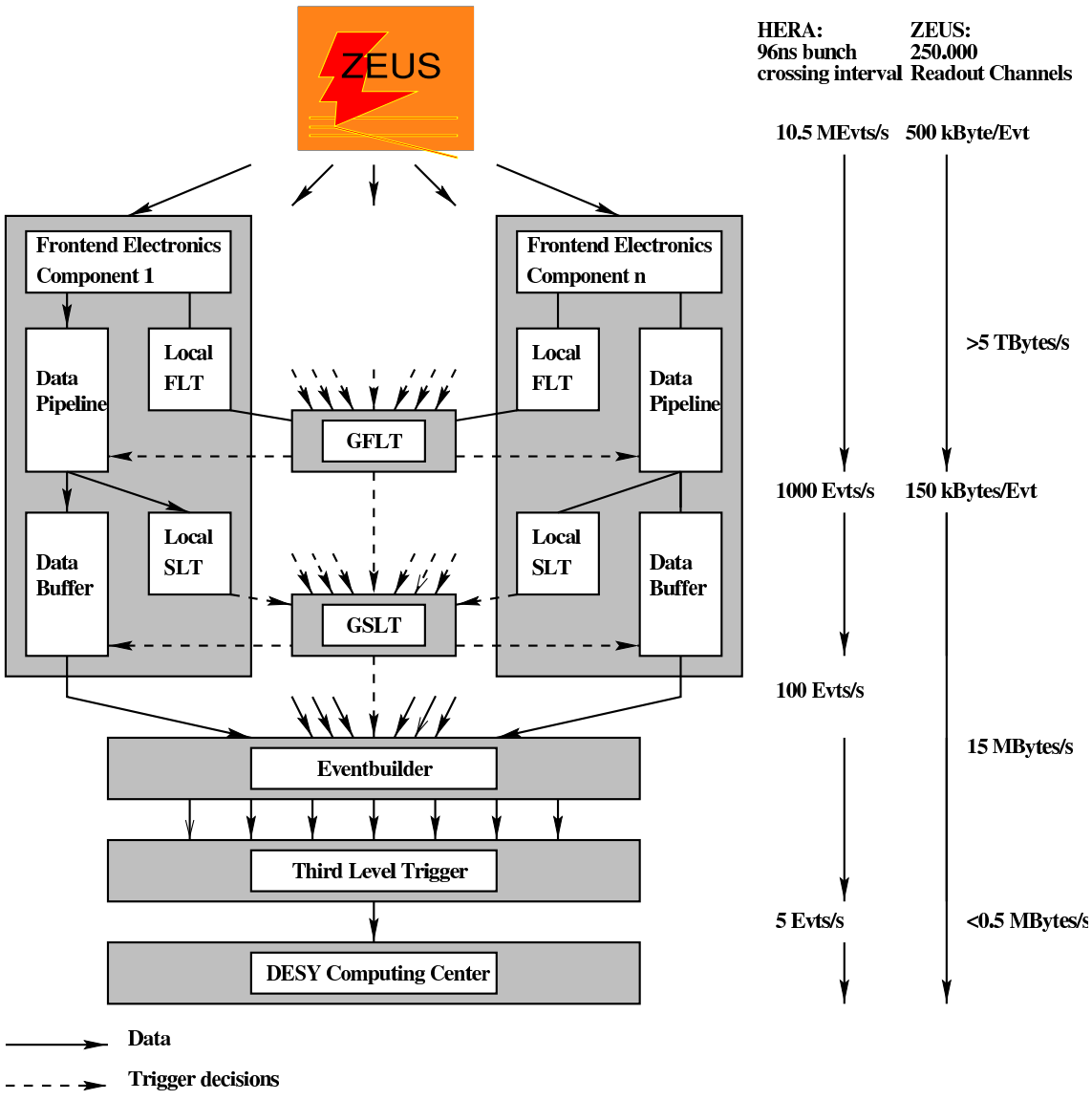

Figure 3.15: ZEUS trigger and DAQ scheme
Data flow and trigger decisions are illustrated.

this is longer than the bunch crossing time of 96 ns, the events are pipelined until the event decision is taken. The event rate is reduced to below 1 kHz.

Second level trigger (SLT): The SLT is a software based trigger with a parallel processor system implemented in a transputer network. Similar to the FLT, local SLT decisions are combined to an event decision by the global SLT (GSLT). Since the available computation time is longer than in the FLT, event properties can be calculated to higher precision and complexity. Timing information from the CAL is available at this stage, which is essential to reject beam-gas events. The event decision is taken within 7 ms and the event rate is reduced to $\sim$50 – 100 Hz. Data of accepted events is sent to the *eventbuilder* (EVB), which forms one consistent event record and stores the data until the next trigger level is ready to process. The data structure is based on the ALEPH *data model* (ADAMO) [93].

Third level trigger (TLT): The TLT uses a simplified version of the offline reconstruction software on a computer farm to reconstruct the whole event. At this stage information like kinematic variables, output of electron and jet finders or the topology of the hadronic final state are available. In addition, a classification of the event is performed. The output rate of the TLT is $\sim$5 – 10 Hz and the accepted events are written to tape to be fully reconstructed offline with maximum precision later.

Chapter 4

Search Strategy

This search for isolated leptons in events with large missing transverse momentum focusses on the production of W-bosons and single t-quarks. So the search strategy is geared to the topologies of these kinds of events with emphasis on the search for singly produced t-quarks. The main goal of the search is to set limits on the production of single t-quarks in FCNC, and the search is optimised with respect to this goal. However, single W-boson production is also treated as signal in this search, since the search strategy is also be applicable to these processes.

4.1 Topology of Events with Isolated Leptons and Large Missing Transverse Momentum

As the title indicates, the dominating property of these events is the isolated lepton together with large missing transverse momentum. However, the production mechanisms described in 2.4 lead to further distinct properties, which are described in the following.

4.1.1 Topology of Single W-Boson Production

In W-boson production the isolated lepton and the missing transverse momentum are both due to the leptonic decay of the W-boson. An observation of the scattered beam electron is rare, because this reaction is dominated by the PhP regime. Thus, a sizable momentum transfer to the struck quark with a resulting separate jet is rather unlikely.

For the leptonic decay one expects a lepton with high transverse momentum and missing transverse momentum in the event due to the undetected neutrino. For the leptonic decay $W \rightarrow \tau\nu_\tau$ the signature depends on the subsequent decay of the τ-lepton. For the leptonic τ-decays $\tau \rightarrow e\nu_e\nu_\tau, \mu\nu_\mu\nu_\tau$ the signature is similar to the

corresponding W-decay, except from the large missing transverse momentum from the additional two neutrinos. For the hadronic τ-decay a hadronic jet with small spatial extent and additional missing transverse momentum from the neutrino in the τ-decay is expected.

4.1.2 Topology of Single t-Quark Production

The signature of single t-quark production is very similar to that of W-boson production including the statements on momentum transfers. The main difference arises from the additional b-quark from the t-quark decay, which leads to an additional jet with high transverse energy. Furthermore the isolated leptons are restricted to be positively charged. This signature is unique in HERA physics.

Due to the very small cross section of single t-quark production within the Standard Model (see 2.4.2.1), it is assumed that the observation of singly produced t-quarks at HERA is not to be expected from SM processes.

4.1.3 Topologies of Production Mechanisms in R-Parity Violating Supersymmetry

In all Stop production reactions discussed in 2.4.3.1 the beam electron and the struck quark annihilate, so that they cannot contribute to the final state. Therefore besides the Stop decay products only the proton remnant can be observed. In the decay $\tilde{t}_1 \rightarrow b\tilde{\chi}_j^+$ as shown in Fig. 2.16(a), the isolated lepton and the neutrino carrying the missing transverse momentum originate from the chargino decay. Such events also contain a jet from the b-quark and additionally possible decay products from the neutralino. Anomalous W-boson production as shown in Fig. 2.16(b) leads to the signature of interest via the leptonic W-decay. Again, additional hadronic decay products would be expected. The topology of the RPV Stop decay as shown in Fig. 2.16(c) depends on the subsequent τ-decay. In case of a hadronic decay the event signature would be a narrow jet from the τ-decay, a jet from the b-quark and missing transverse momentum in the direction of the τ-jet from the τ-neutrino. If the τ decays leptonically, the narrow jet is replaced by the corresponding lepton. In this case the missing transverse momentum is carried by the two neutrinos.

4.2 Background Processes

4.2.1 Standard Model ep Background

SM processes contribute to the signature of interest via mismeasurements producing fake leptons and large missing transverse momentum. In a search for singly

produced t-quarks also the SM W-boson production contributes. More specifically, these processes are considered:

Charged current deep inelastic scattering: CC DIS events are characterised by missing transverse momentum coming from the scattered neutrino in the final state. These result in signal events, if a hadron is misidentified as an isolated lepton.

Neutral current deep inelastic scattering: In NC DIS events the scattered beam electron usually is identified within the main detector. If the hadronic final state or the electron is mismeasured or the event contains muons or neutrinos, a significant missing transverse momentum can arise. Events which are not identified as NC are the main source of background for e-type signal events.

Photoproduction: In PhP processes the scattered electron carries only a small transverse momentum and escapes the detector through the beampipe. Only a mismeasurement of the hadronic final state can lead to significant missing transverse momentum, which in conjuction with a fake isolated lepton might mimic a signal event. The fraction of such mismeasurements is small in PhP. However, these events contribute to the signature of interest through the high PhP cross section.

Lepton pair production: To mimic a signal event in this case, a significant missing transverse momentum needs to be reconstructed in addition to at least one of the two leptons. This is mainly the case for μ-pair production, which is the dominating source of background for μ-type signal events.

Single W-boson production: On the one hand, single W-boson production acts as signal. On the other hand, in searches for single t-quark production these events are part of the background. The signature has already been described in 4.1.1.

4.2.2 Non-ep Background

In addition to ep-interaction, there are other sources of background to be considered:

Beam gas interactions: *Beam gas interactions* are interactions of the beam particles with residual gas nuclei inside the beam pipe or elements of the beam line. They are suppressed by VETO for sufficiently high transverse momenta of the interaction products coming from a p-beam interaction.

Halo muons: Beam gas interactions can produce particles which decay into muons ($\pi^{\pm}$, $K^{\pm}$). This leads to a background of muons passing the detector almost parallel to the beamline.

Muons from cosmic showers: When cosmic rays interact within the atmosphere, they produce high-energy muons ("cosmics") which can traverse the CTD. Most of them pass on straight lines from top to bottom, but also horizontal cosmics occur. Cosmics can radiate photons or interact inelasically ($\mu N \rightarrow \nu X$) producing large energy depositions and missing transverse momentum in the CAL. Overlayed cosmic events may adulterate the measured energy in *ep*-events.

Sparks in CAL cells: The PMTs in CAL cells can discharge spontaniously (*spark*), which leads to fake energy depositions. They are identified by a large imbalance between the two independent PMTs in a CAL cell. In cells with only one active PMT, one can suppress sparks by requiring a minimum energy in adjacent cells.

Chapter 5

Data Sample and Monte Carlo Simulations

5.1 Data Sample

In this search, HERA II data from e^+p-collisions taken in the years 2003 and 2004 is analysed. The total integrated luminosity is $\mathcal{L}_{int} = 40.76 \pm 1.86\,\mathrm{pb}^{-1}$.

The integrated luminosities and the average polarisation values of particular running periods are summarised in Tab. 5.1 [94].

Year	Lepton beam	Runs	$\mathcal{L}_{int}$ (pb^{-1})	$\sigma_{\mathcal{L}_{int}}$	P
sum 2003	e^+	295	2.08	5.1%	0.329
2004	e^+	18	0.47	4.2%	0.0
2004	e^+	501	7.90	4.6%	0.331
2004	e^+	714	17.52	4.7%	-0.386
2004	e^+	224	12.80	4.2%	0.325
sum 2004	e^+	1457	38.68	4.5%	0.0
sum 2003 - 2004	e^+	1752	40.76	4.5%	0.017

Table 5.1: Integrated luminosities and polarisation
The integrated luminosities $\mathcal{L}_{int}$ and their uncertainties $\sigma_{\mathcal{L}_{int}}$ are obtained with the photon calorimeter (see 3.2.7). The average polarisation values $\bar{P}$ are obtained with TPOL (see 3.2.8) or with LPOL, if TPOL was not available (62 runs in total).

5.2 Monte Carlo Simulations

Simulations are essential to understand the complex properties of high-energy physics reactions and detector performances. Typically these simulations are done using a statistical sampling method called the *Monte Carlo* (MC) method. It is implemented in so-called MC generator programs, which allow to predict detailed final state properties of various processes. Coupled with a detector simulation program, also the response of the detector to certain reactions can be predicted. In searches for BSM physics, MC predictions of the SM processes are used to find deviations of the data from the Standard Model.

MC simulation of hadronic high-energy physics processes can be divided into three parts:

Hard subprocess: The hard subprocess including the parton showering can be described perturbatively. QCD radiation is treated separately (see 5.2.1.1).

Hadronisation: The hadronisation phase cannot be described perturbatively and has to be modelled. Its output contains the produced particles and their four-momenta.

Detector simulation: The detector simulation takes the produced particles and simulates their interaction with the active and passive ("dead") material of the detector. New particles can be produced, e.g. via photon conversion. The digitisation as a special part of the detector simulation. It translates the particle interactions with the active material into the detector response.

This section describes the simulation of all SM processes considered in this analysis.

5.2.1 Monte Carlo Models

Since only the hard subprocess can be calculated from perturbation theories, the soft subprocesses have to be modelled. Different models exist for the particular phases of the physics process, which are described in the following.

5.2.1.1 QCD Radiation

Although in principle hard QCD radiation[1] belongs to the hard subprocess, it has to be modelled, since it is a higher order process and simulations are available only in LO. Two approaches are commonly used:

[1] initial or final state radiation of additional gluons

Colour dipole model: In the *colour dipole model* (CDM) [95], QCD radiation is described as parton showers evolving from independently radiating colour dipoles. The first dipole is spanned by the struck quark and the proton remnant. The spatial extension of the proton remnant is taken into account as restriction to the phase space for hard gluon radiation close to the proton remnant.

Matrix element and parton shower model: In the *matrix element and parton shower model* (MEPS) higher orders of perturbation theory are summed up to all orders usually using the DGLAP leading-log approximation [20, 21]. Perturbation theory is applicable to parton energies down to about 1 GeV. A planar parton shower is generated with the energy fractions in each branching process determined using the *Altarelli-Parisi splitting functions* [21]. Angular ordering is imposed

5.2.1.2 Fragmentation and Hadronisation

For the simulation of the final part of the physics process two approaches are commonly used:

Lund model: In the *Lund string fragmentation model* [96] the colour field between diverging $q\bar{q}$-pairs is treated as a string of constant energy density of about 1 GeV/fm. The total string energy increases with increasing distance between the $q\bar{q}$-pair, until a new $q\bar{q}$-pair can be created from the vacuum. The string splits in substrings this way until the energy of the initial $q\bar{q}$-pair is dissipated.

Cluster hadronisation: The *cluster hadronisation model* [97] is based on the idea of preconfinement of colour. Gluons are split into $q\bar{q}$-pairs non-perturbatively. Neighbouring quarks and antiquarks are combined to low mass colour singlett clusters, which decay isotropically into hadron pairs or form hadrons by themselves under momentum exchange with neighbouring clusters to adjust the mass.

5.2.2 Simulation of the Signal Processes

In the following the simulation of the signal processes is described in more detail.

5.2.2.1 Simulation of Single W-Boson Production

Events with singly produced W-bosons were simulated with EPVEC 1.0 [24], a LO generator for electroweak vector boson production, which does not include QCD radiation. The CTEQ5D parametrisation of the proton PDFs [98] was used. Hadronic

final states were simulated using the Lund string fragmentation model as implemented in JETSET 7.4 [99].

EPVEC uses two phase space regions to compose the total cross section like

$$\sigma = \sigma(|u| > u_{cut}) + \int^{u_{cut}} \frac{d\sigma}{d|u|} d|u| \,, \tag{5.1}$$

with the square of the four-momentum transfer from the incoming quark to the final state W-boson $u = (p_q - p_W)^2$. The first term arises from W-boson production in the DIS regime. It is calculated using helicity amplitudes for the process $eq \to eWq'$. The second term describes W-boson production in the resolved PhP regime. It is calculated by folding the cross section of the process $qq' \to W$ with the proton PDFs and the effective PDFs of the photon emitted by the incoming electron. The total cross section varies little with u_{cut}, which is set to $25\,\mathrm{GeV}^2$ in this analysis. The W-boson samples used in this analysis are listed in Tab. 5.2.

W production process	σ (pb)	events	$\mathcal{L}_{int}$ (pb^{-1})
W^+ DIS	0.51296	48395	94345
W^- DIS	0.42772	48712	113888
W^+ resolved	0.08198	10000	121981
W^- resolved	0.11409	10000	87650

Table 5.2: MC samples to simulate SM background from events with singly produced W-bosons
The simulated cross sections σ, the numbers of simulated events and the corresponding integrated luminosities $\mathcal{L}_{int}$ are shown.

5.2.2.2 Simulation of Single t-Quark Production

Fot this analysis, events with singly produced t-quarks were simulated using HEXF [100], a generator for excited fermions, which is based on a phenomenological model [101]. An excited u-quark (u^*) with the mass of the t-quark is produced by the exchange of a virtual photon, thus simulating the anomalous coupling $\kappa_{tu\gamma}$ only. The u^*-quark is forced to decay to W^+b then. The proton PDFs were evaluated from the MRS(A) parametrisation [103]. Initial state QED radiation is included using the *Weizsäcker-Williams approximation* [102]. The QCD cascade was simulated by the MEPS model implementation of LEPTO 6.1 [104]. Hadronic final states were simulated using the Lund string fragmentation model implemented in JETSET 7.4 [99]. HEXF uses a fixed mass of the t-quark m_t. So, the simulation was performed with the three masses $m_t = 170, 175, 180\,\mathrm{GeV}$ to study the effect of varying m_t. The

m_t (GeV)	coupling	decay	events
170	$\kappa_{tu\gamma}$	bW	46857
175	$\kappa_{tu\gamma}$	bW	46927
180	$\kappa_{tu\gamma}$	bW	46202

Table 5.3: MC samples to simulate signal events with singly produced t-quarks (HEXF)
The simulated anomalous couplings, the decay of the t-quark and the numbers of simulated events are shown for the different used fixed t-quark masses m_t. Cross sections and therefore also the corresponding integrated luminosities are unknown. For the t-quark mass of 175 GeV a lower limit of $\mathcal{L}_{int} > 218\,\mathrm{pb}^{-1}$ is calculated from the cross section limit given in Eq. 2.26.

Q^2 scale for the proton structure function was set to m_t^2. The HEXF t-quark samples used in this analysis are listed in Tab. 5.3.

To simulate also the anomalous coupling v_{tuZ} and the decay channel $t \to uZ$, single t-quark production was simulated with COMPHEP [47]. Here the proton PDFs were evaluated from the MRST parametrisation [105]. Initial state radiation was not included. For the simualtion of the QCD cascade and the hadronisation, COMPHEP was interfaced to PYTHIA 6.2 [106, 107]. Again, hadronic final states were simulated using the Lund string fragmentation model implemented in JETSET 7.4 [99], and the Q^2 scale for the proton structure function was set to m_t^2. In COMPHEP, the mass of the t-quark was simulated with a finite width. The COMPHEP t-quark samples used in this analysis are listed in Tab. 5.4.

Range of m_t (GeV)	coupling	decay	events
150 – 200	v_{tuZ}	bW	10000
150 – 200	v_{tuZ}	uZ	9000
160 – 190	$\kappa_{tu\gamma}$	bW	14362
160 – 190	$\kappa_{tu\gamma}$	uZ	15725

Table 5.4: MC samples to simulate signal events with singly produced t-quarks (COMPHEP)
The range of the simulated t-quark mass, the simulated anomalous couplings, the decay of the t-quark and the numbers of simulated events are shown. Cross sections and therefore also the corresponding integrated luminosities are unknown. For the t-quark mass of 175 GeV a lower limit of $\mathcal{L}_{int} > 218\,\mathrm{pb}^{-1}$ is calculated from the cross section limit given in Eq. 2.26.

In a detailed comparison at generator level, the CompHEP and Hexf samples used in this analysis were found to agree well [46]. To obtain results which are comparable to the analysis on Hera I data, the Hexf sample generated with $m_t = 175\,\text{GeV}$ was chosen as the default sample for this analysis.

5.2.3 Simulation of Background Processes

In the following the simulation of those Sm processes is described, which are expected to contribute to the selected events in this analysis.

5.2.3.1 Simulation of Deep Inelastic Scattering Processes

For this analysis, CC and NC DIS events were simulated by Lepto 6.5 [104], a generator for deep-inelastic lepton-nucleon scattering, which was interfaced to Heracles 4.5 [108], an event generator for deep-inelastic *ep*-collisions via DjanhoH [109] 1.1. The CTEQ5D parametrisation of the proton Pdfs [98] were used. The simulation of Qcd radiation were based on Cdm as implemented in Ariadne 4.10 [110] or on Meps as implemented in Lepto 6.5. Hadronic final states were simulated using the Lund string fragmentation model implemented in Jetset 7.4 [99]. On the generator level, the simulated events had to exceed lower limits in Q^2. The DIS samples used in this analysis are listed in Tabs. 5.5 and 5.6. Since the cross section of CC Dis depends strongly on the polarisation of the lepton beam, the CC Dis MC samples had to be reweighted according to the average polarisation of the analysed data.

		Cdm		Meps	
Q^2_{min} (GeV)	σ (pb)	events	$\mathcal{L}_{int}$ (pb^{-1})	events	$\mathcal{L}_{int}$ (pb^{-1})
10	44.885	248955	5546.5	248998	5547.5
100	39.649	249998	6305.3	249838	6301.2
5000	3.2850	15000	4566.2	15000	4566.2
10000	0.70626	5000	7079.5	5000	7079.5
20000	0.064348	5000	77702	5000	77702

Table 5.5: MC samples to simulate Sm background from CC DIS events The simulated cross sections σ, the numbers of simulated events and the corresponding integrated luminosities $\mathcal{L}_{int}$ are shown for both used models of final state radiation, Cdm and Meps.

Q^2_{min} (GeV)	σ (pb)	CDM		MEPS	
		events	$\mathcal{L}_{int}$ (pb^{-1})	events	$\mathcal{L}_{int}$ (pb^{-1})
100	8122.	938300	115.53	762975	93.939
400	1167.7	120000	102.77	119999	102.77
1250	197.42	49997	253.25	49811	253.25
2500	58.927	24000	407.28	23999	407.27
5000	14.844	22999	1549.4	24000	1616.8
10000	2.7936	22998	8242.4	22997	8232.0
20000	0.30999	21996	70957	23997	77412
30000	0.054443	11994	220304	10996	201973
40000	0.010874	11955	1099410	10997	1011310
50000	0.0021185	11263	5316500	11998	5663440

Table 5.6: MC samples to simulate SM background from NC DIS events
The simulated cross sections σ, the numbers of simulated events and the corresponding integrated luminosities $\mathcal{L}_{int}$ are shown for both used models of final state radiation, CDM and MEPS.

5.2.3.2 Simulation of Photoproduction Processes

Direct and resolved PhP events were simulated with HERWIG 5.9 [111] using the proton PDF CTEQ4D [112] and the photon PDF GRV LO [113]. Partonic processes were simulated using LO matrix elements, including initial and final state parton showers. Hadronisation is performed using a cluster model. At generator level, the simulated events had to exceed either a lower limit in transverse energy of the hadronic system of 30 GeV or a lower limit in transverse momentum of the hadronic system of 6 GeV. The PhP samples used in this analysis are listed in Tab. 5.7.

PhP process	σ (pb)	events	$\mathcal{L}_{int}$ (pb^{-1})
direct	2830	474160	167.55
resolved	11900	565246	47.500

Table 5.7: MC samples to simulate SM background from PhP events
The simulated cross sections σ, the numbers of simulated events and the corresponding integrated luminosities $\mathcal{L}_{int}$ are shown.

5.2.3.3 Simulation of Lepton Pair Production

Lepton pair production was simulated using the generator GRAPE 1.1j [114] and the proton PDF CTEQ5L [98]. Three kinematic regions were distinguished according to the four-momentum transfer at the proton vertex Q_p^2 and the invariant mass of the hadronic final state M_{had}:

$$Q_p^2 = (p_{e,in} - (p_e + p_{l^+} + p_{l^-}))^2 , \tag{5.2}$$

$$M_{had}^2 = ((p_{e,in} + p_{p,in}) - (p_e + p_{l^+} + p_{l^-}))^2 , \tag{5.3}$$

where $p_{e,in}$ and $p_{p,in}$ are the four-momenta of the incoming electron and proton, respectively, and p_e, p_{l^+} and p_{l^-} are the four-momenta of the outgoing electron and leptons, respectively. The kinematic regions are:

- elastic: $M_{had} = M_p$
- quasi-elastic I: $M_p + M_{\pi^0} < M_{had} < 5\,\text{GeV}$ and
  quasi-elastic II: $5\,\text{GeV} < M_{had}$
- DIS I – IV: $Q_p^2 > 1\,\text{GeV}^2$ and $M_{had} > 5\,\text{GeV}$ with the subprocesses I – IV corresponding to the initial state quark (u, $\bar{u}$, d/s or $\bar{d}/\bar{s}$).

At generator level, the events had to contain at least one lepton with a polar angle of $5^\circ < \theta < 175^\circ$ and at least one lepton with a transverse momentum of $p_T > 5\,\text{GeV}$. The lepton-pair samples used in this analysis are listed in Tab. 5.8.

5.2.4 Detector Simulation

In order to compare the MC simulation with the measured data, the generated MC events are run through a full simulation of the ZEUS detector. This is split into the detector simulation package MOZART and the trigger simulation CZAR. MOZART combines the GEANT 3.21 [115] based simulation of interactions of generated particles with the detector material and the simulation of detector responses. CZAR simulates the trigger decisions and responses for various trigger configurations. In case of a positive trigger decision, it passes the event to the reconstruction program (v. 6). In this analysis, the ZEUS detector simulation in the version num03t0.1 [116] was used.

Leptons	Subprocess	σ (pb)	events	$\mathcal{L}_{int}$ (pb^{-1})
e^+e^-	elastic	13.39127	30000	2240.3
	quasi-elastic I	5.749749	30000	5217.6
	quasi-elastic II	0.2197806	29985	136400
	DIS I	32.63463	29975	918.50
	DIS II	8.258278	30000	3632.7
	DIS III	6.475909	30000	4632.6
	DIS IV	3.660185	30000	8196.3
$\mu^+\mu^-$	elastic	10.20552	30000	2939.6
	quasi-elastic I	4.969400	30000	6036.9
	quasi-elastic II	0.1667154	29000	173950
	DIS I	13.00195	30000	2307.34
	DIS II	2.680569	29000	10819
	DIS III	2.374704	30000	12633
	DIS IV	1.215734	30000	24676
$\tau^+\tau^-$	elastic	6.350449	30000	4724.1
	quasi-elastic I	3.562767	30000	8420.4
	quasi-elastic II	0.144120	30000	208160
	DIS I	5.233473	30000	5732.3
	DIS II	1.047287	30000	28645
	DIS III	0.9540724	30000	31890
	DIS IV	0.4786053	30000	62682

Table 5.8: MC samples to simulate SM background from lepton-pair production
The simulated cross sections σ, the numbers of simulated events and the corresponding integrated luminosities $\mathcal{L}_{int}$ are shown.

Chapter 6

Event Reconstruction

In this chapter the variables used in this analysis are defined.

6.1 Calorimeter Reconstruction

6.1.1 Calorimeter Energy Corrections

In order to suppress the noise, isolated CAL cells with an energy below 80 MeV for EMC cells and 140 MeV for HAC cells were skipped in the reconstruction. Also cells with a large imbalance of

$$\frac{|E_{left} - E_{right}|}{E_{cell}} > 0.7 \tag{6.1}$$

between the two independent PMT responses E_{left} and E_{right} were excluded, if the total energy deposit in the cell E_{cell} was above 1 GeV. To calibrate the energy response of the CAL, constant correction factors are multiplied to the measurements, depending on the CAL part and the cell type. They are listed in Tab. 6.1. This

CAL part	Cell type	Energy correction
FCAL	EMC	+4.0%
	HAC	−5.0%
BCAL	EMC	+4.0%
	HAC	+8.0%
RCAL	EMC	+2.5%
	HAC	+2.5%

Table 6.1: Energy correction factors
Different energy corrections for each cell type in each CAL part.

corrections were applied only to data. The remaining uncertainty in the CAL energy determination is ±1% for the FCAL and BCAL and ±2% for the RCAL [118].

An additional energy correction of a factor of 0.97 was applied to all HAC energies in MC. This correction is specific for analyses performed on the actual 2003/04 e^+p data [119].

Further energy corrections, which are specific for the reconstructed event variables, are described in the following section.

6.1.2 Calorimeter Variables

The total energy deposition in the CAL E_{tot} and its projections onto the ZEUS coordinate axes p_x, p_y and p_z are defined as

$$E_{tot} = \sum_i E_i \,, \tag{6.2}$$

$$p_x = \sum_i E_i \sin\theta_i \cos\phi_i \,, \tag{6.3}$$

$$p_y = \sum_i E_i \sin\theta_i \sin\phi_i \,, \tag{6.4}$$

$$p_z = \sum_i E_i \cos\theta_i \,, \tag{6.5}$$

with the summation index i running over all considered CAL cells (see 6.1.1). θ_i and ϕ_i are the polar and the azimuthal angle of the i-th CAL cell with the energy deposition E_i. The angles were calculated using the reconstructed event vertex and the center of the respective cell. The energy response of each cell was corrected for energy loss in inactive material between the interaction point and the particular cell, separately for identified electrons and hadrons. For cells not associated with electrons (s. 6.4.1), the correction also took into account energy losses in supercracks, back-splash from the CAL and non-uniformities in the response of the cell[1] [120]. In addition, this correction took into account response differences between data and simulation.

The variable

$$E - p_z = E_{tot} - p_z = \sum_i E_i(1 - \cos\theta_i) \tag{6.6}$$

has characteristic distributions for different final states. Due to energy and momentum conservation it peaks at twice the lepton beam energy (55 GeV) for NC DIS events with the scattered beam electron detected in the main detector. The

[1] Eergy measurements of hadrons at small energies are overestimated.

transverse energy

$$E_T = \sum_i E_i \sin\theta_i \tag{6.7}$$

denotes the absolute value of the total energy deposition projected onto the azimuthal plane.

The imbalance of the detected *transverse momentum* p_T and its azimuthal direction ϕ are given by

$$p_T = \sqrt{p_x^2 + p_y^2}\,, \tag{6.8}$$

$$\phi = \arctan\frac{p_y}{p_x}\,. \tag{6.9}$$

The *missing transverse momentum* p_T^{miss} is defined by the negative transverse momentum[2] also taking into account the undetected transverse momentum carried by muons, which escaped the detector. Therefore the transverse momentum of the muon reconstructed by the muon finder (s. 6.4.2) is added in case of a high probability (quality) of its identification:

$$p_T^{miss} = \sqrt{\left(p_x + \sum_i p_{x,i}^{\mu}\right)^2 + \left(p_y + \sum_i p_{y,i}^{\mu}\right)^2}\,, \tag{6.10}$$

$$\phi^{miss} = \arctan\frac{-p_y - \sum_i p_{y,i}^{\mu}}{-p_x - \sum_i p_{x,i}^{\mu}}\,, \tag{6.11}$$

with the summation index i running over all identified muons. The transverse momentum imbalance not taking into account the innermost ring of the FCAL p_T^{ex1IR} is defined similar to p_T:

$$p_T^{ex1IR} = \sqrt{\left(\sum_{i\neq 1IR} E_i \sin\theta_i \cos\phi_i\right)^2 + \left(\sum_{i\neq 1IR} E_i \sin\theta_i \sin\phi_i\right)^2}\,. \tag{6.12}$$

The summation index i runs over all CAL cells except those of the innermost ring of the FCAL. The energies of the cells were not corrected in this case.

6.1.3 Kinematic Variables

Depending on the measured final state, the kinematic variable x, y and Q^2 (see 2.3.1) are usually reconstructed by three algorithms, which are described in the following.

[2] Thus the missing transverse momentum points into the direction of a possibly unmeasured particle.

6.1.3.1 Electron Method

The *electron method* is used in fixed target experiments and is very simple, since only information on the scattered electron is used. The kinematic variables are expressed by:

$$Q_e^2 = 2E_e E'_e (1 + \cos\theta_e) \,, \tag{6.13}$$

$$y_e = 1 - \frac{E'_e}{1E_e} (1 - \cos\theta_e) \,, \tag{6.14}$$

$$x_e = \frac{Q_e^2}{s y_e} \,, \tag{6.15}$$

where E_e is the energy of the electron beam and E'_e and θ_e are the measured energy of the scattered electron and its polar angle, respectively.

6.1.3.2 Double-Angle Method

The *double-angle method* [121] uses information on both, the hadronic final state and the electron. The kinematic variables are expressed by:

$$y_{DA} = \frac{\sin\theta_e (1 - \cos\theta_{hadr.})}{\sin\theta_{hadr.} + \sin\theta_e - \sin(\theta_e + \theta_{hadr.})} \,, \tag{6.16}$$

$$Q^2_{DA} = 4E_e^2 \frac{\sin\theta_{hadr.} (1 + \cos\theta_e)}{\sin\theta_{hadr.} + \sin\theta_e - \sin(\theta_e + \theta_{hadr.})} \,, \tag{6.17}$$

$$x_{DA} = \frac{E_e}{E_p} \frac{\sin\theta_{hadr.} + \sin\theta_e + \sin(\theta_e + \theta_{hadr.})}{\sin\theta_{hadr.} + \sin\theta_e - \sin(\theta_e + \theta_{hadr.})} \,, \tag{6.18}$$

where E_p is the energy of the proton beam and $\theta_{hadr.}$ is the measured polar angle of the hadronic final state. This method does not require a precise knowledge of the calorimeter energy scales.

6.1.3.3 Jacquet-Blondel Method

The *Jacquet-Blondel method* [122, p.391] uses only information on the hadronic final state. The kinematic variables are expressed by:

$$y_{JB} = \frac{E^{hadr} - p_z^{hadr}}{2E_e} \,, \tag{6.19}$$

$$Q^2_{JB} = \frac{\left(p_T^{hadr}\right)^2}{1 - y_{JB}} \,, \tag{6.20}$$

$$x_{JB} = \frac{Q^2_{JB}}{s y_{JB}} \,, \tag{6.21}$$

where E^{hadr}, p_z^{hadr} and p_T^{hadr} are the measured energy, the longidudinal and the transverse momentum of the hadronic final state, respectively.

This method was used in this analysis, since the scattered beam electron is not expected to be reconstructed in the detector. In order to avoid unphysical values $(x, y > 1)$ due to mismeasurements, the calculated values of x and y were regularised.

6.2 Jet Reconstruction

6.2.1 Jet Reconstruction Algorithm

Jets were reconstructed from the energy deposits in the CAL using the *k_T-algorithm* [123] in its longitudinally invariant inclusive mode [124] based on CAL cell energies. The cell energy threshold described in 6.1.1 was raised to 100 MeV for EMC and 150 MeV for HAC cells in the jet reconstruction.

The transverse jet energy E_T^{jet} and its position in the η-ϕ coordinate space were defined as

$$E_T^{jet} = \sum_i E_{T,i} = \sum_i E_i \sin\theta_i \,, \tag{6.22}$$

$$\eta^{jet} = \frac{\sum_i E_{T,i}\eta_i}{E_T^{jet}} \,, \tag{6.23}$$

$$\phi^{jet} = \frac{\sum_i E_{T,i}\phi_i}{E_T^{jet}} \,, \tag{6.24}$$

where the summation index i runs over all cells associated with the jet. E_i, $E_{T,i}$, θ_i, η_i and ϕ_i are the energy, transverse energy, polar angle, pseudorapidity and azimuthal angle of cell i, respectively.

The longitudinally invariant inclusive k_T-algorithm combines CAL cell energies to jets as follows:

1. The algorithm starts with the list of cells (called "particles" here) and an empty list of jets.

2. A distance $d_i = E_{T,i}^2 R_0^2$ is calculated for each particle i with the free parameter R_0 set to 1.

3. A distance $d_{ij} = \min(E_{T,i}^2, E_{T,j}^2) R_{ij}^2$ is calculated for each pair of particles (i, j) with $R_{ij}^2 = \Delta\eta_{ij}^2 + \Delta\phi_{ij}^2$

4. The minimum value of all d_i and d_{ij} is labeled d_{min}.

5. If d_{min} belongs to the set of d_{ij}, the particles i and j are merged into a new entry in the list of particles. The original particles are removed from the list.

6. If d_{min} belongs to the set of d_i, the particle i is removed from the list of particles and enters the list of jets.

7. If particles are left, the procedure is repeated.

8. When no particles are left (i.e. all particles are included in jets), the algorithm finishes.

6.2.2 Jet Energy Corrections

The jet energies were corrected for energy losses in inactive material. These factors were derived from a sample of CC DIS MC events by calibrating the jet energies reconstructed from CAL cells to the corresponding jet energies reconstructed from the true hadronic final state [125]. The accuracy of this calibration was better than 2%. A parametrisation of these correction factors as a function of E_T^{jet} and η^{jet} was applied to both, MC and data. The effects of this correction on jets from b-quarks [46] showed, that a systematic underestimation of the b-quark energy of about 10% is counterbalanced. The remaining uncertainty in reconstructing the b-quark energy was 2%.

Additional jet energy corrections were applied to data in correlation with the global energy corrections described in 6.1.1.

6.2.3 Special Jet Variables

Additional jet variables can be used to distinguish QCD-jets from jets originating from misidentified electrons or from hadronically decaying τ-leptons:

- Jet radius:
  The jet radius R_{90}^{jet} is the radius of the cone in the η-ϕ coordinate space centered around the jet axis, which contains 90% of the total jet energy. Due to the hadronic showers, QCD-jets have a broader energy distribution than lepton-induced jets with narrow electromagnetic showers.

- Electromagnetic energy fraction:
  The electromagnetic energy fraction $E_{EMC}^{jet}/E_{total}^{jet}$ is the fraction of the jet energy detected by EMC cells. For electron-induced jets, this fraction is expected to be large.

- Leading track energy fraction:
  The leading track energy fraction $E_{lt}^{jet}/E_{total}^{jet}$ is the fraction of the jet energy

carried by the most energetic track associated with the jet. For electron-induced jets, this fraction is expected to be close to one. Since jets from hadronically decaying τ-leptons also contain neutral particles, their leading-track fraction is expected to be significantly smaller than one.

6.3 Track and Vertex Reconstruction

6.3.1 Track and Vertex Reconstruction

Tracks were reconstructed from CTD and MVD hits [126]. The transverse momentum of a track p_T^{trk} was derived from its measured signed radius R^{trk} as

$$p_T^{trk} = qR^{trk}B^{ZEUS} \tag{6.25}$$

with the particle charge q[3] and the magnetic field B^{ZEUS} (see 3.2.1). Only tracks with a transverse momentum of $p_T^{trk} > 0.1\,\text{GeV}$ were considered in this analysis. Track charges were determined from the sign of the track radius, but were not considered in this analysis. The event vertex was reconstructed from the reconstructed tracks. Primary vertex tracks were refitted to the event vertex.

A special variable used in this analysis is the *transverse deviation of the vertex position* r_0^{vtx}. It is defined as the distance of the reconstructed event vertex from the measured average vertex in the azimuthal plane. For data this average was taken on a run-by-run basis.

6.3.2 Track Isolation

The definition of *track isolation* in this analysis was based on distances D in the Lorentz-invariant η-ϕ coordinate space. For tracks, the η-ϕ coordinate was evaluated from the momentum vector of the track at its starting point[4]. For jets, the η-ϕ coordinate was evaluated from the momentum four-vector of the jet. The isolation of a track from other tracks was defined as the distance

$$D^{trk} = \sqrt{\left(\Delta\eta_i^{trk}\right)^2 + \left(\Delta\phi_i^{trk}\right)^2} \tag{6.26}$$

of the respective track from the closest neighbouring track i, which was required to be a primary vertex track with $p_T^{trk} > 0.2\,\text{GeV}$. The isolation of a track from jets was defined as the distance

$$D^{jet} = \sqrt{\left(\Delta\eta_i^{jet}\right)^2 + \left(\Delta\phi_i^{jet}\right)^2} \tag{6.27}$$

[3] Usually particles are assumed to have $|q| = e$.

[4] event vertex for primary vertex tracks

of the respective track from the closest neighbouring jet i with a transverse energy of at least $E_T^{jet} > 5\,\text{GeV}$ within a pseudorapidity range of $-1 < \eta^{jet} < 2.5$. If the track was associated with a jet, this jet was skipped, if it contains this track only. A track is associated with a particular jet, if the distance D_i^{jet}, measured between the jet axis and the extrapolation of the track to the CAL surface is less than one. Jets with an electromagnetic fraction of more than 90% and jets with a 90%-radius of less than 0.1 were not considered.

In cases, where no proper neighbouring track and/or jet for calculating a distance was found in the event, the respective isolation was set to a value larger than the geometrical limit.

6.4 Lepton Identification

Leptons in high-energy physics events originate from various sources. So, the used lepton identification algorithms are expected to find leptons from different origins. In general, an identified lepton contributes to the signature of interest, if it matches an isolated track[5]. Further requirements, which are typical for particular leptons and the lepton identification algorithms themselves are described in the following.

6.4.1 Electron Identification

The electron identification in this analysis is based on the electron finder EM [127], which was developed especially for the identification of scattered beam electrons in NC DIS events with high Q^2. It uses seven variables derived from calorimeter and tracking information to calculate the likelihoods for the object to be an electron. The algorithm is tuned to the corresponding distributions from electrons clearly identified by other algorithms. The energy of an electron candidate was calculated from the CAL information, which was corrected for energy loss in inactive material according to test-beam measurements (s. 6.1.2).

Electrons were also required to exceed a value for the product of the likelihoods of 10^{-3} and to have a corrected energy of more than 8 GeV. Furthermore, the energy contained in a cone of radius 0.8 in the η-ϕ-plane may not contain more than 20% not associated to the electron candidate. An electron found in an event is classified as the scattered beam electron, if its acoplanarity is less than 0.14. If more than one electron is found, this criterion is applied to the electron with the highest p_T or – if necessary – to the electron with the 2^{nd}-highest p_T.

As a cross check, the neural-network based electron finder *Sinistra* [128] was compared with EM. Requiring an electron probabilty of 0.9, no deviations were found in the data sample described in 7.2.

[5]The lepton matches an isolated track = The lepton *is* isolated.

6.4.2 Muon Identification

The muon identification in ZEUS uses a number of different muon finding algorithms, which typically match the information from two or more subdetectors[6]. The outcome of these algorithms is combined by the muon finder package GMUON [129]. Besides the kinematical properties of each muon candidate it provides a quality classification flag, which allows for a separation of fake muons from real muons. This classification is defined on the basis of certain quality criteria from each muon finder and their correlations. For example, a muon candidate with a very high probability from the muon finder BREMAT to match a primary vertex track is classified with the highest quality 6 (excellent), whereas a muon candidate with an entry of fair quality from the muon finder MV only is classified with the quality 1 (low). The values of this quality flag range from -2 (bad) to 6 (excellent)[7].

In this analysis, muons with a quality flag of 3 (fair) or more are considered in the calculation of p_T^{miss}. Also muons with a quality flag of 1 (low) or more are considered, if they match an isolated track (see 7.3). The requirement of an isolated track match indicates that the background for the muon reconstruction is very low, so that this reduced quality criterion is applicable [130].

6.4.3 τ-Lepton Identification

Compared to other leptons, τ-leptons decay quickly ($c\tau = 87.11\,\mu m$), and in the present study only their decay products can be identified. The BR of the leptonic decays ($\tau \to \mu\bar{\nu}_\mu\nu_\tau, e\bar{\nu}_e\nu_\tau$) amounts to 35%. Since a missing transverse momentum is already expected from the production of the τ-lepton in a W-boson decay, the missing transverse momentum from the additional neutrinos does not induce a clear signature. Those events cannot be distinguished from "direct" e- or μ-production. In almost 50% of all cases the τ-lepton decays hadronically with only one charged particle visible (*one-prong decay*), which leads to an isolated track ending up in a collimated ("pencil-like") hadronic jet. This is illustrated in Fig. 6.1, where both jet types are shown in one event. These jets can be distinguished from QCD jets on the basis of the jet shape variables introduced in 6.2.3.

In this analysis a simple approach similar to that used in the H1 analysis [131] is chosen to identify τ-leptons, which is described in 7.3. A more sophisticated method based on a discriminator technique [46, 132] might be used in the future after being customised for HERA II data.

[6] A list of the algorithms and the respective subdetectors is found in App. C

[7] A list of the GMUON quality flags including some examples is found in Tab. C.1

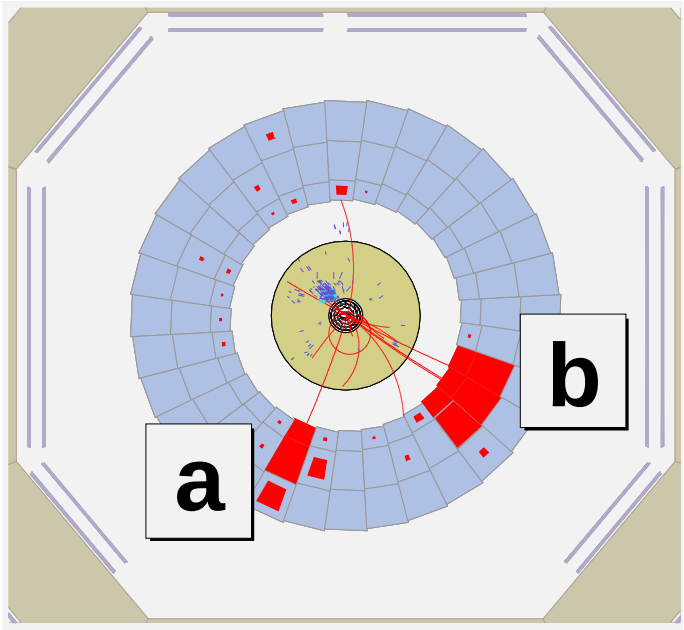

Figure 6.1: τ-Lepton (one-prong decay) and QCD-induced jets
(a) A "pencil-like" τ-lepton induced and (b) a broad QCD-induced jet in the ZEUS detector are shown. The light blue rings depict the CAL. The red segments represent energy depositions. The thin red lines are reconstructed tracks. The picture was extracted from a MC event with a singly produced t-quark.

6.5 Additional Variables

- Acoplanarity:
  The *acoplanarity* ϕ^{obj}_{acopl} of an object is defined as its azimuthal separation from the hadronic system:

$$\phi^{obj}_{acopl} = \pi - \left|\phi^{obj} - \phi^{hadr}\right| , \tag{6.28}$$

  with the azimuthal angles ϕ^{obj} and ϕ^{hadr} of the object and the hadronic system, respectively. The acoplanarity of the event is defined as the acoplanarity of the isolated electron with the highest transverse momentum. For NC DIS events, the acoplanarity is expected to be close to zero, since the scattered beam electron balances the hadronic system, which means that $|\phi^{obj} - \phi^{hadr}|$ is close to π.

- Transverse mass:

The *transverse mass* M_T^{ij} of two objects i and j is defined as:

$$M_T^{ij} = \sqrt{2p_T^i p_T^j \left(1 - \cos\phi^{ij}\right)}\,, \tag{6.29}$$

with the transverse momenta p_T^i and p_T^j of those objects and their azimuthal opening angle ϕ^{ij}. If these two objects are the decay products of a "mother" object, the transverse mass distribution is expected to peak at the mass of the mother object. E.g. if one considers a leptonic decay of a W-boson with an identified lepton and identifies the missing transverse momentum in the event with the undetected neutrino, the transverse mass calculated from the lepton and the missing transverse momentum should peak at the W-boson mass.

- Longitudinal neutrino momentum:
  If one considers a leptonic decay of a W-boson with an identified lepton and identifies the missing transverse momentum in the event with the undetected neutrino, the longitudinal neutrino momentum p_z^ν can be reconstructed from the constraint that the invariant mass of the lepton-neutrino system $M_{l\nu}$ corresponds to the mass of the W-boson M_W:

$$M_{l\nu} = \sqrt{(E_l + E_\nu)^2 - (\vec{p}_l + \vec{p}_\nu)^2} = M_W\,, \tag{6.30}$$

  with E_l, $\vec{p}_l$ and E_ν, $\vec{p}_\nu$ the energy and the momentum vector of the lepton and the neutrino, respectively. This equation is solvable for $p_{z,\nu}$, if one assumes that neutrinos are massless ($E_\nu^2 = \vec{p}_\nu^2$). It yields two solutions which have to be evaluated for their physical meaning. In this analysis, the momentum four-vector reconstructed by the corresponding lepton finder (s. 6.4) was used for this calculation rather than track quantities, since the errors in the track reconstruction become large for high-p_T tracks. In case of a τ-candidate (s. 7.3), the quantities were taken from the corresponding jet.

Chapter 7

Search for Isolated Leptons

The event selection was split into five steps:

1. sample selection,
2. control selection,
3. pre-selection of isolated lepton events
   (From this selection step on, electron, muon and τ-lepton candidates were treated separately.),
4. final selection of W-boson candidates and
5. final selection of single t-quark candidates.

The selection cuts described in this chapter are applied to both, data and MC events, unless noted otherwise.

All references to the MC sample of singly produced t-quarks refer to the HEXF-sample generated with a t-quark mass of 175 GeV (s. 5.2.2.2).

7.1 Sample Selection

This first selection step reproduced roughly the first selection step performed in the HERA I analysis [39,46]. It was performed in order to investigate the effectiveness of the HERA I techniques to reject non-ep background in HERA II data. No distinction regarding the lepton candidates was made.

The following cuts were applied:

- **DST trigger bit selection:**
  The best trigger-based representation of the signature of interest was given by the trigger bit $DST34$, which is designed to give a preselection of CC

events in ZEUS. It mainly requires large total transverse momentum and large transverse momentum excluding the innermost FCAL ring, in particular:

$$p_T > 7\,\text{GeV} \text{ and } p_T^{ex1ir} > 6\,\text{GeV}. \tag{7.1}$$

Even though both cuts were tightened further in this first selection step, the DST selection saves computation time. The trigger efficiencies[1] were found to be 77% for single W-boson production with subsequent leptonic decay and 98% for single t-quark production with a subsequent leptonic decay of the W-boson. A detailed description of the $DST34$ trigger logic is found in App. D.

- **Total transverse momentum:**
  Since the signature of interest contains at least one neutrino in the final state leading to significant missing transverse momentum in the detector, a cut on the measured total transverse momentum was applied:

  $$p_T > 15\,\text{GeV}. \tag{7.2}$$

  The transverse momentum distributions after the sample selection are shown in Fig. 7.1(a).

- **Non-ep background rejection:**

  - Event vertex:
    In order to reduce backgrounds from non-ep interactions, the event vertex was required to be close to the nominal interaction point along the beam axis:

    $$\left|z^{vtx}\right| < 50\,\text{cm}. \tag{7.3}$$

    The longitudinal vertex position distributions after the sample selection are shown in Fig. 7.1(b). In the azimuthal plane the event vertex was required to be reconstructed inside the beam pipe.

  - CAL holes:
    As described in 3.2.4, CAL cells are read out with two independent PMTs. If both PMTs of a cell are "dead", the energy deposition in this cell is lost, which can lead to significant missing transverse momentum. In order to avoid this uncertainty, events with a high-p_T track ($p_T^{trk} > 3\,\text{GeV}$) pointing into the direction of a dead cell are rejected. In particular, the angle

[1] A definition of efficiency is given in 8.2.

between the extrapolated impact point of track i on the CAL surface and the centre of the dead cell j, Ω^{ij}, was required to fulfill

$$\Omega^{ij} < 0.1\,. \tag{7.4}$$

This cut was applied only to data. It rejected 16 events corresponding to 4‰ of all data events, which pass all other cuts in the sample selection.

– CAL timing:
The CAL provides an accurate cell-by-cell timing measurement. Generally the cells are calibrated such, that energy depositions from relativistic particles originating from *ep*-interactions at the interaction point should have a time close to 0 ns. This information can be used to reject non-*ep* background signatures, since they create timing structures, which are inconsistent with those of physics events.

  * Beam-gas interactions and halo muons:
  Particles from beam-gas interactions and halo muons hit the RCAL from the back leading to early times relative to FCAL.

  * Atmospheric muons
  Atmospheric muons impinge on the detector from above leading to a time difference between the upper and the lower CAL parts.

A complete list of the timing cuts is given in Tab. 7.1. No requirement on a minimum number of cells taken into account in the particular CAL parts was applied. The timing cuts were applied only to data.

– Unnaturally localised energy depositions in the CAL [139]:

  * Dead PMTs and sparks:
  Sparks are sudden discharges of CAL PMTs, which can lead to significant mismeasurements. Sparks are identified by a large imbalance between the energies measured by the two PMTs of the cell. The specific cut chosen is $|E^L - E^R|/(E^L + E^R) > 0.8$, where E^L and E^R indicate the energy measured by the "left" and by the "right" PMT, respectively. Uncertainties in the energy measurement can arise from cells with one dead PMT. In this case the energy deposition in the cell is estimated by doubling the energy detected by the working PMT. By definition, the energy imbalance amounts to zero in this case. To reduce these uncertainties, the transverse momentum is calculated excluding those cells ($p_T^{goodbal}$) and compared to the total (uncorrected) transverse momentum. In particular, the following

condition is imposed:

$$0.5 < \frac{p_T^{goodbal}}{p_T^{CAL}} < 2\,. \tag{7.5}$$

* Halo and atmospheric muons:
  Halo and atmospheric muons were rejected by requiring

$$\frac{E^{BHAC}}{E^{BCAL}} < 0.9\,, \tag{7.6}$$

  if the total energy in the BCAL is more than 5 GeV. The same cut was applied to the RCAL energies.
* Energy fraction of highest-E_T cell:
  The fraction of E_T in the highest-E_T cell of the total E_T is a good discriminator against sparks. The following specific cuts were used:
  · highest-E_T cell in HAC:

$$\frac{E_T^i}{E_T} < 0.7\,,\ \frac{p_T^{-i}}{p_T} > 0.3 \text{ and } \frac{E_T^i}{E_T^j} < 0.9\,, \tag{7.7}$$

  · highest-E_T cell in EMC:

$$\frac{E_T^i}{E_T} < 0.8\,,\ \frac{p_T^{-i}}{p_T} > 0.2 \text{ and } \frac{E_T^i}{E_T^j} < 0.95\,. \tag{7.8}$$

  Here i and j denote the highest-E_T cell and the *island*[2] containing i, respectively. The label $-i$ indicates, that this quantity was calculated excluding i. In case of the EMC, the last cut was only applied, if one PMT in i was dead.

– Transverse momentum measured outside the first inner ring of FCAL:
  Proton beam-gas events within the main detector lead to high energy deposits in the inner rings of the FCAL. Therefore it is required:

$$p_T^{ex1ir} > 9\,\text{GeV}. \tag{7.9}$$

– Track quality:
  A "good" track is defined as a vertex-fitted track with $p_T^{trk} > 0.2\,\text{GeV}$. Proton beam-gas events usually contain a large number of low-energy tracks, which are not fitted to the primary vertex [134]. This event signature was rejected by requiring

$$n_{trk}^{good} > 0.2 \cdot (n_{trk} - 20)\ . \tag{7.10}$$

[2] An island is a CAL clustering object. It is formed by energy deposits in adjacent cells of one particular CAL layer [133].

– Atmospheric muons:
Muons from interactions of high-energy cosmic rays in the atmosphere are characterised by a straight track through the detector. If this track runs close to the interaction point, it might be reconstructed as two tracks coming from the event vertex. If an event contained exactly two tracks with a transverse momentum of more than 0.2 GeV, both vertex-fitted and with an opening angle of more than 178°, the event was rejected. A muon identification was not required.

– Cosmic showers:
Cosmic showers originate from high-energy protons hitting the upper atmosphere. In the detector, they are characterised by many muons and a large energy deposition in the BAC. They were rejected by

$$E^{BAC} < 100\,\text{GeV} \text{ and } n_{\mu}^{BAC} < 15\,, \tag{7.11}$$

where E^{BAC} is the energy measured and n_{μ}^{BAC} the number of muons detected in the BAC.

CAL part	Minimum energy (GeV)	Timing cut
CAL	2.0	$\lvert t^{CAL} \rvert < 6\,\text{ns}$
	4.0	$\lvert t^{CAL} \rvert < 5\,\text{ns}$
FCAL, BCAL or RCAL	0.6	$\lvert t^{FCAL,BCAL,RCAL} \rvert < 6\,\text{ns}$
	4.0	$\lvert t^{FCAL,BCAL,RCAL} \rvert < 5\,\text{ns}$
upper or lower CAL half	4.0	$\lvert t^{uCAL,lCAL} \rvert < 6\,\text{ns}$
upper or lower FCAL half	4.0	$\lvert t^{uFCAL,lFCAL} \rvert < 6\,\text{ns}$
FCAL and RCAL	1.0	$\lvert t^{FCAL} - t^{RCAL} \rvert < 6\,\text{ns}$
upper and lower CAL half	1.0	$\lvert t^{uCAL} - t^{lCAL} \rvert < 6\,\text{ns}$
upper and lower FCAL half	1.0	$\lvert t^{uFCAL} - t^{lFCAL} \rvert < 6\,\text{ns}$
upper and lower RCAL half	1.0	$\lvert t^{uRCAL} - t^{lRCAL} \rvert < 6\,\text{ns}$

Table 7.1: Timing cuts
The minimum energy gives the lower limit on the detected energy for applying the cut. It is valid for the corresponding CAL parts independently. The timing cut refers to the average timing in the corresponding CAL parts.

Fig. 7.1 shows the distributions of the transverse momentum p_T and the longitudinal vertex position z^{vtx} after the sample selection. The SM simulation contains the event samples described in 5.2.2.1 and 5.2.3. These samples were weighted according to the integrated data luminosity as well as the simulation of single t-quark

(a) (b)

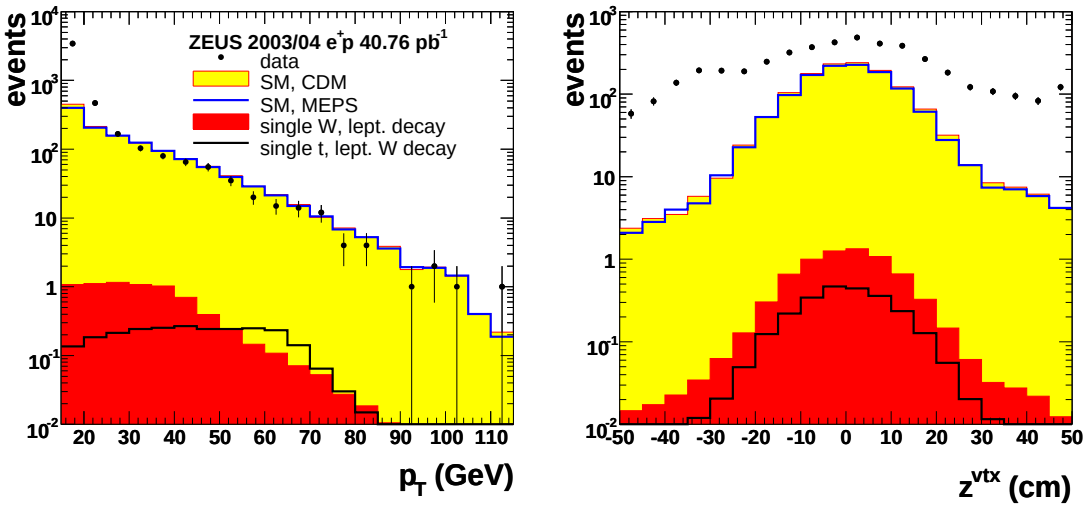

Figure 7.1: Transverse momentum and longitudinal event vertex position after sample selection
(a) Transverse momentum p_T and (b) longitudinal vertex position z^{vtx} for data (dots) and the SM MC with DIS events generated with CDM (yellow area) or MEPS (blue line). Also single W-boson production with subsequent leptonic decay (red area) and single t-quark production with subsequent leptonic decay of the W-boson (black line) are shown. Only events which passed the sample selection are shown.

production, assuming the cross section given in Eq. 2.26. CC and NC DIS events were simulated using both, the CDM and MEPS model (s. 5.2.3.1). Results for both models are shown in the figures. 4475 data events were observed, whereas the SM expectation was 1312.7±10.7 for CDM and 1245.5±9.8 for MEPS, respectively[3]. The efficiencies of the sample selection were 47% for single W-boson production with subsequent leptonic decay (7.28±0.05 events expected) and 89% for single t-quark production with a subsequent leptonic decay of the W-boson. Fig. 7.1(a) shows a significant excess of data for small transverse momenta. For $p_T > 25\,\text{GeV}$, data and SM MC agree well. Fig. 7.1(b) shows the longitudinal vertex distribution. Its simulation was based on measurements [135]. Typically a peak at the nominal interaction point with $z^{vtx} = 0\,\text{cm}$ with an exponential fall towards the edges of the interaction region is expected. The data shows a completely different shape than expected. Besides the greater absolute number of data events compared

[3]Here and in the following, the given uncertainties on the number of selected MC events are statistical uncertainties as defined in Eq. 8.2.

to the SM prediction, a broader peak and a slighter fall towards the edges of the z^{vtx}-distribution were observed in data. This behaviour is characteristic in case of a significant contamination by non-*ep* backgrounds.

Studies on the background conditions in HERA II [136, 137] indicated, that after the HERA upgrade an increased number of particle background events from proton and electron beam-gas interactions can be expected. Indeed, a random eye-scan[4] of the data after the sample selection showed, that it is contaminated by many of those non-*ep* background events. A typical proton beam-gas event is shown in Fig. E.1. Figs. 7.2(a) and (b) illustrate that these events were located at small values of p_T^{hadr}/E_T^{hadr} and large values of the transverse vertex deviation. In addition the SM prediction of r_0^{vtx} is slightly shifted to smaller values with respect to data, which is due to the idealisation of the simulation. The two-dimensional distributions of these variables are shown for data and MC in Figs. 7.2(c) and (d). In the region of small p_T^{hadr}/E_T^{hadr} and large r_0^{vtx} the data shows an significant number of entries, whereas no contribution is seen in the simulation. The number of these entries was similar to the observed total excess in data compared to MC. Therefore, these events were identified with beam-induced particle background and were removed from the data sample as described in the following.

7.2 Control Selection

This selection step was introduced in order to reject the additional non-*ep* background which arises from the harsh background conditions after the HERA upgrade. No distinction regarding the lepton candidates was made.

The following cuts were applied:

- **Transverse momentum:**
  The transverse momentum cut was raised to:

$$p_T > 20\,\text{GeV}. \tag{7.12}$$

  The transverse momentum distributions after the control selection are shown in Fig. 7.3(a).

- **Further non-*ep* background rejection:**
  Based on the distributions shown in Fig. 7.2(c) and (d), events were rejected, if

$$\frac{p_T^{had}}{E_T^{had}} < 0.65 \text{ and } r_0^{vtx} \geq 0.07\,\text{cm}, \tag{7.13}$$

  where r_0^{vtx} is the transverse vertex deviation as defined in 6.3.1.

[4] The eye-scan was performed with the ZEUS *Event Visualisation* program (ZeViS) [138].

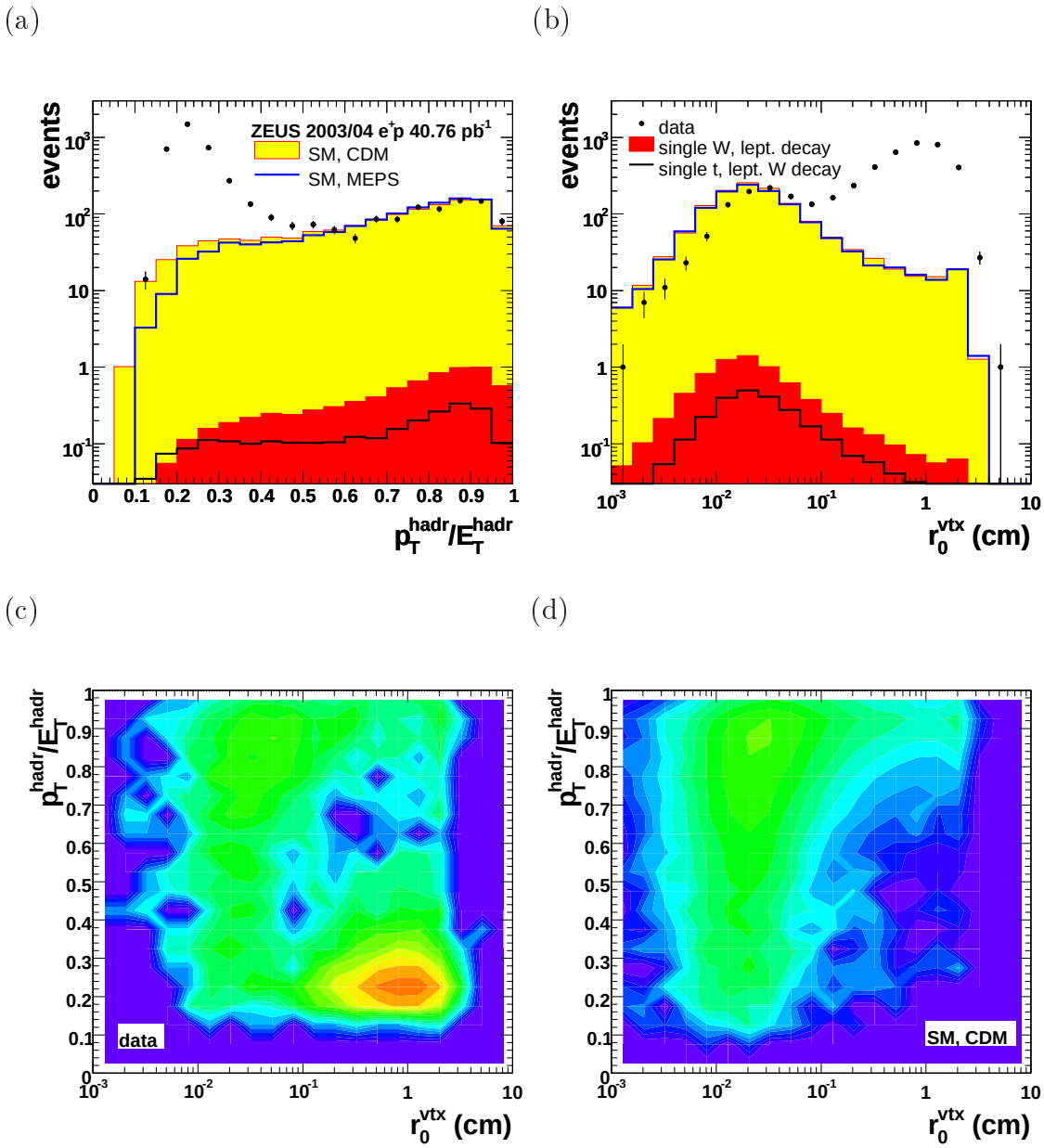

Figure 7.2: p_T^{hadr}/E_T^{hadr} and transverse vertex deviation after sample selection

(a) p_T^{hadr}/E_T^{hadr} and (b) transverse vertex deviation r_0^{vtx} for data (dots) and the SM MC with DIS events generated with CDM (yellow area) or MEPS (blue line). Also single W-boson production with subsequent leptonic decay (red area) and single t-quark production with subsequent leptonic decay of the W-boson (black line) are shown. p_T^{hadr}/E_T^{hadr} vs. transverse vertex deviation r_0^{vtx} for (c) data and (d) SM MC with DIS events generated with CDM. The colour scale ranges from blue (no events) to red with increasing number of events. Only events which passed the sample selection are shown.

After these cuts, 727 events were observed in data, whereas the SM expectation was 843.8±4.7 for CDM and 835.9±4.5 for MEPS, respectively. The background is dominated by CC DIS events (787.3±2.3 for CDM and 787.1±2.3 for MEPS, respectively). The efficiencies of the sample selection were 38% for single W-boson production with subsequent leptonic decay (5.90±0.05 events expected) and 78% for single t-quark production with a subsequent leptonic decay of the W-boson. Fig. 7.3 shows the distributions of the transverse momentum p_T and the longitudinal vertex position z^{vtx} after the control selection. Both variables show a much better

(a) (b)

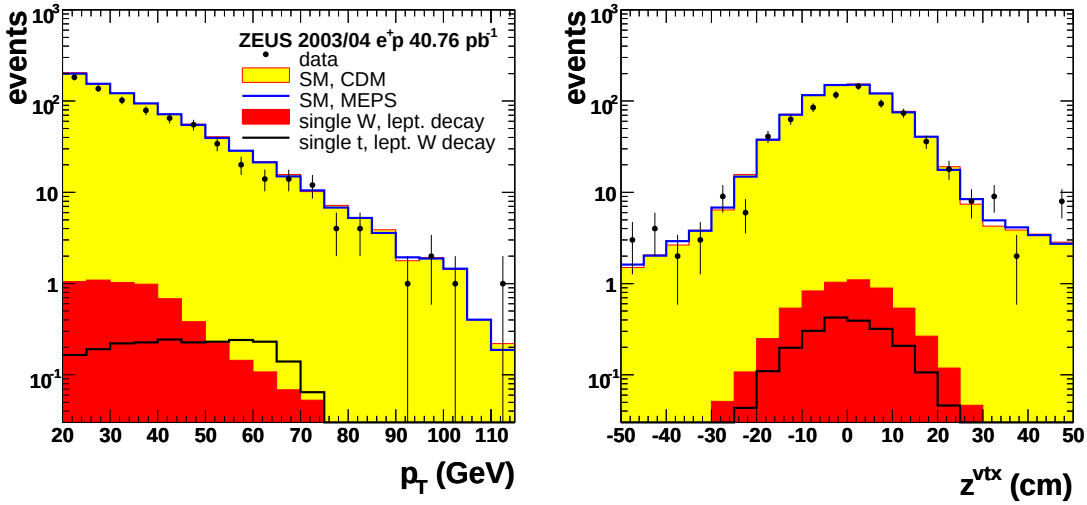

Figure 7.3: Transverse momentum and longitudinal event vertex position after control selection
(a) Transverse momentum p_T and (b) longitudinal vertex position z^{vtx} for data (dots) and the SM MC with DIS events generated with CDM (yellow area) or MEPS (blue line). Also single W-boson production with subsequent leptonic decay (red area) and single t-quark production with subsequent leptonic decay of the W-boson (black line) are shown. Only events which passed the control selection are shown.

description of the data by the MC simulation. The transverse momentum distributions (Fig. 7.3(a)) show an exponential fall with increasing values for both, data and MC. The agreement is fair, data undershoots the MC simulation slightly. The distributions of the longitudinal vertex position (Fig. 7.3(b)) show a peak at the nominal interaction point ($z^{vtx} = 0\,\text{cm}$) and a exponential fall towards the edges of the interaction region.

Fig. 7.4 shows the distribution of kinematic variables, namely the Bjorken scal-

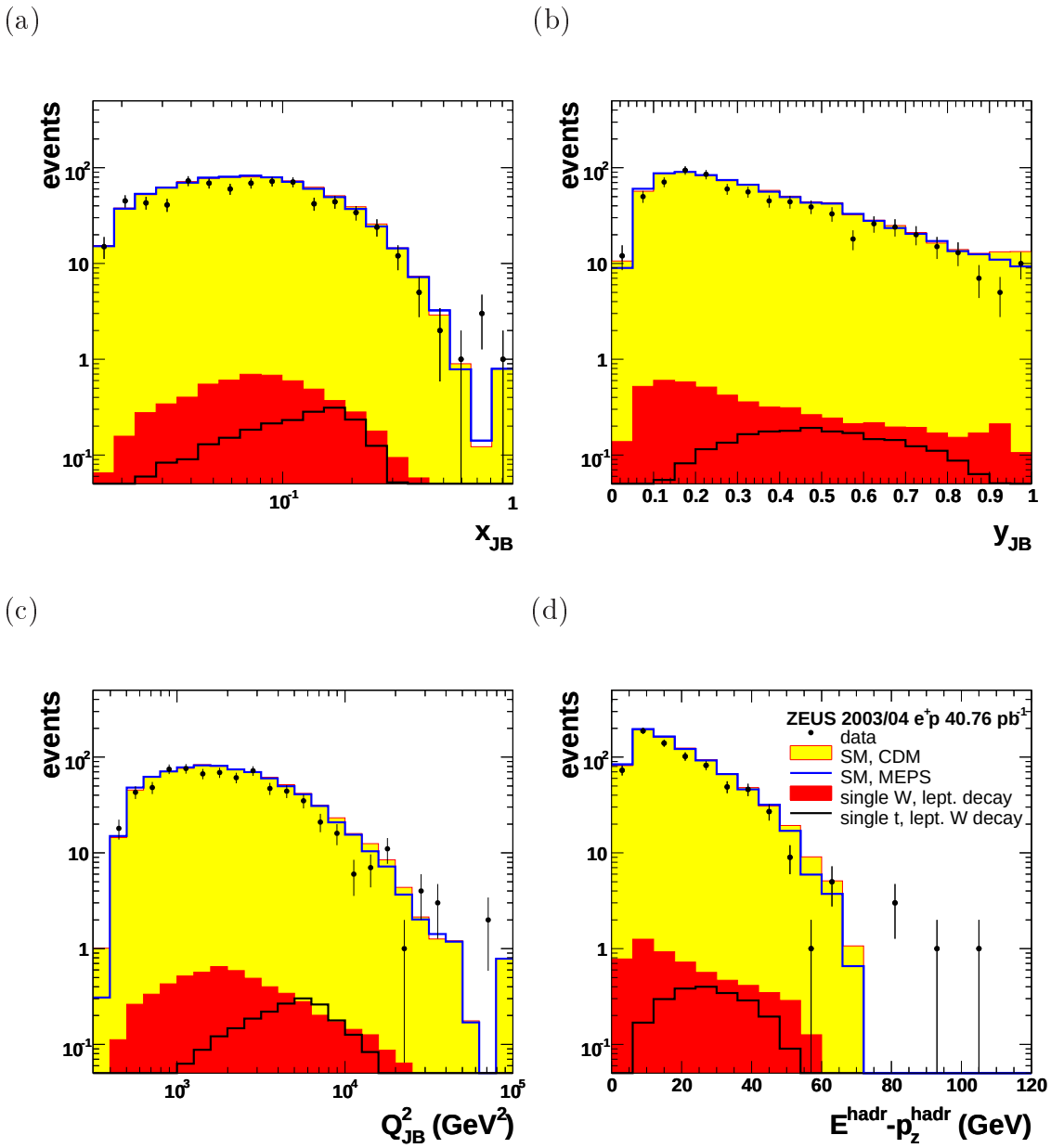

Figure 7.4: Kinematic variables after control selection
(a) Bjorken scaling variable x_{JB}, (b) virtuality y_{JB}, (c) momentum transfer Q^2_{JB} and (d) $E^{hadr} - p_z^{hadr}$ for data (dots) and the SM MC with DIS events generated with CDM (yellow area) or MEPS (blue line). Also single W-boson production with subsequent leptonic decay (red area) and single t-quark production with subsequent leptonic decay of the W-boson (black line) are shown. The index JB indicates that x, y and Q^2 were calculated with the Jacquet-Blondel method. Only events which passed the control selection are shown.

ing variable x_{JB}, the virtuality y_{JB}, the momentum transfer Q^2_{JB} and $E^{hadr} - p_z^{hadr}$, after the control selection. The distribution of $E^{hadr} - p_z^{hadr}$ (Fig. 7.4(d)) shows an exponential fall towards the kinematic limit of 55 GeV. Beyond this value, fluctuations towards large values of the energy measurement in the CAL lead to unphysical values, which are not well reproduced by the simulation. The effect of this mismeasurement is also observed at large values of x_{JB} (Fig. 7.4(a)) and Q^2_{JB} (Fig. 7.4(c)). Outside this extreme region of the phase space, the shape of the data distibutions is described well by the SM prediction.

7.3 Pre-Selection of Isolated Lepton Events

Fig. 7.5 shows the distributions of the track isolation variables D^{trk} and D^{jet} (s. Eqs. 6.26 and 6.27) after the control selection. Both distributions show large peaks

(a) (b)

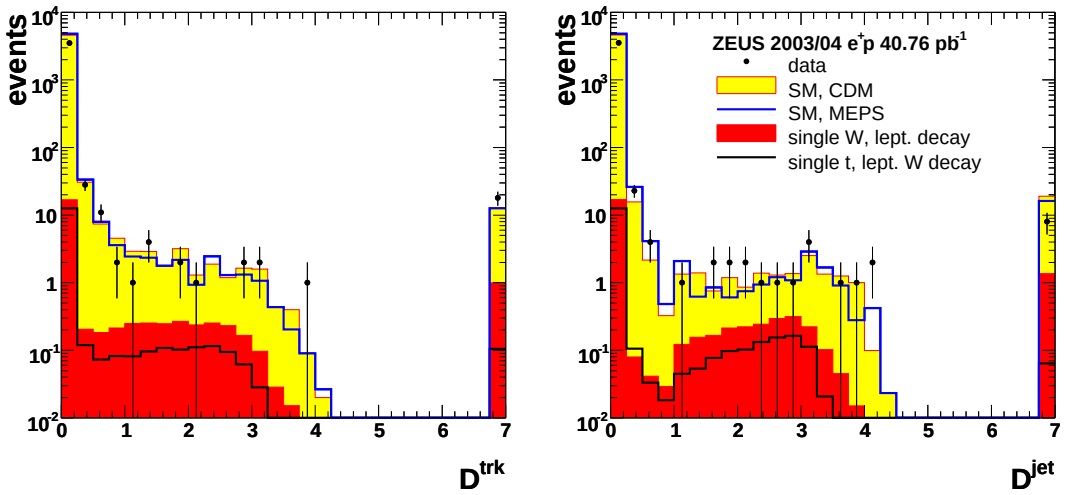

Figure 7.5: Track isolation after control selection
(a) Track isolation from other tracks D^{trk} and (b) track isolation from jets D^{jet} for data (dots) and the SM MC with DIS events generated with CDM (yellow area) or MEPS (blue line). Also single W-boson production with subsequent leptonic decay (red area) and single t-quark production with subsequent leptonic decay of the W-boson (black line) are shown. Only vertex fitted tracks with $p_T^{trk} > 0.2$ GeV in events which passed the control selection are shown.

at $D = 0$ from non-isolated tracks with a steep exponential fall. Accumulations are observed in the region of $\sim 1 \leq D \leq \sim 5$, called isolation region, from tracks which

are isolated from other tracks or jets, respectively. For D^{trk} this accumulation is smeared into the peak from non-isolated tracks. The bin with $D \approx 7$ contains tracks with no neighbouring track or jet according to the restrictions in 6.3.2, where the isolation was set to a large value. For both isolation variables data agrees well with the simulation. The fraction of tracks from single W-boson and t-quark production with subsequent leptonic W-decay is above the average in the isolation region. Cuts on the isolation variables enrich the data sample with events containing isolated leptons. Fig. 7.6 shows the two-dimensional distributions of the track isolation variables of the highest-p_T^{trk} track for MC simulations after the control selection. Both, the W-boson and the t-quark sample (Fig. 7.6(c) and (d), respectively) show a cluster of highest-p_T^{trk} tracks in the intersection of both isolation regions, which is clearly separated from the rest of the events. Also the SM predictions excluding single W-boson production with subsequent leptonic decay (Fig. 7.6(a) and (b)) have events in this region, but the distribution are smeared over the whole range of the isolation variables. The events in the isolation region from the SM predictions are dominated by NC DIS and di-lepton events. In addition, all samples show contributions from events, where no neighbouring track and or jet to the highest-p_T track was found. Cuts on the isolation variables of the highest-p_T^{trk} track enrich the fraction of events with leptonic W-decays in data. In order to select events with isolated leptons, the following cuts were applied as indicated by the red lines in Fig. 7.6:

- **Isolated high-p_T tracks:**
  Only tracks with $p_T^{trk} > 5\,\text{GeV}$ and $\theta^{trk} < 2.35$ were taken into account. Additionally the tracks were required to be fitted to the primary event vertex. Tracks matching a scattered beam electron (s. 6.4.1) or a muon with a bad reconstruction quality (lower than 3, s. 6.4.2) were excluded. Finally the highest-p_T track with
  $$D^{trk} > 0.5 \text{ and } D^{jet} > 1 \tag{7.14}$$
  was chosen as candidate for an isolated high-p_T lepton.

- **Matching of isolated tracks and identified leptons:**
  If the isolated high-p_T lepton candidate track was identified to matched an electron or a muon from the corresponding lepton finder, it was flagged as an electron or muon candidate, respectively. If not, the track was assumed to come from a hadron and was treated as a τ-lepton candidate.

Electron, muon and τ-lepton candidates were treated separately from here on. An isolated track was called an electron or muon candidate, if the track matched a finding of the corresponding lepton finder as described in 6.4.1 and 6.4.2, respectively. Isolated tracks without a lepton match were assumed to originate form hadrons and were passed to the actual τ-lepton identification.

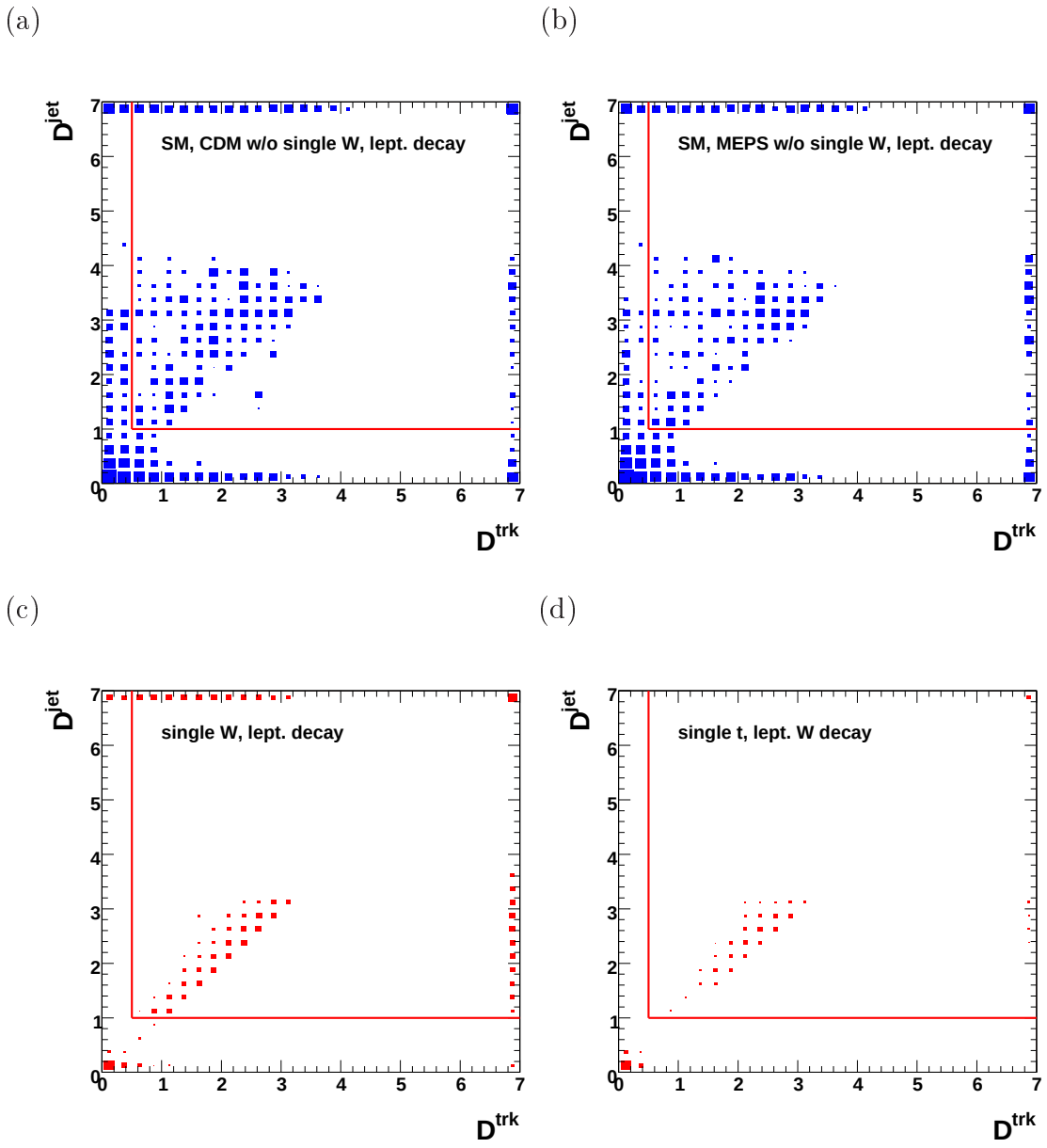

Figure 7.6: Two-dimensional track isolation of highest-p_T^{trk} track in MC after control selection

Track isolation variables D^{jet} vs. D^{trk} for (a) SM MC with DIS events generated with CDM, (b) MC with DIS events generated with MEPS, both excluding single W-boson production with subsequent leptonic decay, (c) single W-boson production with subsequent leptonic decay and (d) single t-quark production with subsequent leptonic decay of the W-boson. Only the highest-p_T^{trk} tracks in events which passed the control selection are shown. Tracks matching a scattered beam electron (s. 6.4.1) or a muon with a bad reconstruction quality (lower than 3, s. 6.4.2) were excluded. The box sizes are proportional to the logarithm of the number of events with identical scales in all figures. The red lines illustrate the applied cuts.

In the electron channel, 5 events were observed in data, whereas the SM expectation was 13.9±1.7 for CDM and 11.5±1.6 for MEPS, respectively. The background is dominated by NC DIS events (10.7±1.7 for CDM and 8.2±1.6 for MEPS, respectively). The efficiencies of the pre-selection in the e-channel were 31% for single W-boson production with subsequent decay to $e\nu_e$ (1.59±0.03 events expected) and 34% for single t-quark production with a subsequent decay of the W-boson to $e\nu_e$. Fig. 7.7 shows kinematic variables of events with an isolated electron candidate. The simulation of the transverse momentum distribution (Fig. 7.7(a)) shows a peak

(a) (b)

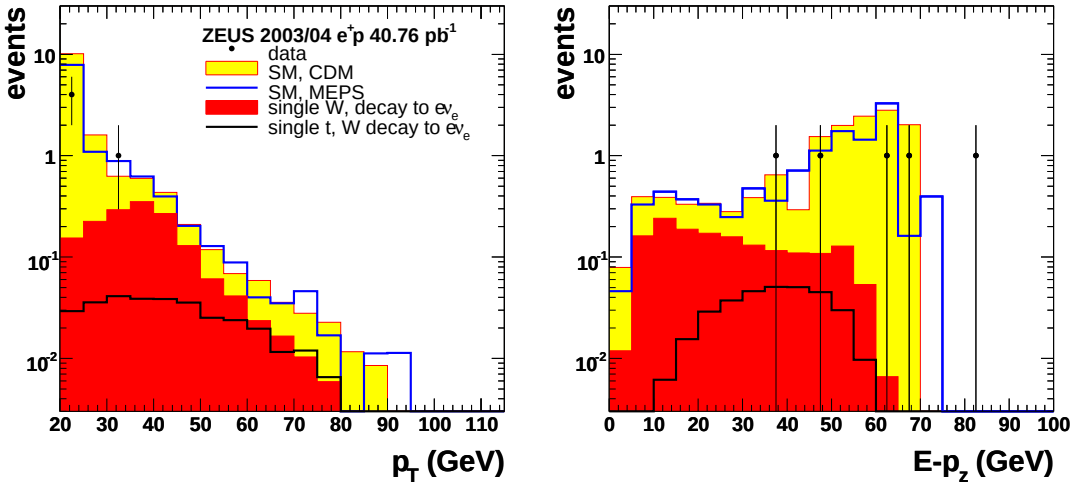

Figure 7.7: Kinematic variables of isolated electron candidate events after pre-selection
(a) Transverse momentum p_T and (b) $E-p_z$ for data (dots) and the SM MC with DIS events generated with CDM (yellow area) or MEPS (blue line). Also single W-boson production with subsequent decay to $e\nu_e$ (red area) and single t-quark production with subsequent decay of the W-boson to $e\nu_e$ (black line) are shown. Only events which passed the pre-selection as isolated electron candidate events are shown.

at small values and a steep exponential fall towards higher values. This is expected from NC DIS events, since the transverse momentum originates from mismeasurements. This behaviour is reproduced by data, though the data undershoots the simulation slightly. Events from SM single W-boson production with subsequent decay to $e\nu_e$ or from the BSM single t-quark production with subsequent decay of the W-boson to $e\nu_e$ tend to have higher transverse momentum from the undetected high-energy neutrino. Also the distributions of $E - p_z$ show the typical behaviour of a sample which is dominated by NC DIS events with a spike at the double lepton

beam energy (55 GeV). The description of the data by the SM prediction is reasonable for this quantity, if the limited statistics are taken into account. Still one event with extremely high $E - p_z$ is observed, where the simulation has no contributions. For W-boson and t-quark production, the expected values are generally below the double lepton beam energy. Fig. 7.8 shows properties of the isolated electron candidates. The acoplanarity angle (Fig. 7.8(a)) was calculated from the track momentum vector. Electrons with a small acoplanarity angle calculated from the momentum vector reconstructed by the electron finder had been removed earlier (s. above and 6.4.1). A peak at small values is observed in the SM prediction as expected from the back-to-back topology of NC DIS events (s. 6.5). Also the distribution for single t-quark production tends to small values, since these events also have a back-to-back topology (s. 2.4.2). However, the distribution is much broader due to the undetected neutrino. For single W-boson production the distribution is mostly flat, since the correlation between the W-boson and the hadronic transverse momenta is weak in most of the production mechanisms (s. 2.4.1). A small enhancement at large values arises from final state W-radiation of the scattered quark (s. Fig 2.9(b)). In this case, the decay products of the W-boson are expected in the same hemisphere as the jet. The distribution of the transverse momentum of the isolated electron p_T^e (Fig. 7.8(b)) for single W-boson production has a clear peak at about half of the W-boson mass due to the energy splitting between the electron and the neutrino. For single t-quark production the distribution is flat. The hadronic transverse momentum with respect to the isolated electron (Fig. 7.8(c)) has a spike at high values in single t-quark production as expected (s. 2.4.2), whereas all other distributions peak at small values with an exponential fall towards large values. For single W-boson production, the transverse mass of the assumed $e\nu_e$-system $M_T^{e\nu}$ (Fig. 7.8(d)) accumulates at the mass of the W-boson as expected. Also in single t-quark production a similar behaviour is observed. The distributions of the SM simulation has its maximum at a slightly smaller value, but a clear distinction is not possible. One data event is reconstructed with $M_T^{e\nu}$ very close to M_W, the others behave as predicted by MC. In general these distributions show reasonable agreement of data and the SM prediction.

In the muon channel, 4 events were observed in data, whereas the SM expectation was 5.4±0.2 for both, CDM and MEPS. The background is dominated by di-muon production (3.8±0.2 events expected). The efficiencies of the pre-selection in the μ-channel were 15% for single W-boson production with subsequent decay to $\mu\nu_\mu$ (0.78±0.02 events expected) and 41% for single t-quark production with a subsequent decay of the W-boson to $\mu\nu_\mu$. Fig. 7.9 shows kinematic variables of events with an isolated muon candidate. The distributions of the transverse momentum (Fig. 7.9(a)) fall exponentially from small to high values except for single t-quark production. In the μ-channel of the W-boson as well as in di-muon events both leptons lead to undetected energy. For W-boson and di-muon production,

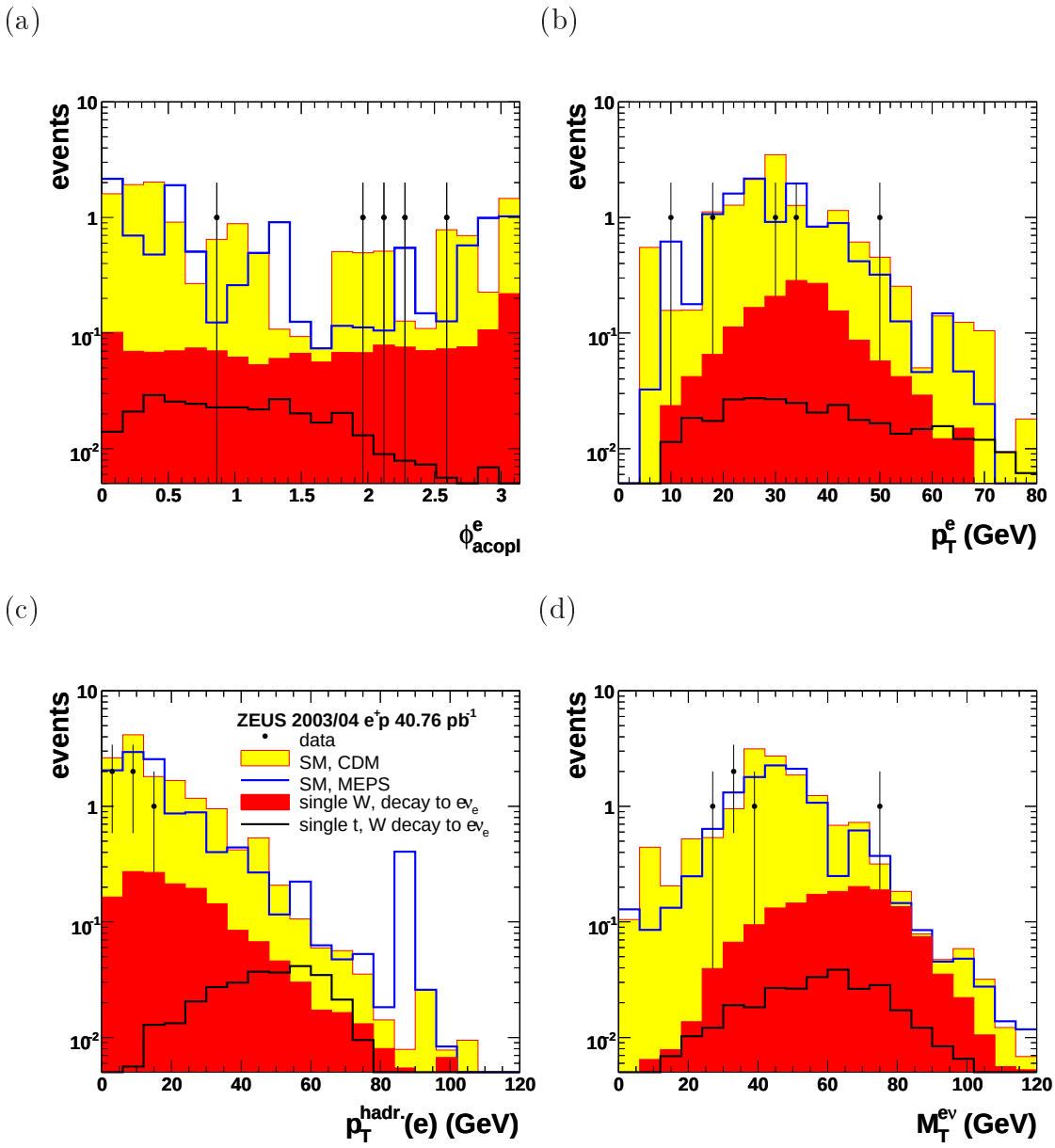

Figure 7.8: Properties of isolated electron candidates after pre-selection (a) Acoplanarity ϕ^e_{acopl} and (b) transverse momentum p^e_T of the isolated electron, (c) hadronic transverse momentum with respect to the electron $p_T^{hadr.}$ and (d) transverse mass of the reconstructed electron-neutrino system $M_T^{e\nu}$ for data (dots) and the SM MC with DIS events generated with CDM (yellow area) or MEPS (blue line). Also single W-boson production with subsequent decay to $e\nu_e$ (red area) and single t-quark production with subsequent decay of the W-boson to $e\nu_e$ (black line) are shown. Only events which passed the pre-selection as isolated electron candidate events are shown.

(a) (b)

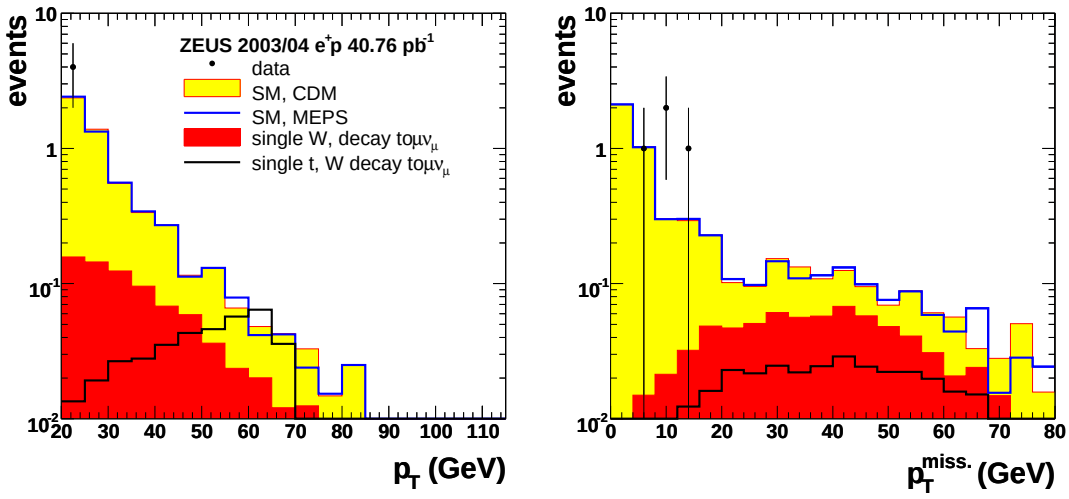

Figure 7.9: Kinematic variables of isolated muon candidate events after pre-selection
(a) Transverse momentum p_T and (b) missing transverse momentum p_T^{miss} for data (dots) and the SM MC with DIS events generated with CDM (yellow area) or MEPS (blue line). Also single W-boson production with subsequent decay to $\mu\nu_\mu$ (red area) and single t-quark production with subsequent decay of the W-boson to $\mu\nu_\mu$ (black line) are shown. Only events which passed the pre-selection as isolated muon candidate events are shown.

this missing energies balance each other, which leads to smaller values in the total transverse momentum. This results in a smaller efficiency of the applied p_T-cuts in W-boson production compared to the e-channel. In single t-quark production, the leptons are expected in the same hemisphere, so that the missing energies add to a large total transverse momentum. This expectation is reproduced by the simulation. Only events with small transverse momentum are observed in the data. The missing transverse momentum (Fig. 7.9(b)) of single W-boson and t-quark production tends to have higher values than the SM background as expected from events with a high-energy neutrino. Since no neutrinos are expected in di-muon production, the missing transverse momentum is small in this case. Data events are observed in a region of the missing transverse momentum, where background dominates, but events with a W-decay also become relevant. Within the limited statistics, agreement of data and SM prediction is observed in these distributions. Fig. 7.10 shows properties of the isolated muon candidates. The MC distribution of the muon azimuth angle ϕ^μ (Fig. 7.10(a)) is flat. Enhancement in data at $|\phi^\mu| = \pi/2$ would be a hint of

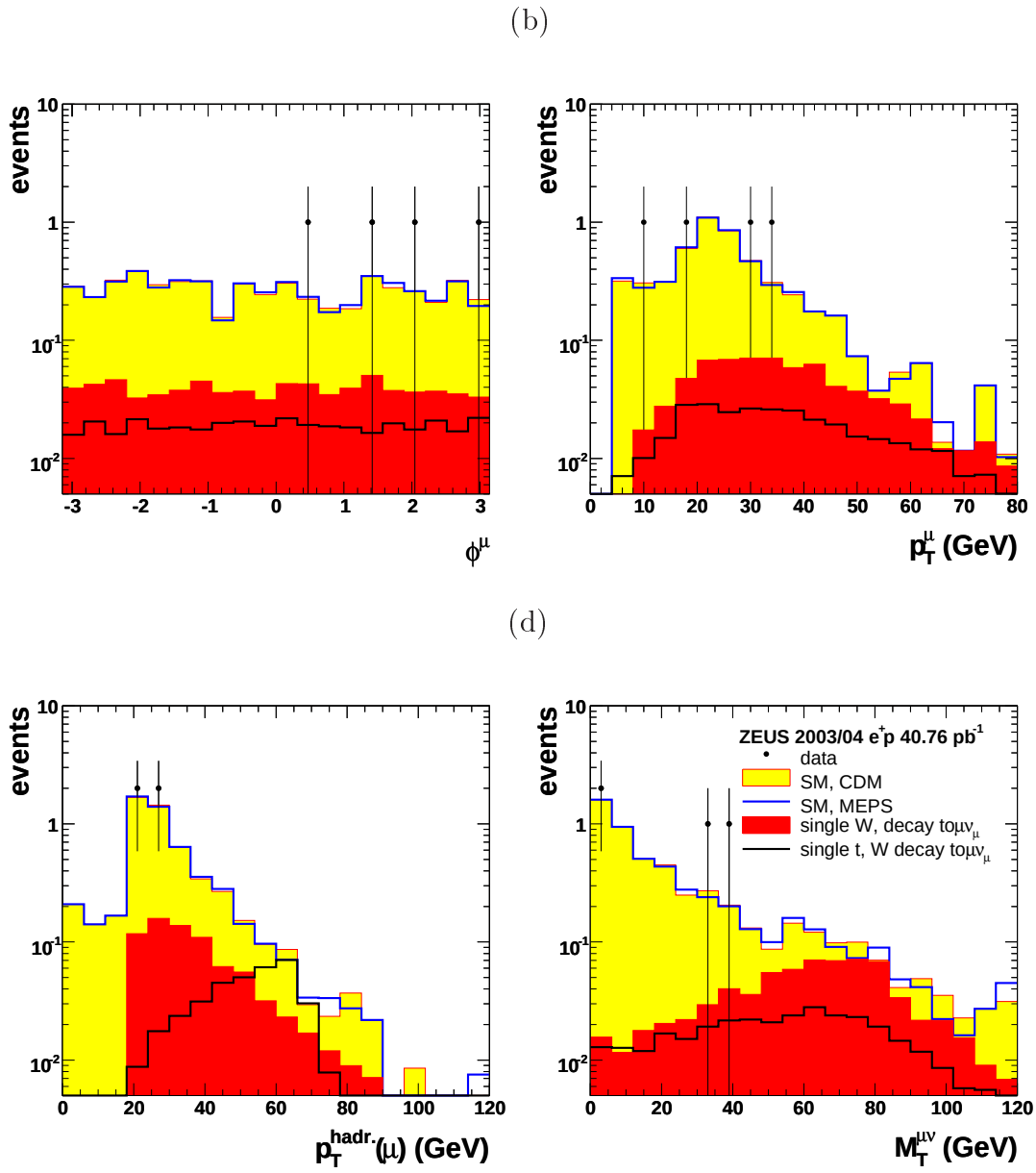

Figure 7.10: Properties of isolated muon candidates after pre-selection (a) Azimuth angle ϕ^μ and (b) transverse momentum p_T^μ of the isolated muon, (c) hadronic transverse momentum with respect to the muon $p_T^{hadr.}$ and (d) transverse mass of the reconstructed muon-neutrino system $M_T^{\mu\nu}$ for data (dots) and the SM MC with DIS events generated with CDM (yellow area) or MEPS (blue line). Also single W-boson production with subsequent decay to $\mu\nu_\mu$ (red area) and single t-quark production with subsequent decay of the W-boson to $\mu\nu_\mu$ (black line) are shown. Only events which passed the pre-selection as isolated muon candidate events are shown.

contamination by atmospheric muon events. This is not observed. The distribution of the transverse momentum of the isolated muon p_T^μ accumulates at small values for data and SM simulations. W-boson and t-quark production peak at a similar value, but with a significant tail towards large values. The distribution of the hadronic transverse momentum with respect to the muon $p_T^{hadr.}$ behaves very similar to the total transverse momentum distribution, since the muon deposits only little energy in the calorimeters. A contribution from di-muon events is found in the simulation at small values of $p_T^{hadr.}$. The distribution of the transverse mass of the assumed $\mu\nu_\mu$-system $M_T^{\mu\nu}$ (Fig. 7.10(d)) for single W-boson and t-quark production is similar to the one for the e-channel. However, the SM background peaks at zero as expected from Bethe-Heitler processes. All distributions show a reasonable agreement of data and SM simulation.

Finally, the remaining isolated tracks without any lepton finder match are assumed to be single hadron tracks. In this channel 12 events were observed in data, whereas the SM expectation was 6.5±0.8 for CDM and 5.9±0.8 for MEPS, respectively. The background is dominated by CC DIS events (5.3±0.2 and 4.7±0.2 events expected for CDM and MEPS, respectively). The efficiencies of the pre-selection in the τ-lepton channel were 3.4% for single W-boson production with subsequent decay to $\tau\nu_\tau$ (0.18±0.01 events expected) and 4.2% for single t-quark production with a subsequent decay of the W-boson to $\tau\nu_\tau$. It has to be taken into account, that these efficiencies include all τ-decay channels, whereas the BR of the τ-lepton decaying into one single charged hadron is about 50%. However, the occurence of at least one additional neutrino in events with τ-leptons (s. 4.1.1) and the uncharged hadrons from the τ-decay make it more difficult to identify the isolated track in this channel. The excess in data is assumed to come mainly from misidentified electrons, which is known not to be reproduced properly in the simulations. In order to reject such events, the properties of the isolated tracks were investigated further. Fig. 7.11 shows some quantities, which are likely to distinguish isolated hadrons from τ-decays from e.g. misidentified electrons. The track-jet matching $D^{jet,ass.}$ (Fig. 7.11(a)) denotes the distance of the isolated track from the momentum axis of the associated jet. All distributions peak at small distances, but for the SM background and data a tail towards large values is observed. The jet radius $R_{90}^{jet,ass.}$ (s. 6.2.3, Fig. 7.11(b)) is expected to be small (collimated "pencil-like" jet) for τ-decays. Single W-boson and t-quark production show an according distribution. However, data and SM prediction have a tail towards large values again. For misidentified electrons the electromagnetic energy fraction of the jet $E_{EM}^{jet,ass.}/E^{jet,ass.}$ (Fig. 7.11(c)) is expected to be close to one. All distributions are almost flat, but for W-boson and t-quark production the distributions are truncated below one. After adding the leading track fraction $E_{trk}^{jet,ass.}/E^{jet,ass.}$ (Fig. 7.11(d)) all distributions peak below two as expected. However, data and SM simulation have tails to large values. This is due to disagreements between energy measurements in the CAL and momentum

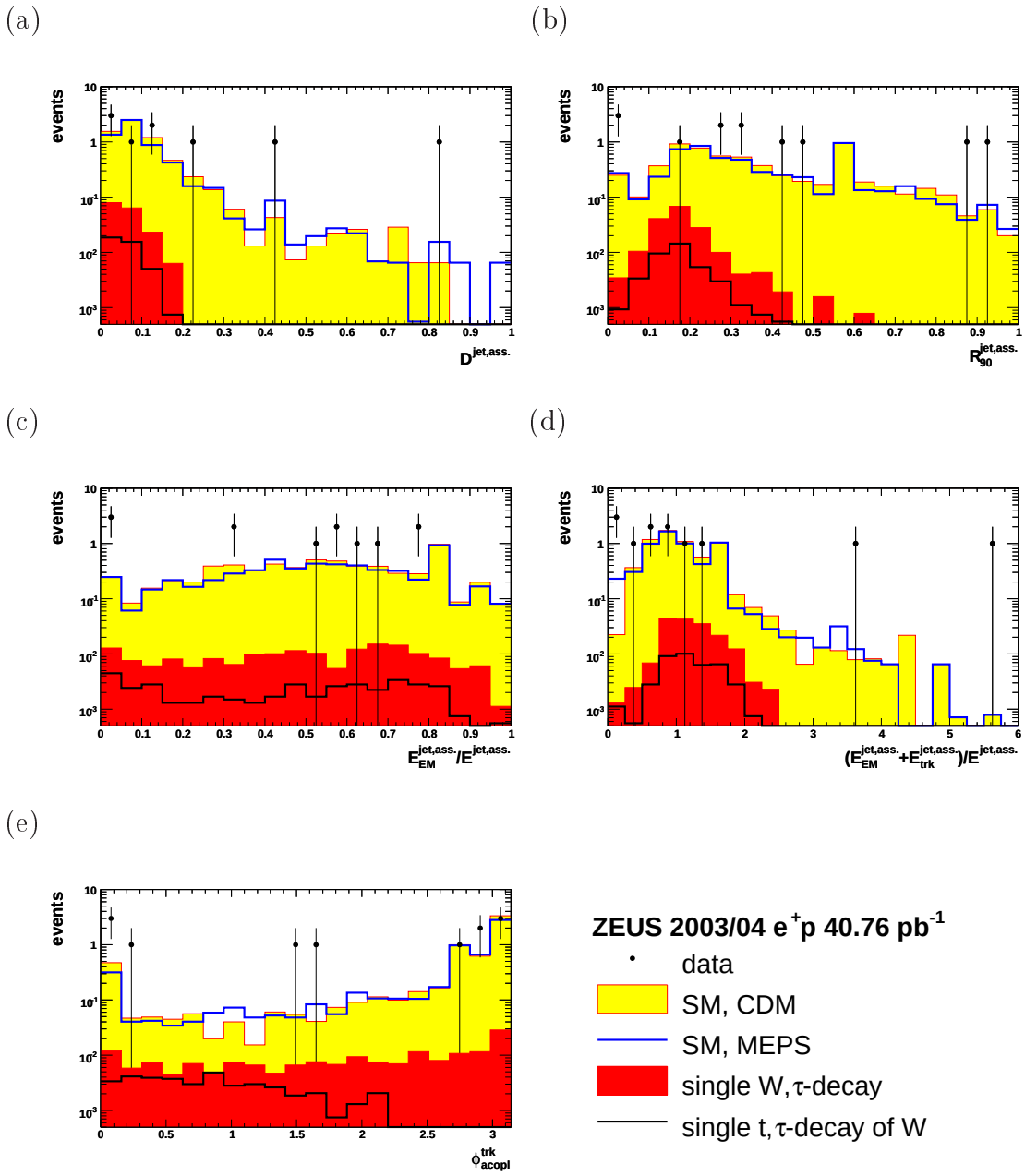

Figure 7.11: Properties of isolated hadronic tracks after pre-selection
(a) Track-jet matching $D^{jet,ass.}$, (b) jet radius $R_{90}^{jet,ass.}$, (c) electromagnetic energy fraction, (d) sum of electromagnetic energy raction and energy fraction of the leading track in the jet and (e) track acoplanarity angle ϕ_{acopl}^{trk} for data (dots) and the SM MC with DIS events generated with CDM (yellow area) or MEPS (blue line). Also single W-boson production with subsequent decay to $\tau\nu_\tau$ (red area) and single t-quark production with subsequent decay of the W-boson to $\tau\nu_\tau$ (black line) are shown. Only events which passed the pre-selection as isolated tracks without lepton matching are shown.

measurements in the CTD, especially for high-p_T tracks with a large error on the measured momentum. For NC DIS events with a misidentified scattered beam electron the track acoplanarity angle ϕ^{trk}_{acopl} (Fig. 7.11(e)) is expected to be very small. Indeed, the SM simulation shows a peak for this variable, which is also observed in data. In summary, the shown quantities are likely to reject background events from SM processes as well as from mismeasurents. In particular, the following cuts were applied:

- **Track-jet matching:**
  The isolated track is required to be very close to the corresponding jet axis:

$$D^{jet,ass.} < 0.2\,. \tag{7.15}$$

- **Jet Radius:**
  A collimated jet is required by:

$$R_{90}^{jet,ass.} < 0.4 \tag{7.16}$$

- **Jet energy fractions:**
  In order to reduce the background from NC DIS, the shown energy fractions are restricted to:

$$\frac{E_{EM}^{jet,ass.}}{E^{jet,ass.}} < 0.95 \text{ and} \tag{7.17}$$

$$\frac{E_{EM}^{jet,ass.} + E_{trk}^{jet,ass.}}{E^{jet,ass.}} < 2. \tag{7.18}$$

  These cuts were based on an optimisation procedure performed on a CC DIS control sample for τ-identification [132]. The particular values were modified according to the actual distributions.

- **Track acoplanarity:**
  In order to reduce the background from NC DIS further, the same cut as for identified electrons is applied:

$$\phi^{trk}_{acopl} > 0.14\,. \tag{7.19}$$

After these cuts, in the channel with an isolated hadronic track (isolated τ-lepton candidate), 1 event was observed in data, whereas the SM expectation was 3.2±0.1 for CDM and 2.8±0.1 for MEPS, respectively. The background is dominated by CC DIS events (2.9±0.1 and 2.6±0.1 events expected for CDM and MEPS, respectively). The efficiencies of the pre-selection in the τ-lepton channel were 2.9% for single W-boson production with subsequent decay to $\tau\nu_\tau$ (0.15±0.01 events expected)

and 3.5% for single t-quark production with a subsequent decay of the W-boson to $\tau\nu_\tau$, where the BR of about 50% for the τ-lepton decaying into one single charged hadron was not taken into account. Fig. 7.12 shows kinematic variables of events with an isolated τ-lepton candidate. The distributions of transverse momentum p_T

(a) (b)

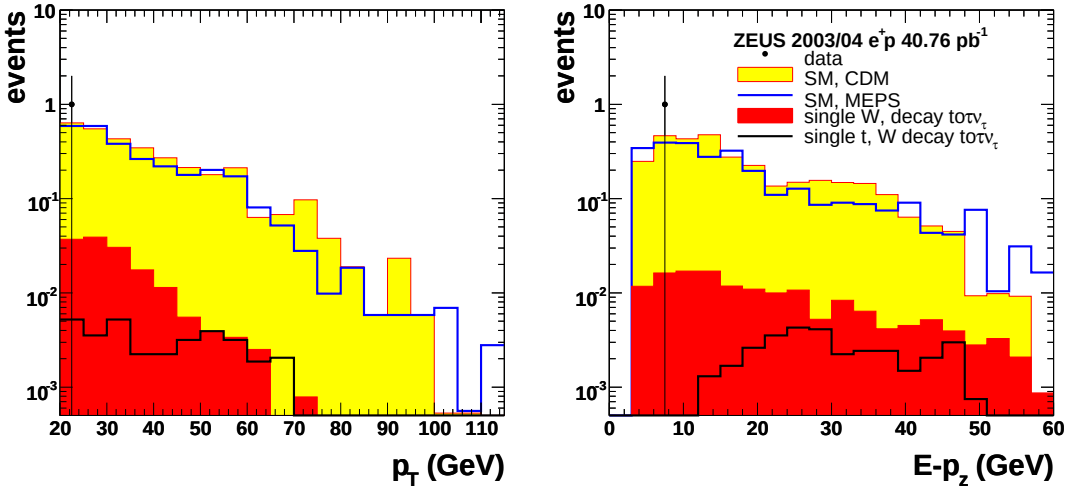

Figure 7.12: Kinematic variables of isolated τ-lepton candidate events after pre-selection
(a) Transverse momentum p_T and (b) $E-p_z$ for data (dots) and the SM MC with DIS events generated with CDM (yellow area) or MEPS (blue line). Also single W-boson production with subsequent decay to $\tau\nu_\tau$ (red area) and single t-quark production with subsequent decay of the W-boson to $\tau\nu_\tau$ (black line) are shown. Only events which passed the pre-selection as isolated τ-lepton candidate events are shown.

(Fig. 7.12(a)) and $E - p_z$ both fall exponentially from small to large values for SM prediction and W-boson production. The data event is found at small values. For single t-quark production these distributions are almost flat for $p_T < 70\,\text{GeV}$ and $10\,\text{GeV} < E - p_z < 50\,\text{GeV}$. The simulation exceeds the data, but statistics are very limited. Fig. 7.13 shows properties of the isolated τ-lepton candidates. The distribution of the track isolation from jets (Fig. 7.13(a)) tends to small values just above the threshold for isolated tracks in the SM background compared to W-boson and t-quark production. This comes from jets in CC DIS events, where final state radiation leads to an additional jet with only one charged track. In the SM MC samples a significant number of events have no neighbouring jet. This events populate the bin at $D^jet \approx 7$. In t-quark production the b-jet is found in most cases. The transverse momentum of the isolated hadronic track p_T^{trk} (Fig. 7.13(b))

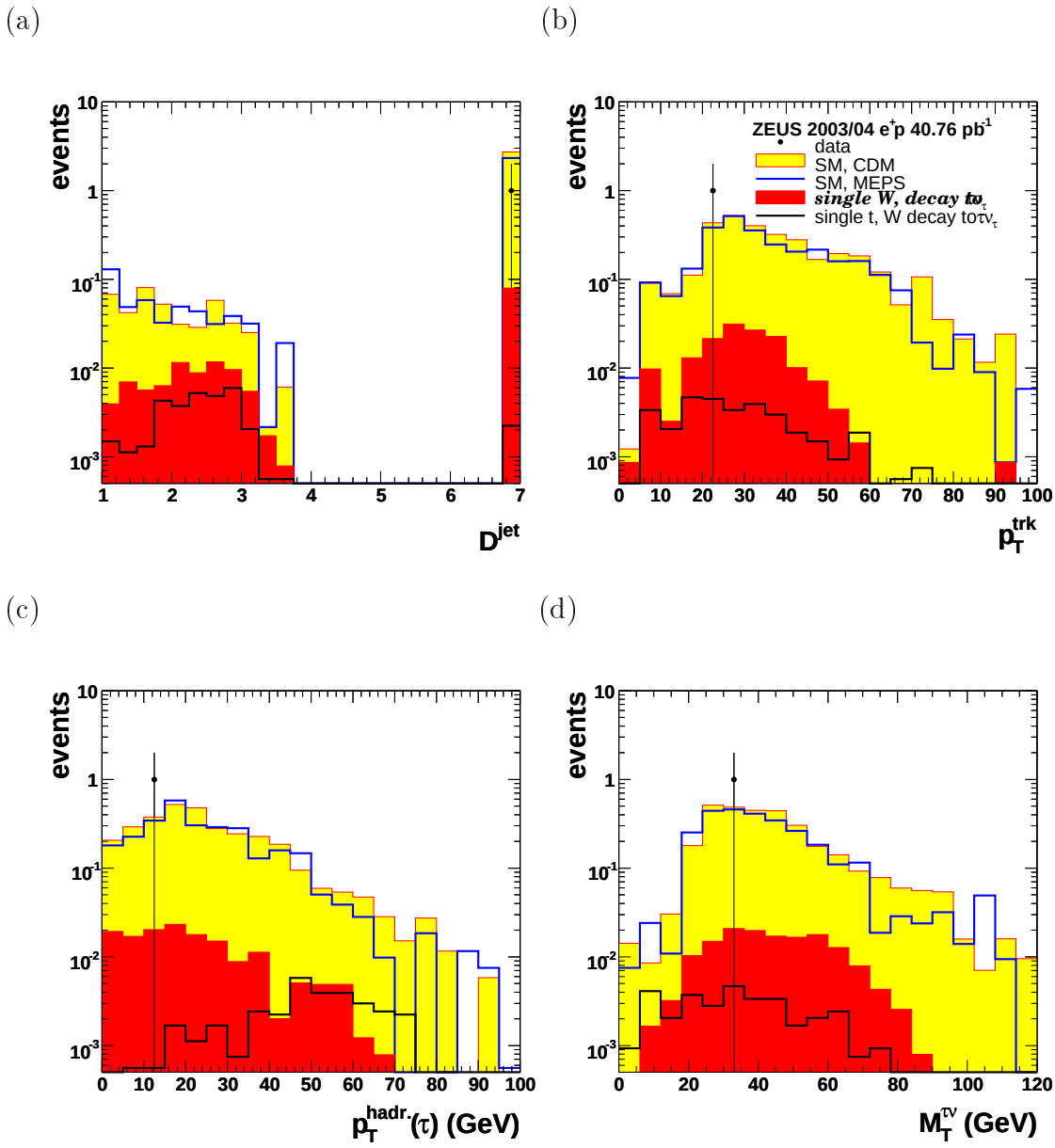

Figure 7.13: Properties of isolated τ-lepton candidates after pre-selection (a) Track isolation from jets D^{jet} and (b) transverse momentum p_T^{trk} of the isolated hadronic track, (c) hadronic transverse momentum with respect to the isolated hadronic track $p_T^{hadr.}$ and (d) transverse mass of the reconstructed track-neutrino system $M_T^{trk\nu}$ for data (dots) and the SM MC with DIS events generated with CDM (yellow area) or MEPS (blue line). Also single W-boson production with subsequent decay to $\tau\nu_\tau$ (red area) and single t-quark production with subsequent decay of the W-boson to $\tau\nu_\tau$ (black line) are shown. Only events which passed the pre-selection as isolated τ-lepton candidates candidate events are shown.

peaks at small values for all samples. For the hadronic transverse momentum with respect to the isolated hadronic track $p_T^{hadr.}$ (Fig. 7.13(c)) a similar behaviour is observed as for the total transverse momentum with tails to very small values. This is due to the fact that the transverse track momenta are generally small. In case of t-quark production, again a accumulation is observed at large values as expected. The transverse mass of the assumed $\tau\nu_\tau$-system $M_T^{\tau\nu}$ (Fig. 7.10(d)) peaks at small values for all simulations. The absence of a peak at the W-boson mass for W-boson and t-quark production is due to the involvement of two neutrinos in this special case, the second one from the τ-lepton decay. The data event is found close to the peaks of the SM simulations.

Considering all channels, data agrees with the SM prediction after the preselection reasonably taking into account the limited statistics. The number of selected events is overestimated by MC, mostly in the e-channel. However, shapes of data distributions are reproduced by the SM prediction, respectively the found event in the τ-channel matches accumulations of the SM distributions. In total, 10 events are observed in data, whereas the SM simulation predicts 22.6±1.7 (CDM) or 19.0±1.5 (MEPS). A list of the data events is given in Tab. 7.2.

7.4 Final Selection of W-Boson Candidates

As described in 6.5, Eq. 6.30 yields two solution for p_z^ν which have to be evaluated for their physical meaning. An event was rejected, if neither solution for the neutrino momentum vector fulfilled all of the following requirements:

$$M_{l\nu-hadr.} < \sqrt{s}\,, \tag{7.20}$$

$$0\,\text{GeV} < E_\nu - p_{z,\nu} < 55\,\text{GeV}, \tag{7.21}$$

$$(E_\nu - p_{z,\nu}) + (E - p_z) < 75\,\text{GeV and} \tag{7.22}$$

$$E_\nu + E_l + E_{hadr.} < 1000\,\text{GeV}, \tag{7.23}$$

where the indices ν, l and *hadr.* indicate properties of the reconstructed neutrino, the isolated track and the hadronic system, respectively. $M_{l\nu-hadr.}$ is the invariant mass of the combined neutrino-track-hadronic system. A cut on the reconstructed transverse mass of the assumed lepton-neutrino system $M_T^{l\nu}$ was not applied, since the distributions in Figs. 7.8(d), 7.10(d) and 7.13(d) give no general handle for this intention.

In order to select candidate events with a leptonic W-boson decay, selection cuts were applied individually for each leptonic channel.

- **Electron channel:**
  NC DIS event with the scattered beam electron found in the detector are the

Run number	Event number	p_T (GeV)	$p_T^{hadr.}(l)$ (GeV)	$M_T^{l\nu}$ (GeV)	p_T^{trk} (GeV)	Cut variable
Electron channel						$E - p_z$ (GeV)
47512	9797	20.4	9.79	31.5	32.0	82.6
50308	1013	20.7	9.56	34.3	18.2	61.3
50410	1276	22.7	5.20	40.6	31.7	65.1
50754	477	31.8	4.21	77.8	50.9	45.2
51108	11802	22.3	16.1	27.5	8.39	38.9
Muon channel						p_T^{miss} (GeV)
48620	14029	23.1	23.9	37.6	34.1	10.5
50482	17061	24.5	26.0	0.18	11.4	14.5
50968	139984	24.2	24.7	2.66	19.1	5.73
51137	36292	23.0	21.3	34.4	30.9	9.58
τ-Lepton channel						D_{trk}^{jet}
51045	19607	22.9	11.6	27.5	24.2	none

Table 7.2: Data events found after pre-selection
The run number, event number, transverse momentum p_T, hadronic transverse momentum excluding the lepton candidate $p_T^{hadr}(l)$, transverse mass of the reconstructed lepton-neutrino system $M_T^{l\nu}$, transverse momentum of the isolated track p_T^{trk}. Furthermore, either $E - p_z$, the missing transverse momentum p_T^{miss} or the track isolation D_{trk}^{jet} are given as characteristic variable, depending on the leptonic channel. The value "none" for D_{trk}^{jet} indicates that no neighbouring jet to the isolated lepton candidate was found. A very large arbitrary value was used in this case.

main source of background in the e-channel of this analysis. A typical property of that event type is the peak in the $E - p_z$-distribution at twice the lepton beam energy as seen in Fig. 7.7(b). To reject those events, the cut

$$E - p_z < 47\,\text{GeV} \tag{7.24}$$

is applied.

- **Muon channel:**
  As shown in Fig. 7.9(b), events from single W-boson and t-quark production in the μ-channel have significant missing transverse momentum. In contrast, the SM background peaks at small values in these distributions. This is expressed by requiring

$$p_T^{miss} > 10\,\text{GeV} \tag{7.25}$$

  in this channel.

- **τ-Lepton channel:**
  In this channel, CC DIS background events were found to have a small isolation of the isolated track from the neighbouring jet (s. Fig. 7.13(a)). This background is reduced by increasing the existing cut on track-jet isolation (s. Eq. 7.14) to
  $$D^{jet} > 1.8\,. \tag{7.26}$$

In the electron channel, 1 event was observed in data, whereas the SM expectation was 3.2±0.5 for CDM and 2.9±0.5 for MEPS, respectively. The background is dominated by NC DIS events (1.2±0.5 for CDM and 0.9±0.5 for MEPS, respectively). The efficiencies of the pre-selection in the e-channel were 21% for single W-boson production with subsequent decay to $e\nu_e$ (1.04±0.02 events expected) and 11% for single t-quark production with a subsequent decay of the W-boson to $e\nu_e$. Fig. 7.14 shows properties of events with a $W \to e\nu_e$ candidate. The distribution of the hadronic transverse momentum with respect to the reconstructed W-boson $p_T^{hadr.}(W)$ has a peak at 40 GeV for single W-boson production and a maximum at larger values for single t-quark production. The SM background accumulates close to zero, but a tail up to large values is observed. The data event is found at the W-boson peak. The number of reconstructed "good" jets (defined in 7.5) peaks at one for t-quark production as expected from the b-jet. In W-boson production, the occurence of zero and one jet are almost equally probable, which is explained by the various production mechanisms. The contribution of the SM background is found to have mostly two good jets reconstructed, which indicates that mismeasurements are more probable in case of di-jet events. Also the data event is found to have two good jets. In the distributions of the transverse mass of the reconstructed track-neutrino system $M_T^{e\nu}$ the same behaviour as for the pre-selection is observed (s Fig. 7.8(d)). Compared to that selection stage, the SM background at large values in the region of the signal MCs has been reduced successfully. The data event has a rather small reconstructed mass. As expected, the mass of the reconstructed electron-neutrino-hadronic system $M^{e\nu,hadr.}$ peaks near the t-quark mass for t-quark production. SM processes peak at smaller values, but far beyond the W-boson mass and with tails to very large values similar to t-quark production. A clear distinction of those processes cannot be made by this quantity. The data event is found between the SM- and the t-quark peaks.

In the muon channel, 2 events were observed in data, whereas the SM expectation was 1.5±0.1 for both, CDM and MEPS. The background is now dominated by di-muon production (0.5±0.1 events expected). The efficiencies of the pre-selection in the μ-channel were 10% for single W-boson production with subsequent decay to $\mu\nu_\mu$ (0.53±0.01 events expected) and 22% for single t-quark production with a subsequent decay of the W-boson to $\mu\nu_\mu$. Fig. 7.15 shows properties of events with a $W \to \mu\nu_\mu$ candidate. Compared to the e-channel, the distributions of the hadronic

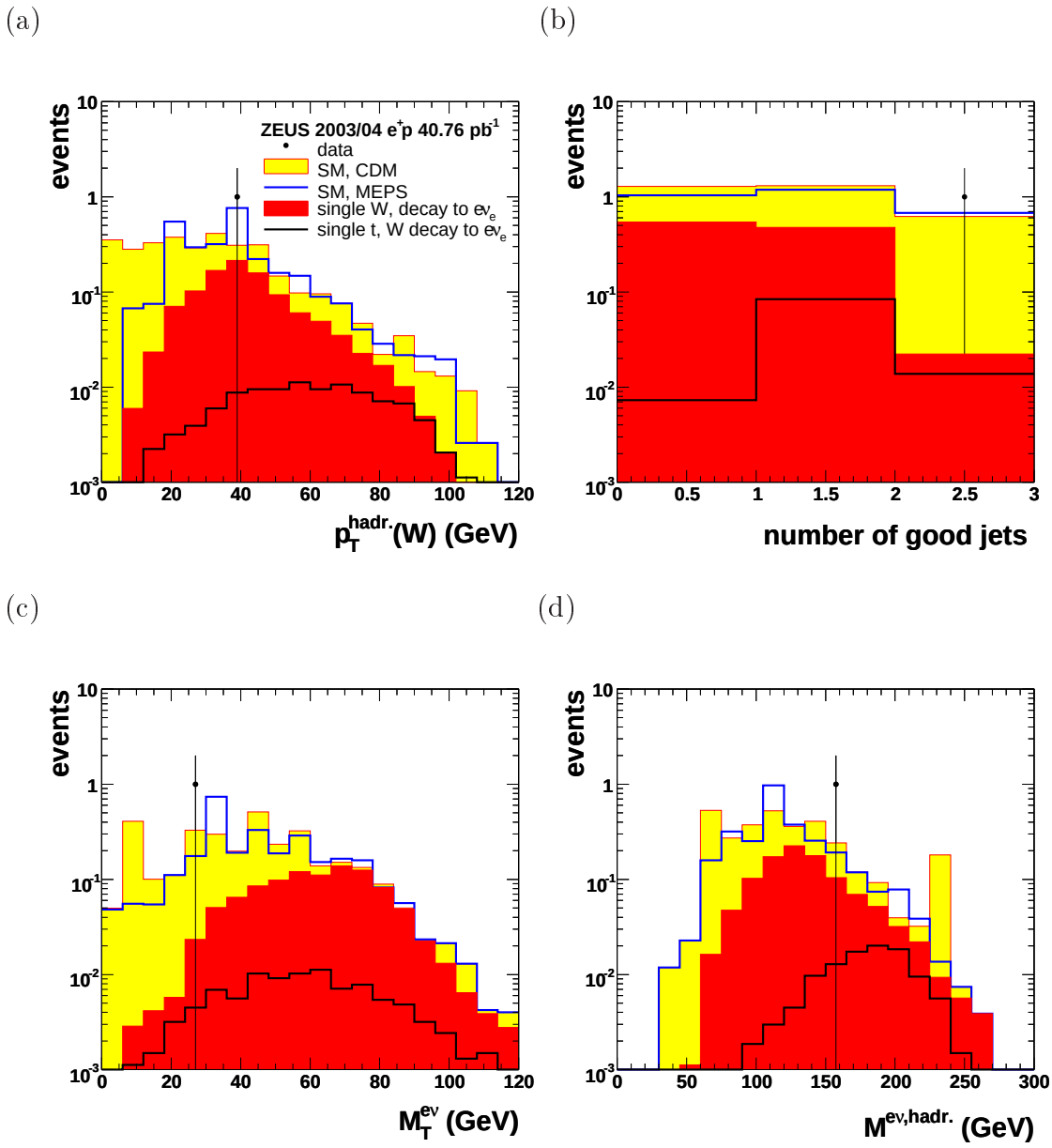

Figure 7.14: Properties of events with a $W \to e\nu_e$ candidate
(a) Hadronic transverse momentum with respect to the reconstructed W-boson $p_T^{hadr.}(W)$, (b) number of good jets, (c) transverse mass of the reconstructed track-neutrino system $M_T^{e\nu}$ and (d) mass of the reconstructed electron-neutrino-hadronic system $M^{e\nu,hadr.}$ for data (dots) and the SM MC with DIS events generated with CDM (yellow area) or MEPS (blue line). Also single W-boson production with subsequent decay to $e\nu_e$ (red area) and single t-quark production with subsequent decay of the W-boson to $e\nu_e$ (black line) are shown. Only events which passed the selection as $W \to e\nu_e$ candidate are shown.

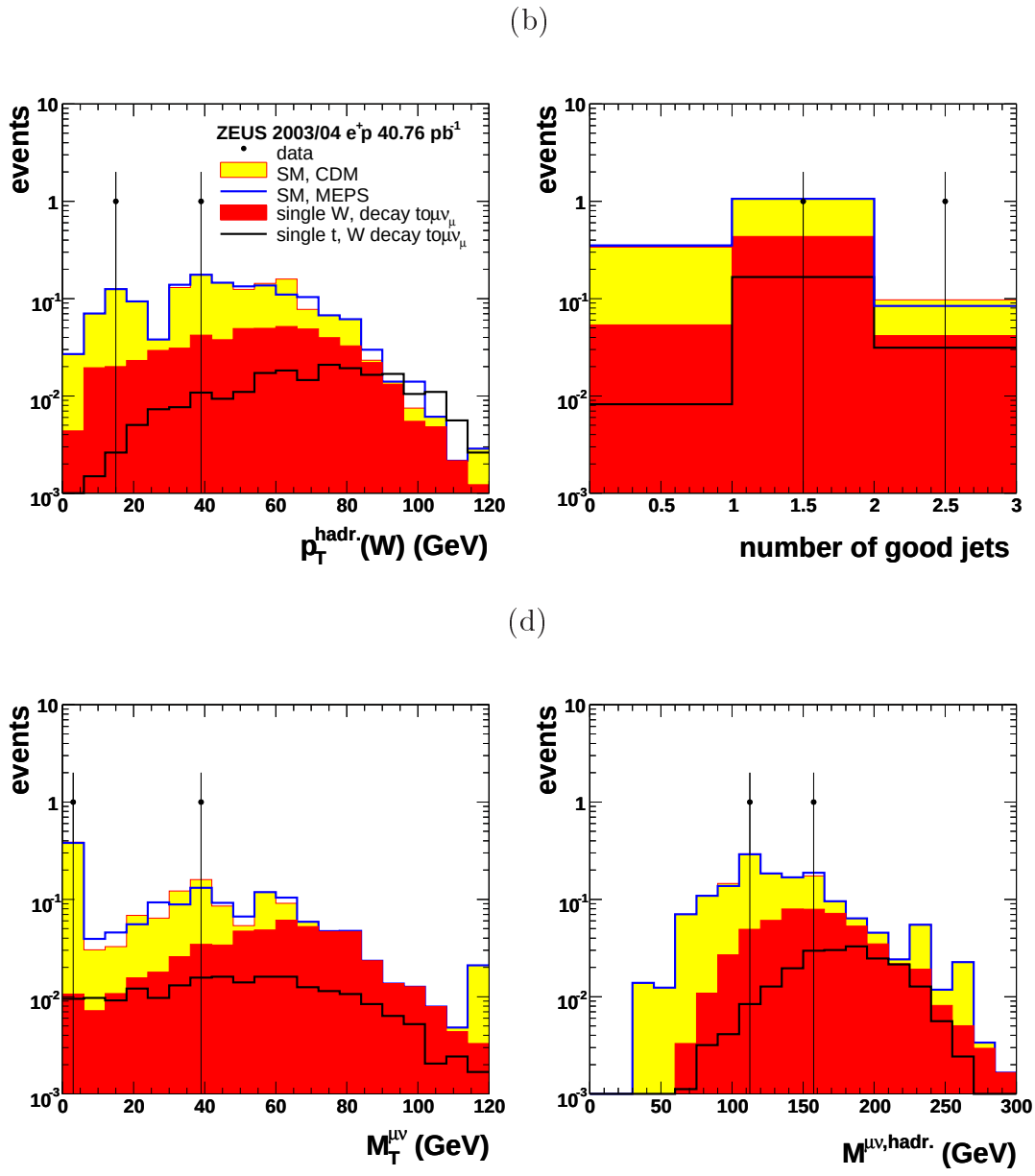

Figure 7.15: Properties of events with a $W \to \mu\nu_\mu$ candidate
(a) Hadronic transverse momentum with respect to the reconstructed W-boson $p_T^{hadr.}(W)$, (b) number of good jets, (c) transverse mass of the reconstructed track-neutrino system $M_T^{\mu\nu}$ and (d) mass of the reconstructed muon-neutrino-hadronic system $M^{\mu\nu,hadr.}$ for data (dots) and the SM MC with DIS events generated with CDM (yellow area) or MEPS (blue line). Also single W-boson production with subsequent decay to $\mu\nu_\mu$ (red area) and single t-quark production with subsequent decay of the W-boson to $\mu\nu_\mu$ (black line) are shown. Only events which passed the selection as $W \to \mu\nu_\mu$ candidate are shown.

transverse momentum with respect to the reconstructed W-boson $p_T^{hadr.}(W)$ are broader. This is explained by the reconstruction of the transverse momentum of the neutrino (s. Eqs. 6.8,6.9), which is not as accurate as in the e-channel. Single t-quark production tends to larger, the SM background to smaller values than single W-boson production, but the distributions interfere with each other. The data events are found at rather small values, where the background expectation dominates slightly. The fraction of events without a good jet is dropped compared to the e-channel in W-boson production. This comes from events, where the W-boson is produced without significant transvere momentum. The transverse momenta of the leptons from the decay balance each other. The same applies to the undetected transverse momenta. This leads to a small total transverse momentum, so that the event is rejected already at the earliest selection stage (s. 7.1). The selection of events from single t-quark production is not affected by this phenomenon and behaves as in the electron case. The di-muon dominated SM background has a maximum at one good jet, where also one data event is found. The other data event has two good jets. The probability to find a W-boson event is about 45% in this bin. The distributions of the transverse mass of the reconstructed track-neutrino system $M_T^{\mu\nu}$ behave as in the e-channel. A significant peak close to zero is found from di-muon production in the SM prediction, where also one data event is found. The other event is located in a region, where the background contribution is still dominant. Also the distributions of the mass of the reconstructed muon-neutrino-hadronic system $M^{\mu\nu,hadr.}$ are similar to those in the e-channel, but broader. One data event has a rather small value close to the maximum of the background, the other is found at the peak of the W-boson distribution.

In the τ-lepton channel, 1 event was observed in data, whereas the SM expectation was 2.3±0.1 for CDM and 2.1±0.1 for MEPS, respectively. The background is dominated by CC DIS events (2.1±0.1 for CDM and 1.9±0.1 for MEPS, respectively). The efficiencies of the pre-selection in the τ-channel were 2.3% for single W-boson production with subsequent decay to $\tau\nu_\tau$ (0.12±0.01 events expected) and 1.7% for single t-quark production with a subsequent decay of the W-boson to $\tau\nu_\tau$. It has to be taken into account, that these efficiencies include all τ-decay channels, whereas the BR of the τ-lepton decaying into one single charged hadron is about 50%. Fig. 7.16 shows properties of events with a $W \to \tau\nu_\tau$ candidate. The distributions are still dominated by SM backgrounds over their whole range. In principle, the signal simulation shows the same behaviour as observed in the e-channel for variables involving the hadronic system, namely the hadronic transverse momentum with respect to the reconstructed W-boson, the number of good jets and the mass of the reconstructed τ-lepton-neutrino-hadronic system. The nature of the dominating CC DIS background explains the observed tendency to larger values in $p_T^{hadr.}(W)$ and $M^{\tau\nu,hadr.}$ for the SM background simulations. The peak for zero good jets comes from the fact that the jets associated with the isolated tracks were removed from

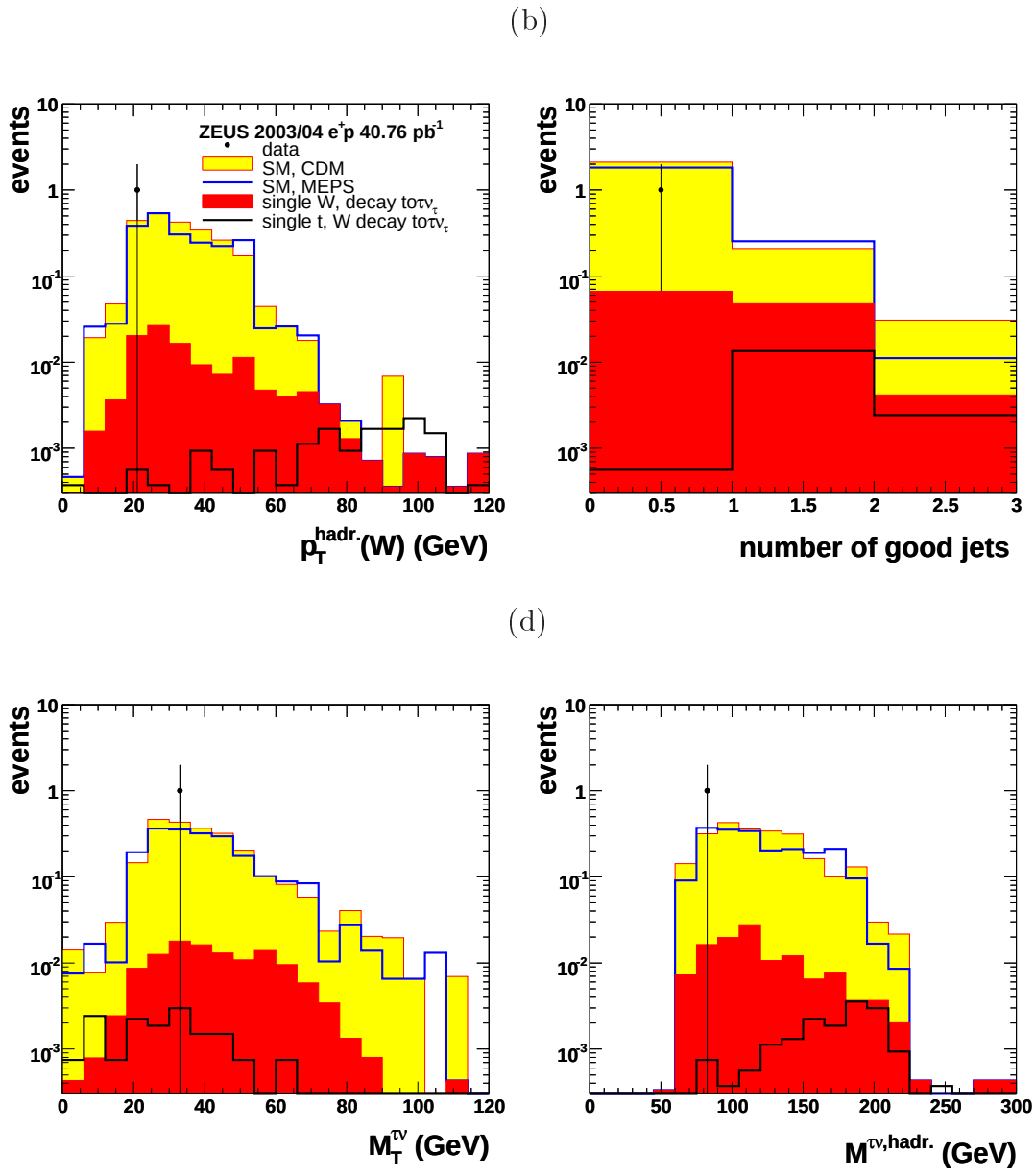

Figure 7.16: Properties of events with a $W \to \tau\nu_\tau$ candidate
(a) Hadronic transverse momentum with respect to the reconstructed W-boson $p_T^{hadr.}(W)$, (b) number of good jets, (c) transverse mass of the reconstructed track-neutrino system $M_T^{\tau\nu}$ and (d) mass of the reconstructed τ-lepton-neutrino-hadronic system $M^{\tau\nu,hadr.}$ for data (dots) and the SM MC with DIS events generated with CDM (yellow area) or MEPS (blue line). Also single W-boson production with subsequent decay to $\tau\nu_\tau$ (red area) and single t-quark production with subsequent decay of the W-boson to $\tau\nu_\tau$ (black line) are shown. Only events which passed the selection as $W \to \tau\nu_\tau$ candidate are shown.

the list of good jets. In the signal distribution of the transverse mass of the reconstructed track-neutrino system $M_T^{\tau\nu}$, significantly smaller values are found than in the other lepton channels. There the second neutrino and the neutral hadrons from the τ-decay do not enter. In contrast, the neutral hadrons are included in the determination of $M^{\tau\nu,hadr.}$ through using the jet rather than the track there (s. 6.5). The data event is found close to the peaks of the SM background in all distributions.

Considering all channels, data and the SM expectations are compatible after the final selection of W-boson candidates. In total four events were observed, whereas the SM simulation predicts 7.1±0.5 (CDM) or 6.5±0.5 (MEPS). A list of the found data events is given in Tab. 7.3. Event display pictures of these events are presented in App. E.2.

Run number	Event number	$p_T^{hadr.}(W)$ (GeV)	$M_T^{l\nu}$ (GeV)	$M^{l\nu,hadr.}$ (GeV)	$n_{jets,good}$
Electron channel					
51108	11802	38.6	27.5	153.8	2
Muon channel					
48620	14029	14.2	37.6	150.2	2
50482	17061	40.5	0.18	109.7	1
τ-Lepton channel					
51045	19607	21.7	27.5	82.1	0

Table 7.3: Data events found after pre-selection
The run number, event number, hadronic transverse momentum excluding the reconstructed lepton-neutrino system $p_T^{hadr}(W)$, transverse mass of the reconstructed lepton-neutrino system $M_T^{l\nu}$, invariant mass of the reconstructed lepton-neutrino-hadronic system $M^{l\nu,hadr.}$ and the number of "good" jets $n_{jets,good}$ (defined in 7.5).

7.5 Final Selection of Single t-Quark Candidates

In order to select candidates for single t-quark production, emphasis is put on the hadronic system in this selection stage. As described in 2.4.2, a jet with large transverse energy E_T^{jet} from the b-quark is expected from the decay of singly produced t-quarks. The following cuts were applied:

- **Jets:**
  Since the b-quark from the t-quark decay is expected to end up in a high-energetic jet, at least one "good" jet with

$$-1 \leq \eta^{jet} < 2.5 \text{ and } E_T^{jet} \geq 5\,\text{GeV} \tag{7.27}$$

is required ($n_{jets,good} \geq 1$).

- **Hadronic transverse momentum:**
  Also the whole hadronic system is expected to have a large transverse momentum. In order to compare the results to a search performed on HERA I data by the ZEUS experiment [1,46], the cut

$$p_T^{hadr.}(W) > 40\,\text{GeV} \tag{7.28}$$

  on the hadronic transverse momentom excluding the reconstructed W-boson was chosen.

In the electron channel, no event was observed in data, while the SM expectation were 0.56±0.04 (CDM) and 0.57±0.04 (MEPS). The efficiencies were 5.7% for W-boson production with subsequent decay in the e-channel (0.29±0.01 events expected) and 8.3% for t-quark production with subsequent W-decay in the e-channel. One data event survived the selection in the muon channel, where the SM expectations were 0.71±0.06 (CDM) and 0.69±0.06 (MEPS). The efficiencies were 6.4% for W-boson production with subsequent decay in the μ-channel (0.33±0.01 events expected) and 18.4% for t-quark production with subsequent W-decay in the μ-channel. No data event was observed in the τ-lepton channel, while the SM expectations were 0.13±0.03 (CDM and MEPS). The efficiencies were 0.6% for W-boson production with subsequent decay in the τ-channel (0.032±0.004 events expected) and 1.4% for t-quark production with subsequent W-decay in the τ-channel. A detailed discussion of these results is presented in 8.

Chapter 8

Results

8.1 Statistical and Systematic Uncertainties

8.1.1 Statistical Uncertainties

On the one hand, statistical uncertainties of the results arise from the limited number of generated MC events. The events of a particular MC sample are weighted to the integrated luminosity of the analysed data $\mathcal{L}_{int}$ with the *weight* factor

$$w^i_{MC} = \mathcal{L}_{int} \cdot \frac{\sigma^i_{MC}}{n^i_{MC,tot.}}\,, \tag{8.1}$$

where σ^i_{MC} is the generation cross section of MC sample i and $n^i_{MC,tot.}$ is its total number of generated events. Then the *statistical uncertainty* $\sigma_{stat.}$ on the number of events selected from a combined MC sample[1] is defined as

$$\sigma_{stat.} = \sqrt{\sum_i n^i_{MC,sel.} \cdot \left(w^i_{MC}\right)^2}\,, \tag{8.2}$$

where $n^i_{MC,sel.}$ is the number of events selected from a particular MC sample i. The sum runs over all included individual MC samples i. All statistical uncertainties on MC expectations quoted in this analysis were calculated according to this definition. The individual statistical uncertainties at particular selection stages are summarised in App. F.

On the other hand, also the numbers of found data events $n_{obs.}$ provide a statistical uncertainty on the results, namely $\pm\sqrt{n_{obs.}}$. If $n_{obs.} = 0$, the statistical error is $+1$.

[1] A combined MC sample contains events from various individual MC samples i with different generation cross sections σ^i_{MC}.

8.1.2 Systematic Uncertainties

In this analysis, positive and negative systematic uncertainties $\sigma^{+}_{sys.}$ and $\sigma^{-}_{sys.}$ were taken into account. They were calculated as:

$$\sigma^{+}_{sys.} = \frac{\sum_i w^i_{MC} \left| n^i_{MC,sel.} - n^{i,+}_{MC,sel.} \right|}{\sum_i w^i_{MC} n^i_{MC,sel.}} \text{ and} \tag{8.3}$$

$$\sigma^{-}_{sys.} = \frac{\sum_i w^i_{MC} \left| n^i_{MC,sel.} - n^{i,-}_{MC,sel.} \right|}{\sum_i w^i_{MC} n^i_{MC,sel.}}, \tag{8.4}$$

where the sum runs over all included individual MC samples i, again. $n^{i,+}_{MC,sel.}$ and $n^{i,-}_{MC,sel.}$ are the numbers of selected MC events for a positive and negative effect of the corresponding systematic variation, respectively, with

$$n^{i,-}_{MC,sel.} < n^i_{MC,sel.} < n^{i,+}_{MC,sel.}\,. \tag{8.5}$$

If several effects of the same sign were found for one variation, the unsigned maximum is quoted. If no effect of a particular sign was found for one variation, it is quoted as zero.

The following sytematic uncertainties were taken into account:

Luminosity measurement: A constant systematic error of 4.5% was applied to all SM simulations due to uncertainties in the luminosity determination (s. 5.1). This has no effect on selection efficiencies, but on all SM expectations.

QCD radiation model: The use of MEPS instead of CDM as QCD radiation model in the simulation of NC and CC DIS events (s. 5.2.1.1 and 5.2.3.1) led to a systematic uncertainty on the background expectation.

CAL scale: The uncertainty of the absolute energy scale of the CAL was assumed to be 1% for the F/BCAL and 2% for the RCAL (s. 6.1.1). For the systematic uncertainties of the signal efficiencies and background expectations, the energy of each CAL cell was varied accordingly.

Mass of the t-quark: The nominal value of 175 GeV for the t-quark mass in the default signal MC sample (s. 5.2.2.2) was varied by ± 5 GeV. The exclusion limits on anomalous single t-quark production were calculated separately for all three masses.

Generator used for the simulation of single t-quark production: The default simulation of processes involving $\kappa_{tu\gamma}$ with the subsequent decay $t \to bW^+$ was

generated using HEXF. A systematic effect for these processes arises from using COMPHEP instead. The exclusion limits were calculated separately for this case.

Single W-boson production cross section: The theoretical uncertainty on the single W-boson production cross section is 15% (s. 2.4.1). This has no effect on selection efficiencies, but on SM expectations.

The individual sytematic effects at particular selection stages are presented in 8.2.

8.2 Signal Efficiencies and Background Expectations

The signal *efficiency* ϵ is defined as:

$$\epsilon = \frac{n_{sel.}^{signal}}{n_{tot.}^{signal}}\,, \tag{8.6}$$

where $n_{sel.}^{signal}$ denotes the (weighted[2]) number of simulated signal events after selection cuts and $n_{tot.}^{signal}$ denotes the total (weighted) number of simulated signal events. In case the signal was simulated with a given cross section[3], the weight normalises the signal MC sample to the integrated data luminosity. Then also the *purity* p of the selected event sample can be calculated as:

$$p = \frac{n_{sel.}^{signal}}{n_{sel.}^{all}}\,, \tag{8.7}$$

with the (weighted) number of all[4] selected MC events $n_{sel.}^{all}$.

8.2.1 Pre-Selection

Tab. F.1 lists the contribution of individual SM MC samples to the selected events after pre-selection as described in 7.3. The main backgrounds are NC DIS in the e-channel, di-μ production in the μ-channel and CC DIS in the τ-channel. PhP processes did not contribute. The SM expectation overestimated the data by about 125%. The purity of the W-boson signal is about 7% in the e-channel, 14% in the μ-channel and 5% in the τ-channel.

Tab. 8.1 summarises the event yields, SM predictions and signal efficiencies after pre-selection. In the e- and μ-channel, the selection efficiencies of single t-quark

[2]S. Eq. 8.1 for a definition of the weight.
[3]In this analyis, that was the case for single W-boson production.
[4]"All" denotes the sum of SM background and SM signal MC.

Sample		e-Channel	μ-Channel	τ-Channel
Data	events	5	4	1
SM (CDM)	events	13.95±1.72	5.41 ±0.24	3.16 ±0.14
SM (MEPS)	events	11.47±1.61	5.40 ±0.24	2.81 ±0.14
W-boson	events	1.59±0.03	0.773±0.018	0.153±0.008
	ϵ (%)	31.3 ±0.5	14.9 ±0.3	2.93 ±0.15
t-quark	ϵ (%)	34.1 ±0.8	40.5 ±0.9	3.45 ±0.26

Table 8.1: Event yields, SM predictions and signal efficiencies after pre-selection
The SM prediction of the number of events is given for the complete SM simulation for both, the CDM- and the MEPS-sample, and for singly produced W-bosons. The complete SM simulation contains the events from W-boson production. Signal efficiencies ϵ were calculated for single W-boson and single t-quark production. The efficiencies and the number of events found in the W-boson sample refer to signal events generated in the W-boson decay channel according to the particular search channel. The quoted uncertainties are statistical uncertainties only.

Sample	e-Channel	μ-Channel	τ-Channel
W-boson e	**31.3**	<0.1	0.1
W-boson μ	1.2	**14.9**	0.1
W-boson τ	5.3	2.3	**2.9**
W-boson hadr.	<0.1	<0.1	<0.1
t-quark e	**34.1**	0	0
t-quark μ	3.7	**40.5**	0
t-quark τ	5.9	3.5	**3.5**
t-quark hadr.	0.5	<0.1	<0.1

Table 8.2: Cross efficiencies of the signals after pre-selection
Efficiencies of particular signal MC samples in the individual search channels. All efficiencies are given in percent. The bold numbers indicate the efficiencies in the "correct" search channel. Uncertainties are neglected.

events is smaller than in the according HERA I analysis at this selection level (∼60%). The reason is illustrated by the comparison of the two-dimensional distributions of the track isolation variables (s. Fig. 7.6 and [46, Fig. 7.8]). The fraction of events, which contain an isolated high-p_T track is smaller in HERA II data. In the μ-channel, the selection efficiency differs between W-boson and t-quark production due to the different behaviour of the transverse momentum in these events (s. Fig. 7.9(a)). The efficiency in the τ-channel is very small compared to the other channels, which was already observed in the HERA I search [1, 46, 131, 140]. It suffers most from the inefficiencies of the track isolation requirement and from cross efficiencies in the other leptonic channels. Tab. 8.2 shows the cross efficiencies of the signals after pre-selection. Efficiencies in the "wrong" search channel are generally small for the e- and μ-channel of the W-boson decay. For τ-leptons, the cross efficiencies in the other leptonic channels are larger than expected from the branching ratios of the τ-lepton decay. Misidentifications of the isolated hadronic track are responsible for this behaviour. The efficiencies of the hadronic decay channel are negligible. The reliablity of this search was not affected by these cross efficiencies, since one individual event was assigned to only one search channel.

8.2.2 Final Selection of W-Boson Candidates

Tab. F.2 lists the contribution of individual SM MC samples to the selected events after the final selection of W-boson candidates as described in 7.4. The background fractions were reduced significantly in each leptonic channel individually. The purity of the W-boson signal increased to 32% in the e-channel, 35% in the μ-channel and remained at 5% in the τ-channel. However, the main background sources stayed the same as quoted in 8.2.1. Also the fact that the SM expectation overestimates the data persisted.

Tab. 8.3 summarises the event yields, SM predictions and signal efficiencies after the final selection of W-boson candidates. The efficiencies in the e- and μ-channel dropped by about 1/3 for W-boson production compared to the previous selection stage. For t-quark production in these channels, the losses were larger, since the reconstruction of the neutrino from the W-boson decay was more difficult in this case. Additional missing momenta from semi-leptonic decays in the b-jet smeared the momenta, which contribute to the neutrino reconstruction (s. Eq. 6.30) and resulted often in solutions, which did not fulfill all the requirements from Eqs. 7.20–7.23.

Tab. 8.4 summarises the systematic uncertainties at this selection stage.

The results from this selection stage were used to calculate a cross section limit on single W-boson production at HERA as described in 8.4.

Sample		e-Channel	μ-Channel	τ-Channel
Data	events	1	2	1
SM (CDM)	events	3.23±0.48	1.50 ±0.10	2.35 ±0.12
SM (MEPS)	events	2.90±0.49	1.50 ±0.10	2.09 ±0.12
W-boson	events	1.04±0.02	0.530±0.015	0.118±0.007
	ϵ (%)	20.5 ±0.4	10.2 ±0.3	2.26 ±0.13
t-quark	ϵ (%)	11.2 ±0.5	22.4 ±0.7	1.70 ±0.18

Table 8.3: Event yields, SM predictions and signal efficiencies after the final selection of W-boson candidates
The SM prediction of the number of events is given for the complete SM simulation for both, the CDM- and the MEPS-sample, and for singly produced W-bosons. The complete SM simulation contains the events from W-boson production. Signal efficiencies ϵ were calculated for single W-boson and single t-quark production. The efficiencies and the number of events found in the W-boson sample refer to signal events generated in the W-boson decay channel according to the particular search channel. The quoted uncertainties are statistical uncertainties only.

8.2.3 Final Selection of t-Quark Candidates

Tab. F.3 lists the contribution of individual SM MC samples to the selected events after the final selection of t-quark candidates as described in 7.5. The main sources of SM background were single W-boson production in the e- and μ-channel and still CC DIS processes in the τ-channel.

Tab. 8.5 summarises the event yields, SM predictions and signal efficiencies after the final selection of t-quark candidates. In the e- and μ-channel, the SM background was reduced by about 70%. The background from W-boson production was reduced by more than 60%, while the t-quark signal was reduced by 20% in this selection stage. Data shows no deviation from the SM prediction. In the τ-channel, where an excess has been observed in the HERA I analysis [1, 46, 131, 140], no hints on a similar result are seen. However, the purity of the t-quark signal of 11% maximum[5] is smaller than in the HERA I analysis as well as the signal efficiency. For a more conclusive statement, the more decided τ-reconstruction method used in the HERA I analysis [46, 132] should be re-used, properly customised for HERA II data.

Tab. 8.6 summarises the systematic uncertainties at this selection stage.

These results were used to calculate limits on single t-quark production at HERA as described in the following.

[5]This maximum purity is achieved by estimating the number of signal events on the basis of the upper cross section limit shown in Eq. 2.26.

Effect	Sample	e-Channel	μ-Channel	e/μ-Channels	τ-Channel	Total
Lumi.	bkg./SM			±4.5		
MEPS	bkg.	-15.0	+0.3	-10.3	-11.4	-10.7
	SM	-10.1	+0.2	-6.9	-10.8	-8.2
CAL scale	bkg.	+0.0 -15.9	+1.2 -5.9	+0.0 -10.7	+2.6 -0.6	+0.0 -5.2
	W	+1.9 -1.2	+0.5 -0.8	+1.0 -0.6	+0.4 -1.2	+0.8 -0.5
	SM	+0.0 -11.2	+1.0 -4.1	+0.0 -7.3	+2.5 -0.0	+0.0 -4.1
$\sigma_{single\,W}$	bkg. SM	±1.4 ±5.8	±1.4 ±6.2	±1.4 ±5.9	±0.1 ±0.8	±0.9 ±4.2
Total sys. uncert.	bkg.	+4.7 -22.4	+4.9 -7.6	+4.7 -15.6	+5.2 -12.3	+4.6 -12.8
	W	+1.9 -1.2	+0.5 -0.8	+1.0 -0.6	+0.4 -1.2	+0.8 -0.5
	SM	+7.3 -16.8	+7.7 -8.7	+7.4 -12.5	+5.2 -11.7	+6.2 -11.0
Stat. uncert.	bkg.	±22.1	±10.3	±15.6	±5.5	±9.4
	W	±1.8	±2.6	±1.6	±5.7	±1.4
	SM	±15.0	±6.7	±10.4	±5.2	±7.2

Table 8.4: Systematic uncertainties in percent after the final selection of W-boson candidates

The quoted systematic effects correspond to the list given in 8.1.2. The effects were determined for the SM background MC sample (bkg.), the SM W-boson production MC sample (W) and the combination of both to a complete SM MC sample (SM). For the W-samples, only the decay channel corresponding to the reconstruction channel was considered, and the quoted uncertainties are given for effects on the selection efficiency. W-decays reconstructed in a "wrong" channel (cross efficiencies) were considered in the background sample. The statistical uncertainties are also quoted for comparison.

Sample		e-Channel	μ-Channel	τ-Channel
Data	events	0	1	0
SM (CDM)	events	0.563±0.042	0.708±0.057	0.133±0.026
SM (MEPS)	events	0.570±0.035	0.689±0.055	0.132±0.026
W-boson	events	0.287±0.011	0.325±0.012	0.031±0.004
t-quark	ϵ (%)	8.45 ±0.41	18.4 ±0.6	1.45 ±0.53

Table 8.5: Event yields, SM predictions and signal efficiencies after the final selection of t-quark candidates
The SM prediction of the number of events is given for the complete SM simulation for both, the CDM- and the MEPS-sample, and for singly produced W-bosons. The complete SM simulation contains the events from W-boson production. Signal efficiencies ϵ were calculated for single t-quark production. The efficiencies and the number of events found in the W-boson sample refer to signal events generated in the W-boson decay channel according to the particular search channel. The quoted uncertainties are statistical uncertainties only.

8.3 Exclusion Limits on Single t-Quark Production

The FCNC coupling of the t-quark to the u-quark is described by the effective Lagrangian in Eq. 2.23 in terms of the couplings $\kappa_{tu\gamma}$ and v_{tuZ}. The values of $\kappa_{tu\gamma}$ and v_{tuZ} determine the production cross section as well as the decay width according to the LO parametrisations in Eqs. 2.24 and 2.26. For the limit setting procedure, both couplings were treated as free parameters. Two-dimensional limits in the $\kappa_{tu\gamma}$-v_{tuZ} plane were obtained, as described in 8.3.1. Also one-dimensional limits were calculated, using various approaches including NLO calculations for $\kappa_{tu\gamma}$ as described in 8.3.2.

For the limit calculations, the results of this analysis in the e- and μ-channel were combined with results from the ZEUS search in HERA I data [1, 39, 46] and a ZEUS search for hadronically decaying W-bosons [39]. The τ-channel of this analysis was not considered due to the small signal efficiency. The model parameters entering the LO limit calculation are listed in Tab. 8.7. The parameter $c_{\gamma,Z}$ for the interference of photon and Z-boson exchange was neglected (s. 2.4.2.2). The experimental parameters entering the LO limit calculation are listed in Tabs. 8.8 [46], 8.9 [46] and 8.10. The efficiencies for the decay channel $t \to u\gamma$ were not evaluated and set to zero.

Effect	Sample	e-Ch.	μ-Ch.	e/μ-Ch.	τ-Ch.	Total
Lumi.	SM			±4.5		
MEPS	SM	+1.2	-2.8	+1.0	-1.1	-1.0
$\sigma_{single\,W}$	SM	±10.5	±8.4	±9.3	±4.0	±8.8
CAL scale	SM	+1.6 -1.0	+3.0 -1.8	+1.2 -0.3	+5.9 -0.3	+1.1 -0.0
	t	+3.0 -4.0	+1.4 -0.1	+1.9 -1.3	+0.0 -2.7	+1.8 -1.4
t-Mass	t	+4.6 -11.5	+0.0 -2.0	+0.4 -5.0	+13.5 -22.8	+1.1 -5.9
COMPHEP	t	+21.2	+9.8	+13.1	+11.3	+11.9
Total sys. uncert.	SM	+11.6 -11.5	+10.0 -10.1	+10.4 -10.3	+8.4 -6.1	+9.9 -9.9
	t	+21.9 -12.2	+9.9 -2.0	+13.2 -5.2	+17.6 -23.0	+12.1 -6.1
Stat. uncert.	SM	±7.4	±8.0	±5.5	±19.2	±5.3
	t	±4.8	±3.3	±2.7	±36.5	±2.6

Table 8.6: Systematic uncertainties in percent after the final selection of t-quark candidates

The quoted systematic effects correspond to the list given in 8.1.2. The effects were determined for the SM background MC sample (bkg.), the SM W-boson production MC sample (W), the combination of both to a complete SM MC sample (SM) and the default t-quark production MC sample (t). For the t-sample, only the decay channel corresponding to the reconstruction channel was considered, and the quoted uncertainties are given for effects on the selection efficiency. The statistical uncertainties are also quoted for comparison.

Parameter at m_t (GeV)	170		175		180	
and $\sqrt{s}$ (GeV)	300	318	300	318	300	318
c_γ	5.451	7.520	4.300	6.076	3.370	4.886
c_Z	0.1808	0.2861	0.1433	0.2340	0.1123	0.1899
Γ_{SM} (GeV)	1.404		1.554		1.713	
$\Gamma_{t\to u\gamma}/\kappa^2_{tu\gamma}$ (GeV)	0.293		0.302		0.310	
$\Gamma_{t\to uZ}/v^2_{tuZ}$ (GeV)	1.297		1.449		1.610	

Table 8.7: Model parameters for LO limit calculation on single t-quark production
The parameters c_γ and c_Z as well as Γ_{SM}, $\Gamma_{t\to u\gamma}$ and $\Gamma_{t\to uZ}$ refer to the LO parametrisations in 2.4.2.2

Parameter at $\sqrt{s}$ (GeV)	300			318		
and m_t (GeV)	170	175	180	170	175	180
$\epsilon_{\gamma,bW}$, $\epsilon_{\gamma,uZ}$ (%)	11.3	16.6	14.0	12.5	16.5	16.5
$\epsilon_{Z,bW}$ (%)	4.57			4.01		
$\epsilon_{Z,uZ}$ (%)	4.48			3.88		
$n_{obs.}$	2	6	5	9	3	8
n_{SM}	1.4	3.3	1.0	10.6	14.3	11.3
$\mathcal{L}_{int}$ (pb^{-1})	45.0			82.2		

Table 8.8: Experimental parameters for LO limit calculation on single t-quark production obtained in analyses of HERA I data in the hadronic channel
The signal efficiencies $\epsilon_{i,j}$ are given, where i denotes the simulated coupling and j denotes the simulated t-decay. $n_{obs.}$ is the number of observed events in data an n_{SM} is the SM expectation.

Parameter at $\sqrt{s}$ (GeV)	300			318		
and m_t (GeV)	170	175	180	170	175	180
$\epsilon_{\gamma,bW}$ (%)	6.49	6.90	7.20	6.69	7.09	7.31
$\epsilon_{\gamma,uZ}$ (%)	3.03					
$\epsilon_{Z,bW}$ (%)	11.07			11.51		
$\epsilon_{Z,uZ}$ (%)	10.25			10.63		
$n_{obs.}$	0			0		
n_{SM}	0.49			1.40		
$\mathcal{L}_{int}$ (pb^{-1})	47.9			82.2		

Table 8.9: Experimental parameters for LO limit calculation on single t-quark production obtained in analyses of HERA I data in the leptonic channels
The signal efficiencies $\epsilon_{i,j}$ are given, where i denotes the simulated coupling and j denotes the simulated t-decay. $n_{obs.}$ is the number of observed events in data an n_{SM} is the SM expectation. Where only one value is given for both $\sqrt{s}$, it was obtained for $\sqrt{s} = 318\,\mathrm{GeV}$.

Parameter at m_t (GeV)	170	175	180
$\epsilon^{\mathrm{HEXF}}_{\gamma,bW}$ (%)	13.47	13.41	12.51
$\epsilon_{\gamma,bW}$ (%)	15.16		
$\epsilon_{\gamma,uZ}$ (%)	13.79		
$\epsilon_{Z,bW}$ (%)	11.06		
$\epsilon_{Z,uZ}$ (%)	10.10		
$n_{obs.}$	1		
n_{SM}	1.27		
$\mathcal{L}_{int}$ (pb^{-1})	40.76		

Table 8.10: Experimental parameters for LO limit calculation on single t-quark production obtained in this analysis (HERA II data, leptonic channels)
The signal efficiencies $\epsilon_{i,j}$ are given, where i denotes the simulated coupling and j denotes the simulated t-decay. The separate values of $\epsilon^{\mathrm{default}}_{\gamma,bW}$ for different t-quark masses were obtained from the HEXF simulation of single t-quark production (s. 5.2.2.2). All further efficiencies were obtained from the corresponding COMPHEP-samples (s. Tab. 5.4). $n_{obs.}$ is the number of observed events in data and n_{SM} is the SM expectation.

8.3.1 Two-dimensional exclusion limits

A two-dimensional likelihood L was defined in the $\kappa_{tu\gamma}$-v_{tuZ} plane as

$$L\left(n_{obs.}|\kappa_{tu\gamma}, v_{tuZ}\right) = \frac{\left(n_{sig.}\left(\kappa_{tu\gamma}, v_{tuZ}\right) + n_{SM}\right)^{n_{obs.}} \cdot e^{-\left(n_{sig.}\left(\kappa_{tu\gamma}, v_{tuZ}\right)+n_{SM}\right)}}{n_{obs.}!}\,, \tag{8.8}$$

where L is the probability to observe $n_{obs.}$ events, when n_{SM} events are expected from SM processes and $n_{sig.}$ are expected from single t-quark production for a given pair $(\kappa_{tu\gamma}, v_{tuZ})$. $n_{sig.}$ is calculated as

$$n_{sig.}\left(\kappa_{tu\gamma}, v_{tuZ}\right) = \mathcal{L}_{int} \cdot \sum_{i,j} \sigma_i^t \cdot BR(j) \cdot \epsilon^{ij} \tag{8.9}$$

with the following parameters:

- the integrated data luminosity $\mathcal{L}_{int}$,
- the single t-quark production cross sections σ_i^t, where i denotes the production either via $\kappa_{tu\gamma}$ or via v_{tuZ},
- the decay branching ratios $BR(j)$ as calculated from the according decay width, where j denotes the decay channel, and
- the selection efficiencies ϵ^{ij} for each combination of i and j,

The sum over the branches i and j runs over the two used couplings $\kappa_{tu\gamma}$ and v_{tuZ} each. Five independent likelihoods were defined, according to the analyses in the leptonic and hadronic channels for the HERA I data taking periods at $\sqrt{s} = 300\,\text{GeV}$ and $\sqrt{s} = 318\,\text{GeV}$ [1, 39, 46] and to this analysis (leptonic channel, HERA II at $\sqrt{s} = 318\,\text{GeV}$). Combined likelihoods were obtained by multiplying the partial likelihoods.

In the $\kappa_{tu\gamma}$-v_{tuZ} plane a two-dimensional probability density p was defined using a Bayesian approach to invert the likelihood:

$$p\left(n_{obs.}|\kappa_{tu\gamma}, v_{tuZ}\right) = \frac{\prod_i L_i\left(n_{obs.}|\kappa_{tu\gamma}, v_{tuZ}\right)}{\int_{\kappa_{tu\gamma}=0}^{\infty}\int_{v_{tuZ}=0}^{\infty}\prod_i L_i\left(n_{obs.}|\kappa_{tu\gamma}, v_{tuZ}\right) d\kappa_{tu\gamma} dv_{tuZ}}\,. \tag{8.10}$$

A uniform a priori probability of $\kappa_{tu\gamma}$ and v_{tuZ} was assumed. The limit at 95% CL was defined as the set of pairs $(\kappa_{tu\gamma}, v_{tuZ})$, where the following relation holds for a constant p_0:

$$\int\limits_{p(n_{obs.}|\kappa_{tu\gamma}, v_{tuZ})>p_0} p\left(n_{obs.}|\kappa_{tu\gamma}, v_{tuZ}\right) d\kappa_{tu\gamma} dv_{tuZ} = 0.95\,. \tag{8.11}$$

(a) (b)

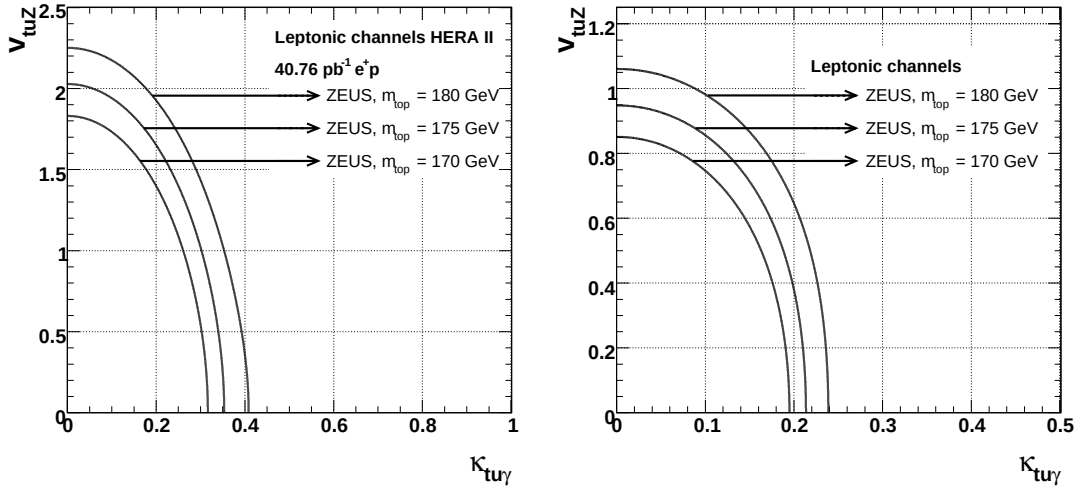

(c)

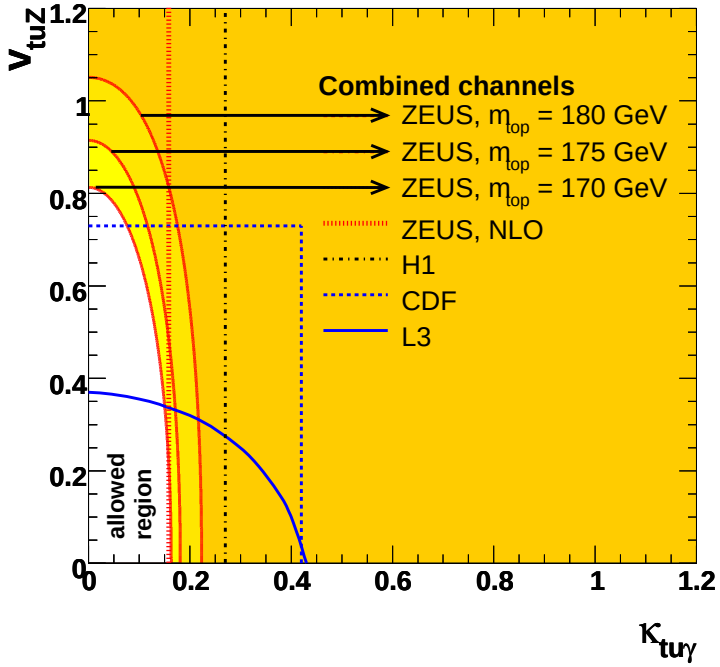

Figure 8.1: Two-dimensional exclusion limits on single t-quark production The exclusion limits for the three considered t-quark masses are shown as obtained from (a) this analysis only, (b) the combined HERA I and II analyses in the leptonic channels and (c) the combined HERA I and II analyses in the leptonic channels and HERA I analyses in the hadronic channel. The latter contains also two-dimensional exclusion limits obtained by the CDF and L3 collaborations, the one-dimensional limit on $\kappa_{tu\gamma}$ obtained by the H1 collaboration and the one-dimensional NLO limit on $\kappa_{tu\gamma}$ obtained in this analysis (s. Tabs. 8.11 and 8.12), all for a t-quark mass of 175 GeV. All limits are given at 95% CL.

Fig. 8.1 shows the resulting limit curves, which include this analysis. The exclusion limits obtained from this analysis only (Fig. 8.1(a)) are not compatitive with the existing limits due to the limited statistics. However, the combination with the HERA I analysis in the leptonic channels (Fig. 8.1(b)) shows an improvement compared to the results of that analysis only. For a t-quark mass of 175 GeV, the limit on $\kappa_{tu\gamma}$ improved from 0.252 in HERA I to 0.213 in the combined analyses, both at 95% CL. Also the combination of all considered analyses (Fig. 8.1(c)) benefitted from this analysis. There the limit on $\kappa_{tu\gamma}$ at $m_t = 175\,\text{GeV}$ improved from 0.198 to 0.181. The limits improve further slightly, when $\epsilon_{\gamma,bW}$ obtained from the COMPHEP simulation is used[6]. There, the obtained limit is $\kappa_{tu\gamma} < 0.209$ at 95% CL for the combined analyses in the leptonic channels and $\kappa_{tu\gamma} < 0.179$ at 95% CL for the combination of all analyses.

8.3.2 One-dimensional exclusion limits

The simplest way to obtain one-dimensional exclusion limits, either for $\kappa_{tu\gamma} = 0$ or $v_{tuZ} = 0$, is to extract them from Fig. 8.1(c) as the intersections of the two-dimensional limit curves with the v_{tuZ} and $\kappa_{tu\gamma}$ axis, respectively.

In addition, a one-dimensional integration over a probability density similar to the procedure decribed in 8.3.1 was performed. A uniform a priori probability of the production cross section σ^t was assumed in this case and the probability densities were defined as:

$$p\left(n_{obs.}|\sigma^t, v_{tuZ}=0\right) = \frac{\prod_i L_i\left(n_{obs.}|\sigma^t, \kappa_{tu\gamma}\left(\sigma^t\right)\right)}{\int_{\sigma^t=0}^{\infty}\prod_i L_i\left(n_{obs.}|\sigma^t\right)d\sigma^t} \text{ and} \tag{8.12}$$

$$p\left(n_{obs.}|\sigma^t, \kappa_{tu\gamma}=0\right) = \frac{\prod_i L_i\left(n_{obs.}|\sigma^t, v_{tuZ}\left(\sigma^t\right)\right)}{\int_{\sigma^t=0}^{\infty}\prod_i L_i\left(n_{obs.}|\sigma^t\right)d\sigma^t}\,. \tag{8.13}$$

The limits on the production cross section at 95% CL were defined as the values $\sigma^{t,lim}_{\kappa_{tu\gamma}}$ and $\sigma^{t,lim}_{v_{tuZ}}$, where the following relations hold:

$$\int_{\sigma^t=0}^{\sigma^{t,lim}_{\kappa_{tu\gamma}}} p\left(n_{obs.}|\sigma^t, v_{tuZ}=0\right)d\sigma^t = 0.95 \text{ or} \tag{8.14}$$

$$\int_{\sigma^t=0}^{\sigma^{t,lim}_{v_{tuZ}}} p\left(n_{obs.}|\sigma^t, \kappa_{tu\gamma}=0\right)d\sigma^t = 0.95\,\text{, respectively.} \tag{8.15}$$

[6]This result is not shown in Fig. 8.1, since it is very close to the result obtained for HEXF at $m_t = 175\,\text{GeV}$.

These cross section limits were used to calculate the one-dimensional limits on the corresponding coupling in LO from Eq. 2.24 as well as in NLO[7].

The one-dimensional exclusion limits obtained from these different approaches in combination of all five likelihoods are summerised in Tabs. 8.11 and 8.12. System-

m_t (GeV)	Approach	$\kappa_{tu\gamma}^{lim}$	$\sigma_{\kappa_{tu\gamma}}^{t,lim}$ (pb^{-1})
170	LO 2-dim	$0.163^{+0.015}_{-0.012}\pm0.001$	$0.200^{+0.038+0.002}_{-0.029-0.003}$
	LO 1-dim	$0.160^{+0.014}_{-0.012}\pm0.001$	$0.193^{+0.035+0.003}_{-0.028-0.002}$
	NLO 1-dim	$0.145^{+0.012}_{-0.011}\pm0.001$	—
175	LO 2-dim	$0.181^{+0.011}_{-0.014}\pm0.001$	$0.199^{+0.037}_{-0.030}\pm0.002$
	LO 1-dim	$0.177^{+0.015}_{-0.013}\pm0.001$	$0.191^{+0.033}_{-0.027}\pm0.002$
	NLO 1-dim	$0.160^{+0.014}_{-0.012}\pm0.001$	—
180	LO 2-dim	$0.223^{+0.017+0.002}_{-0.016-0.001}$	$0.243^{+0.038+0.004}_{-0.034-0.002}$
	LO 1-dim	$0.215^{+0.017+0.002}_{-0.014-0.001}$	$0.227^{+0.035}_{-0.030}\pm0.003$
	NLO 1-dim	$0.195^{+0.015}_{-0.013}\pm0.001$	—
COMPHEP	LO 2-dim	$0.179^{+0.016}_{-0.014}\pm0.001$	$0.195^{+0.036}_{-0.030}\pm0.002$
	LO 1-dim	$0.175^{+0.015}_{-0.013}\pm0.001$	$0.186^{+0.033}_{-0.026}\pm0.002$
	NLO 1-dim	$0.158^{+0.014}_{-0.011}\pm0.001$	—

Table 8.11: One-dimensional exclusion limits on single t-quark production via photon exchange
The one-dimensional exclusion limits for $v_{tuZ} = 0$ for the three t-quark masses m_t used in HEXF and for using COMPHEP are shown as obtained from the axis intersections of the two-dimensional limits (LO 2-dim), the one-dimensional probability density (LO 1-dim) and the NLO calculations (NLO 1-dim). The NLO calculations were performed for the cross section limit obtained with the LO 1-dim approach. The calculations for COMPHEP were performed using the same constants as for the calculations for HEXF at $m_t = 175\,\text{GeV}$. The quoted uncertainties are the statistical (first) and the systematic (second) uncertainty. All limits are given at 95% CL.

atic and statistical uncertainties were calculated by varying the input parameters to the limit setting procedure accordingly to the uncertainties. The systematic effects by varying the t-quark mass and by using different generators for single t-quark production were not considered, since the calculations were made separately for these variation (s. 8.1.2). All uncertainties are dominated by the statistical uncertainty from the number of observed events.

[7]For NLO, calculations were only available for $v_{tuZ} = 0$ [45] (s. 2.4.2.2).

m_t (GeV)	Approach	v_{tuZ}^{lim}	$\sigma_{v_{tuZ}}^{t,lim}$ (pb^{-1})
170	Lo 2-dim	$0.813^{+0.061}_{-0.051}\pm0.004$	$0.189^{+0.030}_{-0.023}\pm0.002$
	Lo 1-dim	$0.822^{+0.065}_{-0.055}\pm0.004$	$0.193^{+0.033}_{-0.025}\pm0.002$
175	Lo 2-dim	$0.915^{+0.070}_{-0.059}\pm0.004$	$0.196^{+0.031}_{-0.025}\pm0.002$
	Lo 1-dim	$0.926^{+0.078+0.005}_{-0.063-0.004}$	$0.201^{+0.034}_{-0.027}\pm0.002$
180	Lo 2-dim	$1.051^{+0.078}_{-0.068}\pm0.005$	$0.210^{+0.032}_{-0.027}\pm0.002$
	Lo 1-dim	$1.087^{+0.092+0.006}_{-0.077-0.005}$	$0.224^{+0.040+0.003}_{-0.030-0.002}$
CompHEP	Lo 2-dim	$0.915^{+0.067}_{-0.058}\pm0.004$	$0.196^{+0.032}_{-0.024}\pm0.002$
	Lo 1-dim	$0.926^{+0.076}_{-0.063}\pm0.005$	$0.201^{+0.034}_{-0.027}\pm0.002$

Table 8.12: One-dimensional exclusion limits on single t-quark production via Z-boson exchange
The one-dimensional exclusion limits for $\kappa_{tu\gamma} = 0$ for the three t-quark masses m_t used in Hexf and for using CompHEP are shown as obtained from the axis intersections of the two-dimensional limits (Lo 2-dim), the one-dimensional probability density (Lo 1-dim). The calculations for CompHEP were performed using the same constants as for the calculation for Hexf at $m_t = 175\,\text{GeV}$. The quoted uncertainties are the statistical (first) and the systematic (second) uncertainty. All limits are given at 95% CL.

8.4 Exclusion Limit on the Single W-Boson Production Cross Sections

Since the event yield after the final selection of W-boson candidates agrees with the Sm prediction neglecting the contribution from W-boson production (s. Tab. 8.3), a limit on the cross section of single W-bosons was set.

The exclusion limit on the single W-boson production cross section was calculated similarly to the one-dimensional cross section limits on single t-quark production introduced in 8.3.2 in the combined e- and μ-channels. In this case, the likelihood was defined as

$$L\left(n_{obs.}|\sigma^W\right) = \frac{\left(n_{sig.}\left(\sigma^W\right)+n_{bkg.}\right)^{n_{obs.}}\cdot e^{-\left(n_{sig.}\left(\sigma^W\right)+n_{bkg.}\right)}}{n_{obs.}!}, \tag{8.16}$$

$$n_{sig.}\left(\sigma^W\right) = \mathcal{L}_{int}\cdot\sum_i \sigma_i^W\cdot\epsilon^i, \tag{8.17}$$

where the sum over i runs over the individual production cross sections either for W^+- or W^--bosons, each for both phase space regions described in 5.2.2.1. The

probability density was defined as

$$p\left(n_{obs.}|\sigma^W\right) = \frac{\prod_i L_i\left(n_{obs.}|\sigma^W\right)}{\int_{\sigma^W=0}^{\infty}\prod_i L_i\left(n_{obs.}|\sigma^W\right)d\sigma^W}\,, \tag{8.18}$$

and the cross section limit at 95% CL was defined as the value $\sigma^{W,lim}$, where the following relation holds:

$$\int_{\sigma^W=0}^{\sigma^{W,lim}} p\left(n_{obs.}|\sigma^W\right)d\sigma^W = 0.95\,. \tag{8.19}$$

The parameters used in the calculation are summarised in Tab. 8.13. The ex-

Parameter	W^+_{DIS}	$W^+_{res.}$	W^-_{DIS}	$W^-_{res.}$
ϵ (%)	19.15	11.17	13.39	8.31
BF (%)	45.13	7.21	37.63	10.04
$n_{obs.}$	3			
$n_{bkg.}$	4.72			
$\mathcal{L}_{int}$ (pb^{-1})	40.76			

Table 8.13: Parameters for W-boson cross section limit calculation
The signal efficiencies ϵ and the branching fraction BF are given for the phase space region of the processes according to 5.2.2.1. BF was obtained from the relations of the production cross sections in the according MC simulation (s. Tab. 5.2). $n_{obs.}$ is the number of observed events in data an $n_{bkg.}$ is the SM background expectation.

perimental parameters $n_{obs.}$ and $n_{bkg.}$ were obtained from the results in the e- and μ-channel of this analysis after the final selection of W-boson candidates (s. 8.2.2). The τ-channel of this analysis was not considered due to the small signal efficiency.

The exclusion limit on the W-boson production cross section at HERA was calculated as

$$\sigma^W < 1.54^{+0.66}_{-0.41}(\text{stat.})^{+0.09}_{-0.04}(\text{sys.})\,\text{pb at 95\% CL.} \tag{8.20}$$

This limit is only 33% above the NLO calculations ($\sigma^W = 1.16\,\text{pb}\,\pm 15\%$, s. 2.4.1).

8.5 Conclusion

A search for events with isolated high-p_T leptons and large missing transverse momentum was performed on 40.76 pb^{-1} of HERA II data in e^+p collisions at 318 GeV.

In the τ-channel of this search, no deviations from the Standard Model were observed. The excess observed in the corresponding HERA I analysis was not supported, but the signal-to-background ratio of the τ-reconstruction method used here is not compatitive with the more sophisticated one used in the HERA I analysis. Also in the e- and μ-channel no deviations from the Standard Model were observed and the limits were calculated in combination of this search with searches for single t-quark production in HERA I data.

Two-dimensional limit curves in the $\kappa_{tu\gamma}$-v_{tuZ} plane and one-dimensional limits were calculated and improved the results of the HERA I analyses. The one-dimensional NLO limit on $\kappa_{tu\gamma}$ for $m_t = 175\,\text{GeV}$ of

$$\kappa_{tu\gamma} < 0.160^{+0.014}_{-0.012}(\text{stat.}) \pm 0.001(\text{sys.}) \text{ at } 95\% \text{ CL} \tag{8.21}$$

is the most stringent so far. Using this limit in Eq. 2.24, the cross section limit on single t-quark production at HERA for $m_t = 175\,\text{GeV}$ is tightened to

$$\sigma_{single\,t} < 0.186^{+0.029}_{-0.012}(\text{stat.})^{+0.002}_{-0.001}(\text{sys.})\,\text{pb}, \tag{8.22}$$

which is 12% lower than the value given in Eq. 2.26. The limits improved further by using COMPHEP also for the simulation of the process involving $\kappa_{tu\gamma}$ with the subsequent decay $t \to bW^+$. They were found to be $\kappa_{tu\gamma} < 0.158^{+0.014}_{-0.011}(\text{stat.}) \pm 0.001(\text{sys.})$ at 95% CL and $\sigma_{single\,t} < 0.183^{+0.028}_{-0.021}(\text{stat.}) \pm 0.002(\text{sys.})\,\text{pb}$.

Also a limit on the single W-boson production cross section at HERA was set at

$$\sigma_{single\,W} < 1.54^{+0.66}_{-0.41}(\text{stat.})^{+0.09}_{-0.04}(\text{sys.})\,\text{pb at } 95\% \text{ CL}. \tag{8.23}$$

Chapter 9

Optimising of Design Parameters of the TESLA Vertex Detector

9.1 Introduction

When designing a new detector, many aspects have to be taken into account. These are not only optimal performance with respect to the physics goals, but also technical feasibility, costs and the time schedule. With the latter constraints the detector can be optimised for maximum physics reach.

Optimising in this sense is done with the help of simulations. Physics events are generated to pass through a detector simulation. The output of these simulation is reconstructed and compared to the truth information. An optimal detector introduces a minimum distortion of the truth information.

In 9.2 the TESLA project is introduced briefly. Then the specific design goals and the technological options for the TESLA vertex detector are described in 9.3. An approach to optimise the design parameters of the TESLA vertex detector on the basis of the SM process $e^+e^- \rightarrow t\bar{t}$ is illustrated in 9.4, and finally the work is summarised in 9.5.

9.2 The TESLA Project

The proposed TeV-Energy Superconducting Linear Accelerator (TESLA) is an e^+e^--collider of 500 GeV total energy, which can be upgraded to 800 GeV [141]. It complements the hadron collider LHC, currently being built at CERN[1], since it uses the advantages of lepton collisions: a clean experimental environment (no "proton remnants") and pointlike colliding particles, which do not involve any structure func-

[1] Conseil Européen pour la Recherche Nucléaire

tion. The very high CMS energy and the high luminosities make the LHC a discovery machine. On the other hand, TESLA is designed for precision measurements. Its primary physics goals are [143]:

- precision measurements of the Higgs particle,
- precision measurements of SM parameters,
- search for and precision measurements of SUSY particles,
- search for dark matter,
- search for other new physics.

To meet this challenge, TESLA is planned as a 33 km long underground facility with a CMS energy of 91.2 – 800 GeV and a peak luminosity of the order of $10^{34}\,\mathrm{cm}^{-2}\mathrm{s}^{-1}$ at 500 GeV. More technical details are given in Tab. G.1. Fig. 9.1 shows a schematic view of the TESLA facility (a) and a map of the proposed tunnel (b).

To reach the goals of the TESLA project, a detector of unprecedented precision is required. More specifically, the following characteristics need to be optimised:

- track momentum resolution, e.g. to determine the recoil mass to $Z \to l\bar{l}$ decays,
- vertex and impact parameter resolution for flavour identification,
- energy-flow for the multitude of multijet topologies (This requires fine 3-D granularity in tracking and calorimetry, with both being inside the coil.),
- good geometrical acceptance and good forward detectors, for measuring missing energy and the luminosity spectrum,
- triggerless and deadtime-free data acquisition,
- high tolerance for machine induced backgrounds.

The layout of the detector is that of a typical quasi-hermetic detector for symmetric high-energy collision experiments containing:

- tracking:
  - a solenoidal magnetic field of 4 T,
  - a five-layer Si-pixel vertex detector VTX (see 9.3),
  - a Si-pixel or -strip disk forward tracker FTD,

(a) (b)

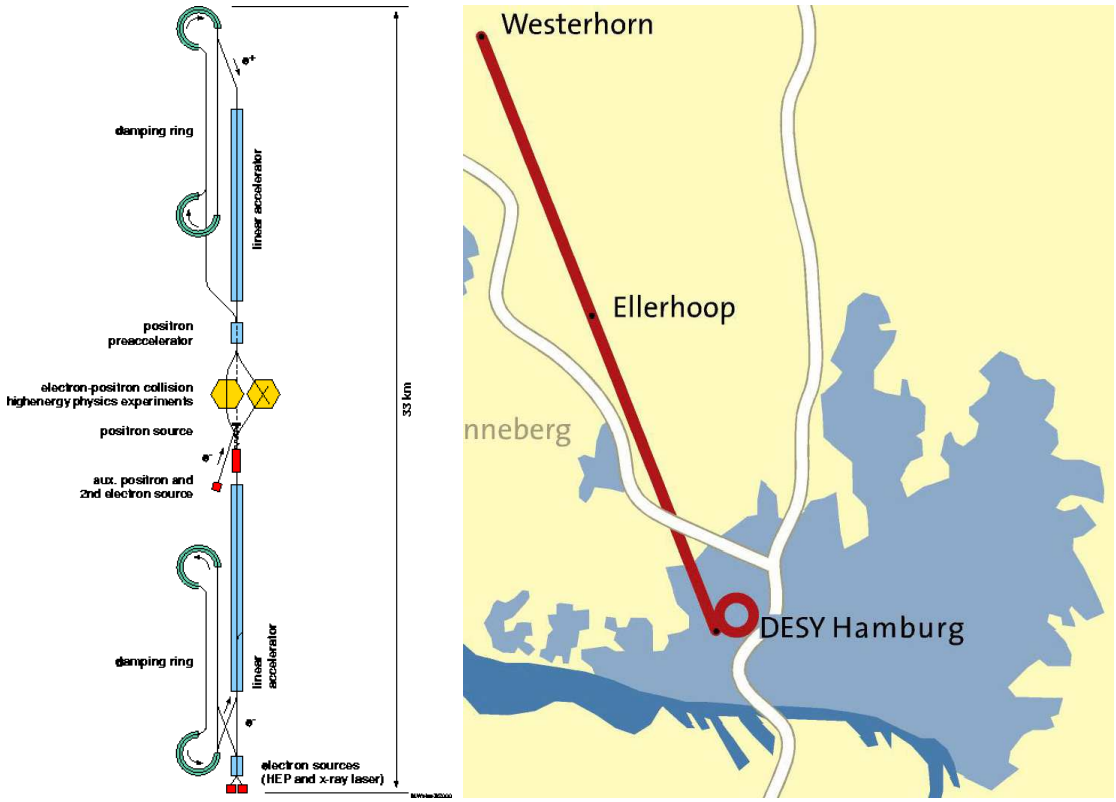

Figure 9.1: The proposed TESLA facility
(a) Schematic view of the planned TESLA accelerator facility. In addition to the main accelerator line and the experimental area, the damping rings and a possible second interaction region are shown. (b) Map of the TESLA tunnel near Hamburg, Germany, extending from the DESY site all the way to Westerhorn with the experimental hall located at Ellerhoop. The light blue area represents the city of Hamburg, the dark blue band the river Elbe and the white lines the motorways A7 (from south to north) and A23 (from Hamburg to north-west).

  - a large volume gaseous central tracking chamber TPC (time projection chamber),
  - a Si-strip intermediate tracker SIT,
  - a forward tracking chamber FCH, built from straw tubes.

  The schematic layout of the tracking detectors is illustrated in Fig. 9.2. The momentum resolution should be

$$\delta\left(\frac{1}{p_T}\right) \leq 5 \cdot 10^{-5} \left(\frac{\text{GeV}}{c}\right)^{-1} . \tag{9.1}$$

- calorimetry:
  - a highly granular electromagnetic calorimeter ECAL,
  - a highly granular hadronic calorimeter HCAL,
  - a low angle tagger LAT

  The desired overall-energy resolution for *energy flow objects* (EFOs [144]) is

$$\frac{\delta E}{E} \simeq 0.3 \, \frac{1}{\sqrt{E(\text{GeV})}} . \tag{9.2}$$

  The granularity of the calorimeter should allow for internal tracking of charged and neutral particles for a complete reconstruction of the energy flow. For this purpose, the coil has to enclose the calorimeters.

- muon detection:
  - the instrumented Fe-yoke MUON
- luminosity measurement:
  - a luminosity calorimeter LCAL

Fig. 9.3 shows the detector layout. A more detailed description of the detector and various design options are found in [145].

9.3 The TESLA Vertex Detector

9.3.1 Design Goals

Besides Higgs production studies, the potential for investigating electroweak symmetry breaking must be met by a detailed study of the decay properties of the Higgs

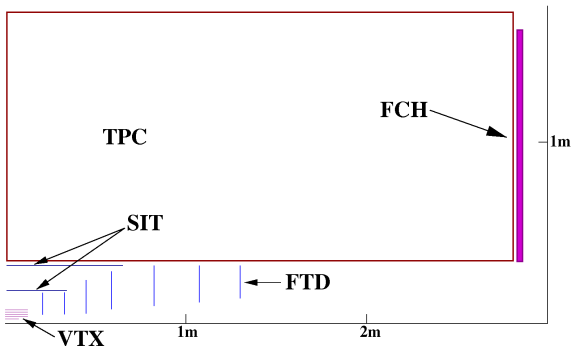

Figure 9.2: Layout of TESLA tracking detectors
The acronyms correspond to those in the text.

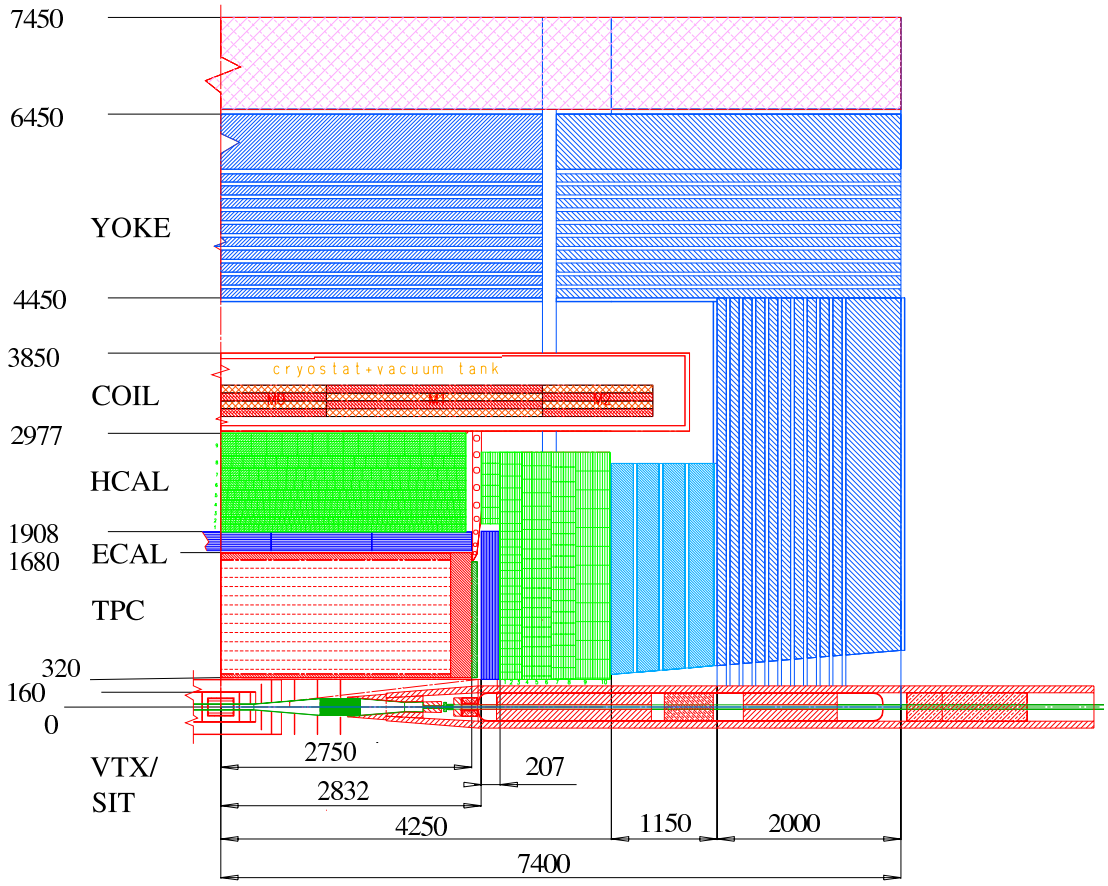

Figure 9.3: TESLA detector layout
A cross section through one quadrant of the detector is shown. All dimensions are in mm. The acronyms for the subdetectors are explained in the text.

boson. Distinguishing between a light Higgs boson decaying into $b\bar{b}$, $c\bar{c}$, gg and $\tau\bar{\tau}$ pairs represents a major challenge for the TESLA vertex detector. An extended Higgs sector with its distinctive signatures with multiple b-jets, several SUSY decay scenarios and also SM processes like $e^+e^- \to t\bar{t}$ are equally challenging. Heavy flavour identification plays a key role in many of the physics goals of a linear collider. It requires excellent tracking efficiency and spatial resolution in order to determine vertex positions and track *impact parameters*. For many analyses it is also mandatory to be able to assign all tracks correctly to their production vertex in order to determine the vertex mass and charge.

For the TESLA vertex detector these requirements lead to a desired impact parameter resolution of

$$\delta\left(IP_{r\phi,z}\right) \leq 5\,\mu\text{m} \oplus \frac{5\,\mu\text{m}\,\text{GeV}/c}{p\sin^{3/2}\theta}\,, \tag{9.3}$$

where $\delta(IP_{r\phi,z})$ denotes the impact parameter resolution in the $r\phi$-plane as well as for the z-coordinate, and p and θ are the track momentum and polar angle, respectively [146]. This translates into a point resolution of less than 5 µm. Furthermore, the best possible polar angle coverage is desirable to cope with the expected multijet environment with jets in the whole polar angle range. A polar angle coverage of $|\cos\theta| \leq 0.96$ for the inner three and $|\cos\theta| \leq 0.9$ for the inner five layers is proposed. The innermost layer of the vertex detector needs to be as close to the beampipe as possible for the best track extrapolation to the vertices possible. To allow for stand-alone tracking, a minimum number of five vertex detector layers is needed with an equidistant layer separation of at least 5 mm to control multiple scattering effects. At small polar angles, one has to pay special attention to the material budget. So, thin sensors or even conical endcaps are to be preferred. In case of CMOS or CCD sensors (see the following section for explanations), the potential for precise tracking to very low momenta is established for a layer thickness of $0.06\%\,X_0 \approx 56\,\mu\text{m}$, where X_0 denotes the radiation length of silicon[2]. Taking into account machine-related issues, the base configuration as shown in Tab. 9.1 consists of $8 \cdot 10^8$ pixels of $20 \times 20\mu\text{m}^2$ integrated in cylindical layers. A schematic view of this configuration can be seen in Fig. 9.4.

9.3.2 Sensor Technologies

Several different sensor technologies are being investigated for the vertex detector of a linear collider. *Research and development* (R&D) on these options is ongoing in parallel to provide a basis for the final choice of the technology. In this section a selection of these technologies is introduced.

[2] $X_0(Si) = 9.36\,\text{cm}$ [4]

Layer	Radius (mm)	Length (mm)	Readout time (µs)	Background (hits/mm^2)
1	15	100	50	4.3
2	26	250	250	2.4
3	37	250	250	0.6
4	48	250	250	0.1
5	60	250	250	0.1

Table 9.1: Key parameters of a CMOS- or CCD-based vertex detector
The quoted readout times are the estimated maxima to cope with the background rate. The background occupancies are integrated over these individual readout times.

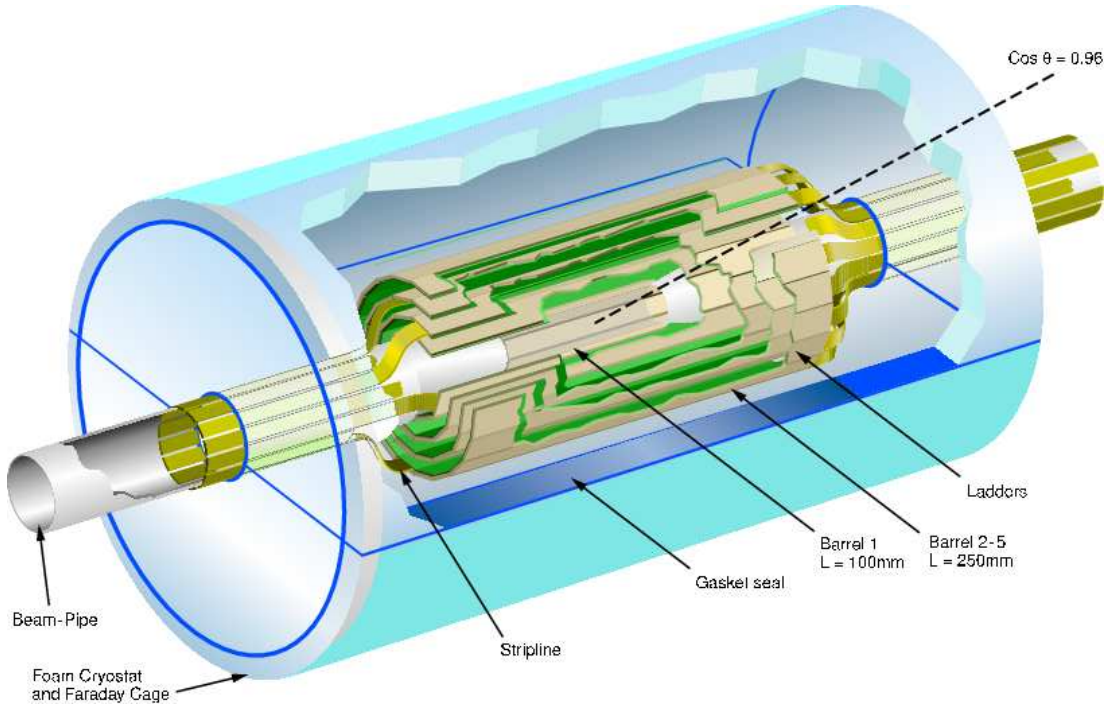

Figure 9.4: Layout of the TESLA-VTX base design
An open view into the VTX including the cryostat is shown. In the centre one can identify the short first layer embedded in the narrowed beampipe.

9.3.2.1 Monolithic Active Pixel Sensors

The basic idea is to make the CMOS[3] technology applicable for *monolithic active pixel sensors* (MAPS) [147] in high-energy physics and to exploit the low costs and existing production infrastructures.

An ionising particle traversing the sensor generates free charges in a low resistivity p-type epitaxial layer of $5-15\,\mu m$ thickness as shown in Fig. 9.5(a). The free electrons diffuse and are collected by implanted n-wells, the pixels. Since the lightly p-doped epitaxial layer is embedded between two heavily p^+-doped media (i.e. p-wells and substrate), electrons reaching the boundary regions are reflected by the potential barriers (see Fig. 9.5(b)) due to the doping profile. No depletion voltage is applied. Part of the readout electronics including the first amplification stage is implanted directly onto the p-wells to optimise the readout noise.

(a) (b)

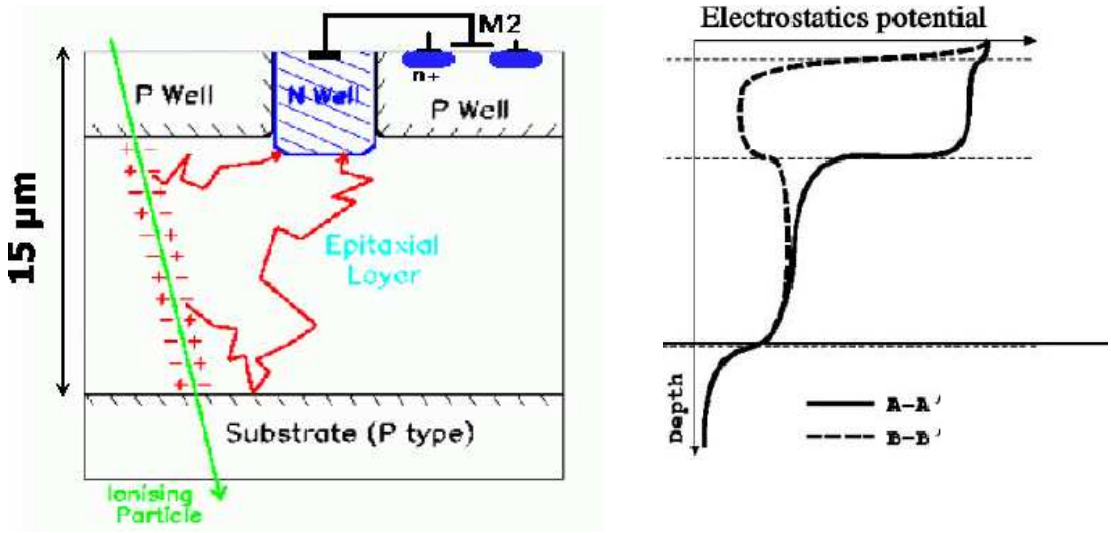

Figure 9.5: Schematic charge collection and potential in a MAPS sensor
(a) The free electrons generated by an ionising particle diffuse thermally to the n-well. Readout electronics (M_2) are implanted into the p-well. (b) The potential gradient is shown at the centre of the n-well (A—A') and at the centre of the p-well (B—B'). The potential barriers at the p/p^+-edges are clearly seen as well as the potential minimum in the n-well.

Advantages are the CMOS production process with low costs, the low noise and good *signal-to-noise ratio* (S/N) at high speed, the radiation hardness and the ho-

[3] Complementary metal-oxide-semiconductor

mogeneous charge collection. Disadvantages are the bad photon detection efficiency at high energies and the possible trench isolation in very deep sub-µm production processes.

This study was performed in order to optimise the design of a vertex detector based on the MAPS technology. It is based on the specifications of the MIMOSA[4] 5 sensor, which are listed in Tab. 9.2.

Year	2001
CMOS process	0.6 µm AMS
Pixels	1020×1024
Pixel size	17×17 µm^2
Epilayer thickness	14 µm
Spatial resolution	1.5 µm
Readout	analog

Table 9.2: Properties of MIMOSA 5 [148]
MIMOSA 5 was the first fabricated "real size" sensor of the MIMOSA series at IRES (Institut de Recherches Subatomiques, Strasbourg, France).

9.3.2.2 Hybrid Active Pixel Sensors

Closely related to MAPS is the technology of *hybrid active pixel sensors* (HAPS) [149]. In this case the readout electronics are situated on a separate chip mounted onto the sensor and connected via bump bonds (hybrid structure). HAPS sensors are depleted in order to use the whole sensor substrate as active volume, which leads to higher signals. There exists already some experience with HAPS detectors, e.g. from the LHC experiments. HAPS sensors are very fast and radiation hard and they have a homogeneous charge collection and a good high-energy photon detection efficiency. Beside that, the sensor architecture sets no limits on the design of the readout chip. However, the noise level is rather high, the sensors are relatively thick and expensive and the bump bonding alignment is problematic.

A special variety of HAPS are *silicon-on-insulator* (SOI) chips [150], which are similar to MAPS chips, but with the electronics separated from the sensor by an insulating layer. Thus the architecture is "quasi-monolithic", as can be seen in Fig. 9.6. The biggest disadvantages of HAPS are remedied by the SOI technology, which shows no alignment problems and is thinner than conventional HAPS. However, at present the development of this technology is slowed down by a lack of wafer material of the quality required for the TESLA VTX.

[4] minimum ionising particle MOS active pixel sensor

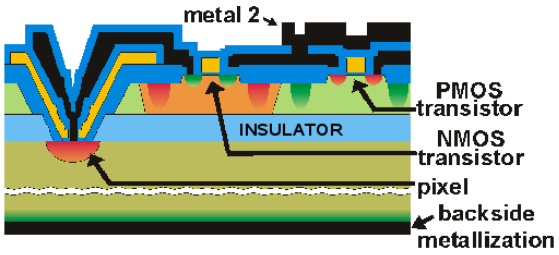

Figure 9.6: Schematic structure of an SOI sensor
The electronics are created on a 1.5 µm thin *Si*-film over the insulating layer called BOX (*buried oxide*).

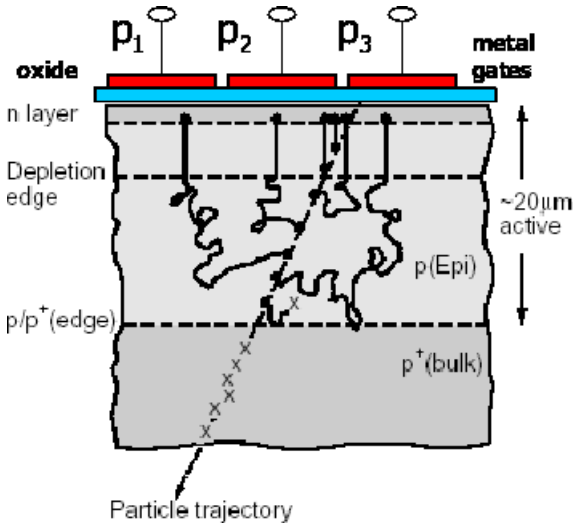

Figure 9.7: Schematic charge collection in a CCD sensor
The free electrons are colleced underneath the anodes ($p_{1,2,3}$).

9.3.2.3 Charge Coupled Devices

A *charge coupled devices* (CCD) pixel detector [151] is a two-dimensional array of potential wells. The signal is generated in a partially depleted, p-type epitaxial layer of typically a $10-30\,\mu m$ thickness. The free electrons diffuse thermally or, in the depleted area, drift towards the potential minimum underneath an anode. Again, a p/p^+-edge between the active volume and the sensor bulk acts as reflection layer for the free electrons. A thin n^+-type layer on the surface moves the potential minimum towards the n^+/p-edge, so that the electrons are collected underneath the sensor's surface (*burried channel* CCD). Then the collected charges are moved through the sensor to be read out at the sensor edge. This is done by a periodical variation of the potential wells (*clocking*). The anodes are realised as MOS gates on top of the n^+-layer, where the depletion voltage is applied. The principle of operation is sketched in Fig. 9.7.

CCDs have been used for tracking devices in the past. The spatial resolution is excellent and the charge collection very homogeneous. On the other hand, the charge collection efficiency is smaller then with other techniques, the radiation hardness has still to be proven and the vendor choice is very limited.

9.3.2.4 Depleted p-Channel Field Effect Transistors

In *depleted p-channel field effect transistors* (DEPFET) [152] the free charge generated in the totally depleted n-type substrate is collected at an internal n^--gate, which is situated under an integrated p-channel transistor. There they modulate the current in the transistor. The depletion voltage is applied from the opposite side.

DEPFETs have a very low noise and a good S/N. The readout is non-destructive, thus repetitive readout is possible. A good photon detection efficiency is possible, the charge collection is homogeneous and the sensors are radiation hard. However, the production process is complicated, expensive and currently not commercially available.

9.4 Optimising of the Design Parameters of the TESLA Vertex Detector

9.4.1 General Strategy

Key parameters for the VTX performance are e.g. the impact parameter resolution, the charge collection efficiency or the signal-to-noise ratio. Thereof, the impact parameter resolution can be customised with the help of simulation studies. Hence it is an important parameter for optimising the VTX design, but it picks out only

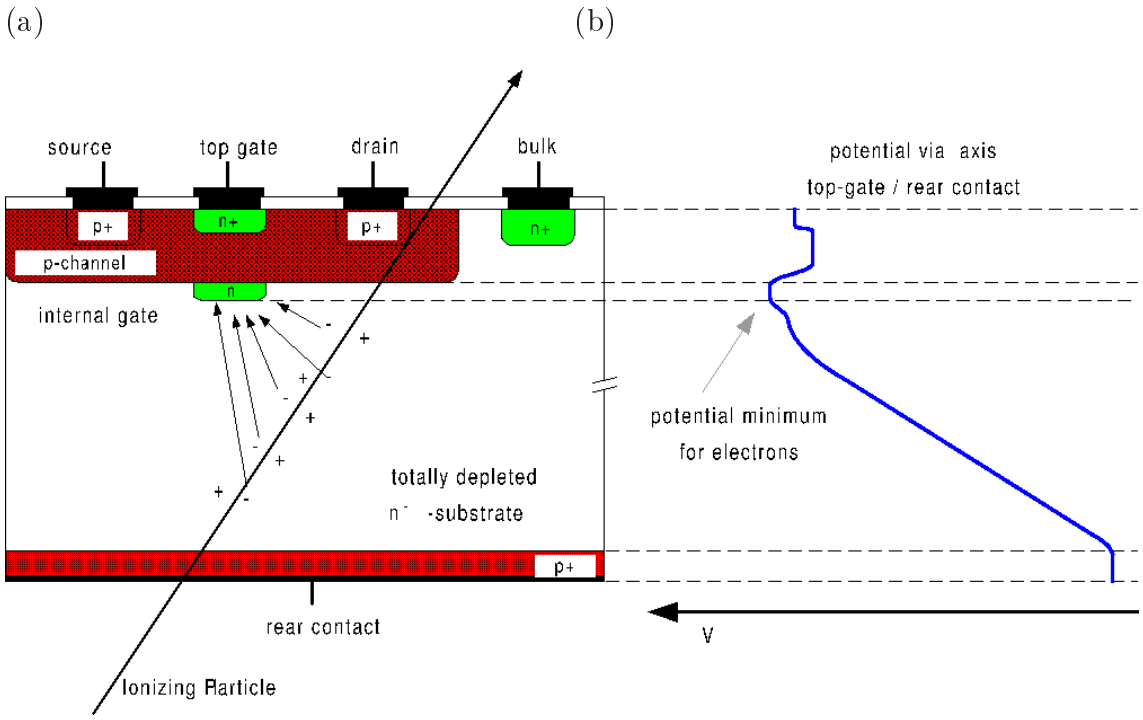

Figure 9.8: Schematic charge collection and potential in a DEPFET sensor
(a) The free electrons are collected at the *internal gate*, where (b) the potential has a local minimum. The transistor channel current from the *source* to the *drain* is modulated by the electric field from the electrons. The pixel is switched on and off by the external *top gate*. The collected charges are removed by switching the connector indicated as *bulk* to *clear*. The sensor is depleted by applying a voltage at the *rear contact*.

one property of one track in a high-energy physics event. To really say something about physics capabilities, a higher stage of reconstruction complexity with more information has to be evaluated, which implies physics interpretations of the reconstructed data. In case of the VTX this stage is represented by a full heavy flavour identification (*heavy flavour tagging*), whose performance is strongly influenced by the impact parameter resolution. However, the heavy flavour tagging typically uses the tracking system only. Only when the effects of other subdetectors are fully taken into account within the framework of a complete analysis, the intrinsic impact of varying VTX designs can be estimated realistically. For this purpose the t-quark production process $e^+e^- \to Z^0/\gamma^* \to t\bar{t}$ at a CMS energy of 500 GeV was chosen in this study.

The signal and the background processes considered are described in the following and the simulation and reconstruction tools used are explained. Finally the analysis

and its outcome are described.

9.4.2 The Signal Process $e^+e^- \to t\bar{t}$

The t-quark is the heaviest fermion in the Standard Model, and all experimental results indicate that it behaves exactly as expected of a third generation SM quark of charge $+2/3$. In particular the direct measurements of its mass by the TEVATRON experiments CDF and D0, yielding a combined result for its mass of 178.0 ± 4.3 GeV [4], are in excellent agreement with earlier extrapolations of electroweak measurents at LEP and SLC[5] [153]. Its large mass close to the expected scale of the electroweak symmetry breaking makes the t-quark particularly interesting [143]. It is likely to play a key role in revealing the origin of electroweak symmetry breaking and in solving the flavour problem. High-precision measurements of its properties and interactions are therefore mandatory at a future collider.

At TESLA the t-quark is mainly produced pairwise in the annihilation process $e^+e^- \to Z^0/\gamma^* \to t\bar{t}$. Further production mechanisms like $Z^0\gamma \to \nu_e\bar{\nu}_e t\bar{t}$, $W^+W^- \to t\bar{b}\bar{\nu}_e e^-$, $Z^0Z^0/e^+e^-\gamma\gamma \to e^+e^-t\bar{t}$ can be neglected here. The production cross section at a CMS energy of 500 GeV is expected to be about 0.6 pb. Thus, TESLA would be e "top-factory" with about 70 $t\bar{t}$-events expected per hour. The t-quark decays rapidly ($\tau \approx 10^{-24}$ s) before it hadronises and almost exclusively through the single mode $t \to bW$. The process is pictured in Fig. 9.9. The two b-quarks result in two

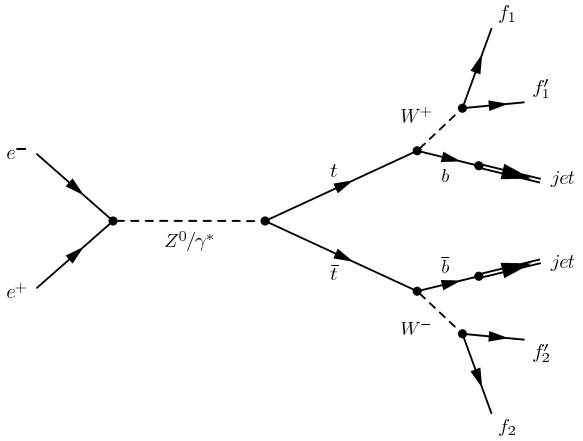

Figure 9.9: Feynman diagram of t-quark pair production at TESLA
Only the decay $t \to bW$ is considered. f_i and f_i' with $i = 1, 2$ denote all possible fermion combinations from the W-boson decays.

hadronic jets. Depending on the W-boson decays, three final states occur:

[5] Stanford Linear Collider at the Stanford Linear Accelerator Center (SLAC)

- six jets (46%): Both W-bosons decay hadronically.
- four jets + $l\nu$ (44%): One W-boson decays hadronically, one leptonically (missing energy from neutrino).
- two jets + $l_1\nu_1$ + $l_2\nu_2$ (10%): Both W-bosons decay leptonically (missing energy from two neutrinos).

In this analysis, the attempt was made to recontruct the $t\bar{t}$ final state from the all-hadronic (six jets) decay channel as descibed in 9.4.5.

9.4.3 The Fast Detector Simulation and Reconstruction Program SGV

For physics analyses within the TESLA detector framework, usually the programs BRAHMS[6] [154] and SIMDET [155] are used. BRAHMS is a full simulation and reconstruction package based on GEANT 3.21 [115]. It provides a detailed detector description and a sophisticated reconstruction toolkit including calorimeter tracking and energy flow anaylsis. However, it is slow and difficult to use for detector design studies. SIMDET is a fast simulation, which relies on parametrisations of the BRAHMS output. It is fast, but the parametrisations have to be regenerated for every new detector configuration by running BRAHMS first. So, even this is of limited use for detector design studies.

SGV[7] [156] is "a fast and simple program for simulating high energy physics experiments at colliding beam detectors" [157]. It was originally developed for and used within the DELPHI experiment, and extensions for TESLA studies exist. It is fast and contains a complete analysis chain from event generation to reconstruction. The detector geometry description is very much simplified, and it is easy to understand ("human readable") and to modify[8]. In addition, different detector descriptions can be treated simultaneously. Therefore it is an excellent tool for a first detector design.

In the following, the functioning principles of SGV are described. Then the implementation of the neural network based heavy flavour tagging is introduced, which originally was not incorporated in SGV.

[6] Beph (the second letter of the hebrew alphabet) reconstruction and analysis helpful montecarlo software

[7] Simulation a grande vitesse

[8] An example is given in App. H.

9.4.3.1 Simulation and Reconstruction

SGV does not simulate detector responses, but rather tracks the particles through the detector and calculates the reconstructed quantities from the given resolutions of the hit detector elements including material effects (multiple scattering), extrapolation effects and Gaussian smearing. Also photon conversion, bremsstrahlung and merging of calorimeter clusters are taken into consideration. No pattern recognition or shower development simulation is performed, which speeds up the processing significantly. In this sense SGV simulates also the reconstruction step. The output of this procedure are track helices, covariance matrices and calorimeter clusters.

In addition, SGV provides an analysis toolkit containing e.g. vertex reconstruction (using algorithms from the Delphi experiment), jet finding (as implemented in PYTHIA), event shape variables and impact parameters. To cope with the capabilities of the VTX and the special requirements of this work, a high-performance heavy flavour tagging was incorporated into SGV, which is described in 9.4.3.2.

Currently SGV uses the generators PYTHIA 5.7/JETSET 7.4 [158], PYTHIA 6 [106, 159] or SUSYGEN [160] to simulate high-energy physics events. In this study, the events samples were generated by PYTHIA 6.2.

The detector geometry is fed into SGV from "human-readable" plain text files. The possible detector configurations are very simple. Only cylinders in parallel with the beam axis and planes perpendicular to the beam axis are used, which can be segmented depending on the azimuthal angle. Detector elements are characterised by:

- the detector type: tracking detectors, calorimeters, taggers, scintillators or dead material,
- their geometrical properties: locations and dimensions,
- material properties: thicknesses in units of X_0 and atomic numbers A,
- spatial and energy resolutions,
- efficiencies and measurement thresholds.

For silicon tracking detectors, the spatial resolution also depends on the angle of incidence. The energy resolution of calorimeters depends on the particle energy. Impacting particles are treated either as *minimum ionising particle* (MIP), electromagnetic or hadronic shower depending on the particle type. As a starting point of this study, a detector description based on the TESLA TDR [145] was used with the specifications of the MIMOSA 5 sensor (see Tab. 9.2) for the VTX. Besides the five-layer geometry (s. Tab. 9.1) including material from e.g. cooling and mechanical support, the used parameters were:

- sensor material: silicon ($A = 14$) of a thickness of 0.015% of X_0,
- point resolution: 1.5 µm in $r - \phi$ and z,
- no restrictions on efficiency and measurement threshold.

9.4.3.2 Neural Network Based Heavy Flavour Tagging

The major task of a vertex detector is to reconstruct the primary and further vertices of a high-energy physics event. The reconstruction of secondary vertices is particularly important for heavy flavour tagging. This, in turn, is essential for the identification and reconstruction of the actual physics process, especially in the regions of interest of a future linear collider like e.g. t-quarks , Higgs physics and SUSY. Only the best possible reconstruction of those processes leads to precision measurements and this is exactly, what a future linear collider will be built for. So, a highest-performance heavy flavour tagging is desired for TESLA applications and the actually used neural network based package [161] is a promising candidate to fulfill the requirements. This package was originally not incorporated in SGV. It was inherited from BRAHMS and the performance of the implementation was tested by comparing it to existing studies on BRAHMS [162]. The heavy flavour tagging package combines three approaches to identify heavy flavour quarks, which are described in the following.

Impact parameter joint probability tag

The impact parameter joint probability tag was introduced by the ALEPH collaboration [163]. It uses the impact parameter information of each charged track in a jet to determine the probability, that the track is consistent with coming from the primary vertex.

The impact parameter d_0 is the distance of closest approach of a track to the primary vertex, measured in the azimuthal ($r\phi$) plane. It is signed according to whether the track helix intersects the jet axis in that plane in front of (positive) or behind (negative) the primary vertex[9]. This distinction is illustrated in Fig. 9.10. The impact parameter significance x_d is defined as

$$x_d = \frac{d_0}{\sigma_{d_0}}\,, \tag{9.4}$$

where σ_{d_0} is the estimated error on d_0 calculated from the track and primary vertex covariance matrices. While the impact parameter significances of tracks from the primary vertex $f(x)$ are expected to be distributed symmetrically around zero

[9] In this sense the locations "in front" and "behind' are given with respect to the opposite flight direction of the jet particles.

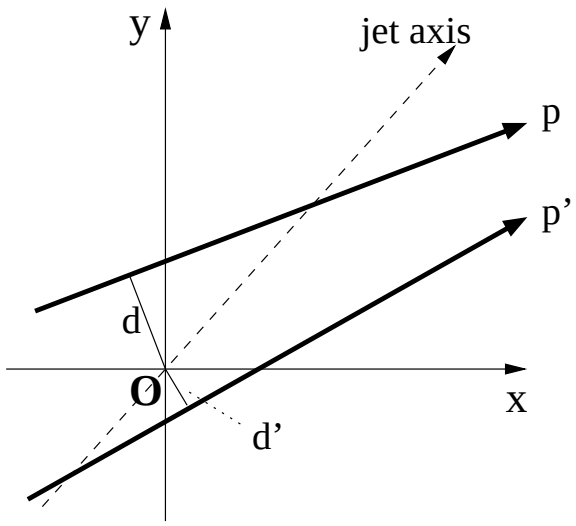

Figure 9.10: Illustration of impact parameter signing
A projection onto the x-y-plane is shown. Particle flight directions are indicated by arrows. The jet axis meets the primary vertex O. Particle p crosses the jet axis in front of O and has a positive impact parameter d. Particle p' crosses the jet axis behind O and has a negative impact parameter d'.

reflecting the finite detector resolution, tracks from secondary vertices tend to positive values. This is the case especially for tracks from heavy flavour decays. Fig. 9.11(a) shows such a distribution from a sample of simulated $e^+e^- \rightarrow q\bar{q}$ events[10]. It is easily realised, that on the positive side the fraction of tracks from b-decays increases with increasing significance. On the negative side this fraction is stable. Generally, the contamination from secondary vertex tracks is low for the negative side of the x_d-distribution. Since $f(x)$ is expected to be symmetric, it therefore is determined using tracks with negative impact parameter significances only. In this analysis it was obtained by fitting the negative part of the distribution with a Gaussian centered at zero and two exponential tails as shown in Fig. 9.11(b). The excess of tracks with high positive x_d is clearly seen.

After obtaining $f(x)$, the probability P_i, that a track i from the primary vertex has a positive impact parameter significance greater than x_0 is given by

[10]The sample for all heavy flavour tagging studies was generated and reconstructed with SGV using PYTHIA 6.2 with final state radiation. $e^+e^- \rightarrow t\bar{t}$ was ignored. The only requirement on the events was, that they needed to have more than 6 tracks. Jets were reconstructed using the "Durham" algorithm as implemented in PYTHIA, which corresponds to the k_T-algorithm described in 6.2.1.

(a) (b)

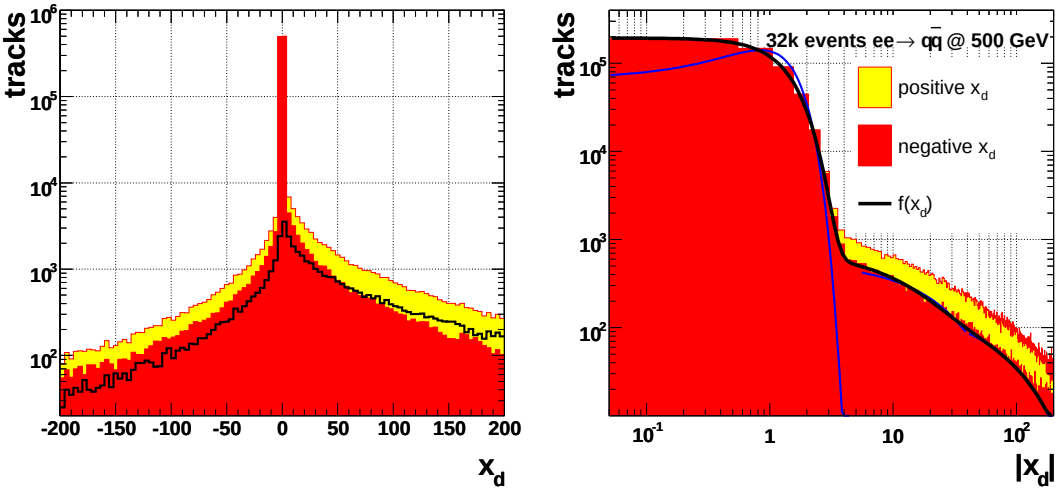

Figure 9.11: Impact parameter significances ($r\phi$)
Only tracks with impact parameters smaller than 2 mm in $r\phi$ as well as in z and with a sufficient number of hits in the tracking detectors are considered. (a) Impact parameter significance ($r\phi$) x_d for all tracks (yellow area), tracks from b-hadron decays (black line) and tracks not from b-hadron decays (red area). (b) x_d for all tracks with positive x_d (yellow area) and $|x_d|$ for all tracks with negative x_d (red area) with fitted $f(x)$ (black line).

$$P_i = \frac{\int_{x_0}^{\infty} f(x)dx}{\int_{0}^{\infty} f(x)dx}\,, \tag{9.5}$$

and the corresponding joint probability P_J, that an ensemble of n tracks comes from the primary vertex is

$$P_J = y \sum_{m=0}^{n-1} \frac{(-\ln y)^m}{m!}\,, \tag{9.6}$$

with

$$y = \prod_{i=1}^{n} P_i\,. \tag{9.7}$$

Ideally, light quark (uds) jets should give a flat distribution of P_J, while b-jets (and to some extent also c-jets) should peak at zero. Fig. 9.12 shows the P_J-distributions of the used sample for impact parameters in $r\phi$, z and three dimensions. The peaks

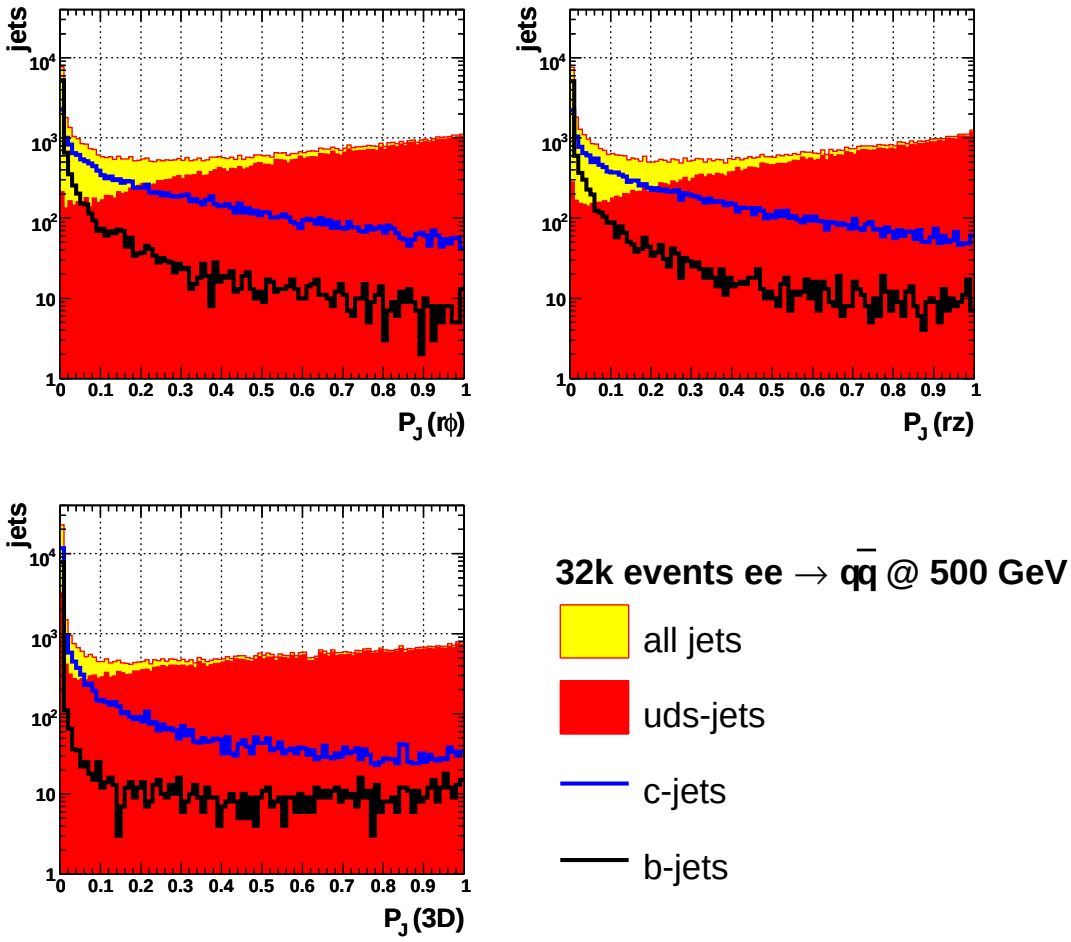

Figure 9.12: Each plot contains the distribution for all jets (yellow area), *uds*-jets (red area), *c*-jets (blue line) and *b*-jets (black line). The distributions are shown for the two-dimensional impact parameters in $r\phi$ (top-left) and in rz (top-right) and for the three-dimensional impact parameter (bottom-left). Each plot contains the distribution for all jets (light shaded area), *uds*-jets (dark shaded area), *c*-jets (grey line) and *b*-jets (black line).

at zero for heavy flavour jets are clearly seen in all three distributions. Also *uds*-jets show a small spike at zero, which originates from K_s- and Λ-decays, which could be vetoed by looking for two-track vertices with compatible masses. Anyway, the two-dimensional impact parameter significances give a better separation than the three-dimensional one, which is discarded for the neural network.

Topological vertex reconstruction

The topological vertex reconstruction algorithm ZVTOP was developed by the SLD[11] collaboration [164] to fully exploit the capabilities of its high-resolution vertex detector. ZVTOP searches for vertices in the three-dimensional coordinate space rather than in track combinations, which becomes impractical for high track multiplicities. Excellent *b*- and also *c*-tagging performance was proven with this algorithm [165].

In ZVTOP each track is represented by a "probability tube" in space, which is a three-dimensional unnormalised Gaussian probability density $f_i(\vec{r})$ derived from the helix parameters of track i. In order to decide which vertex is the primary and to constrain it to be consistent with the IP, also the IP is described by a probability density $f_0(\vec{r})$, which usually is simply a Gaussian ellipsoid centered at the IP. A "vertex density" is then formed from the track[12] probability densities, which is high in regions where many tracks overlap (vertices). One approach to calculate the vertex density $V(\vec{r})$ is

$$V(\vec{r}) = \sum_{i=0}^{n} f_i(\vec{r}) - \frac{\sum f_i^2(\vec{r})}{\sum f_i(\vec{r})}\,, \tag{9.8}$$

where the first term is a measure of multiplicities and the degree of overlap and the second term guarantees $V(\vec{r}) \simeq 0$, if $f_i(\vec{r})$ is significant for only one track. A descriptive two-dimensional example is pictured in Fig. 9.13. To resolve two vertices at $\vec{r}_1$ and $\vec{r}_2$, the minimum V_{min} on the line between $\vec{r}_1$ and $\vec{r}_2$ is determined. The vertices are resolved, if

$$\frac{V_{min}}{\min\left(V(\vec{r}_1), V(\vec{r}_2)\right)} < R_0\,, \tag{9.9}$$

with the tunable parameter $R_0 = 0.6$. One vertex is found at the IP in any case. To each vertex found a unique subset of tracks is associated from the list of overlaps. The vertices are then refitted using the track subsets after removal of tracks, which fit badly with the vertex. Finally an attempt is made to reattach unassociated tracks to the nearest vertex in order to reconstruct e.g. one-prong *B*-decays by assigning the isolated track to the subsequent *D*-decay vertex. In this analysis, ZVTOP was run on jets rather than on whole events or event hemispheres. Two-prong vertices with

[11] SLAC large detector

[12] Since the IP probability density is treated similar to the track probability densities, "track" in this context includes the IP.

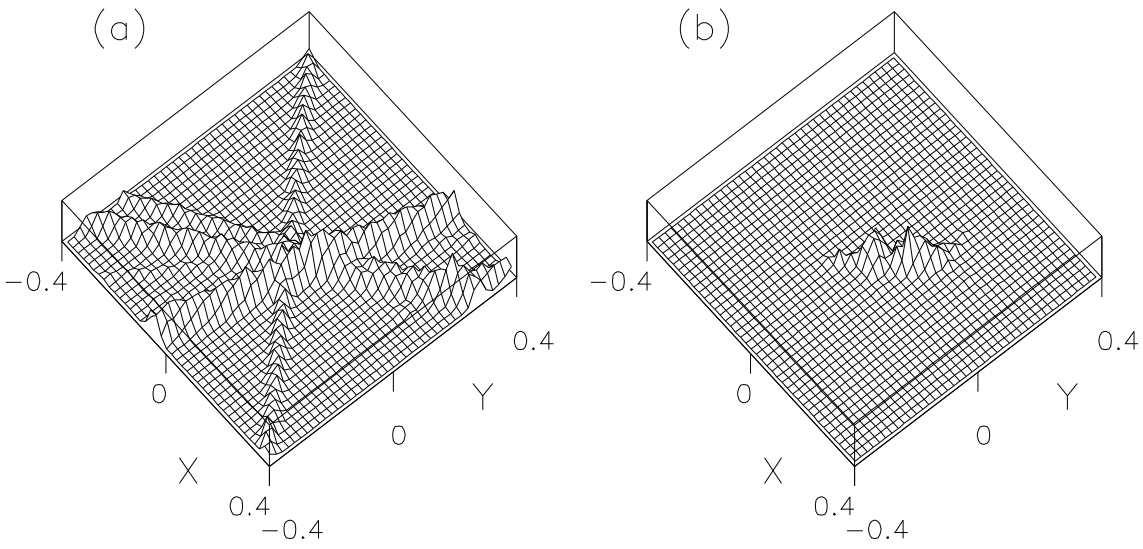

Figure 9.13: The ZVTOP reconstruction concept
A two-dimensional example is shown with arbitrary scales. (a) Tracks are represented by Gaussian tubes of the track probability densities $f_i(\vec{r})$. (b) Vertex probabilities are calculated $V(\vec{r})$, which are greater than zero only in regions where tracks overlap. In this example, the resulting primary (left) and secondary vertex (right) are easily distinguished.

an reconstructed mass of $0.47\,\mathrm{GeV} < m_{corr.} < 0.53\,\mathrm{GeV}$ were rejected to suppress contributions from K_S-decays.

The resulting jet vertex multiplicities are shown in Fig. 9.14(a). Most *uds*-jets have only one vertex – the primary vertex – reconstructed. The jets with two or more vertices are quite pure in heavy flavour decays and a significant number of *b*-jets has three or more vertices reconstructed, which reflects the tertiary vertices from the subsequent *D*-decays. To distinguish *b*- from *c*-jets, the mass of the secondary vertices is calculated including also the tertiary vertices, if present. A correction on the estimated missing invariant mass from neutral products of the *B*- and *D*-decays is applied, which is based on the difference between the vertex momentum vector direction calculated from the visible decay products and the spatial vector of the secondary vertex ("p_T"-correction). The obtained mass distribution is shown in Fig. 9.14(b). For high masses a good purity of *b*-jets is visible as well as the small contamination of the whole sample with *uds*-jets. The sharp cut-off for *c*-jets at around 2 GeV offers the possibility to distinguish *b*- and *c*-jets quite efficiently. Finally ZVTOP calculates a probability P_S, that all tracks assigned to the secondary vertex actually come from one common vertex. It is derived from the χ^2 of the vertex fit and is zero, if no secondary vertex was found in the jet. Fig. 9.15 shows the actual

(a) (b)

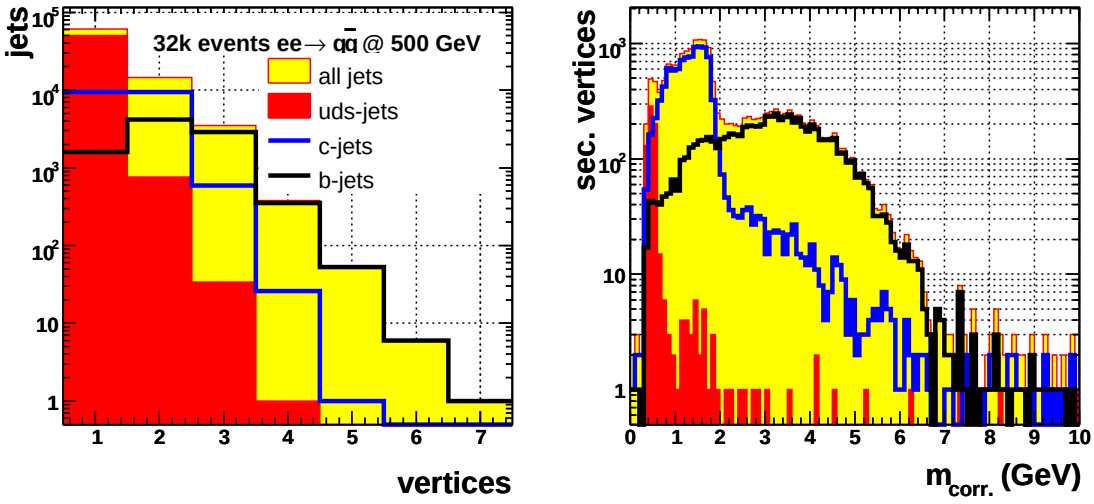

Figure 9.14: ZVTOP vertices and corrected secondary vertex masses
The distributions are shown for all jets (yellow area), *uds*-jets (red area), *c*-jets (blue line) and *b*-jets (black line). Jets with a two-track secondary vertex and an uncorrected secondary vertex mass consistent with a K_S-decay are excluded. (a) Number of vertices per jet found by ZVTOP. The primary vertex is found in any case. (b) p_T-corrected mass of secondary vertices (including tertiary vertex, if present).

probability distributions. The background from *uds*-jets is strongly suppressed, so that a high tagging purity can be achieved.

One-prong charm tag

This method [161] is not used to tag *c*-jets directly, but it is rather likely to be part of a neural network tag.

About half of the *c*-jets have only the primary vertex reconstructed (see Fig. 9.14(a)). However, around 40% of *D*-hadrons decay to only one charged track, so the presence of one single high-momentum track with large impact parameter might be useful to identify *c*-jets. This procedure was applied to jets with only one vertex reconstructed by ZVTOP. All tracks with a momentum larger than 2 GeV and hits in all VTX layers were considered as one-prong charm candidates and were sorted by their impact parameter significances in $r\phi$ (x_d) and rz (x_z). Tracks identified as coming from photon conversion or K_S candidates were removed. The latter were found by forming all two-track vertices from pairs of tracks with $x_d > 3$, and accepting vertices with a $P_S > 1\%$, a radius of less than 2 cm and an invariant mass

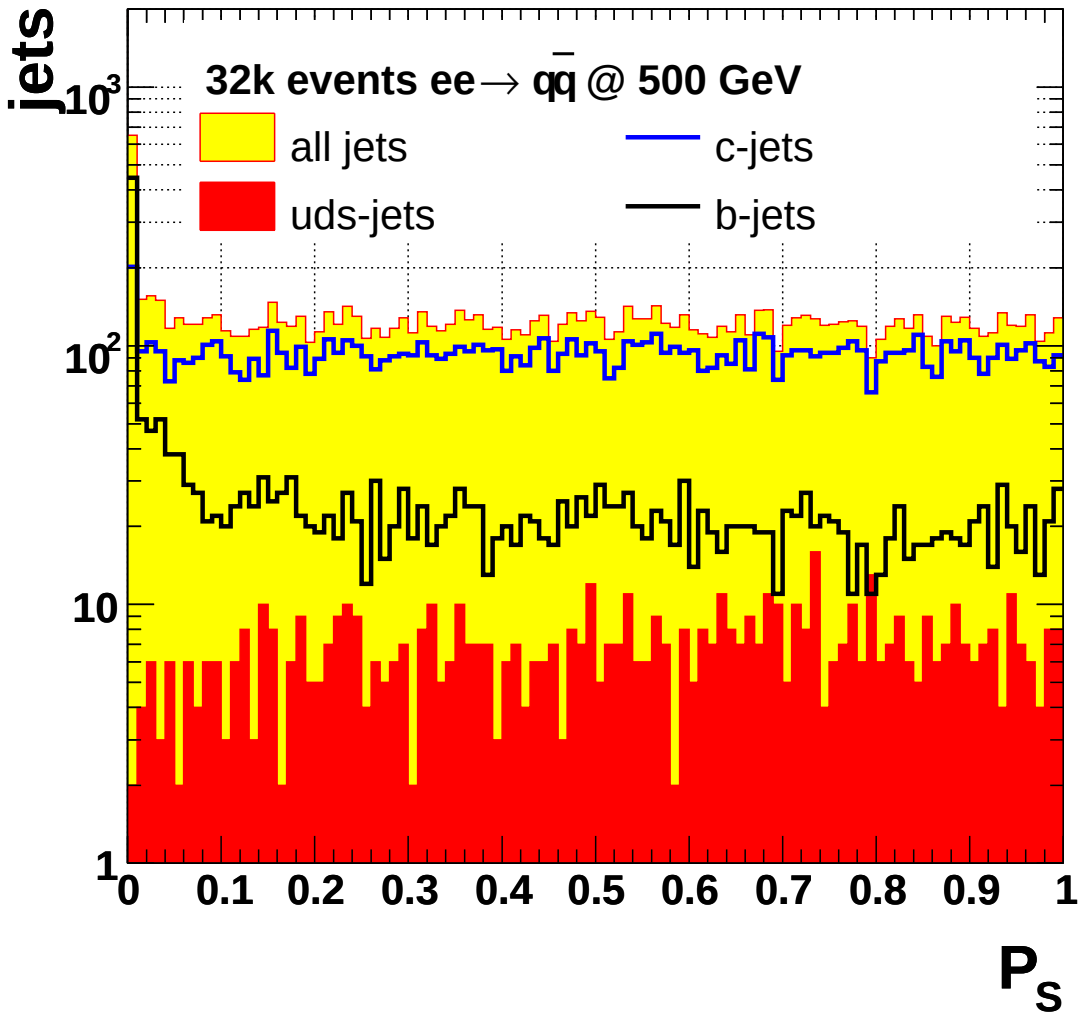

Figure 9.15: ZVTOP secondary vertex probability
Only jets with $P_S > 0$ are displayed for all jets (yellow area), *uds*-jets (red area), *c*-jets (blue line) and *b*-jets (black line).

satisfying $m < 0.02\,\text{GeV}$ for photon conversion or $0.475\,\text{GeV} < m < 0.525\,\text{GeV}$ for K_S-decays. The distributions of impact parameter significances are shown in Fig. 9.16. All distributions are dominated by tracks from c-jets for significances larger than five. However, while c-jets tend to have one single track of large impact parameter significance, b-jets typically also have a second track of large impact parameter significance. An efficient enrichment of the neural network tagging performance is thus expected.

Neural network heavy flavour tag
The neural network heavy flavour tag used in this analysis combines the output of the three independent methods described above. It provides the following output:

- a b-tag probability P_b^{NN} to find b-jets within a sample of hadronic jets,
- a c-tag probability P_c^{NN} to find c-jets within a sample of hadronic jets,
- a b-c-distinction tag D_{bc}^{NN} to separate b- from c-jets in the absence of backgrounds.

Depending on the number of found ZVTOP vertices, the events are split into three classes, which are treated differently. Tab. 9.3 lists the variable used for each class. Some variables were transformed such, that they fit the ranges $0 \leq x \leq 1$ or $-1 \leq x \leq 1$.

The neural network was implemented with the JETNET 3.1 package [166] and trained using five million jets from $e^+e^- \to q\bar{q}$ events. Figs. 9.17, 9.18 and 9.19 display its output. The heavy flavour probabilities for b- and c-jets show a clear distinction of the corresponding heavy flavour from the background. Due to the higher vertex mass and the larger secondary vertex reconstruction efficiency, the b-tagging is more efficient. This can be seen easily in Fig. 9.20, where the purity vs. efficiency for varying cuts on the tagging probabilities is shown. The curves show a better performance in b-tagging than in c-tagging for both, SGV and BRAHMS. On the one hand, the b-tagging performance is better in BRAHMS, which reflects the higher accuracy of its more sophisticated reconstruction. On the other hand, c-tagging is more challenging due to the higher requirements in the reconstruction accuracy. In this case the higher level of idealisation in SGV makes an impact and the performance is better than in BRAHMS.

However, the overall performance of heavy flavour tagging in SGV reached a level comparable to BRAHMS, which made it applicable to the present analysis.

9.4.4 Preselection of t-Quark Pair Production Events

The preselection of t-quark pair production was tuned with respect to the expected SM background to achieve a good purity vs. efficiency of the event sample before

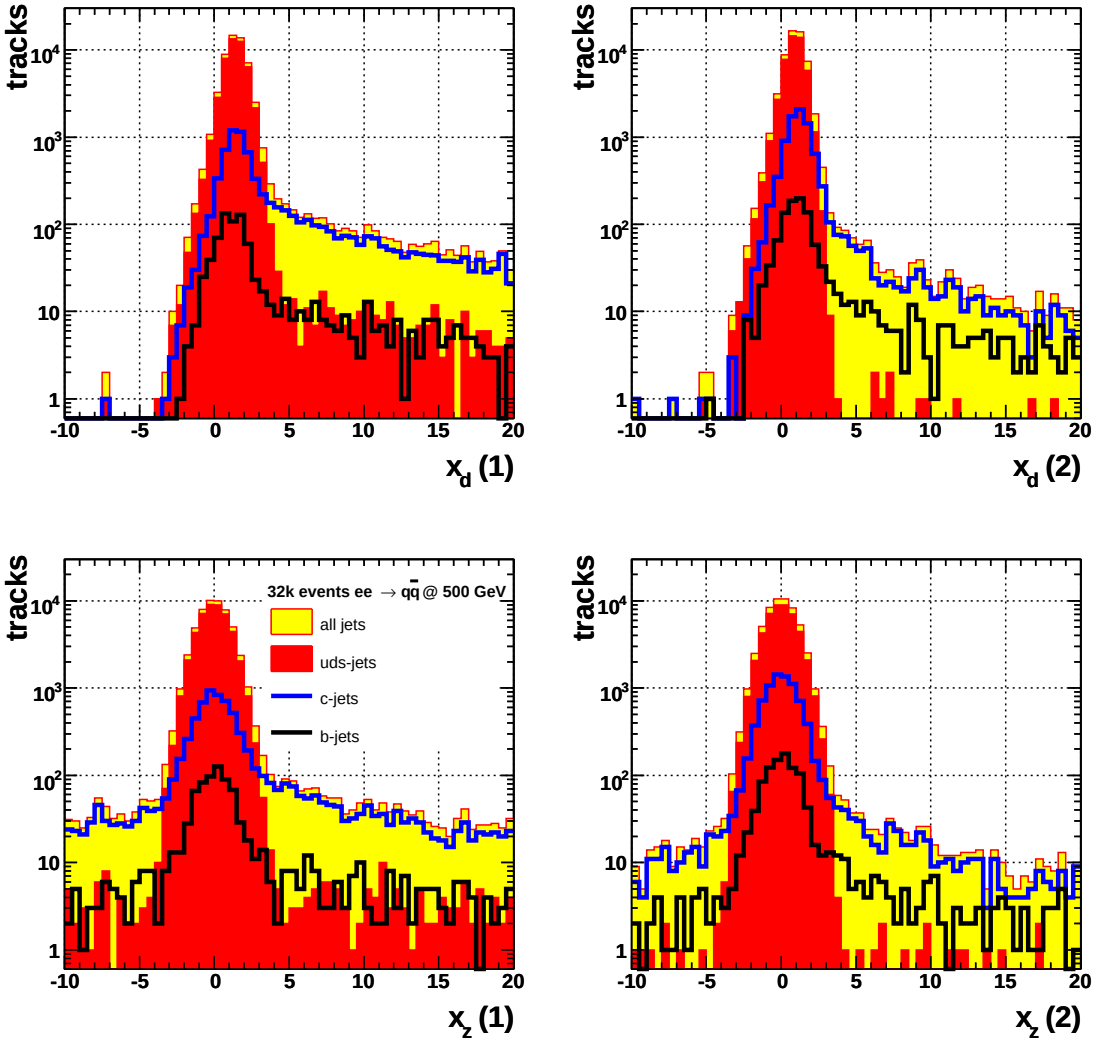

Figure 9.16: Impact parameter significances for one-prong charm tag The distributions are shown for all jets (yellow area), *uds*-jets (red area), *c*-jets (blue line) and *b*-jets (black line). Only tracks from jets with one ZVTOP vertex with $p^{trk} > 2\,\mathrm{GeV}$ hitting all VTX layers are considered. K_S- and photon conversion candidates were removed. First (upper-left) and second (upper-right) most significant track in jet ($r\phi$). First (lower-left) and second (lower-right) most significant track in jet (rz).

Class		≤1 vertex	2 vertices	≥3 vertices
Impact Parameter joint probablity tag	$P_j(r\phi)$	×	×	×
	$P_j(rz)$	×	×	×
One-prong charm tag	$x_d(1)$	×		
	$x_d(2)$	×		
	$x_z(1)$	×		
	$x_z(2)$	×		
	$p(1)$	×		
	$p(2)$	×		
	$\cos\theta(1)$	×		
	$\cos\theta(2)$	×		
ZVTOP	$S_{max} = (L/\sigma_L)_{max}$		×	×
	$L(S_{max})$		×	×
	$m_{corr.}$		×	×
	p		×	×
	n_{trk}		×	×
	P_S		×	×

Table 9.3: Variables used in neural network heavy flavour tag
The classes with two and with three or more vertices use the same set of variables, but with different weights. $p(1,2)$ are the momenta of the tracks with the largest impact parameter significance and $\theta(1,2)$ are their polar angles. L is the decay length measured by ZVTOP with the estimated error σ_L. S_{max} is the largest decay length significance and $L(S_{max})$ the corresponding decay length. p is the jet momentum, n the number of all tracks assigned to non-primary vertices.

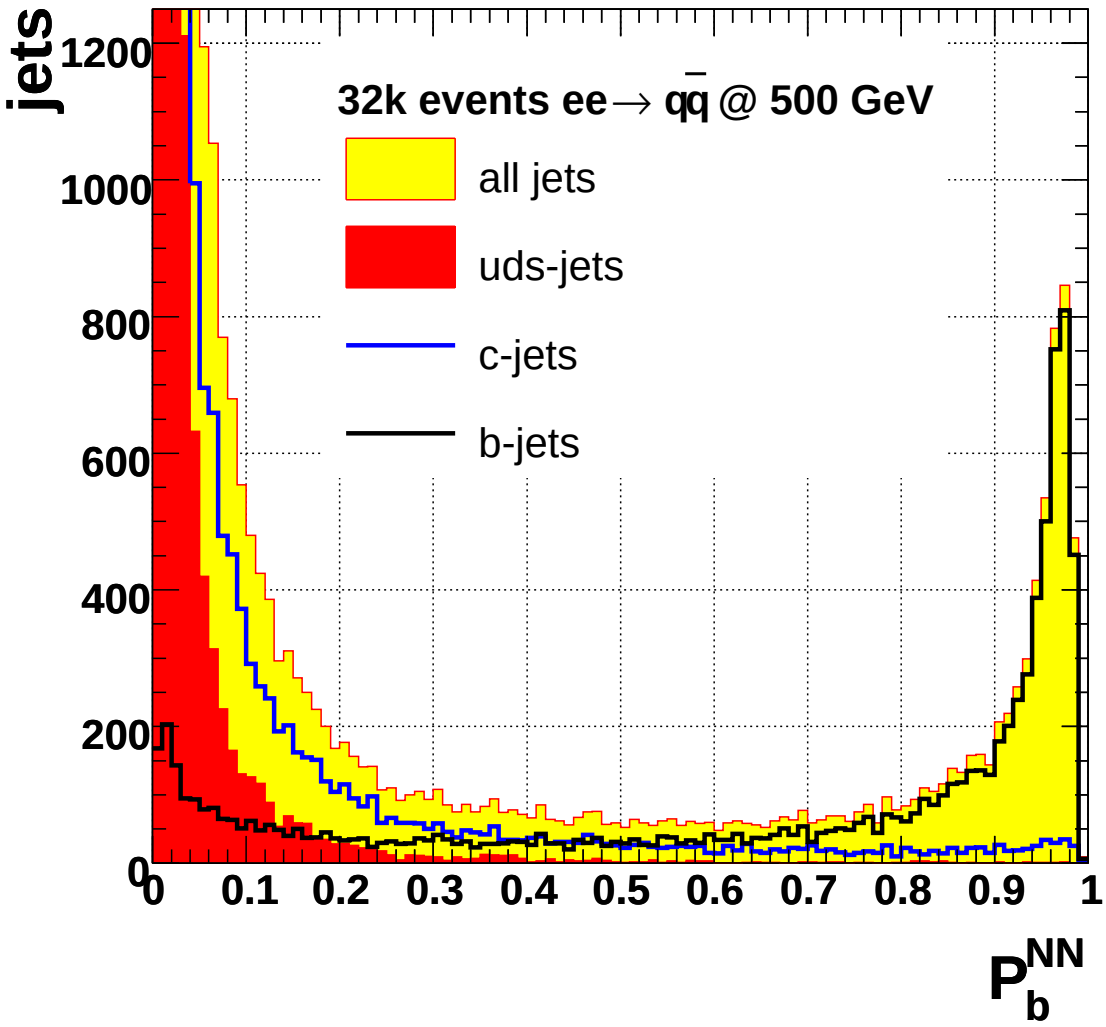

Figure 9.17: Neural network b-probability
Only jets with $P_b^{NN} > 0$ are displayed for all jets (yellow area), *uds*-jets (red area), c-jets (blue line) and b-jets (black line).

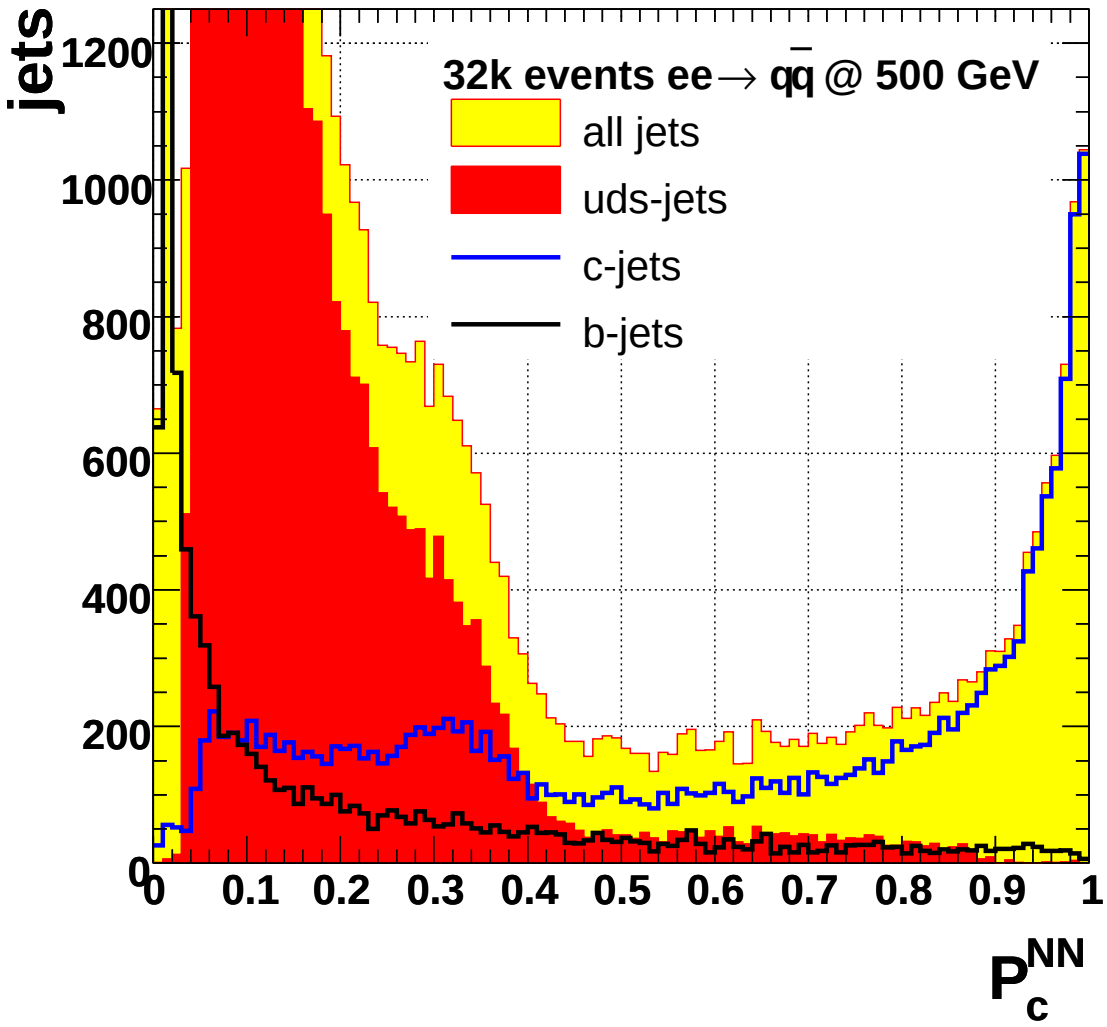

Figure 9.18: Neural network c-probability
Only jets with $P_c^{NN} > 0$ are displayed for all jets (yellow area), *uds*-jets (red area), c-jets (blue line) and b-jets (black line).

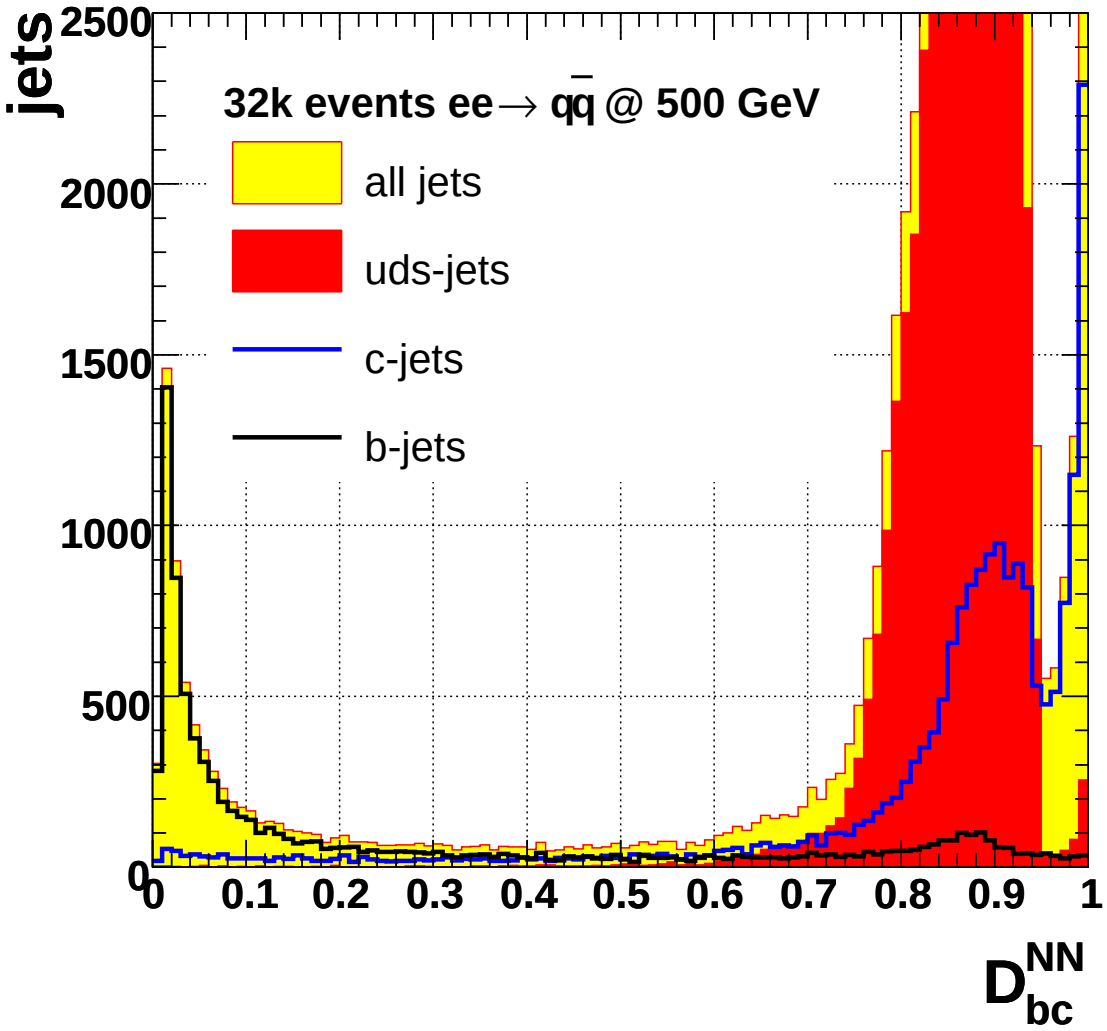

Figure 9.19: Neural network bc-distinctiom
Only jets with $D_bc^{NN} > 0$ are displayed for all jets (yellow area), uds-jets (red area), c-jets (blue line) and b-jets (black line).

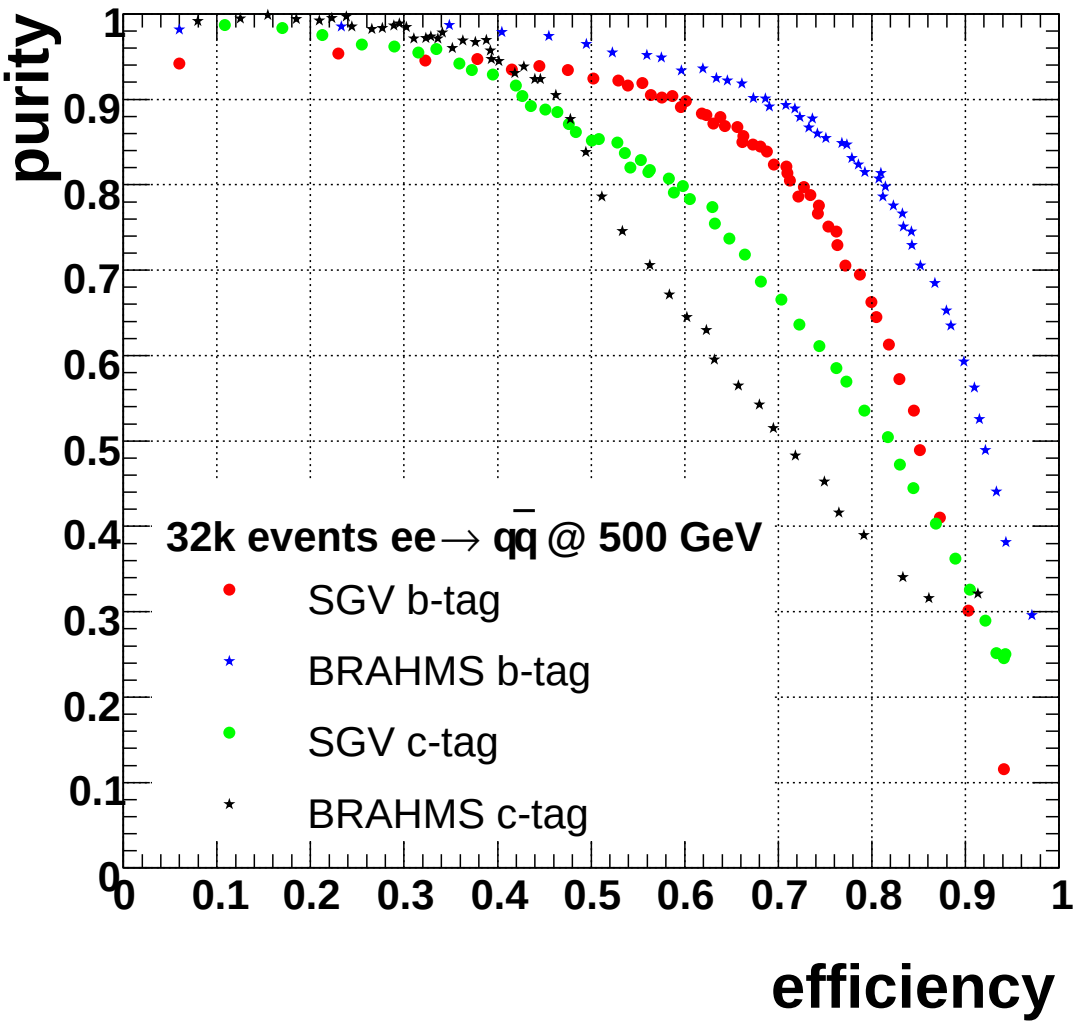

Figure 9.20: Neural network b- and c-tag purity vs. efficiency in SGV and BRAHMS
Results from varying cuts on P_b^{NN} for SGV (red dots) and BRAHMS (green stars) and on P_c^{NN} for SGV (blue dots) and BRAHMS (black stars).

b-tagging and t-quark reconstruction take place. The background arises mainly from other $q\bar{q}$-events and from the production of electroweak gauge boson pairs. Also lepton pair production, Bhabha scattering, prompt photons and PhP were considered. The complete list of the generated event samples is found in Tab. 9.4. The Bhabha process was treated in a special way in this context. Due to its very large cross section only a small test sample in terms of $\mathcal{L}_{int}$ was generated (one million events) to verify, if it was likely that such events would survive the preselection. It was found, that Bhabha processes are not expected to contribute to the selected event sample.

To reject the background, three distincting properties of $t\bar{t}$-events were exploited:

Number of tracks: The occurence of at least two hadronic jets in $t\bar{t}$-events results in a large number of reconstructed tracks compared to events, where mainly leptons form the final state.

Energy-momentum conservation and detected energy: The fraction of missing energy or momentum is expected to be rather small for $t\bar{t}$-events, since a certain amount of energy is carried by the "visible" b-jets in any case. This property can be used to reject events, where a significant energy fraction is carried by neutrinos or is not present in the main interaction due to initial state radiation, if the radiated photon escapes the detector through the beampipe.

Thrust: The *thrust*[13] T is defined as

$$T = \max_{|\vec{n}|=1} \frac{\sum_i |\vec{n} \cdot \vec{p}_i|}{\sum_i |\vec{p}_i|} \,, \tag{9.10}$$

with the momentum vector $\vec{p}_i$ of particle i [167]. The thrust axis is given then by the normalised vector $\vec{n}$, for which a maximum is attained. The allowed range is $0.5 < T < 1$, with a two-jet event corresponding to $T \approx 1$ and an isotropic event to $T \approx 0.5$. Hence a smaller thrust is expected from $t\bar{t}$-events than from all types of background processes except the production of weak gauge boson pairs.

The event properties listed above lead to the following requirements to be applied in the preselection:

- Number of tracks n^{trk}:

$$n^{trk} > 12 \,. \tag{9.11}$$

Fig. 9.21 shows the corresponding distributions after preselection. The tendency of signal events to larger numbers of tracks is visible.

[13] the maximum directed momentum

Process	Decay	σ (pb)	$\mathcal{L}_{int}$ (fb^{-1})	Preselection (%)
Z^0/γ^*	$t\bar{t}$ (signal)	0.5820	9.876	95.1
Z^0/γ^*	$d\bar{d}$	2.152	9.545	2.72
	$u\bar{u}$	2.410	11.08	4.05
	$s\bar{s}$	2.408	10.22	4.25
	$c\bar{c}$	2.396	9.956	4.42
	$b\bar{b}$	2.124	9.801	3.11
	e^+e^-	1.075	18.60	0.0
	$\mu^+\mu^-$	1.080	18.52	0.0
	$\tau^+\tau^-$	1.046	19.12	0.005
	$\nu_e\bar{\nu}_e$	0.8282	24.15	0.0
	$\nu_\mu\bar{\nu}_\mu$	0.8272	24.18	0.0
	$\nu_\tau\bar{\nu}_\tau$	0.8262	24.21	0.0
$Z^0/\gamma^* + \gamma$	$d\bar{d}$	1.132	11.22	2.64
	$u\bar{u}$	1.071	10.27	4.44
	$s\bar{s}$	1.136	10.18	2.78
	$c\bar{c}$	1.068	10.31	4.70
	$b\bar{b}$	1.123	10.86	2.81
	e^+e^-	0.4041	24.75	0.0
	$\mu^+\mu^-$	0.4036	24.78	0.0
	$\tau^+\tau^-$	0.4020	24.88	0.0
	$\nu_e\bar{\nu}_e$	0.4610	21.69	0.0
	$\nu_\mu\bar{\nu}_\mu$	0.4598	21.75	0.0
	$\nu_\tau\bar{\nu}_\tau$	0.4589	21.79	0.0
Z^0Z^0		0.5587	10.39	7.03
W^+W^-		7.678	10.48	3.99
Bhabha		$2.720 \cdot 10^5$	$3.676 \cdot 10^{-3}$	0.0
Prompt photons ($\gamma\gamma$)		8.238	12.14	0.0
PhP ($\gamma\gamma$)	ff	$3.554 \cdot 10^3$	2.814	0.0005

Table 9.4: Generated signal and SM background processes to $e^+e^- \to t\bar{t}$
The generator cross sections σ and the generated integrated luminosities $\mathcal{L}_{int}$ are shown as well as the preselection efficiency.

- Missing energy and momentum:

$$E > 100\,\text{GeV}, \tag{9.12}$$
$$E - p_z > 100\,\text{GeV}, \tag{9.13}$$
$$E + p_z > 100\,\text{GeV}, \tag{9.14}$$

  with the total measured energy E and the longitudinal energy imbalance p_z. Fig. 9.22 shows the corresponding distributions after preselection. In the distribution of the total energy, a spike is seen for background around 300 GeV. This is due to initial state radiation, where one of the incoming leptons radiates a photon, which carries a significant fraction of the initial energy. Since this photon is emitted in the flight direction of the lepton, it escapes the detector through the beampipe and the corresponding energy is not measured. In addition to the resulting energy deficit, this process provides an imbalance in the measured longitudinal momentum p_z. These events are typically characterised by a low value of either $E - p_z$ or $E + p_z$ and polar angles θ of the measured energy imbalance $\vec{p}$ close to the edge of the interval $[0, \pi]$. So, the 300 GeV-spike and the spikes around 0 and 2π in Fig. 9.23(b) are closely related. It is also seen, that the $t\bar{t}$-distribution peaks noticably below the CMS energy of 500 GeV. This is due to the significant fraction of lepton-neutrino pairs originated either from leptonic W-decays or from heavy flavour decays as e.g $B \to D^* l\nu$.

- Thrust:

$$T < T_0 \tag{9.15}$$

  or

$$\left(\frac{T - T_0}{T_1 - T_0}\right)^2 + \left(\frac{\theta - \pi/2}{\pi/2}\right)^2 < 1\,. \tag{9.16}$$

  $T_0 = 0.7$ and $T_1 = 0.9$ are the two parameters of this two-dimensional cut. In summary this cuts reject all events beyond an elliptical curve with $T = T_0$ at the edges of the θ-distribution ($\theta = 0, \pi$) and $T = T_1$ at $\theta = \pi/2$, as illustrated in Fig. 9.23(c). The ellipsoidal shape of the two-dimensional cut in Eq. 9.16 is clearly seen. T_0 and T_1 were tuned such, that the overall preselection efficiency for the $t\bar{t}$-signal stays greater than 95%.

The fractions of events passing the preselection cuts are listed in Tab. 9.4, last column. The achieved purity of $t\bar{t}$-events after the preselection is about 37.5%.

9.4.5 t-Quark Reconstruction

The BR of the all-hadronic decay mode of $t\bar{t}$-events is the largest ($\sim 44\%$). The reconstruction is straight forward, since no missing momenta are expected and no lep-

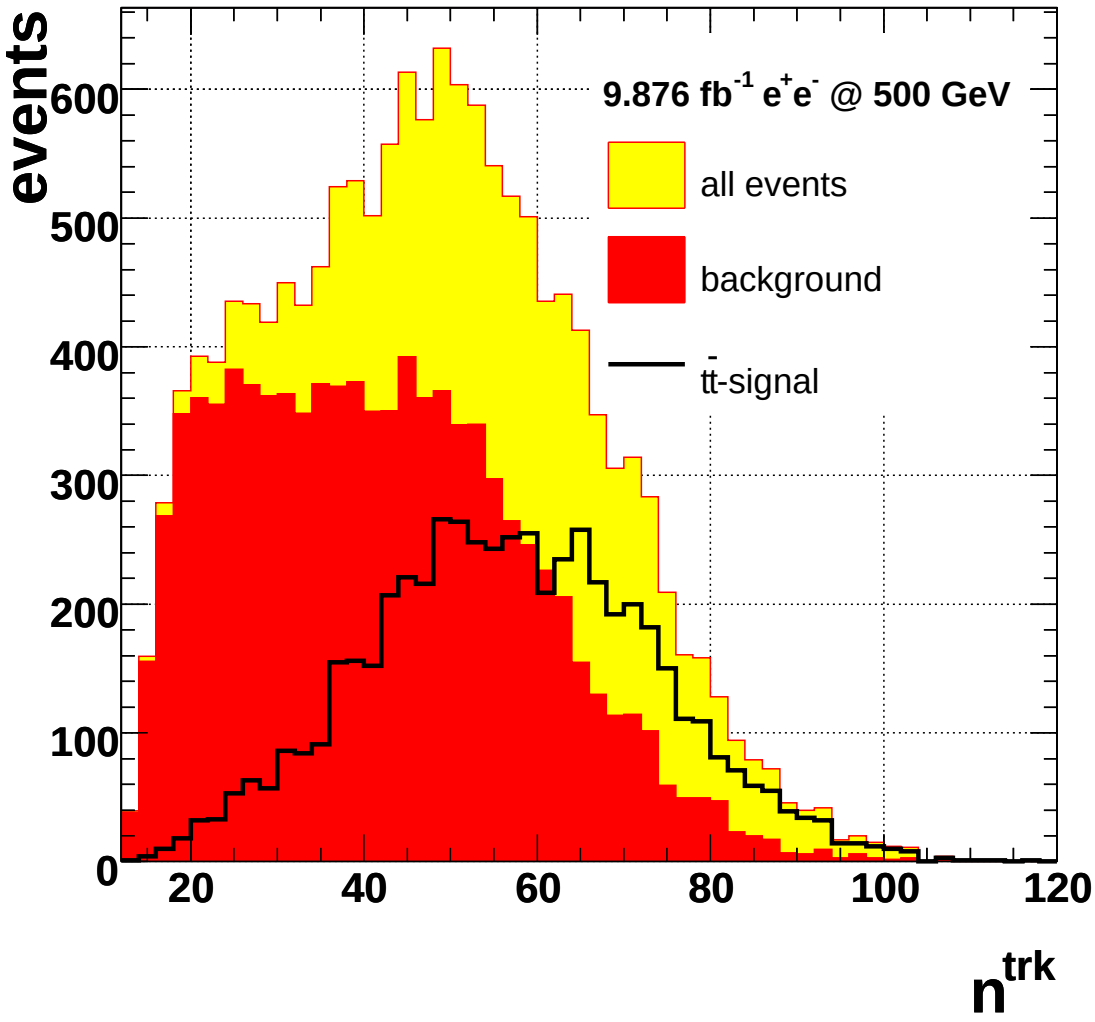

Figure 9.21: Number of tracks
All events (yellow area), background events (red area) and $t\bar{t}$-signal events (black line). The distributions show the number of tracks n^{trk} in the event. Only events fulfilling the preselection requirements are displayed.

(a)

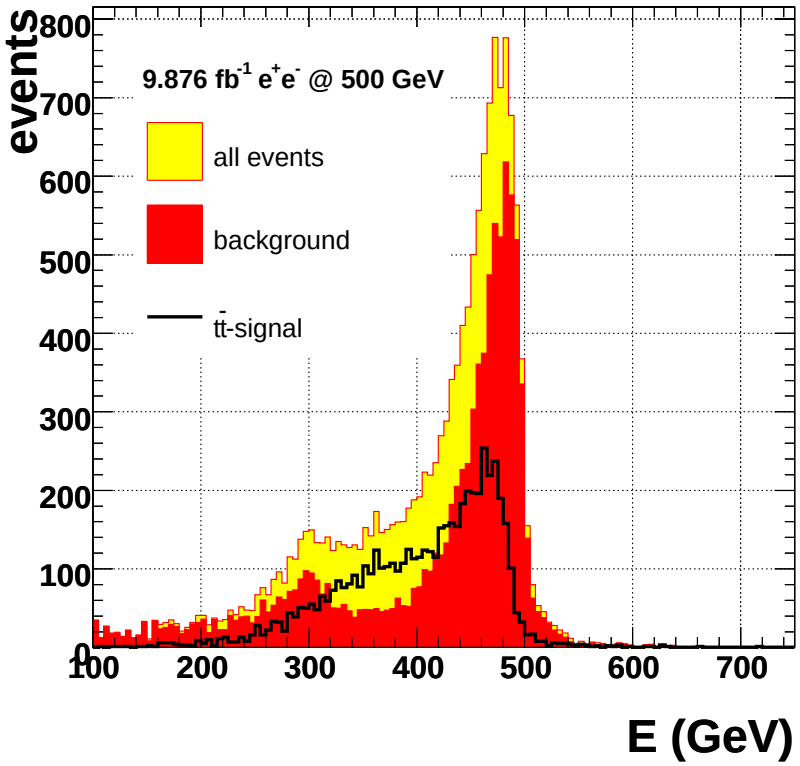

(b)

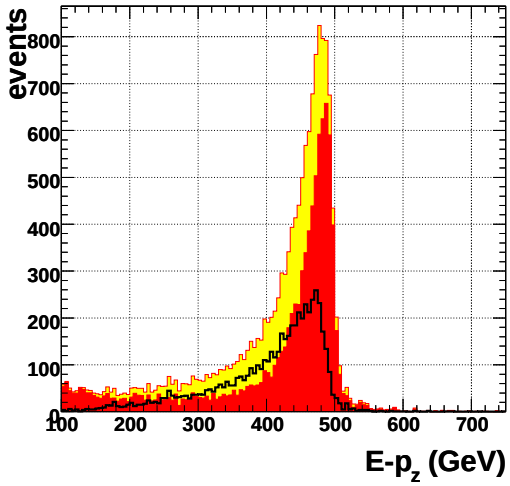

(c)

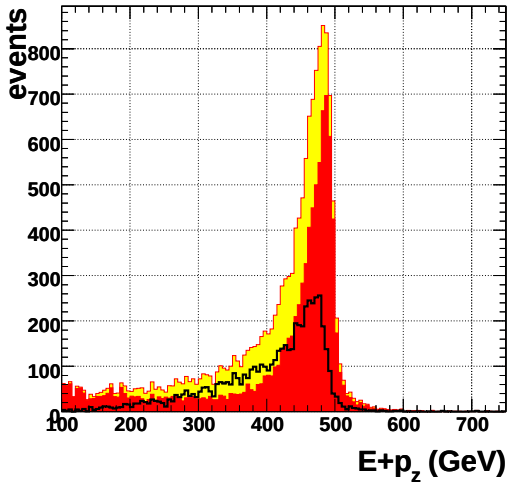

Figure 9.22: Missing energy and momentum
All events (yellow area), background events (red area) and $t\bar{t}$-signal events (black line). The distributions show (a) the total energy E measured in the event and the longitudinal energy imbalances $E - p_z$ (b) and $E + p_z$ (c). Only events fulfilling the preselection requirements are displayed.

(a) (b)

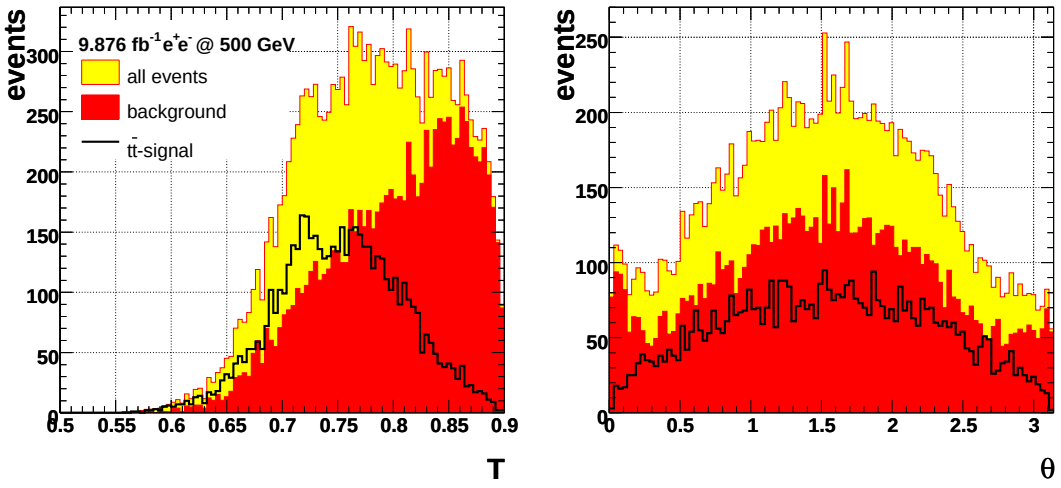

(c)

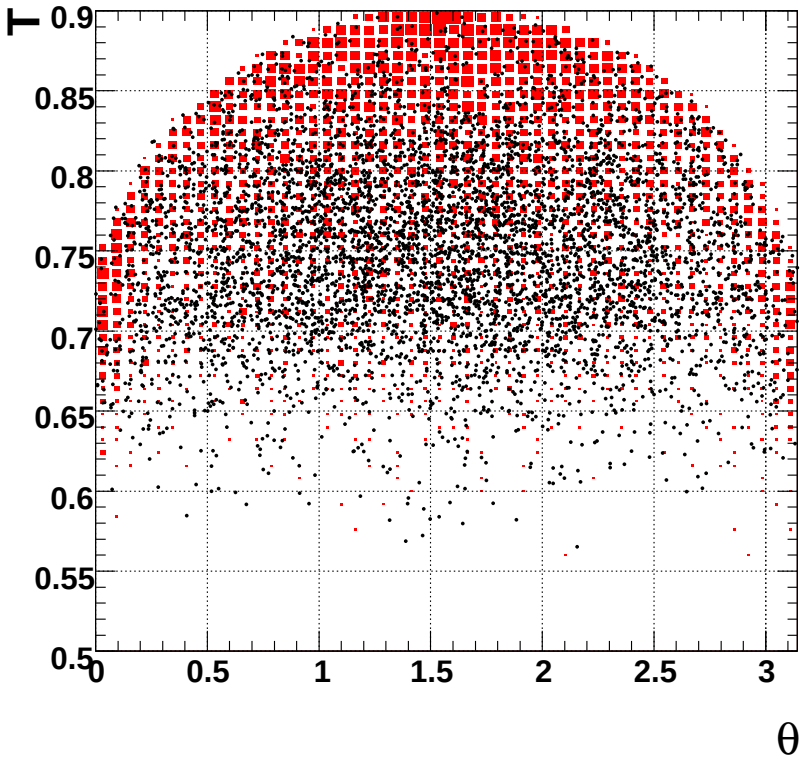

Figure 9.23: Thrust and polar angle
The one-dimensional distributions show (a) the thrust T and (b) the polar angle θ of the total energy imbalance vector $\vec{p}$ for all events (yellow area), background events (red area) and $t\bar{t}$-signal events (black line). (c) The two-dimensional distributions show T vs. θ, where the background is displayed in the red box histogram and the $t\bar{t}$-signal events in the black scatter plot. Only events fulfilling the preselection requirements are displayed.

ton identification is needed. The QCD background from multijet events is expected to be large (see 9.4.4), but it can be reduced significantly by requiring b-tagging. Therefore this is one channel suitable for vertex detector design studies.

9.4.5.1 Reconstruction Method

The reconstruction of the t-quark pole mass is known to be affected by many theoretical uncertainties in this channel. Generally, the extraction of the t-quark pole mass cannot be performed with a precision better than $\mathcal{O}(\Lambda_{QCD})$ [168]. In addition, especially the requirement that the invariant masses of two jet pairs are each consistent with the invariant mass of a W-boson leads to additional problems coming from the incomplete knowledge of the hadronic final state. On top of that, a significant uncertainty on the reconstructed t-quark mass may come from non-perturbative phenomena, which are expected to shift the reconstructed masses in W^+W^-- and $t\bar{t}$-production. Thus, any approach involving the reconstruction of the process $W \to q_1\bar{q}_2$ is bound to lead to a systematic shift in the reconstruction of the t-quark mass.

In this analysis, a simple reconstruction method not involving the direct reconstruction of the W-boson decay was used [169]. Since it has been used for the reconstruction of fully simulated $t\bar{t}$-events at TESLA before, the fast and the full simulation could also be compared. The method is very general and suitable for the reconstruction of any process in which a particle V and an antiparticle $\bar{V}$ are produced and they decay as:

$$e^+e^- \to V\bar{V} \to v_a V_a v_b V_b \tag{9.17}$$

$$V_a \to V_1\bar{V}_2\,,\; V_b \to V_3\bar{V}_4\,, \tag{9.18}$$

without prior knowledge of the masses of the intermediate particles V_a and V_b. The effectiveness of this method is based on the assumption that the initial-state particles V and $\bar{V}$ have similar (but not equal) masses, and on momentum conservation. These two requirements, together with the fact that both initial particles decay into three other particles, are essential for the reconstruction of the invariant masses of V and $\bar{V}$ through six jets in the final state. After the preselection of events with six hadronic jets, which is described later in this section, one starts with the list of these six jets and their momenta p_i. The jets are merged into two groups with three jets each and the summed momenta P_1 and P_2 and invariant masses M_1 and M_2. If one requires exactly one tagged b-jet in each group[14], there remain six possible pairs of three-jet groups in a $t\bar{t}$-event. In order to reduce the number of combinations further, the assumption on the similarity of the masses of the initially produced

[14]High purity and efficiency of the b-tagging are essential for this method.

particles is used:

$$|M_1 - M_2| < \Delta M\,, \tag{9.19}$$

where ΔM is an adjustable cut parameter. Momentum conservation is used to find combinations with a back-to-back topology:

$$\left|\vec{P}_1 + \vec{P}_2\right| < \Delta P\,, \tag{9.20}$$

where again ΔP is an adjustable cut parameter.

Using the full simulation, it has been shown, that this is a robust reconstruction procedure [169]. A reconstructed distribution of the t-quark mass centered at 176 GeV was obtained. The distribution was fit with a Breit-Wigner curve with a fixed width of 9.5 GeV convoluted with a Gaussian with its width used as free fit parameter. The Gaussian width was found to be 5.5 GeV in that analysis. These fit parameters were reference values for the actual analysis.

9.4.5.2 Monte Carlo Studies

In order to test, whether this reconstruction method is usable also within SGV, first some MC studies on jet properties had to be done. These studies were performed with an inclusive event sample[15], which passed the preselection described above. Jets were reconstructed using the "Durham" algorithm as implemented in PYTHIA.

The b-tagging performance is illustrated in Fig. 9.24(a,b). Its quality is similar to that of the b-tagging implementation study discussed in 9.4.3.2. The tendency to higher purities at high efficiencies (low cut values of P_b^{NN}) results from the lower fraction of contributing non-b-jets in the actual event sample. This is an effect of the additional preselection, which enriches the sample with $t\bar{t}$-events. It balances the negative impact of the additional background included in this sample and of the inclusion of initial state radiation. This negative impact is visible from the broader shape of the b-jet spike at large P_b^{NN}. In summary, the b-tagging performance appears to work well for the actual analysis. Figs. 9.24(c-e) show, that a two-dimensional cut in the P_b^{NN}-P_c^{NN} plane might work best. With the requirement $P_b^{NN} \geq 0.5 + 0.5(P_c^{NN} - 0.5)$ a purity of 85.9% could be achieved with an efficiency of 69.6%. This exceeds the capabilities of the pure cut on P_b^{NN} and reaches the performance of the BRAHMS b-tagging (see Fig. 9.24(b)) The distinction tag $D_b c^{NN}$ was not considered here, since it shows no remarkable effect within an inclusive sample.

A central issue of the actual analysis is to obtain the highest achievable purity of $t\bar{t}$-events in the sample. As already mentioned in 9.4.4, $t\bar{t}$-events are more isotropic

[15]"Inclusive" in this sense means: $e^+e^- \to Z^0/\gamma^*(+\gamma), Z^0Z^0, W^+W^-$, including initial and final state radiation. Further background listed in Tab. 9.4 was not considered here.

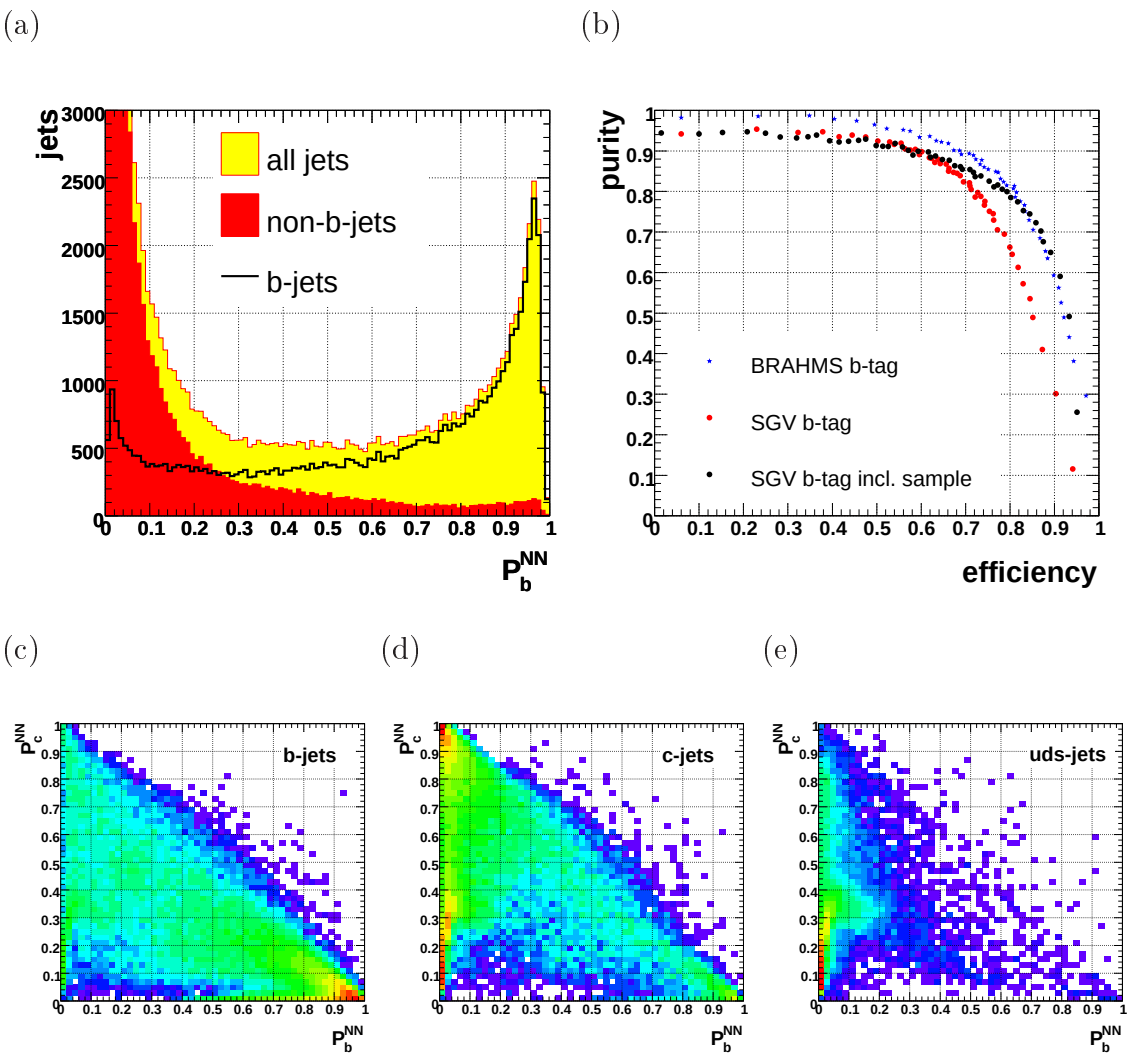

Figure 9.24: b-tagging performance in an inclusive SGV event sample
For the neural network b-probablity (a) only jets with $P_b^{NN} > 0$ are displayed for all jets (yellow area), non-b-jets (red area) and b-jets (black line). The neural network b-tag purity vs. efficiency (b) from varying cuts on P_b^{NN} is shown for the BRAHMS (blue stars) and SGV (red dots) performances taken from Fig. 9.20 and for the inclusive sample (black dots). The neural network c- vs. the b-probablities are shown for (c) b-jets, (d) c-jets and (e) uds-jets.

than the expected background events. This property has been exploited already by using the thrust in the preselection, which relies on the measurement of single particles. However, it is also expected to be seen in the spacial distribution of jets, since the six jets in the all-hadronic decay channel should be well separated from each other. A measure for this is the variable y^k, which describes the minimum distance of k clusters in the event[16]. For the all-hadronic channel, y^6 should be rather large compared to other channels or background. Fig. 9.25(c) shows the corresponding distribution obtained in the BRAHMS analysis. The separation power of this variable is excellent there. The same variable is shown in Fig. 9.25(a) as obtained from SGV. Here the jet reconstructions seems to be unable to separate the all-hadronic $t\bar{t}$-events at all. The distributions of the all-hadronic $t\bar{t}$-events and the background are shifted into the direction of each other and finally merge. Also the use of a different jet reconstruction algorithm[17] does not show any improvement (Fig. 9.25(b)). Obviously the reconstruction of jets in SGV cannot achieve the required accuracy to reconstruct $t\bar{t}$-events properly. This impression is supported by simply looking at the distribution of the number of reconstructed jets in Fig. 9.25(d). Despite the large BR of the all-hadronic channel, only a small number of $t\bar{t}$-events had six jets reconstructed. The purity is quite high, but it decreases quickly when changing the jet reconstruction parameters to gain more six-jet events. The separation power of y^6 did not take any advantage from this variations.

Unfortunately SGV in its present configuration was not able to cope with the requirements of the chosen analysis. It was not able to reproduce adequately the jet properties of the examplary analysis performed with BRAHMS. The reasons for this are not understood yet and need further investigation.

9.4.5.3 Conclusion

The t-quark analysis, which was proposed for the actual design study of the VTX is rather simple and straight forward. However, it requires highest reconstruction accuracy in track and vertex as well as in jet reconstruction. Since the fast MC chosen for this study was designed for an earlier experiment with less resolution than TESLA would have, it dit not provide the accuracy to deal with the potential of a future linear collider. Updates are possible, but so far this was done for the vertex reconstruction only as described in 9.4.3.2. To use this analysis method with SGV successfully, also the jet reconstruction should be updated. Possible questions to be investigated in this context are:

- Are the final state properties of $t\bar{t}$-events comparable on generator level in both, SGV and BRAHMS?

[16] y^k corresponds to $\min(d_{ij})$ as defined in 6.2.1 for k remaining particles or jets in the lists.
[17] JADE-algorithm [170]

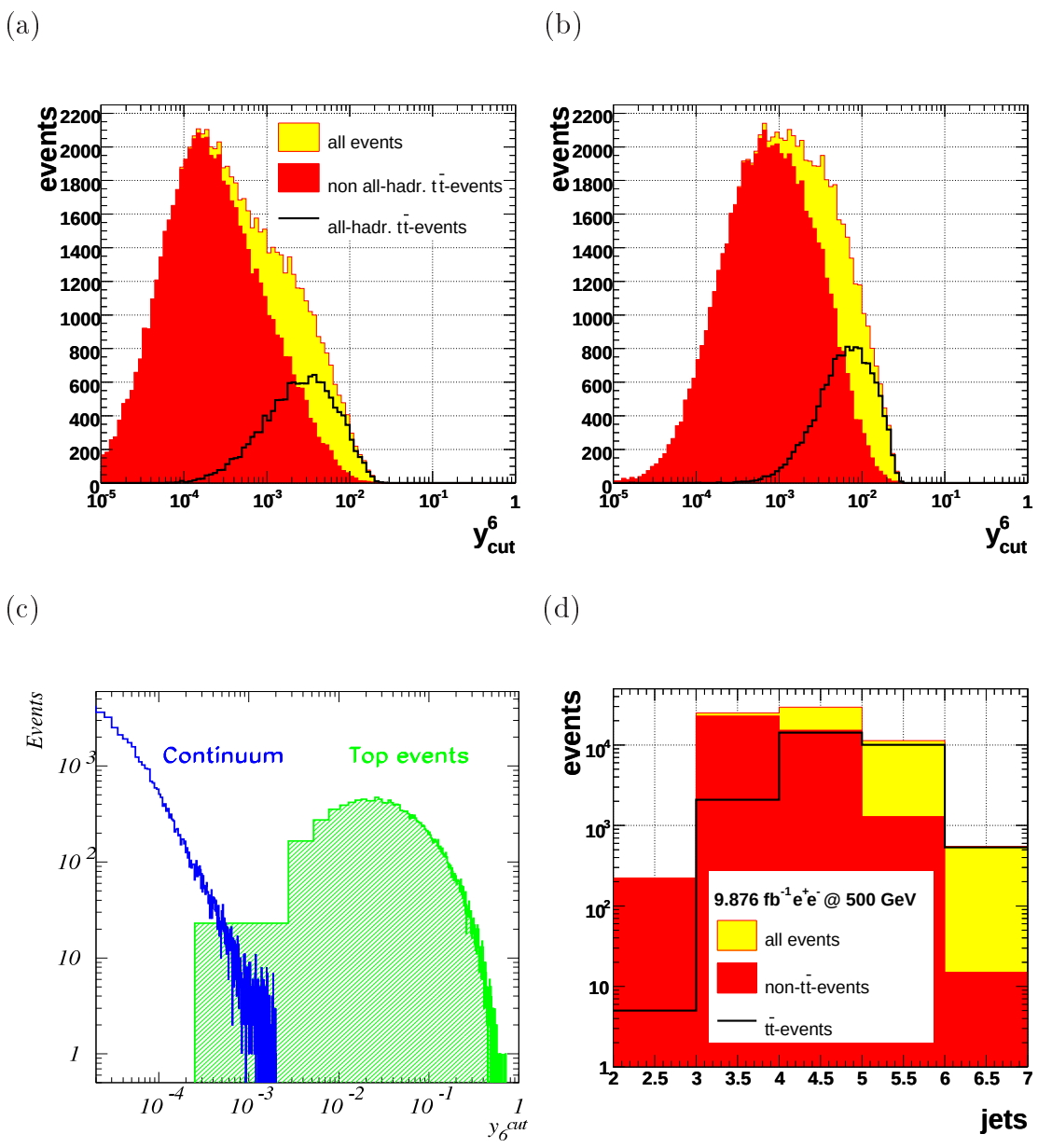

Figure 9.25: y^6 in BRAHMS and SGV and number of jets in SGV
y^6 in SGV obtained (a) with the "Durham" algorithm and (b) with the JADE algorithm for all jets (yellow area), all-hadronic $t\bar{t}$-events (black line) and background evnets (red area). (c) y^6 in BRAHMS [169] for all-hadronic $t\bar{t}$-events (green shaded area) and background (blue line). (d) Number of jets obtained from the inclusive sample used for the b-tagging performance study described above. Distributions are shown for all events (yellow area), $t\bar{t}$-events (black line) and background (red area).

- Does SGV provide calorimeter clusters of the required resolution?
- Do the used "Durham" reconstruction algorithms differ?

As long as this update has not been done, two ways to proceed are possible:

- One stays with a lower level of reconstruction complexity (see 9.4.1) and performs the VTX design study with respect to the vertex reconstruction performance. This is done for example in design studies for a CCD-based vertex detector [171].
- A different process is chosen for the full analysis, which does not rely on the jet reconstruction accuracy as strongly as the t-quark reconstruction presented here. For instance, an analysis of the Higgs branching fractions in the process $e^+e^- \to ZH \to q\bar{q}XY$ compared VTX layouts with varying sensor thicknesses [172]. While the impact seemed to be negligible in the channel $H \to b\bar{b}$, the channel $H \to c\bar{c}$ showed a strong correlation of the sensor thickness with the accuracy of the branching fraction determination.

In both cases full advantage is taken from the SGV functioning principle on the one hand and from the implementation of the neural network heavy flavour tagging on the other hand.

9.5 Summary

This chapter has described the attempt to perform a design study for the TESLA vertex detector. Its goal was to optimise the design parameters of the VTX with respect to a complete physics analysis.

The TESLA project has been introduced and the desired specifications of its vertex detector have been described. The sensor technologies under consideration have been characterised with emphasis on the MAPS option, for which this study was carried out. The optimisation method has been introduced, which relies on a complete analysis of t-quark pair production at a CMS energy of 500 GeV. A preselection was developed, which enriches an inclusive event sample to a fraction of 38% of $t\bar{t}$-events with an efficiency of 95%. The fast simulation and reconstruction program SGV was upgraded with a sophisticated heavy flavour identification to cope with the capabilities of the proposed vertex detector. This heavy flavour identification uses a neural network, whose input uses the results of the topological vertex finder ZVTOP. The performance of the implementation almost reached that of the full TESLA simulation and therefore fulfilled the requirements to be used in this study. Then, the chosen reconstruction method of t-quarks has been introduced, which combines heavy flavour tagging with jet information. For both reconstruction

ingredients, MC studies have been performed to verify the ability of SGV to give results of usable accuracy. The heavy flavour tagging showed a good performance with a b-tagging purity of 86% at an efficiency of 70% in SGV for an inclusive event sample. However, the jet finding resolution of SGV did not meet the requirements at all. The jet reconstruction of SGV could not cope with the highest resolutions achievable in a full simulation and reconstruction program and should be updated. It turned out, that the chosen analysis cannot be performed with SGV in its present status.

For the time being, SGV with the heavy flavour tagging implementation is still used for TESLA vertex detector design studies in channels, which do not need such a good jet resolution as the t-quark reconstruction. However, the successful update of the vertex reconstruction gives hope, that this might be possible even for the jet reconstruction. If so, the advantages of SGV would be usable for linear collider detector design studies in the future.

Chapter 10

Summary

In this thesis a search for events with isolated leptons and large missing transverse momentum with the ZEUS experiment, using an integrated luminosity of $40.76\,\mathrm{pb}^{-1}$ of e^+p-collisions collected during the HERA II running period in the years 2003 and 2004 has been presented. The aim of this work was to look for possible excesses over the SM prediction or, alternatively, to derive limits on the production of single t-quarks at HERA. The addition of these new data improves the results of earlier ZEUS analyses and prepares the ground for the analysis of the full integrated HERA luminosity, which is expected to be about five times larger than the data analysed so far.

Events with singly produced t-quarks lead to isolated leptons and large missing transverse momentum via the decay into a b-quark and a W-boson and the subsequent leptonic decay of the W-boson. The missing transverse momentum originates from the neutrino in this decay. This signature is also expected in single W-boson production with leptonic decay. Additionally, a high-energy jet is expected from the b-quark in single t-quark production. A number of SM processes are backgrounds to these signals through mismeasurements. In the electron channel, these are mainly NC DIS events with a mismeasured hadronic system or electron. Bethe-Heitler muon pair production with one mismeasured muon or hadonic final state can mimic an isolated muon event and CC DIS multi-jet events with a one-track jet or NC DIS events with an unidentified electron and unmeasured energy lead to background in the τ-lepton channel. The observation of an excess over the SM prediction would be an indication of new physics. Processes generating the signature of interest through single t-quarks or other processes in theories beyond the Standard Model have been discussed with emphasis on supersymmetric models. Indeed, an excess with a Poisson probability of 1.8% had been observed by the ZEUS experiment in the τ-lepton channel of HERA I data.

The CC branch of SM single t-quark production at HERA is highly suppressed due to the small values of the off-diagonal elements of the CKM-matrix. FCNC

processes are only present via higher order corrections in the SM and not expected to be observable at HERA, but BSM processes could enhance the production rate significantly. Both, SM and BSM processes are charcterised by an anomalous FCNC coupling[1] with an effective Lagrangian involving an anomalous magnetic coupling $\kappa_{tu\gamma}$ at the $tu\gamma$-vertex and an anomalous vector coupling v_{tuZ} at the tuZ-vertex. Limits on both had been set already by various experiments.

In the presented analysis, first a generic search for events with large missing transverse momentum and isolated tracks was performed. This includes a newly developed rejection of non-ep backgrounds, which is needed due to the harsher background conditions in HERA II. Isolated tracks were identified as electron, muon or hadronic tracks, where the hadronic tracks passed a selection dedicated to isolated one-prong decays of τ-leptons. Data and MC simulations were found to be in reasonable agreement after this selection stage. In the e-channel, five events were found in data with 14.0 expected in the Standard Model. The main contribution comes from badly reconstructed NC DIS events. In the μ-channel, four events were found in data with 5.4 predicted in the Standard Model, mainly from muon pair production. The τ-channel suffered from a low signal efficiency. One event was found in data with 3.2 expected. The main background source were CC DIS events with a jet with only one associated track. Individual background rejection cuts were applied in each channel to select candidate events for leptonically decaying W-bosons. One data event survived in the e-channel, with $3.2^{+0.5}_{-0.7}$ expected, two data events were found in the μ-channel (1.5 ± 0.2 expected) and one in the τ-channel ($2.4^{+0.1}_{-0.3}$ expected). These results were used to derive an upper cross section limit on the production of single W-bosons at HERA of $1.54^{+0.67}_{-0.41}$ pb at 95% CL. This is 33% above the NLO calculation. Finally, a selection was applied to isolate events containing singly produced t-quarks. No data events were found in the e-channel (0.6 ± 0.05 expected), one event was found in the μ-channel (0.7 ± 0.1 expected) and no events were found in the τ-channel (0.1 ± 0.02 expected). These results are consistent with the SM expectation, also in the τ-channel, where an excess had been observed in HERA I data. However, the identification of τ-leptons in their one-prong decay channel differed in both analyses. In this analysis, the signal-to-background ratio is worse, so that a conclusive statement cannot be made here. The results in the e- and μ-channel were used to derive new limits on the anomalous FCNC coupling in combination with the independent searches for single t-quark production in HERA I data in both, the leptonic and hadronic decay channel of the W-boson. In NLO, an upper limit on $\kappa_{tu\gamma}$ of $0.160^{+0.014}_{-0.012}$ at 95% CL was obtained for a t-quark mass of 175 GeV, which improves the former limit by 8%. Together with the most stringent limit on v_{tuZ}, this result is equivalent to an upper cross section limit for the FCNC

[1] Only couplings to the u-quark were considered, since c-quark couplings are suppressed at HERA.

processes considered of $0.186^{+0.029}_{-0.012}$ pb. This improves the former limit by 14%. The use of a different simulation of single t-quark production at the $tu\gamma$-vertex with the subsequent decay $t \to bW^+$ leads to further improved limits of $\kappa_{tu\gamma} < 0.158^{+0.014}_{-0.011}$ at 95% CL and $\sigma_{single\,t} < 0.183^{+0.028}_{-0.021}$ pb.

Also in this thesis, a simulation study for the vertex detector design of the future linear collider ILC on the basis of the TESLA proposal has been presented. An independent fast simulation tool suitable for detector design studies was equipped with a sophisticated heavy-flavour tagging algorithm in order to match the capabilities of the ILC. Today, the resulting software package is used internationally in vertex detector design studies for the ILC.

The TESLA project and the options for the vertex detector sensor technology have been introduced. The study presented in this thesis was carried out for the MAPS technology option. A complete physics analysis chain was applied to a simulated event sample in order to monitor the effects of vertex detector design modifications. The fast simulation and reconstruction program SGV was chosen for this study, because it provides quick and easy modifications of the detector design and is independent of the full simulation, different from the parametrised fast MC program. The chosen physics process was the annihilation into a t-quark pair ($e^+e^- \to t\bar{t}$). In this case, the background rejection and the reconstruction of the t-quarks benefit substantially from an effective b-quark tagging, which in turn relies on the vertex resolution capability of the vertex detector. SGV was equipped with a neural-network based heavy flavour tagging algorithm including the topological vertex finder ZVTOP. For the tagging of b- and c-quark induced jets, the performance of this package with respect to purity vs. efficiency was tested. The sample used contained both, b- and c-quarks as well as light quark jets. The heavy flavour tagging reached the quality of the full TESLA simulation and reconstruction program BRAHMS.

The sensitive performance parameter used was the t-quark mass reconstructed from the all hadronic decay into six jets. A comparable analysis using BRAHMS had been already available for comparison. The t-quark reconstruction algorithm used in that analyis was adapted to the study presented in this thesis. The signal process was simulated and reconstructed with SGV together with the expected background processes. These are pair production of all other quark flavours and all leptons with and without initial state radiation, pair production of gauge bosons, Bhabha scattering and photoproduction. A preselection was developed, which achieved a purity of 38% at a signal efficiency of more then 95% without considering the t-quark decay channels. With this event sample, MC studies were performed to evaluate the applicability of the chosen t-quark reconstruction method to the output of SGV. The b-tagging performance was found to work very well also for b-jets resulting from a t-quark decay. A purity of 86% was achieved at an efficiency of 70%. To

select $t\bar{t}$-events in the all-hadronic decay channel, the BRAHMS analysis exploited the isotropic topology of such events resulting in a clear spatial separation of the six jets. Here the SGV jet reconstruction failed, although the "Durham" jet reconstruction algorithm was used in both analyses. In SGV the spatial distribution of the jets showed no separation power – in most of the all-hadronic $t\bar{t}$-events, not all jets could be reconstructed. The particular reason for this behaviour is not understood yet and needs further investigation.

In summary, it was found that the analysis chosen for the vertex detector design study could not be performed with SGV at its present status. Nevertheless, SGV with the adapted heavy-flavour tagging is very successful in vertex detector design studies using different signal processes or a lower level of reconstruction complexity, where the jet reconstruction is not crucial. As a remedy for the problems discusses, an update of the SGV jet reconstruction should be considered to gain full benefit from the advantages of SGV.

Appendix A

Review of Correlated Searches at HERA

In this chapter, generic searches for events with isolated leptons and large missing transverse momentum and searches for single W-boson or t-quark production performed by the ZEUS and H1 collaborations are summarised.

A.1 ZEUS Searches for Isolated Leptons

In order to search for single t-quark production, the ZEUS collaboration performed a search for events with isolated leptons and large missing transverse momentum in the e- and μ-channel in HERA I data of an integrated luminosity of $\mathcal{L}_{int} = 130.1\,\mathrm{pb}^{-1}$ [1, 39, 46]. The data selection required an isolated high-p_T track identified either as electron or muon and a missing transverse momentum of more than 20 GeV. To select t-quark candidates, at least one high-E_T jet and a missing hadronic transverse momentum of more than 40 GeV were additionally required. No deviations from the Standard Model were observed and limits on single t-quark production were computed in combination with the corresponding search in the hadronic channel (s. App. A.2). The resulting two-dimensional limits in the $\kappa_{tu\gamma}$-v_{tuZ} plane are shown in Fig. 2.15. The limit on $\kappa_{tu\gamma}$ from NLO calculation was set to 0.174 at 95% CL for a t-quark mass of 175 GeV. The results of that search were also used in the calculation of limits on single t-quark production performed in this analysis (s. 8.3).

A similar search in the same data set was performed in order to find events with isolated τ-leptons and large missing transverse momentum [1,46,131,140]. The search considered only τ-leptons with subsequent one-prong decay ($BR(\tau \to h\nu_\tau \geq 0\,\text{neutrals}) \approx 50\%$). Events, which fulfilled the requirements of the search described above without the isolated track being identified as electron or muon were passed to a τ-lepton identification algorithm. This algorithm uses a multi-variate discriminant

method [173] with six observables describing the shape of the jet which is assigned to the isolated track [46, 132]. One data event was found, where 0.07 events were expected from the SM simulation. With a reduced cut on the missing hadronic transverse momentum of 25 GeV, two events were observed in data, whereas only 0.2 were expected. The Poisson probability for this observation is 1.8%.

Further searches for events with isolated high-p_T leptons were performed by the ZEUS collaboration in order to determine the cross section of single W-boson production at HERA. A search performed on $47.7\,\text{pb}^{-1}$ of e^+p data taken at $\sqrt{s} = 300\,\text{GeV}$ determined a cross section estimate of $0.9^{+1.0}_{-0.7} \pm 0.2\,\text{pb}$ and a corresponding upper limit on the cross section of 3.3 pb at 95% CL from the e-channel [174]. A missing transverse momentum of more than 20 GeV and a high-p_T electron ($p_T^e > 10\,\text{GeV}$ from electron finder, $p_T^e > 5\,\text{GeV}$ from tracking) were the main requirements. This search was repeated on $66.3\,\text{pb}^{-1}$ of e^+p data taken at $\sqrt{s} = 318\,\text{GeV}$. The cross section limit set in that search was 2.8 pb at 95% CL [175].

A.2 ZEUS Searches for W-Bosons in the Hadronic Channel

In order to search for single t-quark production, the ZEUS collaboration performed a search in the hadronic decay channel of the W-boson in HERA I data of $\mathcal{L}_{int} = 127.2\,\text{pb}^{-1}$ [39]. Three high-E_T jets and no significant missing transverse momentum were expected with the invariant mass of a two-jet combination compliant with the W-boson mass ($65.5\,\text{GeV} < M^{2j} < 90.8\,\text{GeV}$) and the invariant mass of the three-jet combination compliant with the t-quark mass ($159\,\text{GeV} < M^{3j} < 188\,\text{GeV}$). No deviations from the Standard Model were observed and limits on single t-quark production were computed in combination with the corresponding search in the e- and μ-channel (s. App. A.1). The results of this search were also used in the calculation of limits on single t-quark production performed in this analysis (s. 8.3).

A.3 H1 Searches

The H1 collaboration searched for isolated electrons and muons in events with large missing transverse momentum in HERA I data of $\mathcal{L}_{int} = 118.3\,\text{pb}^{-1}$ [176]. The main selection criteria were a missing transverse momentum of more than 12 GeV, an isolated electron or muon with a transverse momentum of more than 10 GeV and kinematical consistance of the reconstructed lepton-neutrino system with the decay of a W-boson. For a hadronic transverse momentum of more than 25 GeV, an excess of data was observed in both channels, which supported earlier observations [177]. Four electron events were observed, where 1.5 were expected, and six muon events

were observed, where 1.4 were expected. In a strongly correlated search for single t-quark production in the same data set [40], limits were set to 0.55 pb for the cross section an 0.27 for $\kappa_{tu\gamma}$, both at 95% CL. This result also included an analysis in the hadronic channel. At present, in 211 pb^{-1} of combined HERA I + II data, eleven electrons (3.2 expected) and six muons (3.2 expected) are found with a missing hadronic transverse momentum of more than 25 GeV in the event [178].

In the τ-channel, H1 did not observe any deviations from the Standard Model [131, 179]. No candidate event was observed in 108 pb^{-1} of HERA I data, where 0.5 events were expected.

Appendix B

ZEUS Luminosity

Year / running period	$\sqrt{s}$ (GeV)	Integrated luminosity (pb^{-1})		
		HERA delivered	on tape	physics
1993-94 e^-	300	2.17	0.99	0.82
1994-97 e^+	300	70.92	51.14	48.30
1998-99 e^-	318	25.20	17.78	16.68
1999-2000 e^+	318	94.95	73.40	65.88
2002-03 e^+	318	5.20	1.70	0.97
2003 e^+	318	6.53	2.72	**2.08**
2004 e^+	318	77.94	42.30	**38.68**
2003-04 e^+	318	84.47	45.02	**40.79**
1993-2004 e^+	300-318	250.34	169.56	154.77
1993-2004 e^-	300-318	27.37	18.77	17.50
1993-2004 total	300-318	277.71	188.33	172.27

Table B.1: ZEUS integrated luminosities
The bold numbers indicate the data used in this analysis. There, $0.03\,\mathrm{pb}^{-1}$ were skipped in this analysis due to indications from data quality monitoring. In addition, about $150\,\mathrm{pb}^{-1}$ of e^-p-data were recorded by ZEUS in the years 2004-05. The calculation of the final numbers was not finished yet.

Appendix C

Muon Finders

In this analysis, the muon finder package GMuon [129] was used which combines the outcome of several muon finding algorithms. In the following a list of these algorithms is given [181].

GLOMU: Looks for low momentum muons combining CTD, CAL and B/RMUON information [182].

BREMAT: Looks for muons combining CTD and B/RMUON information [183].

MAMMA: matches either tracks or hits in FMUON with clusters in the FCAL and/or CTD tracks.

MPMATCH: Looks for muons combining CTD and FMUON [184].

MUFO: Looks for muons combining CTD and FMUON information.

MIP: Finds prompt muons in the CAL+CTD based on the association of a MIP CAL island to a high momentum track.

MV: Finds prompt muons anywhere in the CAL (+CTD) with a neural network algorithm.

Tab. C.1 gives description and examples of GMuon quality flags.

Quality	Description	Examples
6	excellent quality muon for high bkg. samples	BREMAT 5dof pmatch>0.01 from prim. vtx; MPMATCH or MUFO, p>0.05 or MV
5	very good quality muon for interm./high bkg. samples	all other MPMATCH/MUFO to CTD; good quality MUFO to vertex; noncentral BREMAT 4dof + MV; MAMMA FMU+CAL+CTD; noncentral BAC + MV, good quality; all BREMAT + BAC + MV
4	good quality muon for intermediate bkg. samples	BREMAT 4dof pmatch>0.01 from prim. vtx; lesser quality MUFO to vertex; unmatched FMU + MV; central BAC + MV, good quality; BAC + MIP (p>2); good quality BAC
3	fair quality muon candidate for low bkg. samples	BREMAT 5dof pmatch>0.01 not from prim. vtx; MV prob > 0.95; GLOMU + MV prob > 0.6; MAMMA FMU+CAL; BAC + MV, bad quality; BREMAT + BAC, bad quality; GLOMU + BAC
2	reasonable quality muon candidate for low bg. samples	BREMAT 4dof pmatch>0.01 not from prim. vtx; unmatched FMU track (MFCTS); MV prob > 0.8; GLOMU match; reasonable quality BAC
1	low quality muon candidate	MPMATCH to CTD, pmatch<0.01; MV prob > 0.6
0	unknown or very low quality muon candidate	MIP match only; MV without track or secondary vertex or no vertex
-1	doubtful muon candidate	BREMAT 5dof p<0.01
-2	bad muon candidate	BREMAT 4dof p<0.01; unmatched FMU track with reconstruction problem
-3	alternative reconstruction of muon already in list; quality and use to be judged by user	
-999	simulated MC prompt muon, not identified	
-1000	simulated MC pi/K decay muon, not identified	

Table C.1: GMuon quality flags
For descriptions of the the acronyms, see [181].

Appendix D

Trigger Logic

The only trigger definition used in this analysis was the DST bit 34 (DST34), which usually is used to select CC DIS events. Information from SLT and TLT is combined in this trigger bit. DST34 and the referred SLT and TLT slots are defined in the following.

D.1 DST bit 34

DST34 is set, if the following requirements are fulfilled:

- $EXOTLT2$ or $EXOTLT6$ or $p_T^{ex1IR} > 6\,\text{GeV}$ (for the TLT definitions, s. App. D.2),
- $p_T > 7\,\text{GeV}$,
- In order to reject background from beam-gas interactions, an event is vetoed, if it fulfills all of the following requirements:
  - NOT $EXOTLT2$
  - $p_T^{ex1IR} < 10\,\text{GeV}$,
  - $p_T < 25\,\text{GeV}$,
  - $p_T/E_T < 0.7$,
  - $E - p_z < 10\,\text{GeV}$,
  - $p_T/p_z < 0.8$,
  - $p_x < 0\,\text{GeV}$,
  - $|p_x| < 4\,\text{GeV}$.

D.2 TLT information

The TLT branch $EXOTLT2$ (CC, good track) has the following logic:

- $p_T^{FLT} > 6\,\text{GeV}$ AND
- $n_{trk,good} \geq 1$ AND
- $|z_{vtx}| < 60\,\text{cm}$ AND
- $|t_u - t_d| < 8\,\text{ns}$.

The TLT branch $EXOTLT6$ (CC) has the following logic:

- $EXOSLT4$ (for the SLT definition, s. App. D.3) AND
- $|t_u - t_d| < 8\,\text{ns}$ AND
- $p_T^{FLT} > 6\,\text{GeV}$ AND
  - $n_{trk}^{good} \geq 1$ OR
  - $E_{FCAL} > 10\,\text{GeV}$.

D.3 SLT information

The SLT branch $EXOSLT4$ has the following logic:

- $|t_g| < 7\,\text{ns}$ AND
  - EITHER
    - $p_T > 6\,\text{GeV}$ AND
    - $E_T^{ex2IR} > 6\,\text{GeV}$ AND
    - $n_{trk}^{good} \geq 1$
  - OR
    - $p_T > 9\,\text{GeV}$ AND
    - $E_T^{ex1IR} > 8\,\text{GeV}$ AND
    - $E_{FCAL} > 20\,\text{GeV}$.

Appendix E

Event Pictures in the ZEVIS-Event-Display

ZEVIS [138] is a client-server event-display for the ZEUS experiment, based on the object-oriented data analysis framework ROOT [180].

E.1 Typical Background Event after Sample Selection

A typical background event from proton beam-gas interactions is shown in Fig. E.1. After a proton had interacted in the beamline as described in 4.2.2, a particle cascade was produced. These particles could not be shielded completely and sprayed into the detector. Many entries in the calorimeters were observed without matching tracks and without jet-like clustering. A few particles caused reconstructed tracks, which led to an reconstructed event vertex.

E.2 Candidate Events for Leptonically Decaying W-Bosons

The event pictures of the data events are shown, which survived the final selection of W-boson candidates (s. 7.4).

Fig. E.2 shows a candidate for a W-boson decaying in the electron channel. The isolated electron (thick red line) hits the CAL in the crack between BCAL and RCAL. Its reconstructed energy is 10.6 GeV, the transverse momentum measured from the track is 8.4 GeV. One jet is observed in the FCAL, the second jet was reconstructed from the electron. The missing transverse momentum vector (black arrow, $p_T^{miss} = 22.3\,\text{GeV}$) points into the direction of further hadronic activity in

(a) (b)

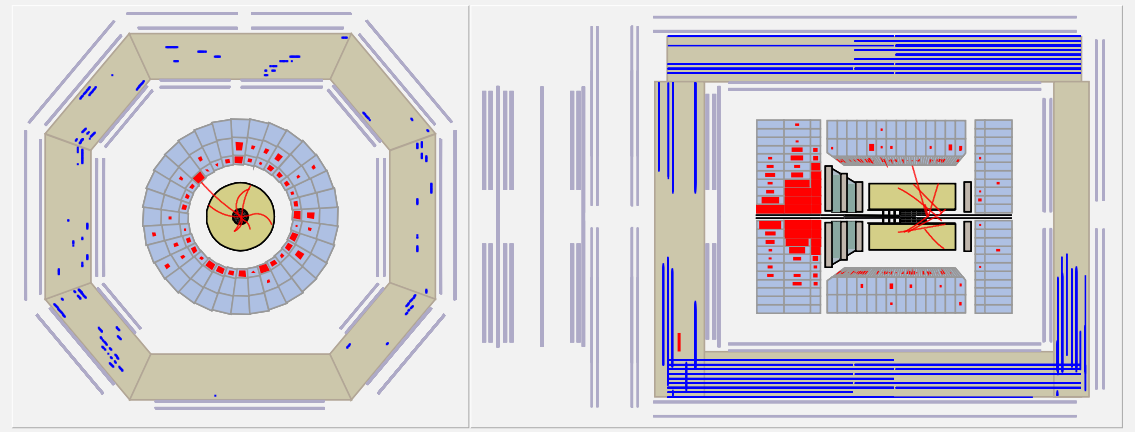

Figure E.1: ZEUS run 45865, event 17231: proton beam-gas event
Event shown in (a) x-y-view and (b) r-z-view. In the x-y-view, the light blue rings depicts the CAL. The red segments represent energy depositions. The thin red lines are reconstructed tracks. The grey octagon represents the BAC. The blue pixels are hits in the BAC pads.

the BCAL, which however was not identified as a jet. It is assumed, that this event shows an NC DIS di-jet process with the jet in the BCAL badly measured. This is also indicated by the rather high $E - p_Z$ of 40.0 GeV, which also is influenced by the assumed mismeasurement. This event failed the final selection of t-quark candidates, since the transverse hadronic momentum neglecting the reconstructed W-candidate of 38.6 GeV was slightly too small.

Fig. E.3 shows a candidate for a W-boson decaying in the muon channel. The isolated muon (thick red line) escapes the detector through the RCAL and the BAC. Its energy is reconstructed as 45.5 GeV ($p_T^{trk} = 34.1$ GeV). The missing transverse momentum vector (black arrow, $p_T^{miss} = 10.5$ GeV) points into the opposite direction in the azimuthal plane. An electron candidate (second isolated track) and a jet are observed in the forward direction. The transverse mass of the reconstructed W-candidate amounts to 37.6 GeV. Various interpretations are possible, but a W-boson which singly produced in the DIS regime cannot be excluded.

Fig. E.4 shows a candidate for another W-boson decaying in the muon channel. The isolated high-quality muon (thick red line) escapes the detector through the BCAL, the RCAL and the BAC. A second high-quality muon is observed in the forward direction. Each muon is strongly correlated with a reconstructed jet and the missing transverse momentum vector (not shown here) points exactly into the flight direction of the isolated muon. The reconstructed transverse W-mass is extremely

(a) (b)

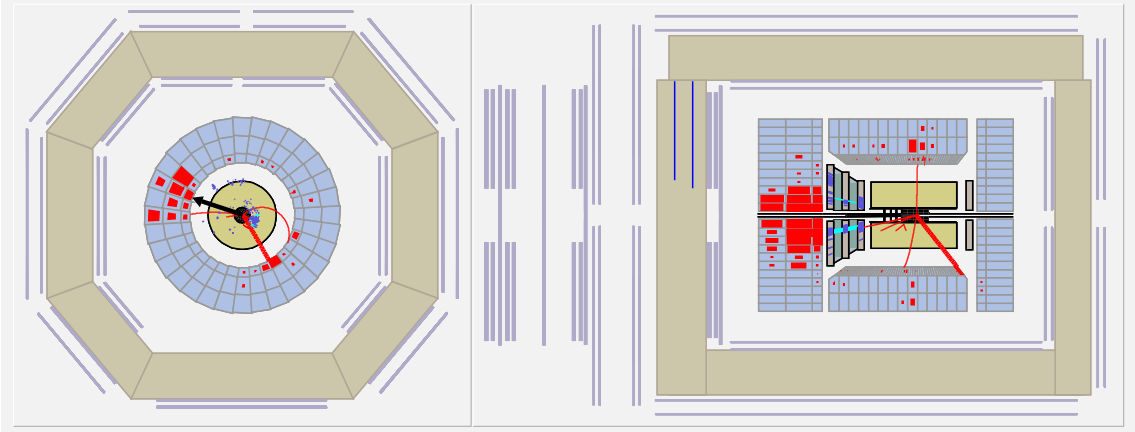

Figure E.2: ZEUS run 51108, event 11802: W-candidate, e-channel
Event shown in (a) x-y-view and (b) r-z-view. In the x-y-view, the light blue rings depicts the CAL. The red segments represent energy depositions. The thin red lines are reconstructed tracks. The thick red line indicates the isolated lepton candidate and the black arrow shows the direction of the missing transverse momentum.

(a) (b)

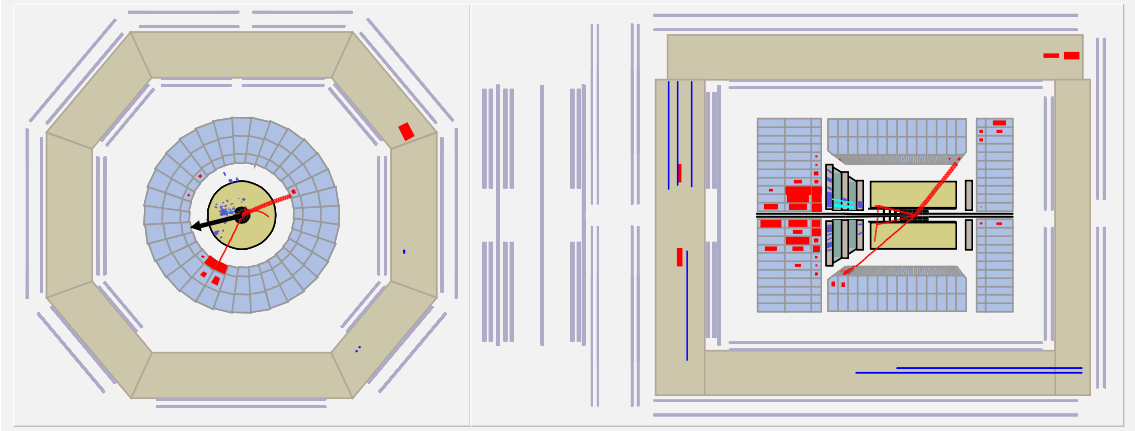

Figure E.3: ZEUS run 48620, event 14029: W-candidate, μ-channel
Event shown in (a) x-y-view and (b) r-z-view. In the x-y-view, the light blue rings depicts the CAL. The red segments represent energy depositions. The thin red lines are reconstructed tracks. The thick red line indicates the isolated lepton candidate and the black arrow shows the direction of the missing transverse momentum.

(a) (b)

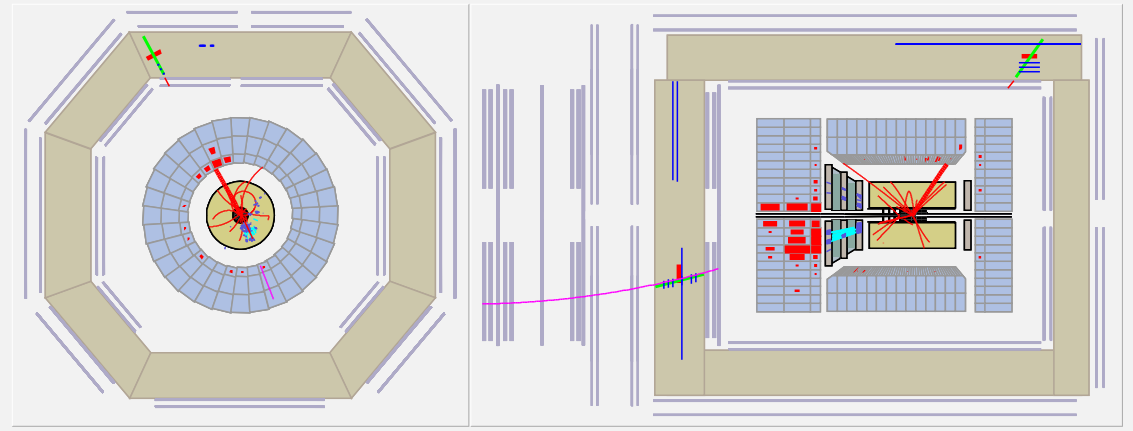

Figure E.4: ZEUS run 50482, event 17061: W-candidate, μ-channel
Event shown in (a) x-y-view and (b) r-z-view. In the x-y-view, the light blue rings depicts the CAL. The red segments represent energy depositions. The thin red lines are reconstructed tracks. The thick red line indicates the isolated lepton candidate and the black arrow shows the direction of the missing transverse momentum.

(a) (b)

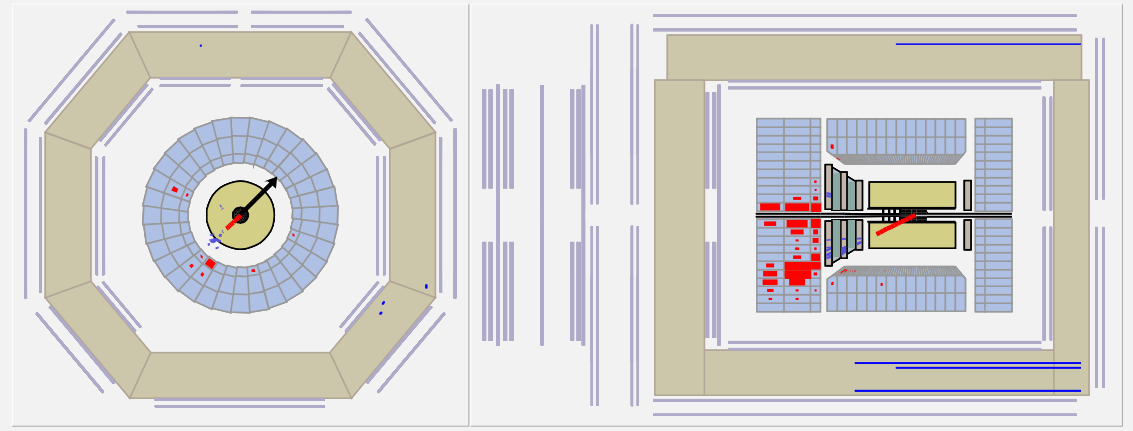

Figure E.5: ZEUS run 51045, event 19607: W-candidate, τ-channel
Event shown in (a) x-y-view and (b) r-z-view. In the x-y-view, the light blue rings depicts the CAL. The red segments represent energy depositions. The thin red lines are reconstructed tracks. The thick red line indicates the isolated lepton candidate and the black arrow shows the direction of the missing transverse momentum.

small (0.2 GeV). It is very likely, that this event shows heavy quark pair production in the PhP regime with both heavy quarks decaying semi-leptonically into muons (s. e.g. [136]). This event passes all selection criteria, since the muon track is the only one associated with the corresponding jet. Due to the large hadronic transverse momentum of 40.5 GeV, this was also the only data event which passed the final t-quark selection.

Fig. E.5 shows a candidate for a W-boson decaying in the τ-lepton channel. The isolated track (thick red line) is the only reconstructed track ($p_T^{trk} = 24.2\,\mathrm{GeV}$) in this event. It points into the direction of a jet of a total energy of 55.0 GeV in the FCAL. The transverse energy of the jet is exactly the same as p_T^{trk}. The missing transverse momentum vector (black arrow, $p_T^{miss} = 22.9\,\mathrm{GeV}$) points into the opposite direction. The reconstructed transverse W-mass is 32.2 GeV. A CC DIS event is likely, but a W-decay cannot be excluded in this case. This event failed the final selection of t-quark candidates by means of all cuts.

Appendix F

Event Yields

Sample	e-Channel	μ-Channel	τ-Channel	Total
PhP	0	0	0	0
NC Dis (Cdm)	10.67 $\pm$1.71	0.001$\pm$0.001	$<$0.001	10.67 $\pm$1.71
CC Dis (Cdm)	0.652$\pm$0.067	0.382$\pm$0.051	2.92 $\pm$0.14	3.96 $\pm$0.16
NC Dis (Meps)	8.21 $\pm$1.61	0.006$\pm$0.005	0.025$\pm$0.025	8.24 $\pm$1.61
CC Dis (Meps)	0.639$\pm$0.066	0.375$\pm$0.051	2.55 $\pm$0.13	3.57 $\pm$0.16
Di-e	0.044$\pm$0.044	0	0	0.044$\pm$0.044
Di-μ	0.376$\pm$0.068	3.80 $\pm$0.23	0.018$\pm$0.018	4.19 $\pm$0.24
Di-τ	0.272$\pm$0.042	0.331$\pm$0.046	0.053$\pm$0.019	0.656$\pm$0.065
Di-l total	0.692$\pm$0.091	4.13 $\pm$0.24	0.071$\pm$0.026	4.89 $\pm$0.25
Background total (Cdm)	12.01 $\pm$1.72	4.51 $\pm$0.24	2.99 $\pm$0.14	19.52 $\pm$1.73
Background total (Meps)	9.54 $\pm$1.61	4.51 $\pm$0.24	2.65 $\pm$0.14	16.70 $\pm$1.34
W-boson e	1.59 $\pm$0.03	$<$0.001	0.006$\pm$0.002	1.59 $\pm$0.03
W-boson μ	0.059$\pm$0.005	0.773$\pm$0.018	0.005$\pm$0.001	0.837$\pm$0.018
W-boson τ	0.274$\pm$0.011	0.120$\pm$0.007	0.153$\pm$0.008	0.546$\pm$0.015
W-boson hadr.	0.013$\pm$0.002	0.002$\pm$0.001	0.001$\pm$0.001	0.017$\pm$0.003
W-boson total	1.94 $\pm$0.03	0.895$\pm$0.019	0.164$\pm$0.008	2.99 $\pm$0.03
Sm (Cdm) total	13.95 $\pm$1.72	5.41 $\pm$0.24	3.16 $\pm$0.14	22.51 $\pm$1.74
Sm (Meps) total	11.47 $\pm$1.61	5.40 $\pm$0.24	2.81 $\pm$0.14	19.69 $\pm$1.63
Data	5 $\pm$2.24	4 $\pm$2.0	1 $\pm$1.0	10 $\pm$3.16

Table F.1: Predicted event yields of individual Sm MC samples after preselection
The background sample summarises all Sm samples without W-boson production. The quoted uncertainties are statistical uncertainties only.

Sample	e-Channel	μ-Channel	τ-Channel	Total
NC Dis (Cdm)	1.21 ±0.48	0	<0.001	1.21 ±0.48
CC Dis (Cdm)	0.467±0.055	0.172±0.034	2.15 ±0.12	2.79 ±0.14
NC Dis (Meps)	0.907±0.487	0	0.025±0.025	0.932±0.487
CC Dis (Meps)	0.447±0.054	0.175±0.034	1.87 ±0.11	2.49 ±0.13
Di-e	0	0	0	0
Di-μ	0.147±0.041	0.481±0.085	0.018±0.018	0.646±0.096
Di-τ	0.146±0.030	0.223±0.038	0.053±0.019	0.421±0.052
Di-l total	0.292±0.051	0.704±0.093	0.071±0.026	1.067±0.109
Background total (Cdm)	1.97 ±0.48	0.876±0.099	2.22 ±0.12	5.07 ±0.51
Background total (Meps)	1.65 ±0.49	0.879±0.099	1.97 ±0.12	4.49 ±0.52
W-boson e	1.04 ±0.02	<0.001	0.004±0.001	1.05 ±0.02
W-boson μ	0.025±0.003	0.530±0.015	0.003±0.001	0.557±0.015
W-boson τ	0.182±0.009	0.090±0.006	0.118±0.007	0.391±0.013
W-boson hadr.	0.003±0.001	0	0.001±0.001	0.004±0.001
W-boson total	1.25 ±0.02	0.620±0.016	0.127±0.007	2.00 ±0.03
Sm (Cdm) total	3.23 ±0.48	1.50 ±0.10	2.35 ±0.12	7.07 ±0.51
Sm (Meps) total	2.90 ±0.49	1.50 ±0.10	2.09 ±0.12	6.49 ±0.52
Data	1 ±1.0	2 ±1.414	1 ±1.0	2 ±1.414

Table F.2: Predicted event yields of individual Sm MC samples after the final selection of W-boson candidates

Samples without contribution in Tab. F.1 are skipped. The background sample summarises all Sm samples without W-boson production. The quoted uncertainties are statistical uncertainties only.

Sample	e-Channel	μ-Channel	τ-Channel	Total
NC Dis (Cdm)	0.036±0.027	0	0	0.036±0.027
CC Dis (Cdm)	0.105±0.026	0.072±0.022	0.098±0.025	0.275±0.042
NC Dis (Meps)	0.010±0.007	0	0	0.010±0.007
CC Dis (Meps)	0.137±0.030	0.052±0.018	0.097±0.026	0.286±0.044
Di-μ	0.007±0.004	0.118±0.042	0	0.125±0.043
Di-τ	0.020±0.011	0.121±0.028	0	0.141±0.030
Di-l total	0.027±0.012	0.240±0.051	0	0.266±0.052
Background total (Cdm)	0.168±0.040	0.311±0.055	0.098±0.025	0.577±0.072
Background total (Meps)	0.175±0.033	0.292±0.054	0.097±0.026	0.563±0.068
W-boson e	0.287±0.011	0	0.003±0.001	0.290±0.011
W-boson μ	0.016±0.003	0.325±0.012	0	0.341±0.012
W-boson τ	0.094±0.006	0.066±0.005	0.031±0.004	0.192±0.009
W-boson hadr.	0.002±0.001	<0.001	0	0.002±0.001
W-boson total	0.399±0.013	0.391±0.013	0.034±0.004	0.824±0.018
Sm (Cdm) total	0.563±0.042	0.708±0.057	0.133±0.026	1.40 ±0.075
Sm (Meps) total	0.570±0.035	0.689±0.055	0.132±0.026	1.39 ±0.071
Data	0 +1.0	1 ±1.0	0 +1.0	1 ±1.0

Table F.3: Predicted event yields of individual Sm MC samples after the final selection of t-quark candidates

Samples without contribution in Tab. F.2 are skipped. The background sample summarises all Sm samples without W-boson production. The quoted uncertainties are statistical uncertainties only.

Appendix G

TESLA – Technical Details

CMS energy	(GeV)	500	800
Accelerating gradient	(MV/m)	23.4	35
Beam pulse length	(µs)	950	860
Bunches/pulse		2820	4886
Bunch spacing	(ns)	337	176
Charge/bunch	(e)	$2 \cdot 10^{10}$	$1.4 \cdot 10^{10}$
Beam size at IP	(nm×nm)	553×5	391×2.8
Bunch length at IP	(mm)	0.3	0.3
Beamstrahlung	(%)	3.2	4.3
Luminosity	($\mathrm{cm}^{-2}\mathrm{s}^{-1}$)	3.4×10^{34}	4.3×10^{34}
Power/beam	(MW)	11.3	17

Table G.1: TESLA specifications
A list of proposed TESLA specifications for the base configuration ($E_{CMS} = 500\,\mathrm{GeV}$) and an upgrade option ($E_{CMS} = 800\,\mathrm{GeV}$) [145].

Appendix H

SGV Description of Default TESLA VTX (MAPS)

As an example for a detector description in SGV, the default configuration of the VTX used in this study with parameters of the MIMOSA 5 sensor is given here. Explanations are given in [157]. More examples of higher complexity, e.g. by segmentation in ϕ, are found via [185].

```
BF:   BFIELD=4.0
TYPE: BARREL_TRACKING
      LAYER: BEAMPIPE
             GEOMETRY:    R=1.5, ZMIN=0.0, ZMAX=999.9
             MATERIAL:    X0=0.00425, A=4
             MEASUREMENT: CODE=0
      LAYER: VXD
             GEOMETRY:    R=1.55, ZMIN=0.0, ZMAX=5.0
             MATERIAL:    X0=0.00015, A=14
             MEASUREMENT: CODE=1, SIG_RPHI=0.00015, SIG_Z=0.00015
      LAYER: VXD
             REPEAT: TIMES=4, DELTA_R=1.1
                     GEOMETRY:    R=2.6, ZMIN=0.0, ZMAX=12.5
                     MATERIAL:    X0=0.00015, A=14
                     MEASUREMENT: CODE=1, SIG_RPHI=0.00015, SIG_Z=0.00015
             ENDREPEAT:
      LAYER: VXD_READOUT
             GEOMETRY:    R=1.55, ZMIN=5.0, ZMAX=8.0
             MATERIAL:    X0=0.02, A=14
             MEASUREMENT: CODE=0
      LAYER: VXD_READOUT
             REPEAT: TIMES=4, DELTA_R=1.1
                     GEOMETRY:    R=2.6, ZMIN=12.5, ZMAX=15.5
                     MATERIAL:    X0=0.02, A=14
                     MEASUREMENT: CODE=0
             ENDREPEAT:
```

```
LAYER: VXD_CRYOSTAT
       GEOMETRY:  R=9.0 , ZMIN=0.0, ZMAX=16.
       MATERIAL:    X0=0.0025, A=6
       MEASUREMENT: CODE=0
LAYER: VXD_SUPPORT
       GEOMETRY:    R=11.0, ZMIN=0.0, ZMAX=16.0
       MATERIAL:    X0=0.0042, A=4
       MEASUREMENT: CODE=0
```

List of Figures

List of Tables

Bibliography

[1] T. Carli, D. Dannheim and L. Bellagamba, Mod. Phys. Lett. A **19** (2004) 1881 [hep-ph/0402012].

[2] P. W. Higgs, Phys. Lett. **12** (1964) 132.

[3] I. J. R. Aitchison and A. J. G. Hey, *Gauge Theories In Particle Physics. A Practical Introduction*, Bristol, UK: Hilger (1982) 341 pp.

[4] S. Eidelman et al. (Particle Data Group), Phys. Lett. B **592** (2004) 1 and 2005 partial update for edition 2006, available on `http://pdg.lbl.gov`.

[5] S. Weinberg, Phys. Rev. Lett. **19** (1967) 1264.

[6] N. Cabibbo, Phys. Rev. Lett. **10** (1963) 531;
M. Kobayashi and T. Maskawa, Prog. Theor. Phys. **49**, 652 (1973).

[7] A. D. Sakharov, Pisma Zh. Eksp. Teor. Fiz. **5** (1967) 32 [JETP Lett. **5** (1967 SOPUA,34,392-393.1991 UFNAA,161,61-64.1991) 24].

[8] E. Lohrmann, *Hochenergiephysik*, 5., überarb. u. erw. Aufl. 2005, Teubner, Stuttgart, Germany, ISBN: 3-519-43043-6

[9] G. 't Hooft, Nucl. Phys. B **35** (1971) 167;
G. 't Hooft and M. J. G. Veltman, Nucl. Phys. B **50** (1972) 318.

[10] D. J. Gross and F. Wilczek, Phys. Rev. Lett. **30** (1973) 1343;
H. D. Politzer, Phys. Rev. Lett. **30** (1973) 1346.

[11] M. Gell-Mann, Phys. Lett. **8** (1964) 214;
G. Zweig, *An SU(3) Model For Strong Interaction Symmetry And Its Breaking. 2* (unpublished), internal note CERN-TH-412.

[12] R. P. Feynman, Phys. Rev. Lett. **23** (1969) 1415.

[13] J. D. Bjorken, Phys. Rev. **179** (1969) 1547.

[14] J. R. Ellis and G. L. Fogli, Phys. Lett. B **213** (1988) 526;
J. R. Ellis, G. L. Fogli and E. Lisi, Phys. Lett. B **292** (1992) 427;
B. Jacobsen, hep-ex/9407002.

[15] K. Müller, *Kern- und Teilchenphysik II: Einführung Supersymmetry* (unpublished), lecture given at the University of Zürich, Switzerland, 2004

[16] M. E. Peskin, lecture given at the European School of High-Energy Physics, 1-14 Sep 1996 Carry-le-Rouet, France, hep-ph/9705479.

[17] D. I. Kazakov, lecture given at the European School on High Energy Physics, August - September 2000, Caramulo, Portugal, hep-ph/0012288.

[18] G. Callan and D. J. Gross, Phys. Rev. Lett. **22** (1969) 156.

[19] D. Pitzl, *HERA structure function measurements and the extraction of the parton distributions and alpha_s* (unpublished), given at the 39th Rencontres De Moriond on QCD and High Energy Hadronic Interactions, March 28 - April 4, 2004, La Thuile, Italy.

[20] Y. L. Dokshitzer, Sov. Phys. JETP **46** (1977) 641 [Zh. Eksp. Teor. Fiz. **73** (1977) 1216];
V. N. Gribov and L. N. Lipatov, Sov. J. Nucl. Phys. **15** (1972) 438 [Yad. Fiz. **15** (1972) 781].

[21] G. Altarelli and G. Parisi, Nucl. Phys. B **126** (1977) 298.

[22] H. Bethe and W. Heitler, Proc. Roy. Soc. Lond. A **146** (1934) 83.

[23] U. Baur and D. Zeppenfeld, Nucl. Phys. B **325** (1989) 253.

[24] U. Baur, J. A. M. Vermaseren and D. Zeppenfeld, Nucl. Phys. B **375** (1992) 3.

[25] S. Moretti and K. Odagiri, Phys. Rev. D **57** (1998) 3040 [hep-ph/9709435].

[26] S. L. Glashow, J. Iliopoulos and L. Maiani, Phys. Rev. D **2** (1970) 1285.

[27] J. A. Aguilar-Saavedra, Acta Phys. Polon. B **35** (2004) 2695 [hep-ph/0409342].

[28] R. Ammar et al., Phys. Rev. Lett. **71** (1993) 674;
S. Chen et al., Phys. Rev. Lett. **87** (2001) 251807 [hep-ex/0108032].

[29] J. A. Aguilar-Saavedra and B. M. Nobre, Phys. Lett. B **553** (2003) 251 [hep-ph/0210360].

[30] T. Han, R. D. Peccei and X. Zhang, Nucl. Phys. B **454** (1995) 527 [hep-ph/9506461];
T. Han, M. Hosch, K. Whisnant, B. L. Young and X. Zhang, Phys. Rev. D **58** (1998) 073008 [hep-ph/9806486].

[31] V. F. Obraztsov, S. R. Slabospitsky and O. P. Yushchenko, Phys. Lett. B **426** (1998) 393 [hep-ph/9712394].

[32] T. Han and J. L. Hewett, Phys. Rev. D **60** (1999) 074015 [hep-ph/9811237].

[33] H. Fritzsch and D. Holtmannspotter, Phys. Lett. B **457** (1999) 186 [hep-ph/9901411].

[34] A. Heister *et al.*, Phys. Lett. B **543** (2002) 173 [hep-ex/0206070].

[35] J. Abdallah *et al.*, Phys. Lett. B **590** (2004) 21 [hep-ex/0404014].

[36] P. Achard *et al.*, Phys. Lett. B **549** (2002) 290 [hep-ex/0210041].

[37] G. Abbiendi et al., Phys. Lett. B **521** (2001) 181 [hep-ex/0110009].

[38] F. Abe et al., Phys. Rev. Lett. **80** (1998) 2525.

[39] S. Chekanov et al., Phys. Lett. B **559** (2003) 153 [hep-ex/0302010];
S. Chekanov et al., *Search for single-top production in e p collisions at HERA. (Addendum)* (unpublished), internal note DESY-03-188, 2003.

[40] A. Aktas et al., Eur. Phys. J. C **33** (2004) 9 [hep-ex/0310032].

[41] J. J. Liu, C. S. Li, L. L. Yang and L. G. Jin, Phys. Lett. B **599** (2004) 92 [hep-ph/0406155].

[42] J. M. Yang, B. L. Young and X. Zhang, Phys. Rev. D **58** (1998) 055001 [hep-ph/9705341].

[43] D. Atwood, L. Reina and A. Soni, Phys. Rev. D **55** (1997) 3156 [hep-ph/9609279].

[44] F. del Aguila, J. A. Aguilar-Saavedra and R. Miquel, Phys. Rev. Lett. **82** (1999) 1628 [hep-ph/9808400];
J. A. Aguilar-Saavedra, Phys. Rev. D **67** (2003) 035003 [Erratum-ibid. D **69** (2004) 099901] [hep-ph/0210112].

[45] A. Belyaev and N. Kidonakis, Phys. Rev. D **65** (2002) 037501 [hep-ph/0102072].

[46] D. Dannheim, *Search for events with isolated leptons and large missing transverse momentum in e p collisions at HERA* (unpublished), PhD thesis, DESY-THESIS-2003-025, 2003.

[47] A. Pukhov et al., hep-ph/9908288;
E. E. Boos *et al.*, MGU-89-63/140.

[48] I. I. Y. Bigi and S. Rudaz, Phys. Lett. B **153** (1985) 335.

[49] W. Porod, Phys. Rev. D **59** (1999) 095009 [hep-ph/9812230].

[50] T. Kon and T. Kobayashi, Phys. Lett. B **409** (1997) 265 [hep-ph/9704221].

[51] W. Porod, D. Restrepo and J. W. F. Valle, hep-ph/0001033.

[52] Y. Fukuda et al., Phys. Rev. Lett. **81** (1998) 1562 [hep-ex/9807003];
Q. R. Ahmad et al., Phys. Rev. Lett. **87** (2001) 071301 [nucl-ex/0106015];
K. Eguchi et al., Phys. Rev. Lett. **90** (2003) 021802 [hep-ex/0212021].

[53] M. Flanz, W. Rodejohann and K. Zuber, Phys. Lett. B **473** (2000) 324 [Erratum-ibid. B **480** (2000) 418] [hep-ph/9911298];
G. Belanger, F. Boudjema, D. London and H. Nadeau, Phys. Rev. D **53** (1996) 6292 [hep-ph/9508317];
G. Ingelman and J. Rathsman, Z. Phys. C **60** (1993) 243.

[54] W. Rodejohann and K. Zuber, Phys. Rev. D **62** (2000) 094017 [hep-ph/0005270].

[55] E. Nardi, E. Roulet and D. Tommasini, Phys. Lett. B **344** (1995) 225 [hep-ph/9409310].

[56] *Hera – A Proposal For A Large Electron Proton Colliding Beam Facility At Desy* (unpublished), internal note DESY-HERA-81-10, 1981.

[57] W. Buchmüller and G. Ingelman (ed.), *Physics at HERA. Proceedings, Workshop, Hamburg, Germany, October 29 - 30, 1991. Vol. 1 - 3* (unpublished).

[58] G. Ingelman, A. De Roeck and R. Klanner (ed.), *Future physics at HERA. Proceedings, Workshop, Hamburg, Germany, September 25, 1995 - May 31, 1996. Vol. 1, 2* (unpublished), internal note DESY-96-235.

[59] M. Seidel, *The Upgraded Interactions Regions of HERA* (unpublished), internal note DESY-HERA-00-01, 2000.

[60] U. Schneekloth (ed.), *The HERA luminosity upgrade* (unpublished), internal note DESY-HERA-98-05, 1998.

[61] U. Holm (ed.), *The ZEUS detector: Status report 1993* (unpublished), internal note ZEUS-STATUS-REPT-1993.

[62] B. Bock et al., Nucl. Instrum. Meth. A **344** (1994) 335.

[63] S. Fourletov, Nucl. Instrum. Meth. A **535** (2004) 191;
ZEUS Coll., *A Straw-Tube Tracker for ZEUS* (unpublished), internal note ZEUS-98-046, 1998.

[64] A. Bamberger et al., Nucl. Instrum. Meth. A **401** (1997) 63.

[65] ZEUS Coll., *A Microvertex Detector for ZEUS* (unpublished), internal note DESY-PRC 97/01, 1997.

[66] D. Dannheim et al., Nucl. Instrum. Meth. A **505** (2003) 663 [hep-ex/0212026];
V. Chiochia, Nucl. Instrum. Meth. A **501** (2003) 60 [hep-ex/0111061];
E. N. Koffeman, Nucl. Instrum. Meth. A **473** (2001) 26;
M. C. Petrucci, Int. J. Mod. Phys. A **16S1C** (2001) 1078;
U. Kötz, Nucl. Instrum. Meth. A **461** (2001) 210;
A. Garfagnini and U. Kötz, Nucl. Instrum. Meth. A **461** (2001) 158;
C. Coldewey, Nucl. Instrum. Meth. A **453** (2000) 149;
E. N. Koffeman, Nucl. Instrum. Meth. A **453** (2000) 89;
C. Coldewey, Nucl. Instrum. Meth. A **447** (2000) 44;
R. Klanner, *The ZEUS microvertex detector* (unpublished), prepared for International Europhysics Conference on High-Energy Physics (EPS-HEP 99), Tampere, Finland, 15-21 Jul 1999;
A. Garfagnini, Nucl. Instrum. Meth. A **435** (1999) 34.

[67] L. A. T. Bauerdick et al., Nucl. Instrum. Meth. A **501** (2003) 340 [hep-ex/0212037].

[68] M.J. Kraan (ed.): *Mechanical Design Vertex Detector* (unpublished), available on
`http://www.nikhef.nl/pub/departments/mt/projects/zeus/vertex/website.html`,
2001.

[69] M. Feuerstack-Raible, Nucl. Instrum. Meth. A **447** (2000) 35;
C. Bauer et al., *The HELIX128 readout chip family for silicon microstrip detectors and microstrip gaseous chambers* (unpublished), given at 4th Workshop on Electronics for LHC Experiments (LEB 98), Rome, Italy, 21-25 Sep 1998.

[70] B. Foster et al., Nucl. Instrum. Meth. A **338** (1994) 254.

[71] R. Hall-Wilton, N. McCubbin, P. Nylander, M. Sutton and M. Wing, *The CTD Tracking Resolution* (unpublished), internal note ZEUS-99-024, 1999.

[72] E. Maddox, *Study of Heavy Quark Production at HERA Using the ZEUS Microvertex Detector* (unpublished), PhD thesis, University of Amsterdam, Amsterdam (Netherlands), 2004

[73] A. D. Tapper, private communication, 2005

[74] A. Andresen et al., Nucl. Instrum. Meth. A **309** (1991) 101;
M. Derrick et al., Nucl. Instrum. Meth. A **309** (1991) 77.

[75] A. Bernstein et al., Nucl. Instrum. Meth. A **336** (1993) 23.

[76] J. Krüger, Nucl. Instrum. Meth. A **315** (1992) 311.

[77] K. T. Pozniak et al., Proc. SPIE **5484** (2004) 186;
T. Jezynski et al., Proc. SPIE **5484** (2004) 180.

[78] G. Battistoni et al., Nucl. Instrum. Meth. **217** (1983) 429.

[79] G. Abbiendi et al., Nucl. Instrum. Meth. A **333** (1993) 342.

[80] M. De Giorgi et al., Nucl. Instrum. Meth. A **378** (1996) 472.

[81] A. Longhin, *Measurement of Beauty Production at HERA with a D^* + Muon Tag* (unpublished), PhD thesis, DESY-THESIS-04-050, 2004.

[82] S. D. Paganis, Int. J. Mod. Phys. A **16S1C** (2001) 1147;
J. Andruszkow et al., Acta Phys. Polon. B **32** (2001) 2025.

[83] R. L. Glueckstern and M. H. Hull, Phys. Rev. **90** (1953) 1026.

[84] A. Kotarba and K. Piotrzkowski, Nucl. Instrum. Meth. A **387** (1997) 235.

[85] L. Bellagamba, C. Fry, M. Kataoka, K. Nagano, U. Stösslein and A. Tapper, *Requirements for the lepton beam polarisation at HERA II* (unpublished), internal note ZEUS-05-003, 2005

[86] S. Chekanov et al., *Measurement of high Q^2 deep inelastic scattering cross sections with longitudinally polarise lepton beams at HERA* (unpublished), submitted to the XXII International Symposium on Lepton-Photon Interactions at High Energy (LP 2005), Uppsala, Sweden, 30 Jun - 5 Jul 2005.

[87] A. A. Sokolov and I. M. Ternov, Phys. Dokl. **8** (1964) 1203.

[88] D. P. Barber et al., Phys. Lett. B **343** (1995) 436.

[89] M. Beckmann et al., Nucl. Instrum. Meth. A **479** (2002) 334 [physics/0009047].

[90] J. Böhme, Acta Phys. Polon. B **33** (2002) 3949.

[91] O. Ota, *Polarimeter status report* (unpublished), given at the ZEUS Collaboration Meeting, Hamburg, Germany, 28 Feb - 4 Mar 2005.

[92] R. Carlin, W. H. Smith, K. Tokushuku and L. W. Wiggers, Nucl. Instrum. Meth. A **379** (1996) 542;
R. Carlin, W. H. Smith, K. Tokushuku and L. W. Wiggers, Nucl. Phys. Proc. Suppl. **44** (1995) 430;
W. H. Smith, K. Tokushuku and L. W. Wiggers, *The ZEUS trigger system* (unpublished), contributed to 10th International Conference on Computing in High Energy Physics (CHEP 92), Annecy, France, 21-25 Sept 1992, internal note DESY-92-150B.

[93] J. C. Hart, *Experience With Adamo In Zeus* (unpublished), in "Erice 1990, Proceedings, Data Structures for Particle Physics Experiments", 51-57;
S. Fisher and P. Palazzi, ADAMO *Reference Manual for Version 3.3* (unpublished), available on
`http://adamo.web.cern.ch/Adamo/refmanual/Document.html`,
1993.

[94] U. Stoesslein, *ZEUS Evtake and Lumi page* (unpublished), available on
`http://www-zeus.desy.de/physics/lumi`,
2005.

[95] G. Gustafson and U. Pettersson, Nucl. Phys. B **306** (1988) 746;
G. Gustafson and U. Pettersson, *Addendum To Dipole Formulation Of QCD Cascades (Lu-Tp-87-9)* (unpublished), internal note LU-TP-87-19

[96] B. Andersson, G. Gustafson, G. Ingelman and T. Sjostrand, Phys. Rept. **97** (1983) 31.

[97] B. R. Webber, Nucl. Phys. B **238** (1984) 492.

[98] H. L. Lai *et al.*, Eur. Phys. J. C **12** (2000) 375 [hep-ph/9903282].

[99] T. Sjostrand, hep-ph/9508391.

[100] K. J. Kim and S. Kartik, preprint LSUHE-145-1993, 1993.

[101] K. Hagiwara, D. Zeppenfeld and S. Komamiya, Z. Phys. C **29** (1985) 115;
U. Baur, M. Spira and P. M. Zerwas, Phys. Rev. D **42** (1990) 815;
F. Boudjema, A. Djouadi and J. L. Kneur, Z. Phys. C **57** (1993) 425.

[102] C. Berger and W. Wagner, Phys. Rept. **146** (1987) 1.

[103] A. D. Martin, W. J. Stirling and R. G. Roberts, Phys. Rev. D **50** (1994) 6734 [hep-ph/9406315].

[104] G. Ingelman, A. Edin and J. Rathsman, Comput. Phys. Commun. **101** (1997) 108 [hep-ph/9605286].

[105] A. D. Martin, R. G. Roberts, W. J. Stirling and R. S. Thorne, Eur. Phys. J. C **14** (2000) 133 [hep-ph/9907231];
A. D. Martin, R. G. Roberts, W. J. Stirling and R. S. Thorne, Eur. Phys. J. C **4** (1998) 463 [hep-ph/9803445].

[106] T. Sjostrand, L. Lonnblad and S. Mrenna, *PYTHIA 6.2: Physics and manual* (unpublished), hep-ph/0108264.

[107] A. S. Belyaev *et al.*, hep-ph/0101232.

[108] A. Kwiatkowski, H. Spiesberger and H. J. Mohring, Comput. Phys. Commun. **69** (1992) 155.

[109] G. A. Schüler and H. Spiesberger, *DJANGO: The Interface for the event generators HERACLES and LEPTO*, in *Physics at HERA. Proceedings, Workshop, Hamburg, Germany, October 29 - 30, 1991. Vol. 3*, 1419-1432 (unpublished, see HIGH ENERGY PHYSICS INDEX 30 (1992) No. 12988).

[110] L. Lönnblad, *Ariadne version 4*, in *Physics at HERA. Proceedings, Workshop, Hamburg, Germany, October 29 - 30, 1991. Vol. 3*, 1440-1445 (unpublished, see HIGH ENERGY PHYSICS INDEX 30 (1992) No. 12988).

[111] G. Marchesini, B. R. Webber, G. Abbiendi, I. G. Knowles, M. H. Seymour and L. Stanco, Comput. Phys. Commun. **67** (1992) 465.

[112] H. L. Lai *et al.*, Phys. Rev. D **55** (1997) 1280 [hep-ph/9606399].

[113] M. Glück, E. Reya and A. Vogt, Phys. Rev. D **46** (1992) 1973.

[114] T. Abe, Comput. Phys. Commun. **136** (2001) 126 [hep-ph/0012029].

[115] R. Brun, F. Bruyant, M. Maire, A. C. McPherson and P. Zanarini, *Geant3* (unpublished), internal note CERN-DD/EE/84-1, 1987.

[116] available on
`http://www-zeus.desy.de/components/funnel/MONTE_CARLO/03/03t0.1.html`,
2005.

[117] R. Mankel, *ZEUS Offline Homepage* (unpublished), available on
`http://www-zeus.desy.de/components/offline/offline.html`,
2004.

[118] S. Chekanov *et al.*, Phys. Lett. B **539** (2002) 197 [Erratum-ibid. B **552** (2003) 308] [hep-ex/0205091].

[119] K. Nagano, *Hadronic Energy Scale checked with NC events* (unpublished), contributed to the ZEUS Collaboration Meeting, Amsterdam, Netherlands, 8-12 Oct 2005.

[120] J. Breitweg *et al.*, Eur. Phys. J. C **11** (1999) 427 [hep-ex/9905032];
J. Grosse-Knetter, *Corrections for the Hadronic Final State* (unpublished), internal note ZEUS-98-031, 1998.

[121] S. Bentvelsen, J. Engelen and P. Kooijman, *Reconstruction of (x,Q^2) and extraction of structure functions in neutral current scattering at HERA* in [57, p.23].

[122] A. Blondel and F. Jacquet in: U. Amaldi (ed.), *Study Of An E P Facility For Europe: Proceedings* (unpublished), Ecfa, Hamburg, Germany, April 2-3, 1979, internal note DESY-79-48

[123] S. Catani, Y. L. Dokshitzer, M. H. Seymour and B. R. Webber, Nucl. Phys. B **406** (1993) 187.

[124] S. D. Ellis and D. E. Soper, Phys. Rev. D **48** (1993) 3160 [hep-ph/9305266].

[125] O. Gonzales, H. Raach and J. Terron *Measurements of the inclusive jet cross sections in NC DIS in the Breit Frame and determination of* α_s (unpublished), internal note ZEUS-02-007, 2002.

[126] G. F. Hartner, Y. Iga, J. B. Lane, N. A. McCubbin and M. Wing, *VCTRAK(3.07/04): Offline Output Information* (unpublished), internal note ZEUS-97-064, 1997;
G. F. Hartner, *VCTRAK Briefing: Program and Math* (unpublished), internal note ZEUS-98-58, 1998.

[127] J. Breitweg *et al.*, Z. Phys. C **74** (1997) 207 [hep-ex/9702015];
A. Kappes, *Verwendung von Neuronalen Netzen zur Identifikation des*

Gestreuten Elektrons in ep-Ereignissen mit hohem Q^2 bei ZEUS (unpublished), diploma thesis, BONN-IB-97-28, 1997.

[128] R. Sinkus and T. Voss, Nucl. Instrum. Meth. A **391** (1997) 360.

[129] A. Geiser, *GMUON* (unpublished), available on `http://www-zeus.desy.de/~geiser/muon/gmuon.html`, 2003.

[130] A. Geiser, private communication, 2005.

[131] L. Lindfeld, Nucl. Phys. Proc. Suppl. **144** (2005) 315.

[132] C. N. Nguyen, *Identification of tau leptons from single $W \to$ tau nu/tau production with the ZEUS detector* (unpublished), diploma thesis, DESY-THESIS-2002-024, 2002

[133] N. Tuning, *ZUFOs: Hadronic final state reconstruction with calorimeter, tracking and backsplash corrections* (unpublished), internal note ZEUS-01-021, 2001.

[134] T. Matsushita, *Search for events witha high energy isolated lepton and large missing transverse momentum in ep collisions at $\sqrt{s} = 300\,GeV$* (unpublished), PhD thesis, Tokyo Metropolitan University, Tokyo (Japan), 1998.

[135] K. Nagano, private communication, 2005

[136] I. Bloch, *Measurement of beauty production from dimuon events at HERA / ZEUS* (unpublished), PhD thesis, DESY-THESIS-2005-034, 2005.

[137] D. Bailey *et al.*, *Study of beam-induced backgrounds in the ZEUS detector from 2002 HERA running* (unpublished), internal note ZEUS-02-018, 2002;
D. Bailey *et al.*, *Addendum - Study of beam-induced backgrounds in the ZEUS detector from 2002 HERA running* (unpublished), internal note ZEUS-02-020, 2002;
D. Bailey *et al.*, *Addendum - Study of beam-induced backgrounds in the ZEUS detector from 2002 HERA running* (unpublished), internal note ZEUS-02-027, 2003.

[138] O. Kind *et al.*, eConf **C0303241** (2003) MOLT002 [hep-ex/0305095].

[139] K. Nagano, *Measurement of Charged-Current e^+p Deep Inelastic Scattering Cross Sections at $\sqrt{s} = 300\,GeV$* (unpublished), PhD thesis, University of Tokyo, Tokyo (Japan), 1998.

[140] S. Chekanov *et al.*, Phys. Lett. B **583** (2004) 41 [hep-ex/0311028].

[141] F. Richard, J. R. Schneider, D. Trines and A. Wagner, *TESLA: The superconducting electron positron linear collider with an integrated X-ray laser laboratory. Technical Design Report Part I: Executive Summary* (unpublished), hep-ph/0106314.

[142] R. Brinkmann, K. Flottmann, J. Rossbach, P. Schmusuer, N. Walker and H. Weise, *TESLA: The superconducting electron positron linear collider with an integrated X-ray laser laboratory. Technical design report Part II: The Accelerator* (unpublished), internal note DESY-01-011, 2001.

[143] J. A. Aguilar-Saavedra *et al.*, *TESLA: The superconducting electron positron linear collider with an integrated X-ray laser laboratory. Technical Design Report Part III: Physics at an e+e- Linear Collider* (unpublished), hep-ph/0106315.

[144] P. Gay, *Energy flow with high granularity calorimeters* (unpublished), prepared for 5th International Linear Collider Workshop (LCWS 2000), Fermilab, Batavia, Illinois, 24-28 Oct 2000

[145] T. Behnke, S. Bertolucci, R. D. Heuer and R. Settles, *TESLA: The superconducting electron positron linear collider with an integrated X-ray laser laboratory. Technical design report Part IV: A Detector for TESLA* (unpublished), internal note DESY-01-011, 2001.

[146] K. Ackermann *et al.*, *Extended joint ECFA/DESY study on physics and detector for a linear e+ e- collider. Proceedings, Summer Colloquium, Amsterdam, Netherlands, April 4, 2003*, DESY-PROC-2004-01 prepared for 4th ECFA/DESY Workshop on Physics and Detectors for a 90-GeV to 800-GeV Linear e+ e- Collider, Amsterdam, The Netherlands, 1-4 Apr 2003

[147] M. Winter, *New developments for silicon detectors*, prepared for 31st International Conference on High Energy Physics (ICHEP 2002), Amsterdam, The Netherlands, 24-31 Jul 2002;
G. Claus *et al.*, Nucl. Instrum. Meth. A **473** (2001) 83;
G. Deptuch, Y. Gornushkin, M. Winter, G. Claus, W. Dulinski and D. Husson, *Monolithic active pixel sensors for a linear collider*, prepared for 5th International Linear Collider Workshop (LCWS 2000), Fermilab, Batavia, Illinois, 24-28 Oct 2000.

[148] *MIMOSA 5*, available on
`http://ireswww.in2p3.fr/ires/recherche/capteurs/mimosa5.html`,
2001.

[149] M. Battaglia *et al.*, Nucl. Instrum. Meth. A **447** (2000) 202 [hep-ex/9911013].

[150] M. Amati *et al.*, Nucl. Instrum. Meth. A **511** (2003) 265.

[151] C. J. S. Damerell, Nucl. Instrum. Meth. A **541** (2005) 178;
C. J. S. Damerell, Rev. Sci. Instrum. **69** (1998) 1549.

[152] R. H. Richter *et al.*, Nucl. Instrum. Meth. A **511** (2003) 250;
P. Fischer *et al.*, *A DEPFET based pixel vertex detector for the detector at TESLA* (unpublished), internal note LC-DET-2002-004, 2002.

[153] D. E. Groom *et al.* (Particle Data Group), Eur. Phys. J. C **15** (2000) 1.

[154] T. Behnke and G. A. Blair, *BRAHMS - Version 102: A Monte Carlo for a detector at a 500-GeV to 800-GeV linear collider* (unpublished), internal note LC-PHSM-2001-005, 2001;
BRAHMS - A GEANT 3 Based Simulation of the TESLA Detector Response (unpublished), available on
`http://www-zeuthen.desy.de/lc_repository/detector_simulation/dev/BRAHMS/readme.html`,
2005.

[155] M. Pohl and H. J. Schreiber, *SIMDET - Version 4: A parametric Monte Carlo for a TESLA detector* (unpublished), hep-ex/0206009;
SIMDET - A Fast Simulation Tool for Linear Collider Detector Studies (unpublished), available on
`http://www-zeuthen.desy.de/lc_repository/detector_simulation/dev/SIMDET/readme.html`,
2003.

[156] M. Berggren, *SGV - Simulation a Grande Vitesse* (unpublished) available on
`http://berggren.home.cern.ch/berggren/sgv.html`,
2002.

[157] M. Berggren, *SGV 2.31 - Simulation a Grande Vitesse, ver2.31, User's Guide* (unpublished), available on
`http://berggren.home.cern.ch/berggren/sgv_ug/sgv_ug.html`,
2003.

[158] T. Sjostrand, Comput. Phys. Commun. **82** (1994) 74;
T. Sjostrand, *PYTHIA 5.7 and JETSET 7.4: Physics and manual* (unpublished), hep-ph/9508391.

[159] T. Sjostrand, L. Lonnblad, S. Mrenna and P. Skands, *PYTHIA 6.3: Physics and manual* (unpublished), hep-ph/0308153;
T. Sjostrand, P. Eden, C. Friberg, L. Lonnblad, G. Miu, S. Mrenna and E. Norbin, Comput. Phys. Commun. **135** (2001) 238 [hep-ph/0010017].

[160] S. Katsanevas and P. Morawitz, Comput. Phys. Commun. **112** (1998) 227 [hep-ph/9711417].

[161] R. Hawkings, *Vertex detector and flavor tagging studies for the TESLA linear collider* (unpublished), internal note LC-PHSM-2000-021, 2000.

[162] S. M. Xella Hansen, M. Wing, D. J. Jackson, N. De Groot and C. J. S. Damerell, *Update on flavour tagging studies for the future linear collider using the BRAHMS simulation* (unpublished), internal note LC-PHSM-2003-061, 2003;
S. Xella-Hansen, D. J. Jackson, R. Hawkings and C. J. S. Damerell, *Flavour tagging studies for the TESLA linear collider* (unpublished), internal note LC-PHSM-2001-024, 2001.

[163] D. Buskulic *et al.*, Phys. Lett. B **313** (1993) 535.

[164] D. J. Jackson, Nucl. Instrum. Meth. A **388** (1997) 247.

[165] K. Abe *et al.*, Phys. Rev. Lett. **80** (1998) 660 [hep-ex/9708015].

[166] C. Peterson, T. Rognvaldsson and L. Lonnblad, Comput. Phys. Commun. **81** (1994) 185.

[167] S. Brandt, C. Peyrou, R. Sosnowski and A. Wroblewski, Phys. Lett. **12** (1964) 57;
E. Farhi, Phys. Rev. Lett. **39** (1977) 1587.

[168] M. Beneke, Phys. Lett. B **434** (1998) 115 [hep-ph/9804241].

[169] S. V. Chekanov and V. L. Morgunov, Phys. Rev. D **67** (2003) 074011 [hep-ex/0301014].

[170] W. Bartel *et al.*, Z. Phys. C **33** (1986) 23;
S. Bethke, habilitation thesis, LBL-50-208, 1987.

[171] S. Hillert, *Physical potential of vertex detector as function of beampipe radius* (unpublished), prepared for 2005 International Linear Collider Physics and Detector Workshop and Second ILC Accelerator Workshop, Snowmass, Collorado, 14-27 Aug 2005;
S. Hillert, *Heavy flavour ID and quark charge measurement with an ILC vertex detector* (unpublished), prepared for 2005 International Linear Collider Workshop (LCWS 2005), Stanford, California, 18-22 Mar 2005.

[172] P. Luzniak, *Measurement of SM Higgs branching fractions and VXD optimization* (unpublished), prepared for 1st Workshop of ECFA Study on Physics and Detectors for a Linear Collider, Montpellier, France, 13-16 Nov 2003.

[173] T. Carli and B. Koblitz, Nucl. Instrum. Meth. A **501** (2003) 576 [hep-ex/0211019].

[174] J. Breitweg *et al.*, Phys. Lett. B **471** (2000) 411 [hep-ex/9907023].

[175] ZEUS Coll., *Search for W production using the electron decay-channel in e^+p collisions at HERA I* (unpublished), paper 4-0259 submitted to 32st International Conference on High Energy Physics (ICHEP 2004), Beijing, China, 16-22 Aug 2004.

[176] V. Andreev *et al.*, Phys. Lett. B **561** (2003) 241 [hep-ex/0301030].

[177] C. Adloff *et al.*, Eur. Phys. J. C **5** (1998) 575 [hep-ex/9806009].

[178] H1 Coll., *Events with an isolated lepton and missing transverse momentum at HERA* (unpublished), paper 637 submitted to International Europhysics Conference on High-Energy Physics (HEP 2005), Lisboa, Portugal, 21-27 Jul 2005.

[179] H1 Coll., *Search for events with tau leptons in ep collisions at HERA* (unpublished), paper 624 submitted to International Europhysics Conference on High-Energy Physics (HEP 2005), Lisboa, Portugal, 21-27 Jul 2005.

[180] R. Brun and F. Rademakers, Nucl. Instrum. Meth. A **389** (1997) 81;
R. Brun, A. Gheata and M. Gheata, Nucl. Instrum. Meth. A **502** (2003) 676;
see also
`http://root.cern.ch/`.

[181] A. Geiser, *ZEUS Analysis: Muons* (unpublished), available on
`http://www.desy.de/~geiser/muon/`,
2003.

[182] G. Abbiendi *et al.*, *Observation of $J/\psi \to \mu^+\mu^-$ in the first 274 nb^{-1} of 1993 run* (unpublished), internal note ZEUS-93-120, 1993.

[183] G. Abbiendi *et al.*, *Global Tracking of muons in the Barrel and Rear region* (unpublished), internal note ZEUS-99-063, 1999.

[184] M. Corradi, *Mpmatch2 Web Page* (unpublished), available on
`http://www-zeus.desy.de/~corradi/ZEUS_ONLY/mpmatch/mpmatch2.html`,
2003.

[185] M. Berggren, *SGV - Simulation a Grande Vitesse - LC specials* (unpublished) available on
`http://berggren.home.cern.ch/berggren/lc/sgv_lc.html`,
2002.

Acknowledgements

The accomplishment of this thesis is the result of combined efforts of many, many people inside and outside the ZEUS collaboration. I owe them all a lot. In particular, I would like to thank:

Prof. Robert Klanner for giving me the opportunity to work on this thesis and for laud and blame; Tobias Haas for being a calm and wise supervisor and for his continous support and trust in my work; Tancredi Carli for initiating this thesis; Dominik Dannheim for sharing all the knowledge and tools of his isolated lepton search; Wolfram Zeuner for his unbelievable patience; Prof. Peter Schleper for asking important questions; the ZEUS High-Q^2 group for being a source of hints, ideas and encouragement, especially James Ferrando, Elisabetta Gallo, Kunihiro Nagano, Alex Tapper and Katarzyna Wichmann; Achim Geiser for his explanations on muon identification; Ingo Bloch for his explanations on particle backgrounds; Chi-Nhan Nguyen and Claus Horn for explaining SUSY and the disriminant method; and, of course, the whole ZEUS collaboration for providing this great experiment.

Thorsten Kuhl for irreplacable help concerning the heavy flavour tagging; Mikael Berggren for all the explanations and discussions on SGV, and Sonja Hillert and Pawel Luzniak for sharing the fun of exploring it; Stefania Xella-Hansen for providing the BRAHMS ntuples; Ties Behnke for valuable advice on TESLA simulations.

Prof. Georg Zimmerer and Eckhart Fretwurst for the experiences in teaching and examining; Matthew Wing for standing in for me in an emergency case; Oliver Gutsche for computing support; Peter Buhmann for support in lab preparation; Felix Harbsmeier for having an open-minded look into the draft; Nicola Coppola for entertaining my kids; and – besides those mentioned already – Devis Contarato, Didar Dobur, Maria Hanulova, Benjamin Kahle, Harald Labes, Damir Lelas, Liz Nuncio-Quiroz, Amita Raval, Raquel Santamarta and Ana Yagues for the great working atmosphere, for friendship, fun, travel companion, catering and just for putting up with me at all.

Danke, Biggi! Danke Andrea, Lucas, Nadine und Nico! Was wäre ich ohne Euch?!

Danke auch an den Rest meiner Familie und an meine Freunde dafür, mir viele Dinge abgenommen zu haben, für die ich so oft keine Zeit hatte.